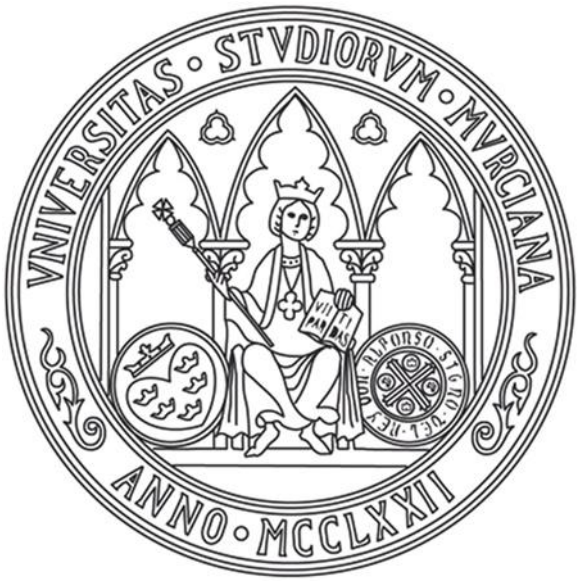

UNIVERSIDAD DE MURCIA

ESCUELA INTERNACIONAL DE DOCTORADO

MGRN1 Como Determinante de la Integridad Genómica y del Fenotipo Maligno de las Células de Melanoma

Dña. Idoya M.ª Martínez Vicente

2021

UNIVERSIDAD DE MURCIA

FACULTAD DE MEDICINA

Departamento de Bioquímica y Biología Molecular B e Inmunología

MGRN1 COMO DETERMINANTE DE LA INTEGRIDAD GENÓMICA Y DEL FENOTIPO MALIGNO DE LAS CÉLULAS DE MELANOMA

MGRN1 as a determinant of genomic integrity and malignant phenotype of melanoma cells

Memoria presentada por Idoya M.ª Martínez Vicente
para optar al grado de Doctora por la Universidad de Murcia
(Tesis Doctoral con Mención Internacional)

Murcia, mayo 2021

The studies carried out in this Doctoral Thesis have been partially financed by grants SAF2015-67092-R and SAF2018_RTI2018-094929-B-I00 from MINECO (Spain) and FEDER (European Community) and 19875/GERM/15 from Fundación Seneca, Comunidad Autónoma de la Región de Murcia (CARM).

Idoya M.ª Martínez Vicente has been the holder of the following pre-doctoral scholarships:

- "Contrato predoctoral (FPU) de la Universidad de Murcia 2017" (01/01/2017-30/04/2017).
- "Ayuda para contratos predoctorales para la formación de doctores 2016" (01/05/2017-31/05/2021). "Programa de Formación del Personal Investigador del Ministerio de Economía, Industria y Competitividad (MINECO)". BES-2016-077334.

Some of the results obtained have been included in the following publications:

- **Idoya Martínez-Vicente**, Marta Abrisqueta, Cecilia Herraiz, Celia Jiménez-Cervantes, Jose Carlos García-Borrón and Concepción Olivares.
  Functional characterization of a C-terminal splice variant of the human melanocortin 1 receptor.
  Experimental Dermatology. 2020 May 31. DOI: 10.1111/exd.14118
- **Idoya Martínez-Vicente***, Marta Abrisqueta*, Cecilia Herraiz, Julia Sirés-Campos, María Castejón-Griñán, Dorothy C.Bennett, Conchi Olivares, Jose Carlos García-Borrón and Celia Jiménez-Cervantes. (*equal contribution).
  Mahogunin Ring Finger 1 Is Required for Genomic Stability and Modulates the Malignant Phenotype of Melanoma Cells.
  Cancers. 2020 Oct 1;12(10):2840. DOI: 10.3390/cancers12102840
- **Idoya Martínez-Vicente**, Celia Jiménez-Cervantes and Jose Carlos García-Borrón.
  Epidermis y fotoprotección. El lado oscuro del Sol.
  Boletín SEBBM nº 206, 2020 Dic.
- Cecilia Herraiz**, Idoya Martínez-Vicente** and Vittoria Maresca.
  The α-melanocyte stimulating hormone/melanocortin-1 receptor interaction: A driver of pleiotropic effects beyond pigmentation.
  Pigment Cell & Melanoma Research. 2021 Apr 21. DOI: 10.1111/pcmr.12980

In addition, it has led to the following Communications to National and International Meetings:

- Genome instability and aberrant cell cycle progression in Mahogunin Ring Finger-1 null mouse melanocytes. **Idoya Martínez-Vicente**, Cecilia Herraiz, Marta Abrisqueta, María Castejón-Griñán, Julia Sirés-Campos, Elena V. Sviderskaya, Dorothy C. Bennett, Conchi Olivares, José Carlos García-Borrón, Celia Jiménez-Cervantes. International Pigment Cell Conference (IPCC) (26/08/2017 to 30/08/2017, Denver, Colorado, USA).
- Mahogunin ring finger 1 as a novel regulator of cell shape, motility and differentiation in melanocytes. Cecilia Herraiz, María Castejón-Griñán, **Idoya Martínez-Vicente**, Marta Abrisqueta, Julia Sirés-Campos, Elena V. Sviderskaya, Dorothy C. Bennett, Conchi Olivares, Celia Jiménez-Cervantes, José Carlos García-Borrón. International Pigment Cell Conference (IPCC) (26/08/2017 to 30/08/2017, Denver, Colorado, USA).
- Induction of a senescent- like phenotype by loss of Mgrn1 expression in mouse melanocytes. **Idoya Martínez-Vicente**, Marta Abrisqueta, María Castejón-Griñán, Conchi Olivares, Cecilia Herraiz, José Carlos García-Borrón, Celia Jiménez-Cervantes. 21st European Society for Pigment Cell Research Meeting (24/09/2018 to 27/09/2018, Rennes, France).
- Downregulation of MGRN1 expression decreases the metastatic potential of melanoma cells *in vitro* and *in vivo*. Cecilia Herraiz; **Idoya Martínez-Vicente**; María Castejón-Griñán; Conchi Olivares; Marta Abrisqueta; Celia Jiménez-Cervantes; José Carlos García-Borrón. 21st European Society for Pigment Cell Research Meeting (24/09/2018 to 27/09/2018, Rennes, France).
- MGRN1 is a regulator of melanoma cells progression through S phase and interacts with CDK2. **Idoya Martínez-Vicente**, Marta Abrisqueta, Ana Lambertos, María Castejón-Griñán, Conchi Olivares, Cecilia Herraiz, José Carlos García-Borrón, Celia Jiménez-Cervantes. 22nd European Society for Pigment Cell Research Meeting (12/09/2019 to 14/09/2019, Brussels, Belgic).
- Mahogunin Ring Finger-1 expression as a determinant of the phenotype and aggressiveness of human melanoma cells. Cecilia Herraiz, **Idoya Martínez-Vicente**, Marta Abrisqueta, Arrate Sevilla, María Dolores Boyano, Santos Alonso, Conchi Olivares, José Carlos García-Borrón, Celia Jiménez-Cervantes. International Pigment Cell Conference (IPCC) (18/06/2020 to 21/06/2020, Yamagata, Japan).
- Increased genomic instability in melanocytes lacking Mgrn1. José Carlos García-Borrón, **Idoya Martínez-Vicente**, Marta Abrisqueta, Cecilia Herraiz, Sara Egea, Sonia Cerdido, Conchi Olivares, Celia Jiménez-Cervantes. International Pigment Cell Conference (IPCC) (18/06/2020 to 21/06/2020, Yamagata, Japan).

- Mgrn1: proteína reguladora de la proliferación y diferenciación de los melanocitos. **Idoya Martínez-Vicente**, Marta Abrisqueta, María Castejón-Griñán, Julia Sirés-Campos, Conchi Olivares, Cecilia Herraiz, José Carlos García-Borrón, Celia Jiménez-Cervantes. III Jornadas Doctorales de la Universidad de Murcia (30/05/2017 a 01/06/2017, Murcia, Spain).
- Genome instability and aberrant cell cycle progression in Mahogunin Ring Finger-1 null mouse melanocytes. **Idoya Martínez-Vicente**, Marta Abrisqueta, María Castejón-Griñán, Julia Sirés-Campos, Conchi Olivares, Cecilia Herraiz, José Carlos García-Borrón, Celia Jiménez-Cervantes. II Jornadas Científicas del IMIB-Arrixaca (27/11/2017, Murcia, Spain).
- Inestabilidad genómica y progression aberrante a través del ciclo celular en melanocitos Mgrn1-KO. **Idoya Martínez-Vicente**, Marta Abrisqueta, María Castejón-Griñán, Julia Sirés-Campos, Conchi Olivares, Cecilia Herraiz, José Carlos García-Borrón, Celia Jiménez-Cervantes. IV Jornadas Doctorales de la Universidad de Murcia (29/05/2018 a 31/05/2018, Murcia, Spain).
- Loss of mgrn1 expression induces senescent-like phenotype in mouse melanocytes. **Idoya Martínez-Vicente**, Marta Abrisqueta, María Castejón-Griñán, Julia Sirés-Campos, Conchi Olivares, Cecilia Herraiz, José Carlos García-Borrón, Celia Jiménez-Cervantes. III Jornadas Científicas del IMIB-Arrixaca (19/11/2018, Murcia, Spain).
- MGRN1: proteína reguladora de la proliferación y progresión a través del ciclo celular en melanocitos y células de melanoma. **Idoya Martínez-Vicente**, Marta Abrisqueta, María Castejón-Griñán, Julia Sirés-Campos, Conchi Olivares, Cecilia Herraiz, José Carlos García-Borrón, Celia Jiménez-Cervantes. V Jornadas Doctorales de la Universidad de Murcia (29/05/2019 a 31/05/2019, Murcia, Spain).
- Loss of mgrn1 increases genomic instability in mouse melanocytes. **Idoya Martínez-Vicente**, Sonia Cerdido, Marta Abrisqueta, Ana Lambertos, Cecilia Herraiz, Conchi Olivares, Celia Jiménez-Cervantes, José Carlos García-Borrón. V Jornadas Científicas del IMIB-Arrixaca (23/11/2020, Murcia, Spain).
- The role of MGRN1 in the cell cycle progression and genomic integrity in human melanoma cells of defined TP53 genotype. Sonia Cerdido, **Idoya Martínez-Vicente**, Marta Abrisqueta, Ana Lambertos, Cecilia Herraiz, Conchi Olivares, Celia Jiménez-Cervantes, José Carlos García-Borrón. V Jornadas Científicas del IMIB-Arrixaca (23/11/2020, Murcia, Spain).

A mis padres Juan y Sagrario,

a mi hermano Alfonso y a Javi

AGRADECIMIENTOS

En primer lugar, me gustaría agradecer a mis directoras, Celia y Cecilia, y a mi tutor, Jose Carlos, por darme la oportunidad de realizar este trabajo, formarme, confiar en mí y apoyarme tanto personal como profesionalmente.

Gracias especialmente a mis compañeras y amigas: Conchi, Ceci, Ana, Julia, María, Marta y Sonia. Sin vosotras esta etapa no hubiera sido lo mismo. He tenido mucha suerte de rodearme de personas como vosotras, siempre dispuestas a escuchar, ayudar y a crear un buen ambiente de trabajo. Gracias también por los buenos momentos fuera del laboratorio.

Quisiera agradecer también a Paco Arques, Fernando y a todos los miembros del departamento de Bioquímica y Biología Molecular B e Inmunología.

A Julieta, Leo, Rebeca y Paula, por ser los mejores compañeros de pasillo, cursos de doctorado, comidas, cafés y risas.

A los Servicios de Cultivos de Tejidos, Microscopía y Biología Molecular de la Universidad de Murcia.

A Lluis Fajas, por permitirme realizar la estancia en su laboratorio, ayudarme y tratarme como una más de su equipo. Gracias también a todos los integrantes del grupo, por hacerme la estancia más fácil y divertida.

También a Lola Boyano y Santos, por abrirme las puertas a colaborar con ellos y ser tan amables conmigo. A las chicas, especialmente a Arrate, por ayudarme en el laboratorio, enseñarme la ciudad y por los buenos ratos.

Al grupo de Ghanem, también por darnos la oportunidad de colaborar y trabajar con ellos. Gracias por ayudarnos en todo lo que necesitamos.

A mis amigos, un pilar fundamental en mi vida. Gracias por apoyarme y quererme en todas mis etapas, especialmente durante esta última. Por ayudarme a desconectar y a disfrutar de nosotros y del tiempo libre.

Por último, me gustaría agradecer a toda mi familia (a mi segunda familia también). Lo más importante para mí. En especial a mis padres, mi hermano y Javi, por quererme y apoyarme incondicionalmente. Os agradezco mucho todo lo que hacéis por mí.

TABLE OF CONTENTS

TABLE OF CONTENTS

ACRONYMS

ACRONYMS

8-oxodG: 8-oxo-7,8-dihydroguanine

AA: acral areas

ACTH: adrenocorticotropic hormone

AJCC: American Joint Committee on Cancer

ALM: acral-lentiginous melanoma

APS: ammonium persulfate

ARRB: β-arrestin

ASIP: agouti signaling protein

ATM: ataxia-telangiectasia-mutated kinase

ATR: ataxia-telangiectasia-mutated and Rad3-related kinase

ATRIP: ATR-interacting protein

BCA: bicinchoninic acid

BrdU: 5-bromo-20-deoxyuridine

BSA: bovine serum albumin

cAMP: cyclic adenosine monophosphate

CDK: cyclin-dependent kinase

CDKN2A: cyclin dependent kinase inhibitor 2A

CHK: checkpoint kinase

CldU: 5-chloro-2'-deoxyuridine

CNS: central nervous system

crRNA: crispr-RNA

CSK: cytoskeletal

CT: computed tomography

Ct: cut-off cycle

CTR: control

DDR: DNA damage response

dNTP: deoxynucleotide triphosphate

dPCR: digital polymerase chain reaction

DQ: DOPAquinone

DSB: double strand break

DT: doubling time

DTT: dithiothreitol

EDTA: ethylenediaminetetraacetic acid

EGTA: ethylene glycol tetraacetic acid

ERK: extracellular signal-regulated kinase

ESCRT-I: endosomal sorting complex required for transport-I

FBS: fetal bovine serum

GPCR: G-protein-coupled receptor

Gαi: G protein subunit Gαi

HERC2: HECT and RLD Domain Containing E3 Ubiquitin Protein Ligase 2

HN: head and neck

HPF: high power fields

HU: hydroxyurea

IAA: iodoacetamide

IdU: 5-iodo-2'-deoxyuridine

LB: lysogeny Broth

L-DOPA: L-3,4-dihydroxyphenylalanine

LE: lower extremities

MAPK: mitogen-activated protein kinase

MCR: melanocortin receptor

md: mahoganoid allele

Mfn1: mitofusin 1

MGRN1: mahogunin RING finger protein 1

MITF: microphthalmia-associated transcription factor

MS: mass spectrometry

NCS: neocarzinostatin

NDP-MSH: synthetic α melanocyte stimulating hormone analogue [Nle4, D-Phe7] αMSH

NEM: N-ethylmaleimide

NLS: nuclear localization signal

NM: nodular melanoma

nt: nucleotides

OCA2: oculocutaneous albinism type 2

ON: overnight

ORF: open reading frame

OS: overall survival

PAM: protospacer adjacent motif

PBS: phosphate buffered saline

PFS: progression free survival

PI: propidium iodide

PI3K: phosphoinositide 3-kinase

PIPES: 1,4-piperazinediethanesulfonic acid

PMSF: phenylmethanesulfonyl fluoride

POMC: proopiomelanocortin

PVDF: polyvinylidene difluoride

Rb1: retinoblastoma-associated protein

RF: RING Finger

RGP: radial growth phase

RHC: red hair color

RNase A: ribonuclease A

ROS: reactive oxygen species

RPA: replication protein A

RT: room temperature

RTK: receptor tyrosine kinase

RT-PCR: real time polymerase chain reaction

SDS: sodium dodecyl sulfate

SEM: standard error of the mean

sgRNA: single-guide RNA

SLC45A2: melanoma antigen AIM1

SN: supernatant

SOB: super optimal broth

SOD1: superoxide dismutase 1

ssDNA: single-stranded DNA regions

SSM: superficial spreading melanoma

TEMED: tetramethylethylene-1,2-diamine

TMB: 3,3′,5,5′-tetramethylbenzidine

TOPBP1: DNA topoisomerase 2-binding protein 1

TPA: 12-O-tetradecanoylphorbol-13-acetate

TR: trunk

tracrRNA: trans-activating CRISPR RNA

TSG101: tumor susceptibility gene 101

TUBB3: tubulin-β-III

TYR: tyrosinase

TYRP: tyrosinase-related protein

UE: upper extremities

UTR: untranslated region

UVR: ultraviolet radiation

VGP: vertical growth-phase

WR: working reagent

αMSH: α melanocyte stimulating hormone

βME: β-mercaptoethanol

ΔΔCt: comparative Ct Method for Relative Quantification

RESUMEN/ABSTRACT

RESUMEN

Mahogunina (Mgrn1) es una E3-ubiquitina ligasa codificada por un gen cuyas mutaciones de pérdida de función dan lugar al ratón *mahoganoide,* caracterizado por un oscurecimiento del pelaje, neurodegeneración espongiforme y defectos cardiacos congénitos. Una de sus funciones conocidas es la regulación de la actividad del receptor de melanocortinas 1 (MC1R). El gen *MC1R*, el mayor determinante de la pigmentación cutánea y de la sensibilidad a la radiación ultravioleta, es muy polimórfico y algunas de sus variantes alélicas se asocian con melanoma. Además, da lugar a distintos transcritos, entre ellos una forma de ayuste alternativo, MC1R-203, con función desconocida.

La influencia de Mgrn1 en la señalización del MC1R y su participación en tráfico endolisosomal, homeostasis mitocondrial, estrés oxidativo y orientación del huso mitótico, podrían contribuir al desarrollo de melanoma y/o a la modulación del fenotipo de los melanocitos malignos. Por ello, nos propusimos: i) caracterizar funcionalmente la isoforma MC1R-203, ii) estudiar el papel de Mgrn1 como modulador del fenotipo maligno en células de melanoma de ratón, iii) analizar el papel de MGRN1 como determinante de la agresividad del melanoma humano y iv) estudiar la base molecular de los efectos fenotípicos de MGRN1 en células de melanoma.

Demostramos que MC1R-203 es minoritario respecto a la isoforma canónica (MC1R) en células HBL. Sin embargo, ambas isoformas presentaron una estabilidad intracelular similar en células HEK293T. Experimentos funcionales indicaron que MC1R-203 no estimuló eficientemente la vía del AMPc, pero activó normalmente la cascada de las ERK1/2. A diferencia de MC1R, MC1R-203 no indujo la ubiquitinación de β-arrestina-2 (ARRB2), una modificación dependiente de la formación de un complejo ternario MGRN1-MC1R-ARRB2, indicando que no actúa como andamiaje entre ARRB2 y MGRN1.

El estudio de Mgrn1 como modulador del fenotipo en melanocitos (melan-a6) y células de melanoma (B16F10) de ratón indicó que la deficiencia de Mgrn1 (disminuida mediante silenciamiento génico transitorio con siRNA o anulada mediante CRISPR/Cas9) promueve un fenotipo caracterizado por mayor pigmentación, mayor número de dendritas y adhesión, menor movilidad celular y menor capacidad de colonización en pulmón. Además, mediante citometría de flujo observamos una progresión anómala del ciclo de células deficientes de Mgrn1, con mayor porcentaje de células en fase S, inestabilidad genómica y daño en ADN (evaluado principalmente

mediante ensayos cometa). Estos resultados sugieren que Mgrn1 podría regular el fenotipo maligno y la integridad genómica de las células de melanoma murino.

Para determinar si la expresión de *MGRN1* podría actuar como factor pronóstico en pacientes de melanoma, analizamos datos públicos (TCGA) y muestras de pacientes junto con sus datos clínicos. Comprobamos que la expresión de *MGRN1* es mayor en muestras de melanoma que en piel normal o *nevi*. Además, la incidencia de mutaciones en *MGRN1* en muestras de melanoma es comparable a la de otros genes asociados a cáncer y una menor expresión de *MGRN1* se asocia con mayor supervivencia. Estos resultados indican que MGRN1 podría ejercer un importante papel en la agresividad del melanoma humano.

La base molecular de los efectos fenotípicos de MGRN1 se estudió en células de melanoma humano HBL. La depleción de MGRN1 alteró la progresión del ciclo celular y aumentó el daño en ADN. Mediante ensayos de hebra de ADN, comprobamos que la ausencia de MGRN1 incrementó el estrés replicativo, con aumento de horquillas de replicación atascadas y deficiente activación del eje ATR-CHK1. Ensayos de inmunoprecipitación de MGRN1 y aproximaciones proteómicas mostraron su interacción con CDK2 y RPA1. La ausencia de MGRN1 disminuyó los niveles de CDK2, y experimentos de inhibición selectiva de esta quinasa sugirieron que la interacción MGRN1-CDK2 contribuye a la respuesta normal al estrés replicativo al participar en la activación correcta del eje ATR-CHK1.

ABSTRACT

Mahogunin (Mgrn1) is an E3-ubiquitin ligase encoded by a gene whose loss-of-function mutations cause the *mahoganoid* mouse phenotype, mainly characterized by coat color darkening, spongiform neurodegeneration and congenital heart defects. One of the best-known functions of MGRN1 is the modulation of the melanocortin 1 receptor (MC1R) signaling. The *MC1R* gene, the major determinant of skin pigmentation and sensitivity to ultraviolet radiation, is highly polymorphic and some of its allelic variants are associated with melanoma. Furthermore, *MC1R* produces different alternative splicing transcripts, including a minority spliceoform, MC1R-203, with unknown function.

The influence of Mgrn1 on MC1R signaling and its functions in endolysosomal trafficking, mitochondrial homeostasis, oxidative stress and mitotic spindle orientation, could contribute to the development of melanoma and/or to the modulation of the phenotype of malignant melanocytes. Within this context, we proposed the following objectives: i) to functionally characterize the MC1R-203 isoform, ii) to study the role of Mgrn1 as a modulator of the malignant phenotype of mouse melanoma cells, iii) to analyze the role of MGRN1 as a determinant of human melanoma aggressiveness and iv) to study the molecular basis of the phenotypic actions of MGRN1 in human melanoma cells.

We found that MC1R-203 expression in HBL cells was much lower than that of the canonical form (MC1R). However, MC1R and MC1R-203 showed similar intracellular stability when transiently expressed in heterologous HEK293T cells. Functional experiments indicated that MC1R-203 did not efficiently activate the cAMP pathway but stimulated normally the ERK1/2 cascade. Unlike MC1R, MC1R-203 was incapable of promoting β-arrestin-2 (ARRB2) ubiquitylation. Since this post-translational ARRB2 modification depends on the formation of an MGRN1-MC1R-ARRB2 ternary complex, this suggested that the MC1R-203 spliceoform was unable to scaffold ARRB2 and MGRN1.

The study of Mgrn1 as a modulator of the phenotype of normal mouse melanocytes (melan-a6) and melanoma cells (B16F10) indicated that Mgrn1 deficiency (decreased expression upon by transient silencing with siRNA or knockout by CRISPR/Cas9) promoted a differentiated phenotype with increased pigmentation, dendricity and adhesion, decreased motility, and low rates of lung colonization. In addition, we observed by flow cytometry that *Mgrn1*-deficient cells showed an increased percentage of cells in the S phase of the cell cycle and an impaired genome stability, with accumulation of DNA damage (mainly evaluated by comet assays). These results suggested that Mgrn1 could regulate the malignant phenotype of mouse melanoma cells.

To determine whether *MGRN1* expression could act as a determinant of prognosis in melanoma patients, we analyzed public data (TCGA) and patient samples along with their clinical data. The results indicated that i) *MGRN1* expression is higher in human melanoma than in normal skin or *nevi*, ii) melanomas display a significant rate of mutations in *MGRN1* comparable with other cancer-associated genes, and iii) low *MGRN1* expression is significantly associated with higher patient survival. These results indicated that MGRN1 could play an important role as determinant of human melanoma aggressiveness.

The molecular basis of the phenotypic effects of MGRN1 was studied in HBL human melanoma cells. Lack of MGRN1 in human melanoma cells led to aberrant cell cycle progression and increased DNA damage. DNA fiber assays showed that the absence of MGRN1 increased cellular replication stress, with accumulation of stalled replication forks and impaired activation of the ATR-CHK1 signaling axis. Immunoprecipitation assays and proteomic approaches showed the interaction of MGRN1 with CDK2 and RPA1. Downregulation of MGRN1 decreased the levels of CDK2, and experiments with a selective inhibitor of the kinase suggested that the MGRN1-CDK2 interaction contributed to the normal response to replicative stress by participating in the efficient activation of the ATR-CHK1 signaling axis.

INTRODUCTION

1. Melanoma

El melanoma es un tumor maligno que se origina en los melanocitos, células especializadas en la síntesis de melanina (1). Dentro de este tipo de tumores, el melanoma cutáneo es el más común, representando en torno al 90 % de los melanomas, aunque también puede aparecer en ojos, superficies mucosas y meninges (2). Es el cáncer menos frecuente dentro de todos los tipos de cáncer de piel, pero es el más letal, responsable de más del 80 % de las muertes producidas por estos tumores (3). A continuación, esta introducción se centrará principalmente en aspectos moleculares del melanoma cutáneo.

1.1. Melanocitos

Los melanocitos son células especializadas y dendríticas que derivan de la cresta neural y migran hacia la epidermis, folículo piloso y úvea ocular durante el desarrollo embrionario. En menor medida, los melanocitos también se localizan en otros tejidos, como mucosas, cóclea, cerebro, corazón, pulmones e incluso tejido adiposo (4, 5). Su principal función es la síntesis de melaninas, pigmentos fotoprotectores responsables de la coloración de la piel, el pelo y los ojos, en respuesta a la radiación ultravioleta (RUV), entre otros estímulos. Estos pigmentos se sintetizan y almacenan en orgánulos intracelulares especializados, denominados melanosomas. Los melanocitos de la piel se disponen generalmente en la lámina basal de la epidermis y, a través de sus dendritas, transfieren los melanosomas a los queratinocitos circundantes, protegiéndolos del daño en ADN inducido por la RUV (6-8) (Figura 1A). A su vez, los queratinocitos regulan de forma paracrina la producción de pigmentos en los melanocitos, así como su diferenciación, proliferación y respuesta al daño en ADN, entre otros procesos (9).

1.1.1. Melanogénesis y tipos de melaninas

La melanogénesis o síntesis de melaninas es un proceso complejo constituido por diferentes etapas que tienen lugar en los melanosomas. Se han establecido cuatro estadios de maduración de los melanosomas (I a IV) (10, 11) (Figura 1B). En el estadio I los premelanosomas carecen de actividad melanogénica, siendo durante el estadio II cuando se produce la incorporación de las enzimas melanogénicas, transferidas a través de vesículas de la vía biosintética-secretora (12). En los estadios II y III los melanosomas melanogénicamente activos van depositando acúmulos de melaninas hasta llegar al estadio IV (melanosomas maduros). Estos melanosomas maduros, repletos de pigmentos y prácticamente sin actividad melanogénica, son transferidos a los queratinocitos circundantes.

La biosíntesis de melaninas tiene lugar a través de una ruta enzimática compleja denominada vía de Raper-Mason (13) (Figura 1C). En esta vía intervienen tres metaloenzimas: tirosinasa (TYR) y las dos proteínas relacionadas con la tirosinasa (TYRP1 y TYRP2) (14). La melanogénesis comienza con la oxidación del aminoácido L-tirosina en dos reacciones sucesivas catalizadas por la enzima limitante del flujo, TYR: hidroxilación de L-tirosina a L-3,4-dihidroxifenilalanina (L-DOPA) y oxidación de L-DOPA a L-DOPAquinona (DQ) (13, 15-17). A partir de DQ, la vía conducirá a la síntesis de eu- o feomelanina, dos tipos de pigmentos estructural y funcionalmente distintos, en función del contenido melanosomal en compuestos de bajo peso molecular con grupos sulfhidrilo libres (cisteína o glutatión). Si la concentración intracelular de estos compuestos es baja y/o la actividad TYR es alta, se favorecerá la producción de eumelaninas con la participación de TYRP1/2 (14, 18-20). En cambio, cuando la concentración de cisteína o glutatión es elevada y/o la actividad TYR es baja la ruta favorecida es la de síntesis de feomelaninas. En este caso, se produce la conjugación de los compuestos tiólicos con DQ formando cisteinilDOPA, que se oxida y polimeriza dando lugar a las feomelaninas sin intervención de las TYRP (21, 22).

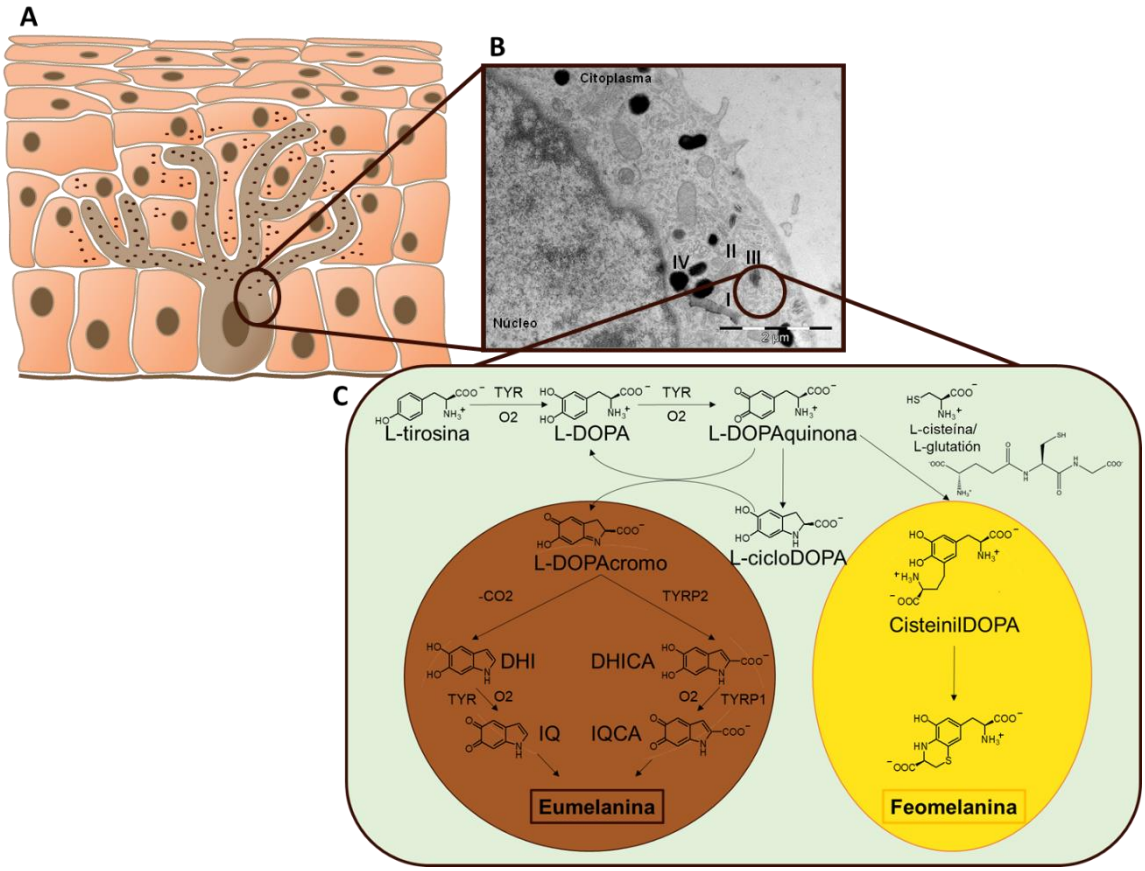

Figura 1. A) Asociación entre melanocitos y queratinocitos. Transferencia de los melanosomas a los queratinocitos en la epidermis. **B) Micrografía electrónica de un melanocito humano.** Se muestran los

cuatro estadios de maduración de los melanosomas. **C) Ruta de biosíntesis de eu- y feomelaninas.** Adaptada de Martínez-Vicente et al., 2020 (23).

En los melanocitos se producen mezclas de ambos pigmentos en proporciones variables que determinan el color de la piel y el riesgo a desarrollar cáncer de piel. Las eumelaninas, oscuras (de color marrón a negro) y menos solubles, son fotoprotectoras, ya que absorben y disipan la RUV e inactivan especies reactivas de oxígeno (ROS) (17). Por otro lado, las feomelaninas, más claras (de color rojo a amarillo) y fotosensibilizadoras, inducen la producción de ROS al ser irradiadas por RUV (24). Además, pueden dar lugar a la depleción de reductores intracelulares (glutatión reducido y NAD(P)H), induciendo un estado prooxidante incluso en ausencia de RUV (25).

1.1.2. Transformación de los melanocitos en células tumorales

Debido a la acumulación de alteraciones genéticas y epigenéticas, probablemente inducidas por la RUV, en genes que regulan la proliferación, diferenciación, apoptosis y adhesión celular, los melanocitos pueden sufrir una transformación gradual a través de una serie de fases caracterizadas por cambios histológicos y genéticos, que desembocan en la formación de un melanoma (3, 26, 27) (Figura 2). De acuerdo con el modelo propuesto por Clark, el desarrollo del melanoma comienza con la proliferación aberrante de los melanocitos, resultando en un *nevus* melanocítico benigno (3, 26, 28). Se trata de una población clonal de melanocitos que forman una lesión hiperplásica benigna que no progresa debido a los mecanismos de senescencia celular (28). Como consecuencia de la acumulación de mutaciones, algunos *nevi* superan la senescencia y experimentan un crecimiento displásico (*nevus* atípico o lesión premaligna) (3, 28). Estas lesiones pueden progresar hacia la Fase de Crecimiento Radial (*Radial Growth Phase*, RGP), caracterizada por la expansión superficial de los melanocitos, limitada a la epidermis y con incapacidad de metastatizar (26, 28). Esta fase se puede prolongar a lo largo de meses o años y se asocia a un buen pronóstico, ya que los melanomas de crecimiento radial pueden ser extirpados quirúrgicamente (28). Finalmente, las células pueden progresar a la Fase de Crecimiento Vertical (*Vertical Growth Phase*, VGP), en la que invaden la dermis y adquieren la capacidad de metastatizar, pudiendo invadir órganos como hígado, pulmón y cerebro (3, 28). Para el melanoma metastásico hay pocas opciones terapéuticas disponibles, por lo que se asocia a un mal pronóstico (28). Sin embargo, no todos los melanomas requieren de un *nevus* preexistente como

precursor y muchos no siguen una progresión lineal, omitiendo fases intermedias y alcanzando directamente la fase metastásica (28).

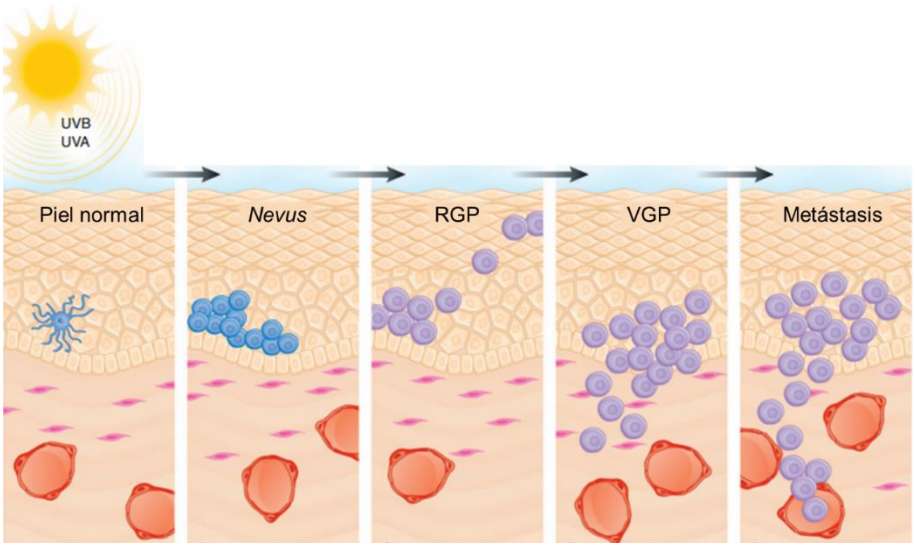

Figura 2. Esquema del modelo de iniciación y progresión del melanoma. Adaptada de Zaidi et al., 2008 (3).

1.2. Epidemiología

En las últimas décadas, la incidencia de melanoma ha aumentado en todo el mundo de forma constante y más rápida que la de casi cualquier otro tipo de cáncer (1). Sin embargo, este aumento en la tasa de incidencia no se acompaña de un incremento similar en la mortalidad, que ha permanecido relativamente estable en los últimos años. Esta diferencia puede deberse al diagnóstico precoz de la enfermedad debido a un mejor cribado (29).

Las tasas de incidencia y mortalidad difieren considerablemente entre la población mundial debido a factores como la localización geográfica, grupos étnicos, edad y sexo (1).

1.2.1. Incidencia

La incidencia del melanoma varía en función de la raza y grupo étnico. El riesgo de desarrollar melanoma cutáneo es mucho más elevado en la población blanca que en individuos de origen hispano, asiáticos o de raza negra (30). Sin embargo, los melanomas acrales y mucosos se desarrollan principalmente en africanos y asiáticos, con bajas tasas de incidencia pero elevada mortalidad (31). Esta tendencia se debe al menos en parte a los diferentes fenotipos de pigmentación de la piel de acuerdo a la raza (32).

También se observan diferencias según la localización geográfica. Las mayores tasas de incidencia se han reportado en la población de raza caucásica de Australia y Nueva Zelanda, con alrededor de 60 casos por 100.000 habitantes y año. En Estados Unidos la incidencia fue de unos 29 casos por 100.000 habitantes en 2020 (https://gco.iarc.fr/today (33)). Se diagnosticaron 96.445 nuevos casos en 2020 (4,2 % de todos los cánceres) y se alcanzaron las 7.201 muertes. Por otro lado, África y Asia presentan las menores tasas de incidencia, encontrándose Japón entre los países con menos casos de melanoma, al presentar menos de 2 casos anuales por 100.000 habitantes (http://gco.iarc.fr/today (33)).

En cuanto a Europa, se reportan anualmente alrededor de 20 casos por 100.000 habitantes, pero la incidencia no es homogénea dentro del continente, existiendo un claro gradiente norte-sur (http://gco.iarc.fr/today (33)). Las tasas de incidencia más elevadas corresponden a los países nórdicos, mientras que los países del sur reportan cifras más bajas (30). Así, Holanda y los países escandinavos presentan las mayores tasas de incidencia (alrededor de 45 casos por 100.000 habitantes al año) y Albania la incidencia más baja, con aproximadamente 2 casos por 100.000 habitantes por año (http://gco.iarc.fr/today (33)).

Probablemente, estas diferencias entre la población europea se deben a que los individuos que viven en los países del sur de Europa se encuentran más protegidos frente a la RUV, ya que tienen la piel más pigmentada (30). Por otro lado, también influyen las exposiciones solares vacacionales cortas, intensas y esporádicas, típicas en los individuos de los países del norte de Europa. Por último, hay que destacar que sólo 20 de los 41 países europeos tienen buenos registros de tumores (29, 32).

Generalmente, los hombres son los más afectados por el melanoma. Sin embargo, en la mayoría de los países del oeste y norte de Europa se encuentran mayores tasas de incidencia en mujeres. Independientemente, el incremento en la incidencia de melanoma se asocia a la edad, acentuándose en personas mayores de 60 años (https://seer.cancer.gov/ (34)). Además, en los últimos años se ha observado un aumento de los casos en individuos más jóvenes, la mayoría mujeres. Este hecho puede deberse a un incremento en la exposición recreacional a la luz UV y, particularmente, a las cabinas de bronceado artificial (29).

1.2.2. Mortalidad

Como se ha señalado anteriormente, la tasa de mortalidad del melanoma también varía según la localización geográfica, grupos étnicos, edad y sexo. Sin embargo, no se ha

detectado un incremento en la mortalidad similar al que se ha observado en la incidencia durante las últimas décadas.

Aunque el melanoma representa sólo el 4 % de todos los cánceres de piel, es el responsable de la mayoría de las muertes producidas por estos tumores (3). El diagnóstico precoz juega un papel fundamental en la supervivencia. Una detección del melanoma en estadios tempranos resulta en un mejor pronóstico, con una supervivencia a cinco años de alrededor del 95 %. Al contrario, para los pacientes a los que se diagnostica en estadios avanzados el pronóstico es mucho peor, ya que en estos casos la supervivencia a cinco años disminuye hasta aproximadamente el 10-20 % (https://seer.cancer.gov/ (34)).

También existen diferencias en el pronóstico del melanoma según el género de los individuos. De hecho, numerosos estudios han demostrado un mejor pronóstico para el sexo femenino que para el masculino, observándose un incremento en los índices de mortalidad en personas mayores de 60 años, particularmente en hombres (https://seer.cancer.gov/ (34)). Por último, se ha descrito una menor supervivencia en individuos de estatus socioeconómico bajo (35).

1.3. Subtipos de melanoma

1.3.1. Melanoma cutáneo

El melanoma cutáneo supone el 90 % de los casos de melanoma. De acuerdo con criterios clínicos e histopatológicos se han descrito cuatro subtipos principales de melanoma cutáneo:

Melanoma de extensión superficial: es la forma más común de melanoma (70 %). Aunque puede aparecer en casi cualquier parte del cuerpo, ocurre con más frecuencia en áreas de exposición solar intermitente como el torso en hombres, las piernas en mujeres y la zona alta de la espalda en ambos. Suelen desarrollarse sobre un *nevus* preexistente, pero pueden aparecer *de novo*. Estos melanomas presentan una fase de crecimiento radial lento, que puede desarrollarse a lo largo de varios meses e incluso años. En la fase de crecimiento radial, el melanoma queda restringido a la epidermis y, por lo tanto, no es capaz de producir metástasis (36, 37) (Figura 3A).

Melanoma nodular: es el tipo más agresivo y el segundo más frecuente (10-15 %). Aparece comúnmente en el torso, piernas y brazos de hombres de avanzada edad. Se caracteriza por no presentar fase de crecimiento radial, sino que se produce una fase de crecimiento vertical rápida, en la que el melanoma invade la dermis y puede producir metástasis (37, 38) (Figura 3B).

Léntigo maligno/Léntigo maligno melanoma: representa alrededor del 4-15 % de los casos de melanoma. Se desarrolla a menudo en personas de edad avanzada, en zonas de exposición solar acumulada como la cara y el cuello. Presenta una progresión lenta, con una fase de crecimiento radial que puede durar varias décadas. Tras esta fase, comienza el crecimiento vertical en un 5 % de los casos, que da lugar al paso de léntigo maligno a léntigo maligno melanoma (1, 37) (Figura 3C).

Melanoma lentiginoso acral: es el menos frecuente (4-10 %) pero el más común en individuos de raza negra y oriental. Se presenta en las palmas de las manos, plantas de los pies, debajo de las uñas y en las mucosas. De manera similar al melanoma de extensión superficial y al léntigo maligno melanoma, su fase de crecimiento intraepidérmica es larga (36, 39) (Figura 3D).

Además de estos subtipos de melanoma, existen otras presentaciones atípicas, como el melanoma desmoplásico, el melanoma mixoide o el melanoma "spitzoide" (37).

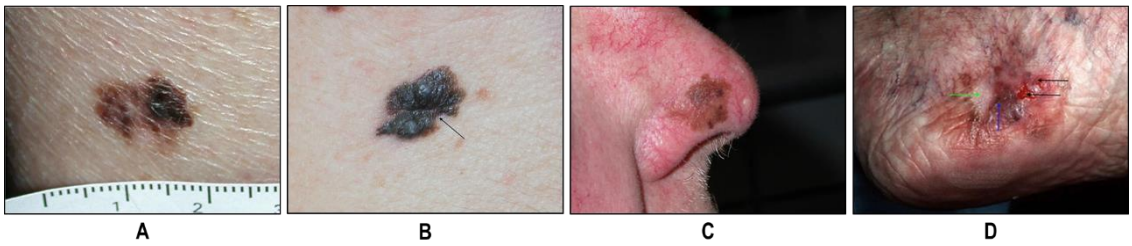

Figura 3. Imágenes clínicas de los subtipos de melanoma cutáneo. A) Melanoma de extensión superficial. B) Melanoma nodular. C) Léntigo maligno. D) Melanoma lentiginoso acral. Adaptada de Jones et al., 2020 (40).

1.3.2. Melanoma no cutáneo

El melanoma también puede encontrarse en superficies mucosas (melanoma de las mucosas) y ojos (melanoma uveal). Estos subtipos de melanoma son menos comunes que el melanoma cutáneo y biológicamente distintos, presentando sus propios patrones de extensión y respuesta a tratamientos sistémicos.

Melanoma Uveal

El melanoma uveal puede originarse en cualquiera de los tres componentes de la úvea, el iris, el cuerpo ciliar o la coroides. Esta última es la región más común, donde se originan el 80 % de los casos. El melanoma uveal suele diagnosticarse en exámenes rutinarios de la vista. Sin embargo, es común que los pacientes presenten visión borrosa o manchas en el campo visual cuando la enfermedad está más avanzada. En general, tiene un mal pronóstico. Aproximadamente, el 50 % de los pacientes con melanoma

uveal desarrollan metástasis. Debido a la ausencia de drenaje linfático en los ojos, la diseminación a órganos distantes se produce a través de la circulación sanguínea (41).

Melanoma de las mucosas

Estos tumores pueden originarse en cualquier superficie mucosa. Cerca de la mitad de los casos se originan en la cavidad oral, cavidad nasal y senos paranasales, mientras que la otra mitad aparece en la superficie mucosa anal y genital. Con baja frecuencia, este tipo de melanoma puede desarrollarse en el tracto urinario, esófago, intestino delgado y vesícula biliar. Generalmente son difíciles de detectar y presentan un mal pronóstico, especialmente aquellos que aparecen en sitios internos, pudiendo desarrollarse durante largos periodos de tiempo antes de ser diagnosticados (41).

1.4. Factores de riego

El melanoma se considera una enfermedad multifactorial, resultado de complejas interacciones entre factores de riesgo ambientales y factores dependientes del individuo, entre los que se incluyen los factores genéticos.

1.4.1. Factores ambientales

El principal factor de riesgo para el desarrollo de melanoma es la exposición a la RUV, debido a sus efectos genotóxicos (30). El riesgo más elevado se asocia con la exposición solar intermitente y con la historia de quemaduras solares a lo largo de la vida del individuo, particularmente durante la infancia (42). Además, la exposición a RUV artificial también juega un papel importante en la aparición de melanoma, detectándose un riesgo mayor de desarrollar melanoma en individuos que utilizan cámaras de bronceado (43, 44).

1.4.2. Factores dependientes del individuo

La frecuencia de melanoma es mayor en personas de piel, pelo y ojos claros, abundantes pecas, sensibilidad al sol y tendencia a desarrollar *nevi* benignos o atípicos (45). Según se discute más adelante, este fenotipo cutáneo se asocia a mutaciones en el gen MC1R (7), que codifica para el receptor de melanocortinas 1. Además, el riesgo de aparición de melanoma también es mayor para individuos que presentan un melanoma previo (46) y para pacientes inmunodeprimidos, a causa de enfermedades o tratamientos inmunosupresores (47).

Se han descrito diversas alteraciones genéticas, tanto germinales como somáticas, que contribuyen de forma importante al desarrollo del melanoma (48, 49).

1.4.2.1. Factores genéticos: mutaciones somáticas

Las mutaciones a nivel somático son responsables de alrededor del 90 % de los melanomas. Estas alteraciones dan lugar a melanomas esporádicos, pero también pueden favorecer el desarrollo de melanomas hereditarios, producidos por mutaciones germinales (50).

Gran parte de las mutaciones somáticas identificadas como causantes de melanoma activan constitutivamente rutas de señalización como la vía de las MAPK (proteína quinasa activada por mitógenos) ERK1 y ERK2 (quinasas reguladas por señales extracelulares) o de PI3K (fosfatidilinositol 3-quinasa) (51) (Figura 4).

Con mayor frecuencia, estas mutaciones afectan a la vía de señalización de ERK1/2 y ocurren mayoritariamente en los genes *BRAF*, *NRAS* y *NF1* (50). En función de la presencia o ausencia de alteraciones somáticas en estos genes, los melanomas han sido clasificados en 4 subtipos moleculares: BRAF, NRAS, NF1 y triple negativo (52).

Las mutaciones activadoras en *BRAF* se han detectado en alrededor del 50-70 % de los pacientes con melanoma y la más habitual es la denominada V600E, una sustitución de valina por ácido glutámico en la posición 600 (53, 54). Por su parte, *NRAS* se encuentra mutado en el 20-30 % de los melanomas esporádicos de forma excluyente con las mutaciones en *BRAF* (55). Asimismo, se han identificado mutaciones de pérdida de función en *NF1*, regulador negativo de RAS, que están presentes en alrededor del 12-18 % de melanomas (56). En consecuencia, la activación no controlada de esta vía da lugar a la estimulación constante de la proliferación y la supervivencia celular (57). Es de resaltar que esta vía se activa en condiciones normales aguas abajo de receptores con actividad tirosina quinasa (RTKs) controlada por ligandos mitogénicos como KITL/SCF capaces de inducir la proliferación de los melanocitos.

La activación de cKIT, un RTK reconocido por KITL/SCF, estimula la señalización de las vías MAPK y PI3K, claves para la proliferación, migración, diferenciación y supervivencia de los melanocitos (32). Recientemente, se han identificado mutaciones activadoras en *KIT* en el 38 % de los melanomas mucosos, 17 % de los melanomas con daño solar crónico y 6 % de los melanomas acrales, subtipos de melanoma en los que las mutaciones en *BRAF* y *NRAS* no son comunes (58, 59).

La vía de señalización PI3K es otra ruta frecuentemente hiperactivada en melanoma. La alteración molecular más común en esta vía de señalización ocurre en el gen supresor tumoral *PTEN,* que codifica para una fosfatasa que se comporta como regulador negativo de la vía. Mutaciones que producen inactivación o pérdidas alélicas de *PTEN*,

detectadas en el 20 % de los melanomas, desembocan en un incremento de la actividad de AKT, efector principal de la ruta PI3K. Como resultado, AKT modula la función de numerosos sustratos promoviendo la proliferación, supervivencia e invasión celular (60, 61).

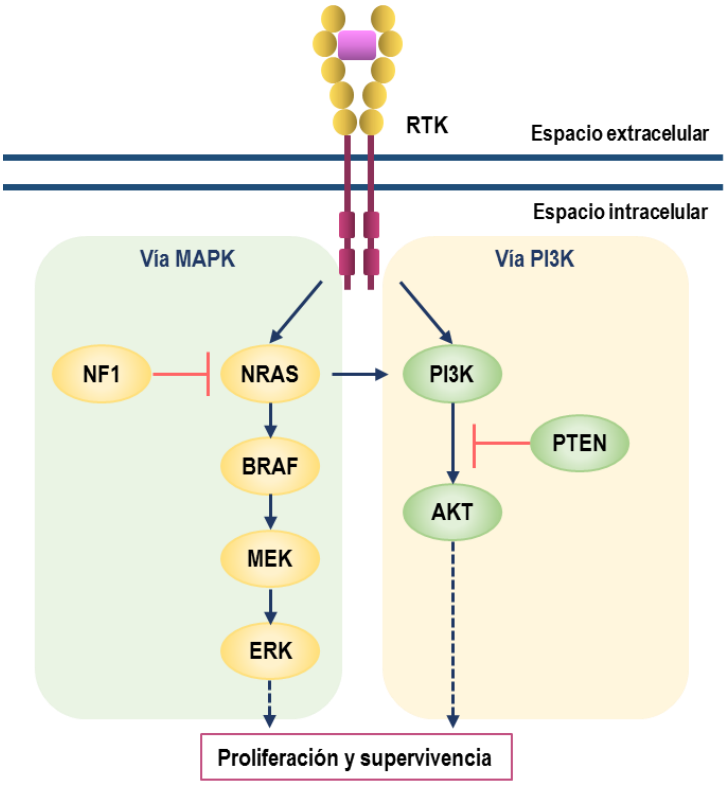

Figura 4. Señalización intracelular simplificada de las vías MAPK y PI3K.

Además de las alteraciones descritas en estas vías de señalización, destacan algunas mutaciones que afectan a procesos moleculares desregulados en el melanoma, como el mantenimiento de los telomeros (*TERT*), control del ciclo celular (*CDKN2A*), apoptosis (*TP53*) y remodelación de la cromatina (*ARID2*) (50, 62, 63).

1.4.2.2. Factores genéticos: mutaciones germinales

Cerca del 8-12 % de los pacientes de melanoma presentan antecedentes familiares, por lo que se han llevado a cabo numerosos estudios para identificar genes potenciales de susceptibilidad al melanoma (64).

Actualmente, los genes de susceptibilidad al melanoma se clasifican en dos grandes grupos:

Genes con alta penetrancia, pero con baja prevalencia:

Las mutaciones en estos genes están presentes en pocos individuos, pero son de alta penetrancia, es decir, su presencia se asocia a un riesgo elevado de desarrollar melanoma. Se encuentran en familias con dos o más casos de melanoma y se heredan de forma autosómica dominante (65). Entre ellos destacan el gen *CDKN2A* (inhibidor 2A de quinasa dependiente de ciclina) y el *CDK4* (quinasa dependiente de ciclina 4).

El primero y más importante, *CDKN2A*, es un gen supresor de tumores que codifica dos proteínas reguladoras del ciclo celular, $p16^{INK4a}$ y $p14^{ARF}$ (66, 67). Esto se debe a la presencia de dos promotores alternativos, uno más externo que regula la expresión de $p14^{ARF}$ y otro más interno para $p16^{INK4a}$ (Figura 5). Cada promotor determina el uso de un exón 1 diferente, mientras que los exones 2 y 3 se comparten en $p16^{INK4a}$ y $p14^{ARF}$. Sin embargo, los exones 2 y 3 codifican en dos marcos de lectura distintos, de manera que la secuencia de las dos proteínas es totalmente diferente. La existencia de dos exones 1 específicos de $p16^{INK4a}$ y $p14^{ARF}$, y de otros dos exones comunes hace posible que existan mutaciones que incidan en cada una de las proteínas específicamente, y mutaciones que afectan simultáneamente a las dos (68, 69). La mayoría de las mutaciones descritas inactivan específicamente a $p16^{INK4a}$, pero algunas pueden afectar a $p14^{ARF}$ (68). La proteína $p16^{INK4a}$ inhibe la actividad del complejo Ciclina D1-CDK4/6, complejo que permite la transición de la fase G1 a la fase S del ciclo celular mediante fosforilación de la proteína del retinoblastoma (Rb) (70). La $p14^{ARF}$ es una proteína estabilizadora de p53, ya que impide su degradación por HDM2, induciendo parada del ciclo celular y apoptosis (71, 72). Las mutaciones en *CDKN2A* se asocian con la predisposición a melanoma de aproximadamente el 20-40 % de las familias que presentan varios miembros afectados (73).

El segundo gen de alta penetrancia, *CDK4*, actúa como oncogén y está implicado en la progresión del ciclo celular durante la fase G1. Las mutaciones en este gen son mucho menos frecuentes, han sido detectadas en muy pocas familias y se encuentran en el dominio de unión a $p16^{INK4a}$, impidiendo la inhibición de CDK4 (74, 75) (Figura 5).

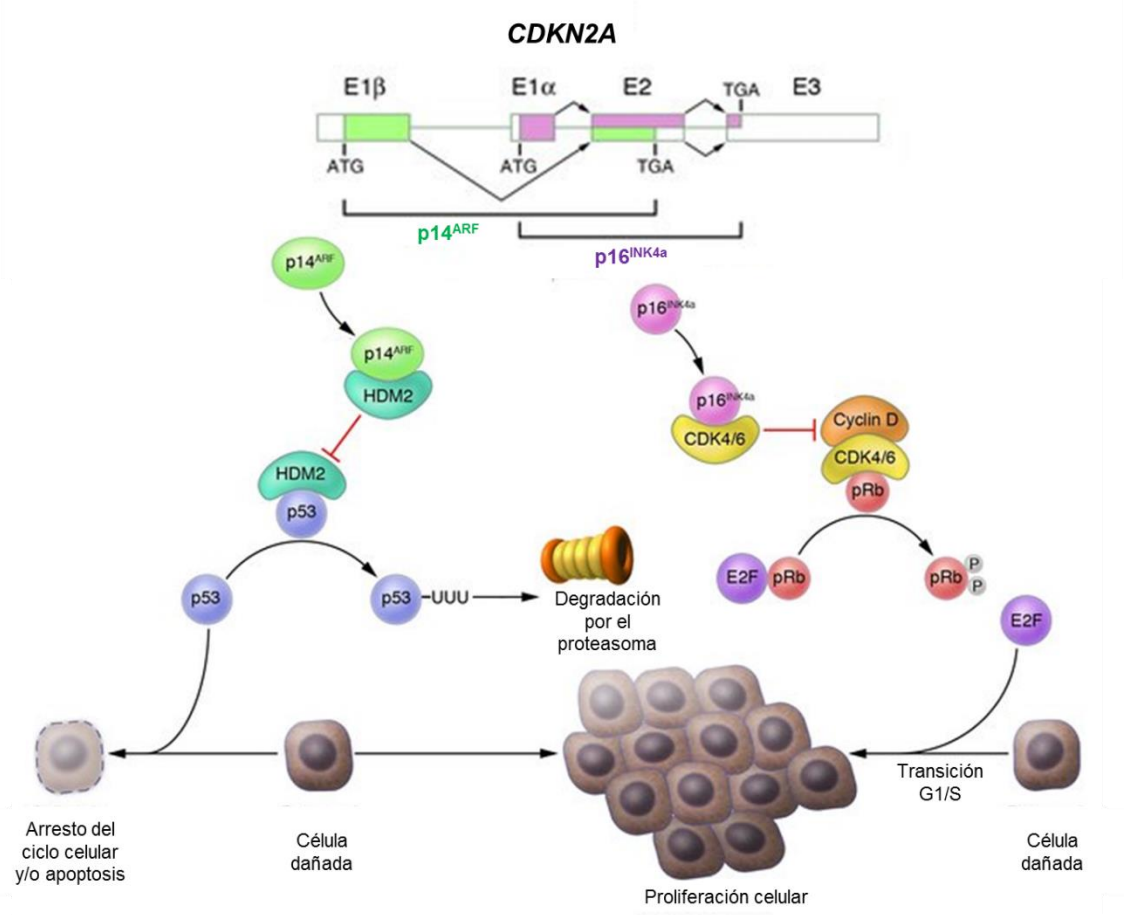

Figura 5. Mecanismo de acción de las proteínas $p14^{ARF}$, $p16^{INK4a}$ y CDK4, implicadas en el control del ciclo celular. Adaptado de Chudnovsky et al., 2005 (69).

Genes con baja penetrancia, pero con alta prevalencia:

Aunque son genes cuyos polimorfismos o mutaciones son frecuentes en la población general, su penetrancia es baja (76) y se asocian a un riesgo bajo o moderado para desarrollar melanoma. Entre ellos se encuentran los genes *TYR*, *TYRP1*, *OCA2* (albinismo oculocutáneo tipo 2), *SLC45A2* (antígeno de melanoma AIM1), *HERC2* (E3 proteína ligasa 2 con dominio HECT y RLD), *ASIP* (proteína de señalización agouti), *MITF* (factor de transcripción asociado a microftalmia) y *MC1R*, siendo este último el más importante (77-79).

1.5. MC1R

MC1R es considerado el principal gen de susceptibilidad al melanoma, ya que las mutaciones en este gen son muy frecuentes en la población. Es un gen muy polimórfico, alrededor del 50 % de los individuos caucásicos son portadores de al menos un alelo mutado, y algunas de sus variantes alélicas presentan una clara asociación con el riesgo a desarrollar melanoma (80).

El gen *MC1R,* que codifica al receptor de melanocortinas 1, es el mayor determinante de la pigmentación de la piel y de la sensibilidad a la RUV (7, 81). Ejerce un efecto protector frente a esta radiación mediante el aumento de la síntesis del pigmento oscuro y fotoprotector, eumelanina, en detrimento de la síntesis de feomelanina, más clara y fotosensibilizadora que predomina en ausencia de activación del receptor (81-83). Además, MC1R media la inducción de mecanismos antioxidantes y de reparación del daño en el ADN (84-86).

Muchas variantes de *MC1R* de pérdida de función son incapaces de activar la síntesis de eumelaninas, lo que da lugar a un aumento en la cantidad relativa de feomelaninas. Estas variantes se asocian con el fenotipo RHC (del inglés “Red Hair Color”), caracterizado por pelo de color rojizo y piel clara (80, 87), presencia de pecas (88), propensión a quemaduras solares y reducida capacidad de bronceado (89). También se han asociado con un incremento en el riesgo a desarrollar melanoma (90, 91) y cáncer de piel no-melanoma (92).

Las variantes alélicas de *MC1R* se clasifican en “R” o “r” según su penetrancia. Así, las variantes D84E, R142H, R151C, I155T, R160W y D294H, que están asociadas con más fuerza al fenotipo RHC, se denominan “R”, mientras que las variantes “r”, como V60L, V92M y R163Q, son las que presentan una asociación más débil (93, 94) (Figura 6). El riesgo a desarrollar melanoma conferido por los alelos “R” es aditivo, siendo mayor para los individuos que tienen los dos alelos “R” que para los que presentan uno o ninguno (95).

La susceptibilidad a desarrollar melanoma también se asocia con algunas de estas variantes de manera independiente de sus características fenotípicas, lo que sugiere que algunas variantes juegan un papel en el desarrollo de melanoma a través de procesos distintos a la pigmentación (96-98). Se ha descrito que estos polimorfismos dan lugar a una ineficiente reparación del daño en ADN y un aumento del estrés oxidativo, lo que supone un factor de riesgo independiente de la melanogénesis (85, 86). Además, *MC1R* puede interaccionar con otros genes de susceptibilidad al melanoma. La presencia de una variante alélica del *MC1R* junto a una mutación en *CDKN2A* incrementa significativamente su penetrancia, aumentando el riesgo de desarrollar melanoma del 50 % al 83 % y disminuyendo la edad de diagnóstico del melanoma de 58,1 a 37,8 años, comparado con individuos que solo presentan una mutación en *CDKN2A* (99). También se ha descrito que variantes del *MC1R* confieren un mayor riesgo de desarrollar melanomas con mutaciones V600E en *BRAF* (100).

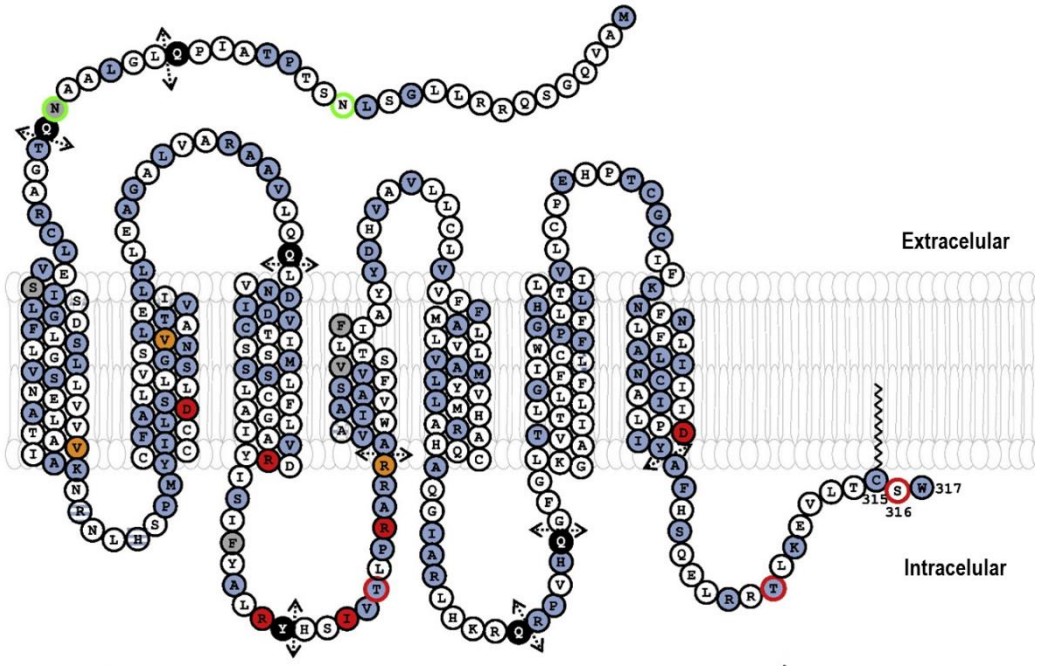

Figura 6. Estructura primaria y polimorfismos del MC1R. En azul se indican las posiciones polimórficas no asociadas a características funcionales. Las posiciones de las variantes "R" y "r" se muestran en rojo o naranja, respectivamente. En gris aparecen las inserciones-deleciones y en negro seguido de una flecha, los codones de stop prematuro. Las posiciones que presentan tanto inserciones-deleciones como codones de stop prematuro se encuentran marcadas mediante rayas azules y blancas. Las Ser/Thr fosforilables se indican con un borde rojo y las Asn que se glicosilan con un borde verde. Adaptada de Herraiz et al., 2017 (101).

1.5.1. Transcritos del gen MC1R

El gen *MC1R* humano (Ensembl ID ENSG00000258839), localizado en la región cromosómica 16q24.3, presenta una estructura relativamente compleja. Además de presentar un elevado grado de polimorfismo, contiene 4 exones y da lugar a distintos transcritos como resultado de un proceso de splicing intra- e intergénico (102). Dos de los transcritos, MC1R-202 (Ensembl ID ENST00000555147.2) y MC1R-204 (Ensembl ID ENST00000639847.1), comparten el mismo marco abierto de lectura (ORF) de 954 nucleótidos (nt) formado por los exones 2, 3 y 4, con retención de dos intrones entre los exones 2-3 y 3-4 (101) (Figura 7). Sin embargo, presentan diferentes regiones no traducidas 5' (5'UTR).

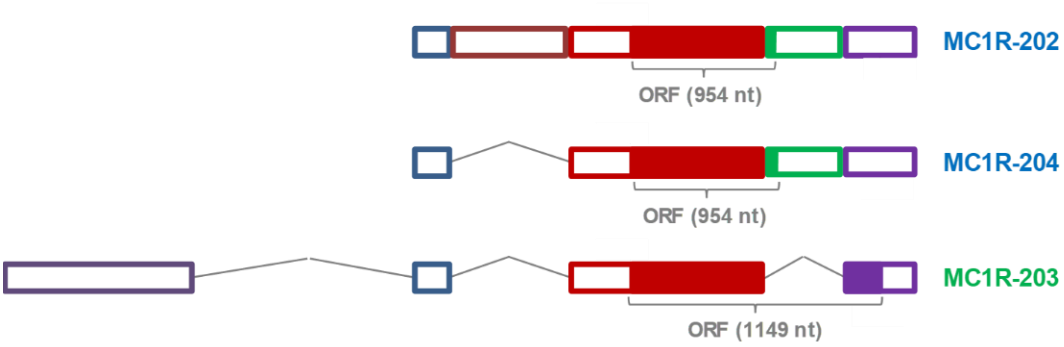

Figura 7. Representación esquemática de los transcritos del gen MC1R (MC1R-202, MC1R-204 y MC1R-203). Los exones se representan mediante cajas (las UTRs sin relleno y las secuencias codificantes coloreadas) y debajo se indica el número de nucleótidos de cada ORF.

Estos transcritos dan lugar a la proteína canónica de 317 aminoácidos, denominada MC1R para simplificar, con la estructura característica de un receptor acoplados a proteínas G (GPCR) de clase A, cuya función se ha explicado anteriormente (102, 103). Tan y colaboradores, describieron otro transcrito minoritario, conocido como MC1R-203 (ID ENST00000555427), que contiene los exones 1-4 y presenta un marco de lectura abierto de 1149 nt (Figura 7) que da lugar a una proteína de 382 aminoácidos (104), idéntica a la de MC1R hasta el residuo Ser316, a partir del cual se encuentran 66 aminoácidos adicionales en el extremo C-terminal (101) (Figura 8). Por lo tanto, ambas proteínas comparten el extremo N-terminal extracelular, así como los siete fragmentos transmembrana característicos de la superfamilia de GPCRs y los bucles intracelulares 1, 2 y 3 implicados en la interacción con los efectores citosólicos, lo que sugiere que podrían ser similares farmacológicamente (104). Sin embargo, la diferencia en la cola C-terminal intracelular podría suponer alteraciones funcionales significativas, ya que esta extensión es esencial para la eficiente expresión del MC1R en la superficie de la membrana plasmática y para su correcto acoplamiento funcional a la cascada del AMPc (105). Además, contiene los residuos Thr308 y Ser316, cuya fosforilación conduce a la desensibilización e internalización del MC1R (106). Hasta ahora, se desconoce la función y relevancia fisiológica de este transcrito minoritario. Por último, el transcrito MC1R-201 (Ensembl ID ENST00000539976.1) carece de un marco de lectura abierto funcional y no parece dar lugar a ninguna proteína (102).

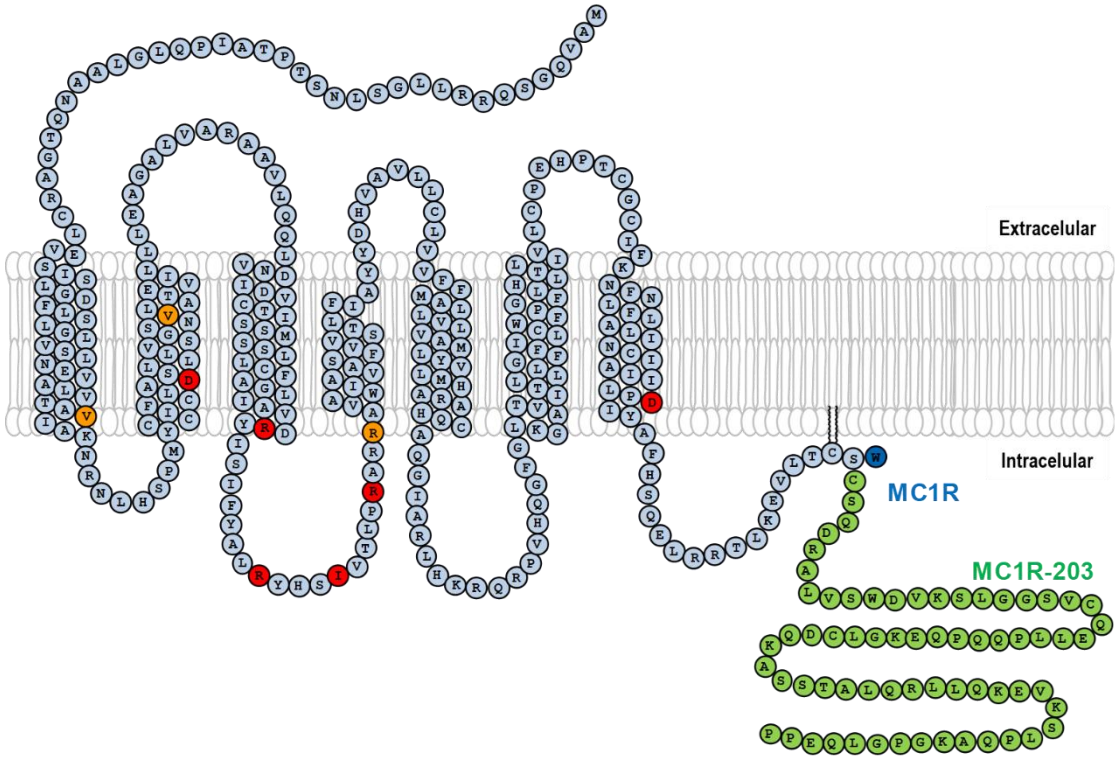

Figura 8. Secuencia de aminoácidos y estructura primaria de las proteínas MC1R y MC1R-203. Los aminoácidos asociados a polimorfismos se muestran en rojo y naranja (en rojo las variantes "R" y en naranja las "r"). El Trp317 C-terminal en MC1R se muestra en azul oscuro y los 66 aminoácidos extra del MC1R-203 en verde.

Además de estas isoformas de splicing intragénico, han sido descritas dos variantes de splicing intergénico (102, 107). La formación de estas variantes se encuentra favorecida por la alta densidad genética de la región 16q24 (102, 108) y la inusual e ineficiente señal de poliadenilación en el gen *MC1R* humano, lo que permite el splicing intergénico entre *MC1R* y el gen aguas abajo *Tubulina-β-III* (*TUBB3*) (102, 107, 109). Este proceso da lugar a dos quimeras MC1R-TUBB3, denominadas Iso1 e Iso2, que contienen la secuencia completa del MC1R fusionada con extensiones en C-terminal derivadas de TUBB3, con marco de lectura correcto para Iso1 y alterado para Iso2 (102, 107). Resultados de nuestro grupo han demostrado que la expresión en membrana de estas quimeras MC1R-TUBB3 se encuentra fuertemente reducida, mayormente debido a un tráfico anterógrado aberrante. Además, ambas variantes heterodimerizan eficientemente con MC1R, pudiendo comportarse como formas dominante negativas al promover la retención intracelular de la forma canónica. Por otro lado, se comportan como variantes "R" en cuanto a señalización, ya que su acoplamiento funcional a la vía del AMPc se encuentra comprometida, pero la activación de las ERKs permanece eficiente (102, 110).

1.5.2. Vías de señalización del MC1R

El gen *MC1R* codifica un receptor transmembrana perteneciente a la superfamilia de los GPCRs, el receptor de melanocortinas 1, expresado principalmente en los melanocitos de la piel (81, 111). La unión de los agonistas αMSH (hormona estimulante de los melanocitos) o ACTH (hormona adrenocorticotropa) al receptor activan secuencialmente a la proteína Gs y a la enzima adenilato ciclasa, que incrementa la producción de AMPc (adenosina monofosfato cíclico) intracelular (112). Este estimula la producción de eumelanina fotoprotectora y la proliferación de los melanocitos a través de la expresión de MITF, responsable de la transcripción del gen de la enzima melanogénica TYR, entre otros genes implicados en la melanogénesis (95, 113). Además, en la regulación de la melanogénesis también intervienen factores paracrinos, como la ASIP (114). La unión de la ASIP al receptor MC1R impide su activación por αMSH o ACTH, bloqueándose la producción de AMPc y la eumelanogénesis (Figura 9). Por lo tanto, el incremento de los niveles de la ASIP en ratones con mutaciones en *agouti*, provoca un aumento de la coloración amarilla en el pelaje y obesidad, debido a la inhibición competitiva por ASIP de la unión de melanocortinas al MC1R y MC4R (receptor de melanocortinas localizado en el hipotálamo e implicado en el control de la ingesta de alimentos y del metabolismo energético), respectivamente (115, 116).

Además, la unión del MC1R a sus agonistas es capaz de activar otras vías de señalización independientes de la vía del AMPc, como la vía de las MAP quinasas ERK1 y ERK2, que es estimulada mediante la transactivación del receptor con actividad tirosín quinasa cKIT (117) (Figura 9). La activación de esta vía es responsable de la proliferación, diferenciación y migración celular (118). Sorprendentemente, la mayoría de los alelos RHC son capaces de activar ERK1/2 de forma comparable al alelo MC1R silvestre, a pesar de su reducida capacidad para activar la vía de AMPc (117, 119). Por último, resultados recientes de nuestro grupo, han demostrado que algunas variantes de MC1R son capaces de estimular la vía de AKT, mediando la protección frente al daño oxidativo (84). Tras la exposición a RUV, el MC1R silvestre recluta a la fosfatasa PTEN, regulador negativo de esta vía, evitando su ubiquitinación y degradación por el proteasoma, de manera que limita la actividad de AKT. Sin embargo, las variantes RHC no son capaces de unir PTEN eficientemente, lo que puede contribuir a explicar una señalización por AKT aumentada (120).

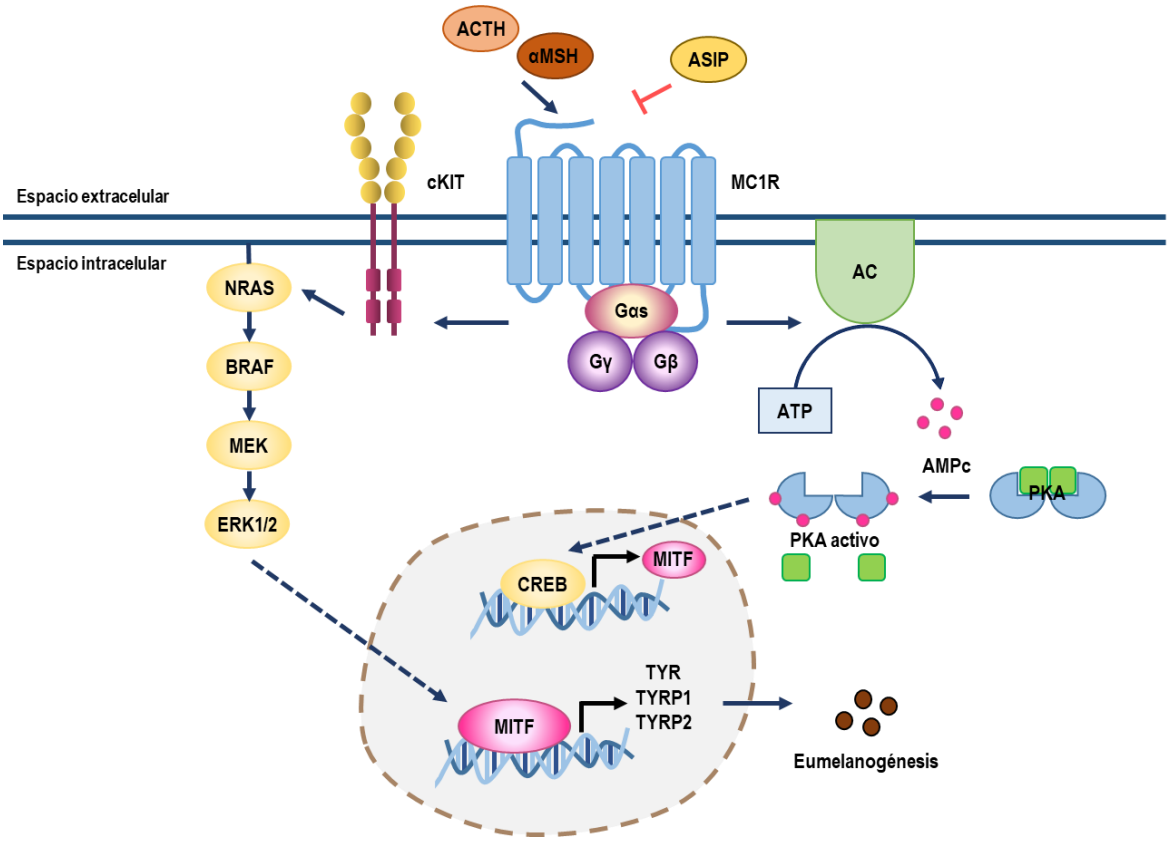

Figura 9. Esquema simplificado de las principales vías de señalización activadas por MC1R.

Además, MC1R juega un papel central en la pigmentación inducida por la RUV (bronceado). En queratinocitos, las lesiones provocadas en el ADN por la incidencia de la RUV promueven la estabilización e incremento de la actividad de TP53, que activa la transcripción del gen *POMC* (proopiomelanocortina) (121). Las hormonas αMSH y ACTH, derivadas de POMC, son liberadas al medio extracelular y activan al MC1R en los melanocitos (112). Como respuesta, la activación de la vía de AMPc incrementa la transcripción de MITF, promoviendo un aumento de la expresión de las enzimas melanogénicas y de la síntesis de eumelaninas (113, 122). Estas se transfieren a los queratinocitos, donde se disponen alrededor del núcleo para proteger al ADN de un mayor daño inducido por nuevas exposiciones al sol (Figura 10).

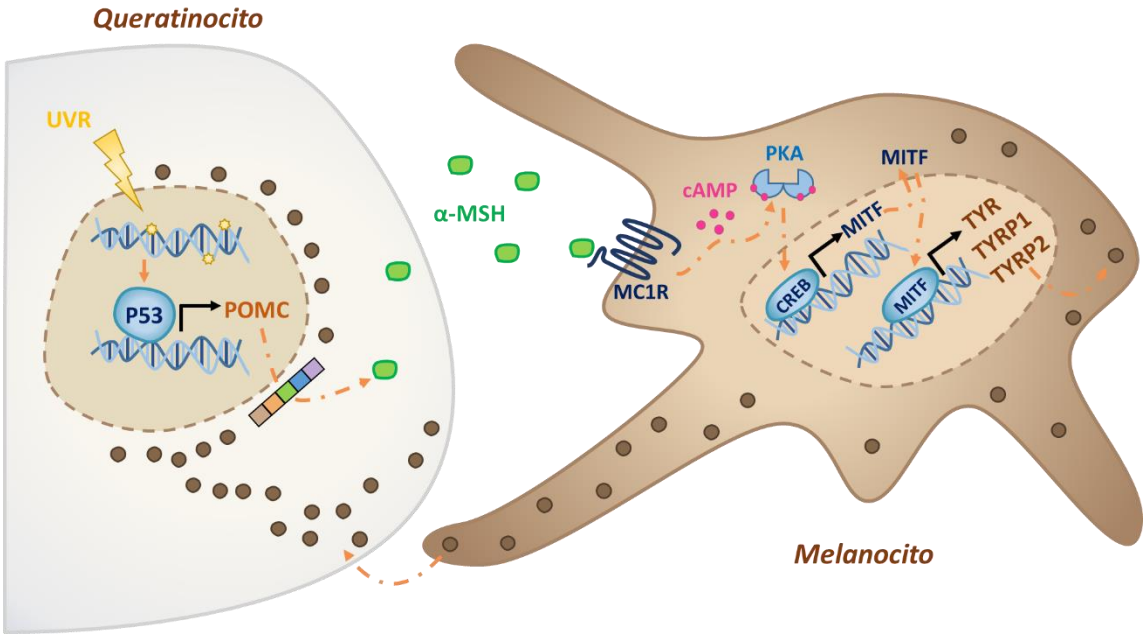

Figura 10. Esquema del mecanismo molecular del bronceado. Martínez-Vicente et al., 2020 (23).

Se han identificado varias proteínas reguladoras de la señalización a través de MC1R, como son las β-arrestinas (ARRB) y la mahogunina (Mahogunin Ring Finger-1, MGRN1). Estudios realizados por nuestro grupo han puesto de manifiesto que aunque MC1R interacciona con las dos isoformas de arrestina ARRB1 y ARRB2, solo la ARRB2 media la desensibilización e internalización del receptor (123). En cuanto a MGRN1, aspectos como su función y relación con MC1R se pasan a describir más adelante.

1.5.3. MC1R y riesgo de melanoma

Como se ha comentado previamente, la asociación entre las variantes RHC y la susceptibilidad a desarrollar melanoma no se debe exclusivamente a su incapacidad para activar la síntesis de pigmentos fotoprotectores (eumelaninas), ya que individuos de piel oscura portadores de estas variantes también presentan un incremento en el riesgo a desarrollar melanoma (96-98, 124). Por ello, se ha estudiado la capacidad que presentan los alelos RHC y silvestre para activar vías de reparación del daño en ADN y estimular antioxidantes intracelulares. Por un lado, en melanocitos expuestos a RUV, el MC1R silvestre estimulado por αMSH induce defensas antioxidantes (como la expresión de catalasa, γ -glutamilcisteinil sintetasa, glutatión transferasa y glutatión peroxidasa) (85, 125) y mecanismos de reparación de ADN (como reparación de bases oxidadas y fotoproductos inducidos por RUV), de forma dependiente de AMPc (84, 101, 126). Además, αMSH puede prevenir la apoptosis inducida por RUV en los melanocitos (85, 127). En conjunto, estas respuestas contribuyen a reducir la inestabilidad genómica y mutagénesis en melanocitos. Por el contrario, se ha asumido que las variantes RHC no

son capaces de activar estos mecanismos, ya que su acoplamiento a AMPc no es eficiente, lo que se asocia a un incremento de la apoptosis inducida por RUV, una ineficiente reparación del daño en ADN y un aumento del estrés oxidativo. Estos factores explicarían el componente independiente de la melanogénesis de la asociación de variantes RHC con el melanoma (7, 85, 86).

Sin embargo, no podemos ignorar la implicación de otras rutas de señalización de MC1R en la activación de defensas antioxidantes, reparación de ADN y supervivencia. Se ha demostrado que la activación de la vía de AKT por MC1R variante en melanocitos de genotipo RHC también es capaz de mediar la reparación de daño oxidativo en ADN (84) (Figura 11). Por lo tanto, estos melanocitos pueden activar vías de reparación de ADN mediante mecanismos independientes a la vía de señalización de AMPc (84). Por otro lado, MC1R variante no es capaz de inducir la expresión de enzimas antioxidantes, lo que junto al hecho de que las feomelaninas poseen propiedades prooxidantes, señala al estrés oxidativo como un componente importante de la carcinogénesis cutánea en células de genotipo RHC (84).

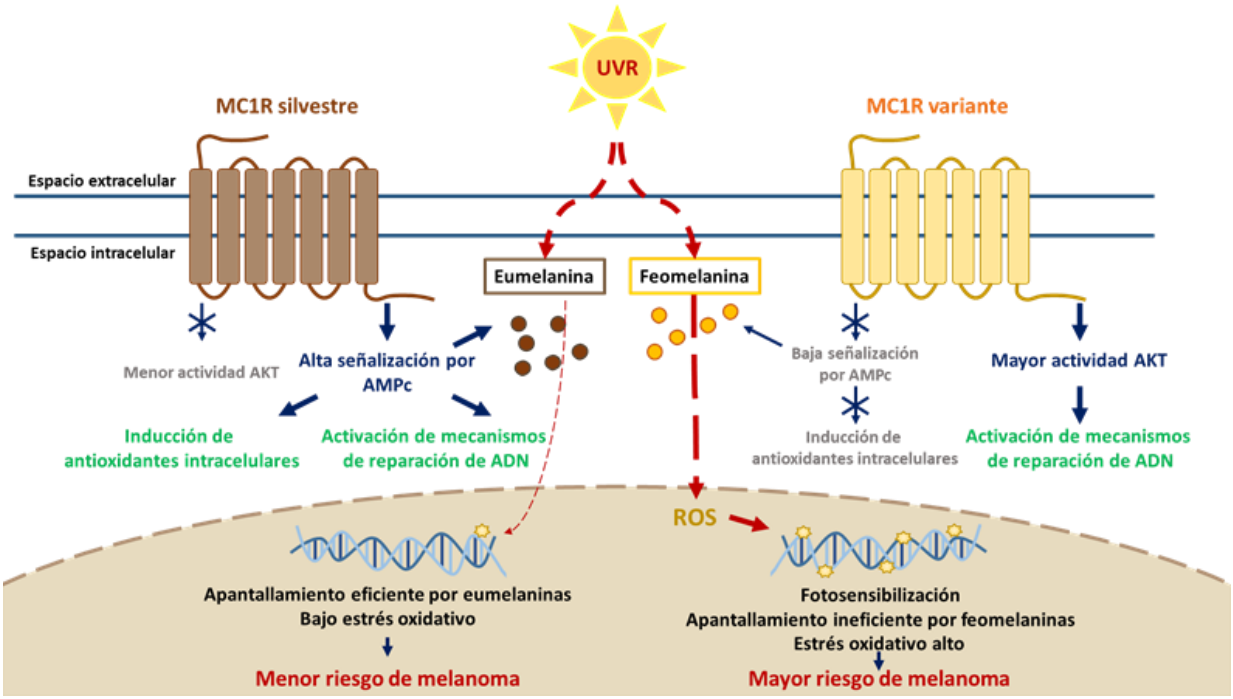

Figura 11. Papel del MC1R en la fotoprotección y bases moleculares de la asociación del MC1R variante con el melanoma. Martínez-Vicente et al., 2020 (23).

2. Mahogunin Ring Finger 1

Mahogunina es una proteína de expresión ubicua, que contiene un dominio "C3HC4 RING finger" característico de enzimas con actividad E3-ubiquitina ligasa y está implicada en la melanogénesis y en la regulación de la señalización por MC1R (128). El gen que la codifica (*Mgrn1*) fue identificado en ratón por clonación posicional del alelo *mahoganoide (md).* La mutación *mahoganoide* es una mutación de pérdida de función que está causada por la inserción retroviral de 5Kb en el intrón comprendido entre los exones 11-12 del gen *Mgrn1* (129). Dicha inserción anula la expresión de la proteína.

El fenotipo *mahoganoide* de los ratones homocigóticos para el alelo mutante se caracteriza por el oscurecimiento del pelaje, con acúmulos de eumelaninas en la región dorsal, orejas y cola de los animales (128) (Figura 12). Este fenotipo muestra una clara analogía con el de los ratones que presentan mutaciones de ganancia de función en *Mc1r* o de pérdida de función en *Asip* (130).

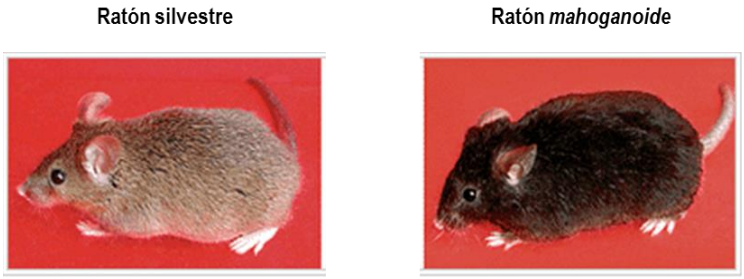

Figura 12. Fenotipo del ratón silvestre y del ratón *mahoganoide*, homocigoto para la mutación con pérdida de función de *Mgrn1*. Fotos del laboratorio del profesor Greg Barsh, HHMI, Universidad Standford.

Además, el ratón *mahoganoide* presenta neurodegeneración espongiforme con características típicas de enfermedades priónicas pero sin acumulación de proteínas priónicas (128) y con vacuolización en el sistema nervioso central (SNC) (131). Estos ratones también muestran disfunción mitocondrial, con una menor expresión y actividad de la cadena de transporte de electrones y un aumento del estrés oxidativo en el SNC (132). Además, manifiestan defectos congénitos de corazón, elevada mortalidad embrionaria y un incorrecto establecimiento del eje corporal izquierda-derecha (133). La deficiencia de Mgrn1 también provoca infertilidad en ratones machos, disrupción de la secreción hormonal y reducción de la movilidad espermática (134). El conjunto de estas evidencias demuestra que Mgrn1 está implicada en una amplia variedad de funciones biológicas.

Hasta ahora no se ha descrito en humano un fenotipo patológico asociado a la mutación de *MGRN1* similar al fenotipo *mahoganoide* del ratón. Además, las mutaciones

puntuales de *MGRN1* no son comunes (135-137). Curiosamente, la secuenciación del exoma de pacientes con Parkinson descubrió mutaciones *de novo* en *MGRN1*. Se comprobó que MGRN1 se expresa en la sustancia negra del cerebro y se encuentra diferencialmente expresada en modelos de Parkinson en ratón. Por ello, se sugirió que MGRN1 podría estar implicada en el incremento del riesgo de sufrir Parkinson (136). Otro estudio en pacientes de osteosarcoma mostró amplificaciones frecuentes de la región 16p13, donde se localiza *MGRN1* (138). Adicionalmente, se ha descrito que *MGRN1* presenta una marcada hipometilación de los sitios CpG en las células sanguíneas de pacientes con cáncer de mama (139). Estos datos sugieren que MGRN1 podría estar sobreexpresada en algunos tipos de cáncer.

2.1. Isoformas de MGRN1

El gen *Mgrn1* de ratón se localiza en el cromosoma 16 y consta de 17 exones. El procesamiento alternativo de los exones 12 y 17 da lugar a 4 isoformas de Mgrn1 (130). Su ortólogo humano, el gen *MGRN1*, también se encuentra en el cromosoma 16 y está constituido por 17 exones. Las células de melanoma humano también expresan 4 isoformas de MGRN1, resultado del procesamiento alternativo de un mismo transcrito primario (140). Estas isoformas se nombran según la longitud de la secuencia codificante del exón 17 (L, de long, para la versión larga y S, de short, para la versión corta) y la presencia (+) o ausencia (-) del exón 12 (140). Así, (+)L y (-)L serán las isoformas que contienen la versión larga del exón 17, con y sin el exón 12, respectivamente, mientras que (+)S y (-)S son las isoformas que contienen la versión corta del exón 17, con o sin exón 12 (140) (Figura 13).

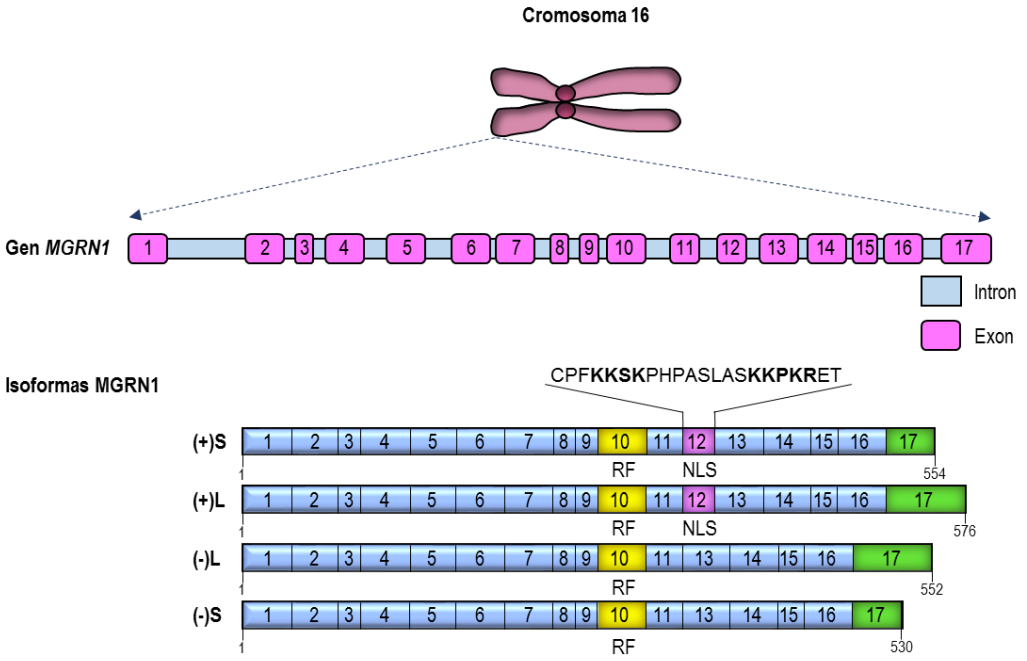

Figura 13. Esquema de la estructura del gen *MGRN1* y de las distintas isoformas de MGRN1. En la estructura genómica se encuentran los exones en rosa y en azul los intrones. En cuanto a las cuatro isoformas de la proteína, resalta en amarillo el dominio RING Finger (RF), codificado por el exón 10. En rosa se indica la señal canónica de localización nuclear (NLS), determinada por el exón 12 y ausente en las isoformas (-). Finalmente, el color verde hace referencia a la secuencia de aminoácidos codificada por el exón 17, de distinta longitud en las isoformas L y S.

La existencia de cuatro isoformas de Mgrn1 con distintos patrones de expresión en los tejidos sugiere que podrían tener funciones distintas (130). En piel son más abundantes las isoformas (+), mientras que la isoforma (-)S es la más expresada en cerebro. Las (-)S, (+)S y (-)L se expresan tanto en cerebro como en riñón y corazón y las cuatro isoformas se expresan casi al mismo nivel en el hígado (130, 141). El análisis de las funciones *in vivo* de cada isoforma determinó que las isoformas (-)S y (-)L rescatan todos los fenotipos mutantes examinados y son suficientes para mantener el desarrollo normal de los ratones, su pigmentación y la integridad neuronal. Por otro lado, la isoforma (+)S rescata el fenotipo de viabilidad embrionaria y parcialmente los fenotipos de pigmentación y neurodegeneración espongiforme. Sin embargo, la isoforma (+)L presenta un menor efecto de rescate del fenotipo del mutante. El conjunto de estos resultados indican que estas isoformas no son equivalentes funcionalmente (141). No obstante, la sobreexpresión de cualquiera de las cuatro isoformas rescata, al menos parcialmente, el fenotipo de pigmentación en ratones mutantes, indicando que el efecto en pigmentación es más sensible a los niveles de MGRN1 que a una isoforma específica (130).

2.2. Localización subcelular de MGRN1

Dos de las isoformas de MGRN1 contienen una secuencia NLS de localización nuclear de 19 aminoácidos formada por dos bloques de aminoácidos básicos y codificada por el exón 12 (140, 142) (Figura 13).

La localización subcelular de las isoformas que expresan el exón 12 (+) es diferente a la de las isoformas que no lo contienen (-) y depende, entre otros factores, de la presencia o ausencia de MCRs (MC1R y MC4R). Así, en células HEK293T y en ausencia de estos receptores, ambas isoformas se localizan en el citosol y unidas a la membrana plasmática, mientras que la coexpresión con el MC1R o MC4R da lugar a la translocación de las isoformas (+) al núcleo (140).

Se ha descrito que MGRN1 se transloca del citoplasma al núcleo en neuronas envejecidas, donde potencia la respuesta transcripcional al estrés proteotóxico, disminuyendo los signos de envejecimiento neuronal y aumentando las habilidades cognitivas en ratones viejos (143). Mgrn1 también ejerce una función neuroprotectora

regulando el procesamiento de la proteína precursora amiloidea, retrasando su maduración y procesamiento proteolítico (144). Además, algunas formas de proteínas priónicas interaccionan con Mgrn1 y la secuestran en el citosol, lo que altera su función e incluso la anula en algunas regiones del cerebro, con la consiguiente disfunción neuronal (145). En conjunto, estos hallazgos apuntan a que Mgrn1 desempeña una función nuclear clave en la protección contra algunos tipos de estrés, al menos en neuronas pero quizás también en otros tipos celulares.

2.3. Funciones de MGRN1

Todas las isoformas de Mgrn1 y su ortólogo humano (MGRN1) comparten la secuencia codificada por los exones 1-11, y, por lo tanto, expresan el dominio RING Finger codificado por el exón 10 (130, 140) (Figura 13). Este dominio RING Finger es un elemento estructural clave de E3 ubiquitina ligasas (146) y se ha demostrado que Mgrn1 presenta esta actividad enzimática *in vivo* (128) e *in vitro* (147).

El motivo RING Finger, definido por la secuencia de aminoácidos C4HC3, es un pequeño dominio capaz de coordinar dos átomos de zinc. Estos dominios pueden interactuar específicamente con enzimas conjugadoras de ubiquitina (E2) y ubiquitinar proteínas específicas, por lo que muchas proteínas que contienen un dominio RING Finger actúan como E3 ubiquitina ligasas (148). Las E3 ubiquitina ligasas catalizan la conjugación de proteínas con unidades de ubiquitina, marcándolas para su degradación en el proteasoma, pero también regulan otras funciones como la endocitosis, degradación lisosomal, exportación nuclear, reparación de ADN, remodelado de histonas y activación de quinasas y factores de transcripción (149).

A través de su actividad ubiquitina ligasa, MGRN1 está implicada en una amplia variedad de funciones biológicas, que podemos dividir en los siguientes bloques:

a) Tráfico endolisosomal

El primer sustrato de MGRN1 que se identificó fue la proteína TSG101 (gen de susceptibilidad tumoral 101), un componente del complejo ESCRT-I (complejo de clasificación endosomal requerido para el transporte-I) clave en el tráfico endosomal. MGRN1 interacciona con TSG101 y promueve su multimonoubiquitinación, modulando su actividad y, por lo tanto, regulando la vía de degradación endolisosomal (heterofagia) (147). Asimismo, TSG101 facilita la autofagia, ya que regula la fusión de los lisosomas tanto con endosomas tardíos como con anfisomas (Figura 14). La depleción de MGRN1 da lugar a la disfunción de la vía de degradación lisosomal, lo que podría relacionarse con la neurodegeneración espongiforme (150). Otra función de la proteína TSG101 es

mitigar la apoptosis mediada por estrés del retículo endoplásmico (RE). En células carentes de MGRN1 la predisposición a apoptosis por estrés aumenta, y este aumento de apoptosis en determinadas regiones del cerebro y en cardiomiocitos puede causar neurodegeneración y defectos congénitos del corazón (151). Por otro lado, MGRN1 interacciona con una ubiquitina ligasa con dominio HECT que también participa en el tráfico endosomal, la proteína NEDD4, pero en este caso no produce su ubiquitinación (152).

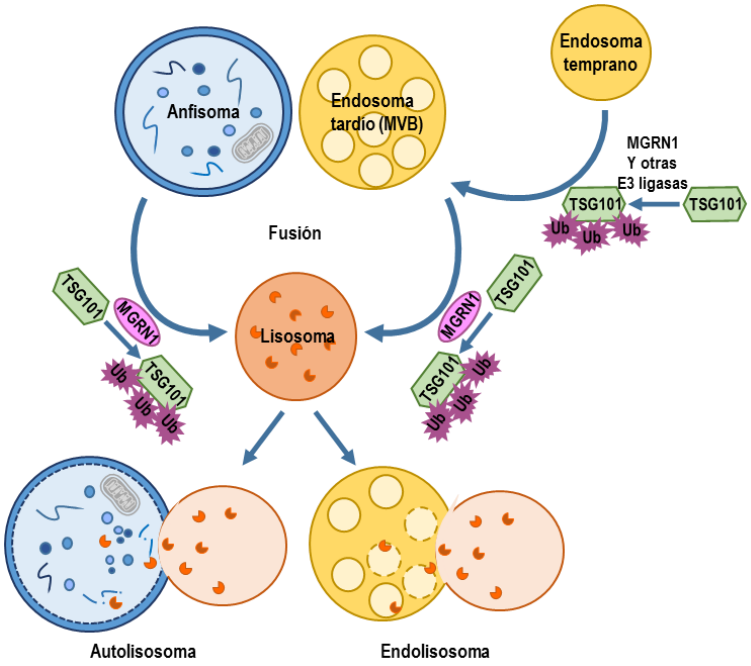

Figura 14. Esquema de la función de MGRN1 en el tráfico endolisosomal. La proteína TSG101 multimonoubiquitinada por MGRN1 regula la fusión entre lisosomas y anfisomas/endosomas tardíos. Adaptado de Majumder & Chakrabarti, 2015 (150).

b) Homeostasis mitocondrial y respuesta al estrés celular

También se ha descrito que MGRN1 ejerce un papel clave en la homeostasis mitocondrial y en la respuesta al estrés celular, eventos relacionados con la neurodegeneración. MGRN1 ubiquitina a Mitofusina 1 (Mfn1), paso esencial para la fusión mitocondrial (153), e interacciona con GP78 regulando la mitofagia, la formación de uniones mitocondria-RE y la degradación proteica asociada al RE (154). Asimismo, la depleción de MGRN1 da lugar a disfunción mitocondrial, acompañada de niveles más bajos de algunas proteínas mitocondriales, despolarización de la membrana mitocondrial y un aumento del estrés oxidativo (132, 155). Por otro lado, en condiciones de estrés aumenta la expresión de MGRN1, que interacciona con la chaperona Hsp70 asociada a proteínas desplegadas o que han perdido su conformación nativa, promoviendo su degradación mediante autofagia. La autofagia inhibe la agregación de

estas proteínas, aumentando así la supervivencia celular en condiciones de estrés (155). En el mismo sentido, MGRN1 interacciona con proteínas que contienen fragmentos extendidos de poliglutamina, como huntingtina y ataxina-3, y con agregados de poliglutamina, y facilita la eliminación de estas proteínas. Así, MGRN1 reduce la formación de los agregados y confiere citoprotección frente a la proteotoxicidad inducida por poliglutamina (156). También reduce la agregación de la SOD1 (superóxido dismutasa 1) mutada, disminuyendo su efecto proteotóxico y la degeneración de neuronas motoras que da lugar a la esclerosis lateral amiotrófica (157) (Figura 15).

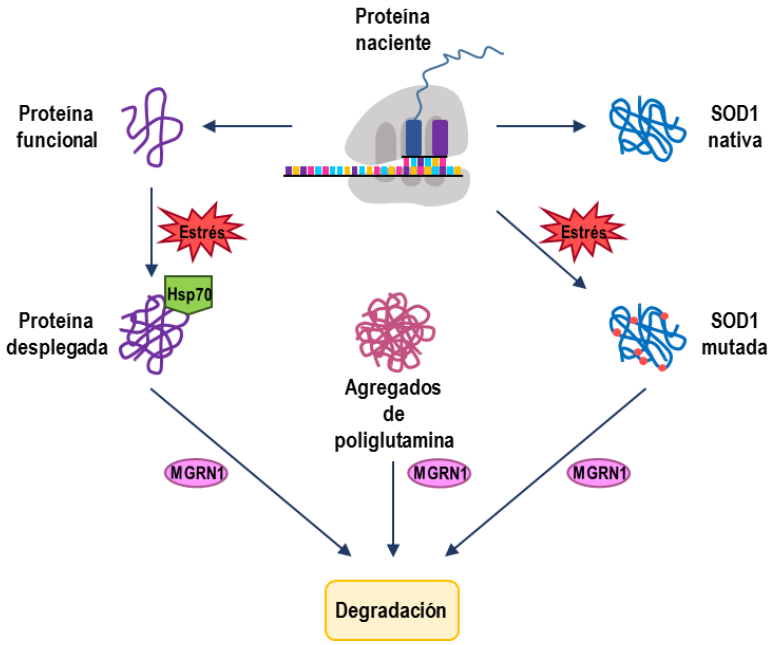

Figura 15. Esquema del papel de MGRN1 en la protección frente a la proteotoxicidad. La proteína MGRN1 interacciona con proteínas desplegadas, agregados de poliglutamina y SOD1 mutada para mediar la degradación de estas proteínas.

c) Orientación del huso mitótico y establecimiento del eje embrionario izquierda-derecha

MGRN1 interacciona con la proteína del citoesqueleto α-tubulina y regula la polimerización de los microtúbulos y la correcta orientación del huso mitótico (Figura 16). Además, α-tubulina es modificada postraduccionalmente por MGRN1, aumentando su estabilidad, lo que podría ser un evento clave en el establecimiento del eje embrionario izquierda-derecha (158). Los defectos en el establecimiento de la lateralidad embrionaria se relacionan con la presencia de malformaciones cardíacas, craneofaciales y el incremento en la mortalidad embrionaria observados en los ratones *mahoganoides* (133, 159). Por otro lado, MGRN1 también asegura la posición adecuada

del huso mitótico mediante la estabilización de la subunidad αi de la proteína G (Gαi) en el cortex de células mitóticas (160) (Figura 16).

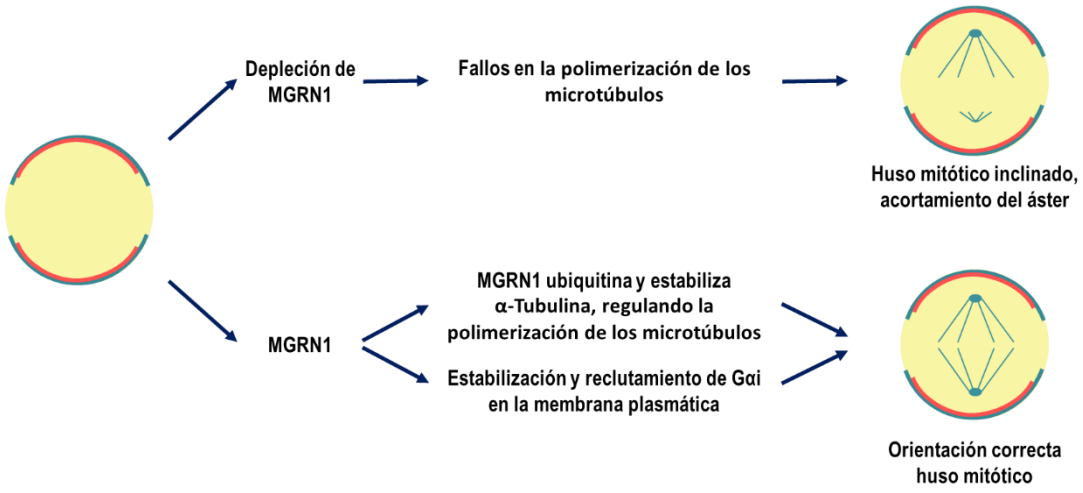

Figura 16. Esquema del efecto de MGRN1 en la orientación del huso mitótico y mecanismo de acción. Adaptado de Srivastava & Chakrabarti, 2015 (159).

d) Pigmentación y modulación de GPCRs

Como se ha comentado anteriormente, los ratones *mahoganoides* se caracterizan por el oscurecimiento de su pelaje. Para explicar el papel de MGRN1 en la pigmentación se sugirió que MGRN1 podría ubiquitinar al MC1R, promoviendo su internalización o degradación por el proteasoma (161). Sin embargo, resultados de nuestro grupo demostraron que el receptor MC1R no era ubiquitinado ni internalizado en presencia de MGRN1, sino que las cuatro isoformas de MGRN1 interaccionan con MC1R e impiden su señalización mediante competición con la subunidad αs de la proteína G (Gαs), inhibiendo así la producción de AMPc (Figura 17). Este es también el mecanismo por el que MGRN1 inhibe la señalización de MC4R (140). Además, un estudio posterior concluyó que la degradación de Mc4r en el SNC está impedida en células carentes de Mgrn1 (162). Sin embargo, el receptor MC2R sí es ubiquitinado en presencia de MGRN1 y ambas proteínas interaccionan en la corteza adrenal, lo que sugiere que MGRN1 podría estar implicada en la señalización y/o degradación del MC2R (163). Por tanto, el mecanismo por el que MGRN1 regula la actividad señalizadora de los distintos miembros de la subfamilia de los receptores de melanocortinas (MCRs) podría ser diferente y específico del receptor concreto considerado, pero en general MGRN1 ejercería un efecto inhibidor, por lo que las mutaciones con pérdida de función del gen *MGRN1* causarían una ganancia de la capacidad señalizadora de los MCR. En cualquier caso, la inhibición de MC1R por MGRN1 puede contribuir al fenotipo de pigmentación de los ratones *mahoganoides*, aunque algunos resultados no publicados de nuestro

grupo indican que este no es el único mecanismo molecular de la hiperpigmentación de dichos ratones.

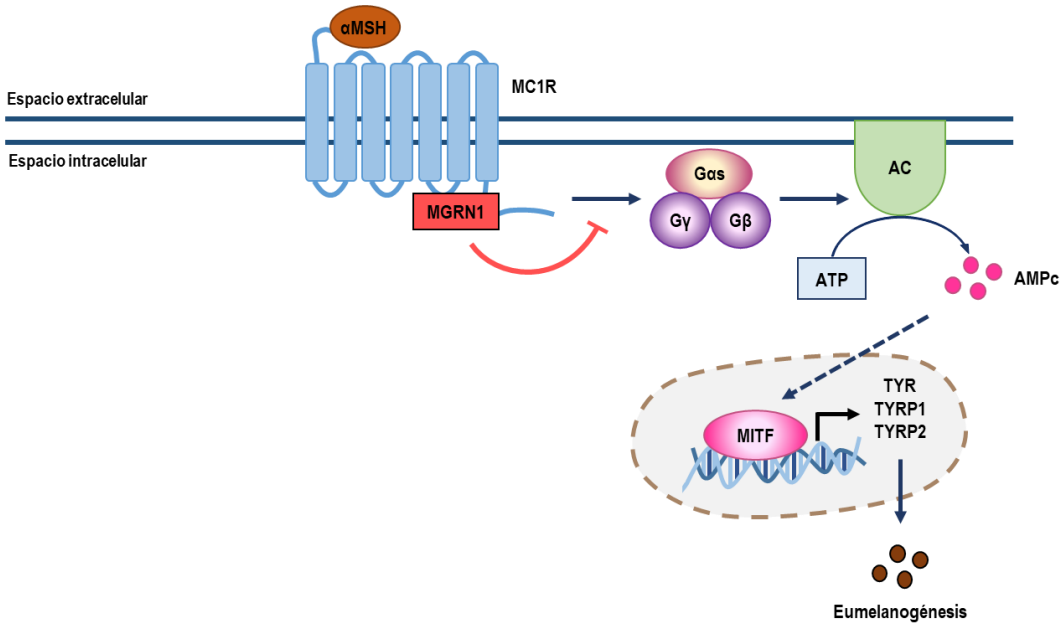

Figura 17. Esquema del papel de MGRN1 en la melanogénesis. MGRN1 interacciona con MC1R e inhibe la vía de señalización del AMPc mediante competición con Gαs.

Por último, MGRN1 participa en la poliubiquitinación de las β-arrestinas ARRB1/2, proteínas citosólicas de unión a MC1R, siendo solo la ARRB2 capaz de producir la desensibilización e internalización del receptor. La poliubiquitinación de ARRB se produce en presencia de MC1R funcional y expresado en membrana, que actúa como andamiaje molecular facilitando la formación de un complejo ternario ARRB-MC1R-MGRN1 (164). Las consecuencias funcionales de la ubiquitinación de las ARRB por MGRN1 permanecen desconocidas.

2.4. MGRN1 y melanoma

El conjunto de funciones biológicas en las que participa MGRN1 sugieren su posible relación con la aparición o desarrollo de melanoma. Como se ha destacado previamente, MGRN1 está implicada en la modulación de MC1R y, por lo tanto, en la melanogénesis (128). Así, cambios en la pigmentación o en las respuestas de reparación de ADN inducidas por MC1R podrían desembocar en un aumento de la carcinogénesis cutánea. Por otro lado, su importante papel como reguladora del tráfico endolisosomal (147), de la homeostasis mitocondrial y del estrés oxidativo (132, 155), así como la inducción de inestabilidad genómica como consecuencia de alteraciones del huso mitótico (147), señalan una posible asociación entre la expresión de MGRN1 y la incidencia o pronóstico de este tipo de tumores. En base a estos indicios, nos planteamos el estudio del papel que ejerce MGRN1 en el desarrollo de melanoma.

AIMS

AIMS

The melanocortin 1 receptor (MC1R) and its intracellular partner Mahogunin Ring Finger 1 (MGRN1) play key roles in the biology of melanocytes and melanoma cells. MC1R is a major regulator of the amount and type of pigment synthesized by melanocytes, and of hormonally induced DNA repair. However, the functional properties of many MC1R variants, including certain spliceoforms, remain uncharacterized. On the other hand, the multiple pathological implications of the *mahoganoid* mouse mutation of *MGRN1* clearly underline the important physiological functions of MGRN1 and suggest its possible relationship with melanoma genesis and/or progression. These pathological effects of MGRN1 loss include mitochondrial dysfunction with increased oxidative stress, aberrant microtubule dynamics and stability with altered mitotic spindle orientation, defects of microtubule-dependent transport of intracellular organelles, deregulation of the transcriptional response to proteotoxic stress, and others. However, despite its relationship with components of the cytoskeleton, no study on the regulation by MGRN1 of cell shape and movement of normal melanocytes and melanoma cells has yet been reported. Moreover, the likely roles of MGRN1 in maintaining genomic stability and normal cell cycle progression also remain unexplored.

Within this context, this work proposed the next aims:

1. To analyze the expression of the MC1R-203 spliceoform in HBL human melanoma cells and its signaling properties.
2. To determine the effects of Mgrn1 ablation on mouse melanocyte morphology and on the motility, cell cycle progression, genomic stability and growth and invasiveness of mouse melanoma cells.
3. To assess the possible role of MGRN1 as determinant of human melanoma aggressiveness and prognosis.
4. To elucidate the role of MGRN1 in the maintenance of genomic integrity in human melanoma cells.

MATERIALS AND METHODS

1. Reagents

- **AppliChem GMBH** (Darmstadt, Germany): sodium dodecyl sulfate (SDS), methanol, sodium chloride, glycine and acetic acid glacial.
- **Biolegio BV** (Nimega, Nertherlands): primers for RT-PCR.
- **Biotools, B & M Labs** (Madrid, Spain): DNA polymerase.
- **Bio-Rad** (Richmond, VA, USA): TEMED and Extra Thick Blot Paper Protean XL Size.
- **Calbiochem** (Darmstadt, Germany): synthetic α melanocyte stimulating hormone (αMSH) analogue [Nle4, D-Phe7] αMSH (NDP-MSH), phosphatase inhibitors (imidazole, sodium fluoride, sodium o-vanadate and β-glycerol phosphate).
- **Dako** (Glostrup, Denmark): fluorescence mounting medium.
- **Dharmacon Inc.** (Lafayette, CO, USA): Cas9 Nuclease Expression plasmid with puromycin selection marker, trans-activating CRISPR RNA (tracrRNA), crispr-RNA5, crispr-RNA6, crRNA Non-targeting Control #1, DharmaFECT Duo Transfection Reagent, mouse Mgrn1 siRNA oligonucleotides siGENOME 1 and 4, human MGRN1 siRNA oligonucleotides siGENOME 1-4, DharmaFECT 4 Transfection Reagent and Non-targeting siRNA #2.
- **Fermentas** (Barcelona, Spain): DNA ladder and restriction endonucleases.
- **Gibco BRL-Life Technologies** (Gaithersburg, USA): OptiMEM, DMEM-GlutaMAX™, fetal bovine serum (FBS), trypsin-EDTA and penicillin/streptomycin sulfate.
- **Invitrogen** (Carlsbad, CA, USA): kit SuperScript™ First-Strand Synthesis System for RT-PCR, lipofectamine™ 2000, Library Efficiency DH5α, DNA ligase, pcDNA3 plasmid, SYBR™ Green I Nucleic Acid Gel Stain 10,000X, DAPI, eBioscience™ Phalloidin eFluor™ 570, CellTracker™ Green CMFDA Dye, CellTracker™ Orange CMTMR Dye, CellTrace™ CFSE Dye and kit Click-iT® EdU Microplate Assay.
- **Labotaq** (Sevilla, Spain): RedSafe™ Nucleic Acid Staining Solution (20,000x).
- **Merck** (Darmstadt, Germany): ethanol and sucrose.
- **Millipore** (Billerica, MA, USA): Polyvinylidene difluoride (PVDF) ImmobilionNy+ Blotting Membrane (Immobilon-P).
- **Panreac Quimica** (Barcelona, Spain): hydrogen chloride (HCl), glycerol, Tween-20, potassium hydroxide (KOH), 4 % neutral buffered formalin and sodium acetate ($NaCH_3COO$).

- **Probus** (Barcelona, Spain): copper (II) sulfate and sodium tetraborate.

- **Prolabo** (Barcelona, Spain): acrylamide/bisacrylamide.

- **Pronadisa** (Madrid, Spain): Lysogeny Broth (LB) agar medium and Super Optimal Broth (SOB) medium.

- **Qiagen** (Hilden, Germany): RNeasy® Mini kit and QIAquick Gel Extraction Kit.

- **R&D Systems** (Minneapolis, MN, USA): Cyclic AMP Direct ELISA kit.

- **Roche Applied Sciences** (Mannheim, Germany): complete™ Mini EDTA-free Protease Inhibitor Cocktail tablets.

- **Scharlab** (Barcelona, Spain): ethylenediaminetetraacetic acid (EDTA), potassium chloride (KCl) and magnesium chloride ($MgCl_2$).

- **Sigma-Aldrich** (St Louis, MO, USA): β-mercaptoethanol (βME), bovine serum albumin (BSA), iodoacetamide (IAA), N-ethylmaleimide (NEM), phenylmethanesulfonyl fluoride (PMSF), Igepal CA-630, ampicillin, anti-FLAG M2– Peroxidase conjugate antibody, GenElute HP Plasmid Maxiprep Kit, GenElute HP Plasmid Miniprep Kit, ammonium persulfate (APS), sodium deoxycholate, triton X-100, bromophenol blue, MTT, tert-Butyl hydroperoxide solution (Luperox® TBH70X), proteinase K, ribonuclease A (RNase A), hydroxyurea (HU), ammonium acetate (NH_4Ac), ethylene glycol tetraacetic acid (EGTA), 1,4-piperazinediethanesulfonic acid (PIPES), Neocarzinostatin (NCS), 5-iodo-2'-deoxyuridine (IdU), 5-chloro-2'-deoxyuridine (CldU), EZview™ Red Anti-HA Affinity Gel, SU9516 and dithiothreitol (DTT).

- **Teknokroma Analítica S.A.** (Barcelona, Spain): Oligonucleotide sequences.

- **Thermo Fisher Scientific** (Waltham, Massachusetts, USA): ECL Plus Western Blotting Detection System, Pierce™ BCA Protein Assay Reagent A, Tris, disodium phosphate (Na_2HPO_4), monopotassium phosphate (KH_2PO_4), sodium hydroxide (NaOH), agarose, PageRuler Prestained Protein Ladder, formaldehyde, Power SYBR Green PCR Master Mix and Pierce™ Silver Stain for Mass Spectrometry Kit.

- **Trevigen** (Gaithersburg, MD, USA): Alkaline Comet Assay.

- **VWR** (Radnor, Pennsylvania): Plastic used for cell culture.

- **Zymo Research** (Orange, CA, USA): Kit DNA Clean & Concentrator™.

2. Cell culture

Mouse melan-md1 and melan-a6 cells were obtained from the Wellcome Trust Functional Genomics Cell Bank (a gift from Dr. D. Bennett, St George's University of London, UK) and were grown in RPMI medium enriched with 10 % fetal bovine serum (FBS), 200 nM 12-O-tetradecanoylphorbol-13-acetate (TPA), 100 U/ml penicillin and 100 µg/ml streptomycin sulphate. Mouse melanoma B16F10-luc cells (a gift from Prof. JN Rodríguez-López, University of Murcia, Spain), human HEK293T cells (provided by the Tissue Culture Service, SAI, University of Murcia) and human melanoma HBL cells (a gift from Prof. G. Ghanem, LOCE-Institut J. Bordet, Université Libre de Bruxelles, Belgium) were grown in DMEM enriched with 10 % FBS, 100 U/ml penicillin and 100 µg/ml streptomycin sulphate.

Cell lines were grown in a ThermoQuest incubator (Forma Scientific, Marietta, OH, USA) at 37 ºC and 7.5 % CO_2 for mouse melanocytes or 5 % CO_2 for the rest of the lines used.

Cell cultures were routinely maintained by seeding approximately 5×10^5 cells in a 75 cm^2 flask with 10 ml of culture medium until reaching 85 % confluence. For cells collection, cultures were washed with phosphate buffered saline (PBS: 137 mM NaCl, 2.7 mM KCl, 10 mM Na_2HPO_4, 1 mM KH_2PO_4, pH 7.2) and detached by treatment with Trypsin/EDTA (0.5 % trypsin, 0.2 % EDTA in PBS). Finally, cells were centrifuged at 2000 rpm for 5 min. Cells were cultured for a maximum of five passages and their phenotype was verified in every experiment.

2.1. Cell cultures on thick layers of collagen I

Collagen I matrices were prepared using atelopeptide fibrillar bovine dermal collagen (no. 5005-B; PureCol, Advanced BioMatrix) at a final concentration of 1.7 mg/ml in DMEM and allowed to polymerize for 4 h (100 µl per well in 96-well plates, 300 µl per well in 24-well plates, 700 µl per well in 12-well plates). After polymerization, cells were seeded on top of collagen in medium containing 10 % FBS and allowed to adhere for 12 h. Cells were imaged after 24-48 h in culture in 1 % serum media.

3. RNA extraction

RNA was isolated using the RNeasy® Mini kit. Cells were first washed with cold PBS 1X and then 350 µl of RLT buffer and 3.5 µl of βME were added. Samples were lysed and homogenized with gentle shaking. A volume of 350 µl of 70 % ethanol was added to samples and the mixes were transferred to RNeasy spin columns. After centrifugation 15 s at 9000 g, the flow-through liquid was discarded and samples bound to columns were washed according to manufacturer’s instructions. Then, columns were placed in

new tubes and 30 µl of RNase free water was added onto the membrane of the columns. After centrifugation 1 min at 9000 g, the RNA was eluted and its concentration was determinated by measuring the absorbance at 260 nm with the spectrophotometer Thermo Scientific™ NanoDrop 2000c (Thermo Thermo Scientific). The purity of RNA was determined by the A_{260}/A_{280} ratio of the isolated RNA.

4. cDNA synthesis

cDNA was synthesized using the commercial kit SuperScript™ First-Strand Synthesis System for RT-PCR. One µg of RNA was mixed with dNTPs (deoxynucleotide triphosphates) mix and oligo(dT). The mixture was incubated at 65 ºC for 5 min for denaturation. Then, the samples were placed at room temperature (RT) during 2 min and later on ice for 5 min. Samples were incubated at 42 ºC for 2 min with $MgCl_2$, DTT, RNaseOUT™ and retrotranscriptase buffer. Then, SuperScript II Retrotranscriptase enzyme was added and samples were incubated at 42 ºC for 50 min and then at 70 ºC for 15 min. Samples were chilled on ice for 5 min and, finally, 1 µl of RNase H was added and mixture was incubated at 37 ºC for 20 min.

5. Semi-quantitative PCR

MC1R and *MC1R-203* transcripts were amplified from HBL cells. Total RNA from HBL cells was reverse-transcribed to cDNA and amplified by PCR using 2 mM $MgCl_2$, 0.2 mM dNTPs, 1 U DNA *Taq* polymerase and 1 µM each primer (Table 1). PCR was performed with common forward and reverse primers complementary to shared sequences in exon 3 and 3'UTRs, respectively (Figure 1).

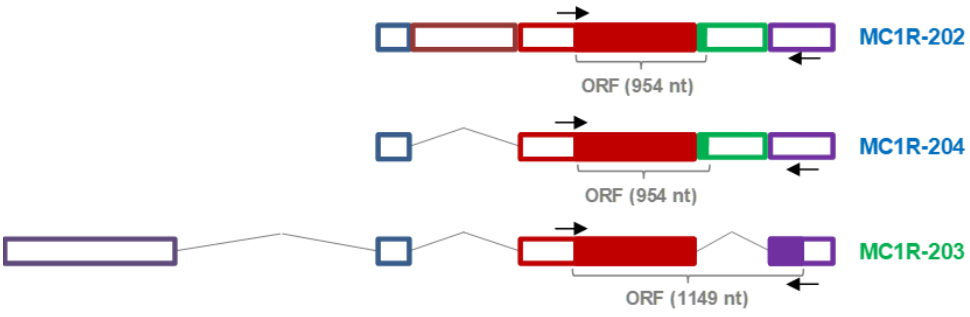

Figure 1. Structure of the MC1R gene splice variants. Exons are depicted in coloured boxes (empty for UTRs, filled for coding sequences), and the number of nucleotides in the corresponding ORFs is shown below. The position of PCR primers is shown by arrows above (forward primers) or below (reverse primers) the graph.

Reaction mixtures were incubated for 2 min at 95 ºC, followed by 30 cycles of denaturation at 95 ºC for 1 min, annealing at 68 ºC for 1 min and extension at 72 ºC for

2 min, and one final 10 min extension at 72 ºC. *GAPDH* gene was used as a quality control.

DNA fragments corresponding to both isoforms were identified by agarose gel electrophoresis. Twenty µl of sample were run on a 1.5 % agarose gel with 1 % Red Safe nucleic acid staining reagent solution. For electrophoresis, 1X TAE buffer was used at 90 V during 30 min. PCR products were detected using a UV Gel Doc 1000 transilluminator (BioRad, Richmond, VA, USA).

Target	**Oligo**	**Sequence 5' → 3'**
MC1R and *MC1R-203*	Forward	GATCGAATTCGCCGCCATGGCTGTGCAGGGAT
MC1R and *MC1R-203*	Reverse	GATCCTCGAGCTAGGGGGGCTCCTGCAAACCTG
GAPDH	Forward	ACCACAGTCCATGCCATCAC
GAPDH	Reverse	TCCACCACCCTGTTGCTGTA

Table 1. Primer sequences employed for *MC1R*, *MC1R-203* and *GAPDH* amplification by PCR.

6. Expression constructs

pcDNA3 vector was selected to create all expression constructs. MC1R-203 expression construct was obtained by A/T TOPO Cloning. Both MC1R-203 and Flag-tagged MC1R (formerly reported (165)) expression constructs, were digested with BamHI and NotI restriction enzymes to subclone MC1R-203 transcript into Flag-tagged pcDNA3. Expression constructs used and previously described are listed in Table 2.

Expression constructs (pcDNA3)	**Gene**
Flag-tagged MC1R	*MC1R*
Flag-tagged MC1R-203	*MC1R-203*
ARRB2	*ARRB2*
HA-tagged MGRN1 S(+)	*MGRN1 S(+)*

Table 2. Expression constructs.

First, MC1R-203 construct and Flag-MC1R construct in pcDNA3 expression vector were double-digested separately with BamHI and NotI restriction enzymes by incubation at 37 ºC for 1 h. Each digestion was run in a 1.5 % agarose gel and bands corresponding to Flag-tagged pcDNA3 and MC1R-203 transcript were isolated with QIAquick Gel Extraction Kit, according to manufacturer's instructions. Ligation was performed in a

molar ratio of 1:2 (vector: insert) incubating at RT for 2 h with 1 U of T4 DNA ligase. Finally, ampicillin resistant DH5α competent cells were transformed with ligation mixture.

7. Sequencing

Flag-tagged MC1R-203 construct was verified using Sanger sequencing (Molecular Biology Platform, University of Murcia) of the plasmid obtained using the commercial kit "GenElute HP Plasmid Miniprep Kit" (Gigma-Aldrich). Sequence was compared with MC1R-203 sequence obtained from Ensembl database (https://www.ensembl.org/index.html). Primers used for sequencing are described in Table 3.

Target	**Oligo**	**Sequence 5'→ 3'**
Flag-tagged *MC1R-203*	Forward	GCAAATGGGCGGTAGGCGTC
Flag-tagged *MC1R-203*	Reverse	CTAGAAGGCACAGTCGAGGC

Table 3. Primers sequences employed for Flag-tagged MC1R-203 construct sequencing.

8. Transient transfection

Lipofectamine 2000 were employed as a transfection reagent. Lipofectamine at 1 mg/ml and DNA plasmids (Table 4) were diluted in OptiMEM and incubated 10 min at RT. Then, diluted DNA was mixed with Lipofectamine solution for 20 min at RT. The final volume was adjusted with DMEM supplemented with 10 % SBF and the mix was added to cells (quantities in Table 5). Cells were processed 24 h after transfection.

DNA plasmid	**Gene**	**Supplier**
Flag-tagged *MC1R*	*MC1R*	Research group
Flag-tagged *MC1R-203*	*MC1R-203*	Research group
ARRB2	*ARRB2*	Research group
HA-tagged *MGRN1 S(+)*	*MGRN1 S(+)*	Research group
MYC-tagged *MGRN1 S(+)*	*MGRN1 S(+)*	Research group
pcDNA3	Negative control	Invitrogen

Table 4. DNA plasmid used for transient transfection.

Plate format	DNA plasmid (µg)	Lipofectamine 2000 (µl)	Final volumen (µl)
6-well	0.6	1.5	1000
12-well	0.3	1	500
24-well	0.15	0.75	350

Table 5. Transient transfection conditions.

9. RNAi Transfection

Mouse cells were seeded in a 6-well plate and transfected the next day with individual mouse Mgrn1 siRNA oligonucleotides siGENOME 1 or 4, or a stoichiometric mixture of these oligonucleotides, at a final concentration of 30 nM, using OptiMEM and 5 µl/well DharmaFECT 4 Transfection Reagent. Alternatively, human cells were transfected with a stoichiometric mixture of human MGRN1 siRNA oligonucleotides siGENOME 1-4. Non-targeting siRNA #2 was used as control. Seventy-two h later, cells were used for the desired experiment. siRNA sequences are specified on Table 6.

Name	Sequence
siGENOME Non-Targeting siRNA #2 (siCTR)	UAAGGCUAUGAAGAGAUAC
siGENOME Mgrn1-1 (si-01)	GAUGGCAGCUUCUCCGUGA
siGENOME Mgrn1-4 (si-04)	CGUAGAGGACAUCGACAUA
siGENOME Human MGRN1-1 (si-01)	CGAAGGAGAUGUGGUGGAA
siGENOME Human MGRN1-2 (si-02)	GAGCACCUUGUCCCUUUA
siGENOME Human MGRN1-3 (si-03)	GAACUCGGCCUAUCGCUAC
siGENOME Human MGRN1-4 (si-04)	AAGAUUGACUUCUCGGAAU

Table 6. Sequence of control and Mgrn1-directed siRNA.

10. Protein extraction

According to subcellular localization of protein of interest, an appropriate lysis buffer was used. For membrane proteins extraction, cells were resuspended in lysis buffer I (50 mM Tris-HCl pH 7.5, 1 mM EDTA, 1 % Igepal). In contrast, for nuclear proteins extraction, cells were resuspended in lysis buffer II (150 mM sodium chloride, 1.0 % Triton X-100, 0.5 % sodium deoxycholate, 0.1 % SDS, 50 mM Tris, pH 8.0). Both lysis buffers were supplemented with 0.1 mM PMSF, 10 mM IAA, 10 mM NEM and phosphatase inhibitors (200 mM imidazole, 100 mM NaF, 100 mM sodium o-vanadate and 1 M β-Glycerol

phosphate). Then, lysis extracts were gentle shaking and centrifuged for 30 min at 15000 g at 4 ºC. Protein concentration in supernatants was measured by the BCA (Bicinchoninic Acid) assay.

11. Protein measurement

The BCA assay was used for total protein quantification. First, the standard curve was prepared using a BSA (Bovine Serum Albumin) stock solution (2 mg/ml) and diluting it from 0 to 30 µg/ml. Fifteen µl of standards and samples dilutions were pipetted into duplicate wells in a 96-well microplate. Then, we added 285 µl of working reagent (WR) solution into each well. The WR solution was prepared by adding 1 part of BCA Reagent B (containing 4 % cupric sulfate) to 50 parts of BCA Reagent A (containing sodium carbonate, sodium bicarbonate, bicinchoninic acid and sodium tartrate in 0.1 M sodium hydroxide). The microplate was incubated for 30 min at 37 ºC and the absorbance at 562 nm was measured on a BioTek™ ELx800™ microtiter plate reader (BioTek, Bedfordshire, UK). Protein amount was obtained by using linear regression analysis from BSA standard curve.

12. Immunoblotting

12.1. Protein electrophoresis

Cell lysates containing 20 µg protein were incubated in 4X loading sample buffer (250 mM Tris pH 6.8, 8 % SDS, 20 % glycerol, 0.08 % bromophenol blue and 3.2 M β-mercaptoethanol) for at least 20 min at RT or boiled at 95 ºC for 5 min (membrane protein samples were not boiled). Electrophoresis was performed on polyacrylamide gels in the presence of SDS (sodium dodecyl sulfate). Polyacrylamide gels are composed of a stacking gel (4 % acrylamide/bisacrylamide, 1 cm height and 1 mm thickness) and a resolving gel (8-15 % acrylamide/bisacrylamide, 6 cm height and 1 mm thickness). The catalysis of sulfate radicals released from ammonium persulfate (APS) in the presence of TEMED leads to polymerization of the gels. After polymerization, 20 µl of samples were loaded into each well and electrophoresis was performed at 15 mA/gel (stacking gel) and 25 mA/gel (resolving gel) for 2 h, using a dissociation running buffer (25 mM Tris, 190 mM glicine, 0.1 % SDS, pH 8.3). Discontinuous sodium dodecyl sulfate polyacrylamide gel electrophoresis (SDS-PAGE) was carried out according to Laemmli method with some modifications and using a Mini-Protean II/III cell and a PowerPac™ Basic Power Supply (Bio-Rad).

12.2. Transfer and protein detection

After electrophoresis, proteins were transferred onto a PVDF membrane (Immobilon-P) 0.45 µm pore size. First, membranes were pre-treated following the manufacturer's instructions and then, membranes and gel were incubated in transfer buffer (48 mM Tris, 39 mM Glicine, 0.04 % SDS, 20 % methanol) for 5 min. Transfer was performed in a semidry transfer system (Trans-Blot® Turbo™ Transfer System, Bio-Rad) at 1.25 A for 20 min. After transfer, membranes were blocked with 4 % BSA in TBS (20 mM Tris, 137 mM NaCl, pH 7.4)/0.1 % Tween-20 for 1 h with moderate shaking, to avoid nonspecific binding of the antibody. Membranes were incubated with the primary antibody overnight (ON) at 4 ºC with moderate shaking. Then, membranes were washed several times with TBS/0.1 % Tween-20 and incubated with the secondary antibody (1:10000 dilution) in 2 % BSA in TBS/0.1 % Tween-20 for 1 h. An additional wash was performed upon secondary antibody incubation. For detection of blotted proteins, the ECL (Enhanced chemiluminescence) Plus reagent (Thermo Fisher Scientific) was used and light emission was captured with Fusion Solo.6S (Vilber Lourmat, Collégien, France). If required, membrane stripping was carried out with 0.5 M NaOH for 10 min with gentle shaking followed by a 10 min washing step in H_2O. ERK2 or GAPDH were used as loading control and utilized to determine relative abundance of target proteins with ImageJ software (National Institutes of Health, Bethesda, MA, USA). Antibodies used in this work are summarized in Table 7.

Primary Antibody	Catalog number	Working Dilution	Secondary antibody
Flag HRP (Sigma-Aldrich)	A8592	1:10000	---
ARRB2 (Cell Signaling)	3858	1:10000	anti-rabbit IgG-HRP (Millipore)
p-ERK1/2 (Santa Cruz)	sc-136521	1:5000	anti-mouse IgG-HRP (Santa Cruz)
ERK2 (Santa Cruz)	sc-1647	1:10000	anti-mouse IgG-HRP (Santa Cruz)
ACTIN (Sigma-Aldrich)	A2066	1:5000	anti-rabbit IgG-HRP (Millipore)
MGRN1 (Proteintech)	11285-1-AP	1:2000	anti-rabbit IgG-HRP (Millipore)
MITF (Cell Signaling)	12590	1:5000	anti-rabbit IgG-HRP (Millipore)
GAPDH (Santa Cruz)	sc-25778	1:10000	anti-mouse IgG-HRP (Santa Cruz)
p-ATR (phospho Thr1989) (Abcam)	ab227851	1:2000	anti-rabbit IgG-HRP (Millipore)
ATR (Santa Cruz)	sc-515173	1:2000	anti-mouse IgG-HRP (Santa Cruz)
CHK1 (Santa Cruz)	sc-8408	1:2000	anti-mouse IgG-HRP (Santa Cruz)
p-CHK1 (phospho Ser317) (Cell Signaling)	D12H3	1:5000	anti-rabbit IgG-HRP (Millipore)
p-CHK2 (phospho Thr68) (Cell Signaling)	C13C1	1:2000	anti-rabbit IgG-HRP (Millipore)
P53 (Abcam)	ab131442	1:2000	anti-rabbit IgG-HRP (Millipore)
p-P53 (phospho Ser15) (Cell Signaling)	9284	1:2000	anti-rabbit IgG-HRP (Millipore)
p-ATM (phospho Ser1981) (Santa Cruz)	sc-47739	1:2000	anti-mouse IgG-HRP (Santa Cruz)
RPA70 (Santa Cruz)	sc-48425	1:2000	anti-mouse IgG-HRP (Santa Cruz)
RPA32 (GeneTex)	GTX113004	1:2000	anti-rabbit IgG-HRP (Millipore)
ATRIP (Cell Signaling)	2737	1:2000	anti-rabbit IgG-HRP (Millipore)
CDK2 (Santa Cruz)	sc-6248	1:5000	anti-mouse IgG-HRP (Santa Cruz)
HA (Sigma-Aldrich)	H9658	1:2000	---
RB (Santa Cruz)	sc-102	1:2000	anti-mouse IgG-HRP (Santa Cruz)
FOXM1 (Santa Cruz)	sc-376471	1:2000	anti-mouse IgG-HRP (Santa Cruz)

Table 7. Antibodies used for detection of proteins by SDS-PAGE and Western blot.

13. Isolation of Chromatin-bound Proteins

Cells (0.5×10^6) were collected by trypsinization, washed with PBS 1X and resuspended in 100 µl of Cytoskeletal (CSK) Buffer (10 mM PIPES pH 6.8, 100 mM NaCl, 300 mM sucrose, 3 mM $MgCl_2$, 1 mM EGTA, 50 mM NaF, 0.1 mM Na_3VO_4 and 0.1 % Triton X-100) supplemented with protease inhibitors. Samples were briefly vortexed and incubated in ice for 10 min. Soluble ('Cytosol + Nucleosol') and insoluble fractions were separated in a microfuge (1500 rpm, 5 min). The supernatant constituted the soluble fraction and the pellet (insoluble fraction) was washed twice with CSK buffer. SDS–PAGE loading buffer was added to the insoluble fraction (constituting the chromatin-associated fraction) and chromatin-bound/unbound proteins were analyzed by SDS-PAGE.

14. Co-precipitation Assay

For mass-spectrometry analysis 24×10^6 HBL cells were transiently transfected with 30 µg MGRN1 S(+)-HA plasmid or pcDNA3 as control while for Western blotting analysis we transfected 4×10^6 cells with 5 µg of plasmids. After 48 h, cells were lysed with lysis buffer I (50 mM Tris-HCl pH 7.5, 1 mM EDTA and 1 % Igepal, supplemented with protease and phosphatase inhibitors) and cell lysates were incubated with anti-HA antibody attached to agarose beads (EZview™ Red Anti-HA Affinity Gel) for 2 h at 4 ºC. Upon centrifugation for 1 min at 1500 rpm, the complexes were washed with IP100 buffer (25 mM Tris pH 7.5, 5 mM $MgCl_2$, 1.0 % Triton X-100, 10 % glycerol, 100 mM KCl and 0.3 mM DTT, supplemented with protease and phosphatase inhibitors) for 5 times, eluted by boiling in 1 x loading sample buffer (4x LSB: 250 mM Tris pH 6.8, 8 % SDS, 20 % glycerol, 0.08 % bromophenol blue and 3.2 M β-mercaptoethanol), and then subjected to silver staining to check the correct precipitation of MGRN1 (using Pierce™ Silver Stain for Mass Spectrometry Kit) or Western blotting analysis. Resulting samples were also analyzed by mass-spectrometry by Protein Analysis Facility hosted by the University of Lausanne. Results were analyzed with the software MASCOT and Scaffold (http://www.matrixscience.com/ and www.proteomesoftware.com) to count the number of spectra detected by spectrometry that matched to a particular protein. We used the CRAPome website (http://www.crapome.org), which contains a list of unspecific proteins identified in a large number of negative control experiments to discard possible artifacts.

15. cAMP assay

15.1. Sample preparation

HEK293T cells were seeded in 12-well plates, with duplicates for each condition and two additional wells for protein determination. Cells were transiently transfected with *MC1R* and *MC1R-203*-encoding plasmids as previously described. Eighteen h after transfection, serum was deprived for 3 h and cells were stimulated with NDP-MSH (10^{-7} M, 30 min or 3 h). Then, cells were washed with PBS at 4 ºC. We added 200 µl 0.1 N HCl preheated at 70 ºC and we collected the sample containing released cAMP. Samples were dried in a Speed-Vac Maxi Dry Plus (Heto), washed twice with H_2O and dried again. Finally, each sample was resuspended in the specific volume of lysis buffer for cAMP detection supplied by the commercial kit.

15.2. cAMP quantification

The amount of cAMP in samples were determined using the commercial "Cyclic AMP Direct ELISA kit" based on the competition for binding to the cAMP antibody between the cAMP from samples and a given concentration of cAMP-peroxidase conjugate provided by the kit. The amount of cAMP-peroxidase conjugate that bound to the antibody is inversely proportional to the concentration of cAMP in the sample.

Reaction consisted on 25 µl of neutralization solution, provided by the kit, and 50 µl of samples or cAMP standards or alternatively, 75 µl of dilution buffer as nonspecific binding control. Next, we added 25 µl of cAMP-peroxidase conjugate and finally, 25 µl of cAMP-specific antibody. The binding reaction was initiated by the addition of the antibody. After 2 h of incubation time, wells were washed and a TMB (3,3′,5,5′ Tetramethylbenzidine) peroxidase substrate solution was added. After 30 min, the reaction was stopped, and the absorbance was measured at 450 nm in a BioTek™ ELx800™ microtiter plate reader. A cAMP standard curve was included using known concentrations of cAMP. Data are shown as pmoles/µg protein relative to the control.

16. Generation of CRISPR/Cas9-Based Mgrn1-KO Cells

Target sequences for CRISPR-RNA from Dharmacon are specified on Table 8. Efficiencies and potential off-targets were determined using the Breaking-Cas web server (http://bioinfogp.cnb.csic.es/ tools/breakingcas) (166). Cells were co-transfected with 2.5 µg Cas9 Nuclease Expression plasmid with puromycin selection marker, 50 nM trans-activating CRISPR RNA (tracrRNA), 50 nM crispr-RNA5 (crRNA) or crispr-RNA6 and 6 µg/ml DharmaFECT Duo Transfection Reagent (all from Dharmacon). For negative control cells, we transfected 50 nM crRNA Non-targeting Control #1. After

incubation at 37 ºC for 72 h, puromycin-resistant clonal cells were selected. Confirmation and selection of positive clones was performed by automated sequencing after PCR amplification of a 700-pb fragment on exon 1 using genomic DNA as template.

Crispr-RNA	Target sequence	PAM	Genomic Location (strand)	Score efficiency	Off-targets
crRNA5	CGCGATGCGGCGACTCAGGA	TGG	Chr16: 4886393-4886415 (-)	95.1	11
crRNA6	GGACTTCGGAGGGTAGCGAT	AGG	Chr16: 4886450-4886472 (-)	92.6	37

Table 8. Target and protospacer adjacent motif (PAM) sequences, genomic location, score efficiency and number of off-targets for each crRNA.

Genomic DNA isolation was performed using the phenol-chloroform method followed by precipitation of DNA with ethanol. Briefly, cells were disrupted with lysis buffer (50 mM Tris-HCl, 20 mM NaCl, 1 mM EDTA, 0.1 % SDS) and incubated with proteinase K (150 µg/ml) for 2 h at 55 ºC. For the extraction of nucleic acids, a phenol:chloroform:isoamyl alcohol (25:24:1) reagent was mixed with the samples and the different phases were separated by centrifugation. Aqueous phase was isolated and DNA precipitation was achieved by incubation with sodium acetate and ethanol (0.1:2.5 ratio) for 12 h at -20 ºC.

Amplification of a ~700-pb fragment centred on targeted sequence on exon 1 was carried out by PCR. Thirty rounds of PCR were performed (denaturation for 30 sec at 95 ºC, annealing 1 min at 56 ºC and extension 45 sec at 72 ºC) followed by a 10 min extension at 72 ºC. Primers for Mgrn1 were provided by Biolegio BV (Biolegio BV, Nimega, Netherlands). Their sequences are: Mgrn1-e1 forward: 5'-GCGTTGGTGCGGCCTGTTTTGG-3' and Mgrn1-e1 reverse: 5'-CTGCCCTGAATGAGAGGGAAAGGT-3'.

17. Generation of CRISPR/Cas9-Based MGRN1-KO Cells

The crRNA and tracrRNA can be fused together to create a chimeric, single-guide RNA (sgRNA) (167). First, we designed the sgRNA oligos, 20-nt guide sequence base pairs with the opposite strand which must immediately precede a 5′-NGG PAM (Table 9). Efficiencies and potential off-targets were determined using the Breaking-Cas web server (http://bioinfogp.cnb.csic.es/tools/breakingcas) (166). To generate the sgRNA expression construct, sgRNA oligos were cloned into the pSpCas9(BB)-2A-Puro vector plasmid (Addgene plasmid ID: 48139) for co-expression with Cas9, as described in (167). To this end, the oligo pairs encoding the 20-nt guide sequences were annealed

and ligated into the plasmid. Finally, ligated CRISPR plasmid was transformed in *E. coli* and validated by sequencing. Cells were transfected with 0.5 µg of the CRISPR plasmid (pSpCas9(sgRNA)) and 1 mg/ml Lipofectamine™ 2000. For negative control cells, we transfected no-insert, pSpCas9(BB)-only negative control. After incubation at 37 ºC for 72 h, puromycin-resistant clonal cells were selected. Confirmation and selection of positive clones was performed by automated sequencing after PCR amplification of a 500-pb fragment on exon 1 using cDNA as template. Thirty rounds of PCR were performed (denaturation for 1 min at 95 ºC, annealing 1 min at 64 ºC and extension 1 min at 72 ºC) followed by a 10 min extension at 72 ºC. Primers sequences are: hMGRN1-screening forward: 5'-CCTGGTCCGGGCCATGTC-3' and hMGRN1-screening reverse: 5'-CCTTTTAGGTTTCTTGCTGGCCAGGGAGGC-3'.

sgRNA oligo	Target sequence (5' → 3')	PAM	Genomic Location (strand)	Score efficiency	Off-targets
sgRNA2	ATTCTCAGCCGCCGCATCGC	GGG	Chr16: 4624826-4690972 (+)	96.5	48
sgRNA3	CATCGACATCCAGGCGAACT	CGG	Chr16: 4624826-4690972 (+)	94.3	38
sgRNA4	GGACTTCGGAGGGTAGCGAT	AGG	Chr16: 4624826-4690972 (-)	91.7	49

Table 9. Target and protospacer adjacent motif (PAM) sequences, genomic location, score efficiency and number of off-targets for each sgRNA, whose maximum score efficiency was less than 1.5, so they were not considered relevant.

18. Melanin Content Measurement

Melanin content was determined after alkaline solubilization using a colorimetric assay (168). Pellets from each cell line were treated with 100 µl of 0.85 M potassium hydroxide (KOH) for 4 h at 100 ºC. Next, absorbances at 405 nm of the obtained products were measured using an ELx800™ microtiter plate reader (BioTek™, Winooski, VT, USA). Protein amount (µg) in each sample were calculated using the following equation:

Abs (405 nm) = (0.0165 x µg melanins) + 0.003

Data were presented as relative melanin content per microgram of protein.

19. *In Vitro* Cellular Adhesion

Adherent cells were detached using a non-enzymatic cell dissociation solution (Sigma-Aldrich, C5789) and seeded on a thick layer of Collagen I (1.7 mg/ml) prepared as mentioned above or on a thin layer of Matrigel (20 µl at 7–9 mg/ml; ECM Gel, from Sigma) polymerized on top of a thick layer of collagen I (60 µl at 1.7 mg/ml) in a 96-well plate. Percentage of adhering cells was calculated as the number of cells remaining after washing.

20. 2D and 3D Migration Assays

For 2D migration assays, an artificial gap was made by scratching a confluent cell monolayer and cells were incubated in 1 % FBS-containing media. The closure of this gap was monitored at time 0 and after 24 h. The area of the gap at both time points was measured using ImageJ and data were presented as % wound closure. In 3D migration assays, cells were embedded in serum-free bovine collagen I (2.3 mg/ml) to a final concentration of 1.5×10^4 cells/100 µl in a 96-well plate and processed as previously described (169). Quadruplicates per condition were performed. A 3D migration index was calculated as number of migrating cells at 50 µm/total number of cells.

21. Random migration

Cells were seeded on a thick layer of collagen I as indicated above. Tracking of cell migration within collagen matrices was performed as described (170) over a period of 16 h starting after the gel was set. Individual cells were tracked in a semiautomated manner by repeated random selection of cells in movie frames and manual tracing of migration pathways using the Manual Tracking plugin from ImageJ. Any cells moving through convection were excluded.

22. Confocal Fluorescence Microscopy Imaging

Cells were fixed with 4 % p-formaldehyde in PBS for 10 min, permeabilized with 0.3 % Triton-X 100 for 15 min and blocked in 4 % BSA for 1 h at RT. Then, samples were incubated with primary antibodies (Table 10) at 4 ºC ON in a humidified chamber. After 3 washes with 1x PBS/0.05 % Tween 20, cells were labeled with secondary antibodies (Table 10) for 1 h in the dark at RT. Samples were washed again and incubated with DAPI (10 µg/ml, for nuclear staining) for 10 min at RT. Finally, after an additional wash step, samples were mounted using a mounting media from Dako. Images were taken with a SP8 Leica laser scanning confocal microscope and software (Leica Microsystems GmbH, Wetzlar, Germany) with HCXPL APO CS 40x or 63x objective lenses. Backscattered light (reflectance) was collected to image the matrix surrounding cells.

Nuclear fluorescence signal was quantified by calculating the pixel intensity in single cell nuclei relative to the nucleus area. The number of foci in each nucleus was calculated by producing a single pixel for each local maxima/foci and calculating the number of detected maxima/foci in each region defined by the nuclear stain. At least 200 randomly selected cells per condition were quantified using ImageJ.

For 8-oxodG staining, cells were fixed with -20 ºC MeOH followed by -20 ºC acetone. Then, fixed cells were treated with 0.05 N HCl for 5 min on ice and incubated with 100 µg/ml RNAse at 37 ºC for 1 h. After that, DNA was denatured with 0.15 N NaOH in 70 % EtOH for 4 min. Finally, samples were incubated with 5 µg/ml proteinase K at 37 ºC for 10 min and non-specific binding were blocked with 5 % BSA in PBS at RT for 1 h before incubation with anti-8-oxodG antibody (Table 10). The following steps were the same as described above.

Antibody	Supplier	Catalog number	Working Dilution
γ-H2AX	Abcam, UK	ab2893	1:100
HA	Sigma-Aldrich, USA	H9658	1:2000
8-oxodG	Trevigen, USA	4354-MC-050	1:250
p-ATR (phospho Thr1989)	GeneTex, USA	GTX128145	1:100
RPA70	Santa Cruz Biotechnology, USA	sc-48425	1:100
CDK2	Santa Cruz Biotechnology, USA	sc-6248	1:150
MYC	Sigma-Aldrich, USA	C3956	1:2000
Alexa Fluor 488-anti-rabbit	Invitrogen, USA	A-11070	1:400
Alexa Fluor 568-anti-mouse	Invitrogen, USA	A-11019	1:400
Alexa Fluor 488-anti-mouse	Invitrogen, USA	A-11017	1:400

Table 10. Antibodies used for confocal microscopy.

23. DNA fiber assay

DNA fiber assay was performed as described in (171) with some modifications. Briefly, cells were labeled with 25 µM IdU for 20 min. After labeling with the first nucleotide analogue, cells were washed with PBS and treated with 2 mM HU for 2 h, then washed again and labeled with 100 µM CldU for 20 min. Next, cells were washed with ice cold PBS, harvested and resuspended in ice cold PBS at a final concentration of 5×10^5 cells/ml. Two µl of the cell suspension were transferred to a microscope slide SuperFrost (VWR international, 631-0910) and dried for 2-5 min (the drop should not dry completely).

Then, 7 µl of the lysis solution (200 mM Tris-HCl pH 7.5, 0.5 % SDS and 50 mM EDTA) were applied on top of the cell suspension, mixed by gently stirring with a pipette tip and incubated for 2 min. Slides were tilted to 15 º to allow the DNA to spread. Slides were fixed for 10 min with methanol/acetic acid (3:1) solution, washed twice in H_2O and incubated in 2.5 M HCl for 80 min, followed by three washes with PBS for 5 min. Then, slides were placed horizontally in a humidified chamber. After blocking with 200 µl 5 % BSA in PBS for 20 min, 50 µl of the primary antibody solution (Table 11) were pipetted onto each slide and slides were incubated for 2 h at RT. Subsequently, slides were washed tree times with PBS for 5 min. Next, slides were incubated for one hour with the secondary antibodies (Table 11). Slides were washed three times with PBS and allowed to dry. Then, a drop of Vectashield mounting medium (Vector lab, H-1000) was spotted, coverslips (24x50 mm thickness Nº1, Scientific Laboratory Supplies LTD, MIC3234) were applied and images were taken using a SP8 Leica laser scanning confocal microscope (Leica Microsystems GmbH, Wetzlar, Germany) with HCXPL APO CS 63x objective lens. Pictures were then segmented and quantified using a fully automated algorithm, FiberQ (172). FiberQ is an open-source collaborative initiative available in the GitHub repository (https://github.com/pierreghesqui/FiberQ).

Antibody	Supplier	Catalog number	Working Dilution
Primary antibody (rat) anti-BrdU (cross-reacts with CldU)	Abcam, UK	ab6326	1:400
Primary antibody (mouse) anti-BrdU (cross-reacts with IdU)	BD Biosciences, USA	347580	1:25
Secondary antibody (sheep) anti-mouse Cy3	Sigma-Aldrich, USA	C2181	1:500
Secondary antibody (goat) anti-rat Alexa Fluor 488	LifeTechnologies, USA	A110060	1:400

Table 11. Antibodies used for DNA fiber assay.

24. Real Time PCR (RT-PCR o qPCR)

Gene expression analysis by real time PCR was performed on cDNA. The primers were designed to amplify sequences between 50 and 150 bp size. The total G + C content of these primers was 40-60 % and the annealing temperature 58-60 ºC. Furthermore, the presence of more than two G or C bases in the last five nucleotides of the 3' end was avoided. The exact sequence of the primers used is detailed in Table 12.

This technique was performed in 96-well plates on a 7500 Fast Real Time PCR equipment from Applied Biosystem (Warrington, UK). Ten µl SYBR Green PCR Master Mix, 1 µl cDNA, 2 µl 0.5 µM primer mix, and 7 µl nuclease-free water (total volume 20 µl) were added to each well. Reaction mixtures were incubated for 10 min at 95 ºC, followed by 40 cycles at 95 ºC for 15 s and 60 ºC for 1 min. One final cycle at 95 ºC for 15 s, 60 ºC for 1 min, 95 ºC for 30 s and 60 ºC for 15 s.

Fluorescence data was collected at each cycle and its analysis was performed with the Applied Biosystem 7500 SDS Software application. Gene expression quantification was carried out by calculating the cut-off cycle (Ct) for a fluorescence threshold within the exponential phase and was normalized with a control gene (Rpl35 or ACTB) using the Comparative Ct Method for Relative Quantification (ΔΔCt).

Target gene	Primer sequence (5'→ 3')
Mgrn1	Fw: GTCGTCCAGTCCAGTTTCCCTAT Rv: TGCGTCTTCTTTGTACCTCACAAG
Rpl35	Fw: AAGCTCTCCAAGATACGAGTCGTT Rv: TATTTCTTGCCCTTGTAGAATTTCCT
MKi67	Fw: ACTTGCTCTGGCCTACCTGGTCTTA Rv: CCACCAAAGGATACACGTCTTCTCT
MGRN1	Fw: GGCTGTGGTGGACGAAGGA Rv: GGTCCACAATTTGCTTCTGCTT
ACTB	Fw: GACAGGATGCAGAAGGAGATCA Rv: GCTCAGGAGGAGCAATGATCTT

Table 12. Primers used for real-time PCR.

25. Digital PCR (dPCR)

RNA samples isolated from 49 *nevi* and 33 melanomas biopsies were kindly supplied by Dr. Santos Alonso Alegre and Dr. María Dolores Boyano López from the University of the Basque Country. Prior to dPCR analysis, RNA was converted to cDNA using the Kit Maxima First Strand cDNA Synthesis Kit (ThermoFisher), following the manufacturer's instructions.

To detect gene expression differences smaller than two-fold, digital PCR was performed on the QuantStudio™ 3D Digital PCR System (Applied Biosystems). First, we mixed cDNA with QuantStudio™ 3D Digital PCR Master Mix V2 (Applied Biosystems) and Taqman Gene Expression Assays (Table 13).

Target	Dye	Reference	Supplier
MGRN1	FAM	Hs01005100_m1	Applied Biosystems
GAPDH	VIC	Hs02758991_g1	Applied Biosystems

Table 13. Taqman Gene Expression Assays used.

The resulting dPCR reaction mix was loaded onto a QuantStudio™ 3D Digital PCR Chip v2 (Applied Biosystems), containing 20,000 independent reaction wells. To detect the presence or absence and the number of copies of the DNA molecules of interest in each independent reaction chamber, PCR was performed using the ProFlex™ 2x Flat PCR System (Applied Biosystems) and read using the QuantStudio™ 3D Digital PCR Instrument (Applied Biosystems). The instrument determines the location and intensity of the fluorescent signals in each image, the dye associated with each fluorescent signal, and the significance of the signal. Finally, data were analyzed using the QuantStudio™ 3D AnalysisSuite™ Software (Applied Biosystems), which generates copies/µl for each sample based on copies/reaction generated and dilution factor of the sample. To analyze gene expression differences between samples, we used dPCR quantification of *GAPDH* as endogenous control. Results are calculated as:

Relative *MGRN1* expression (%) = (*MGRN1* copies/µl) / (*GAPDH* copies/µl) × 100

26. Cell Proliferation Assays

Three different methods were used:

26.1. Manual counting

For manual counting, cells were seeded and manually counted using a hemocytometer at the different time points from 24 to 96 h. Normalized cell number values were plotted using GraphPad Prism (GraphPad Software, San Diego, CA, USA, www.graphpad.com) and doubling times were calculated by nonlinear regression using an exponential growth equation.

26.2. Cell labeling assay

A cell labeling assay was performed by labeling cells with CellTrace™ (CFSE, Invitrogen) followed by flow cytometric measurements of the fluorescence intensity of cells using a FACScan system (Becton Dickinson, Franklin Lakes, NJ. USA), 488 nm excitation and 517 nm emission). Arbitrary units of fluorescence normalized with fluorescence intensity

at time 0 h were plotted using GraphPad Prism and half-life values were obtained by nonlinear regression using a one phase decay equation.

26.3. MTT assay

Cells were incubated with MTT solution and absorbances at 570 nm and at 690 nm (background) were measured using an ELx800™ microtiter plate reader (BioTek™, Winooski, VT, USA). Normalized absorbance values were plotted using GraphPad Prism and doubling times were calculated as for the manual counting assay.

27. 3D Spheroid Assays

Spheroid cell culture was performed using the hanging drop method, adapted from Del Duca et al. (173). Briefly, spheroids of cells were collected and resuspended in a collagen I solution (1.7 mg/ml in DMEM), added on top of a thin layer of previously polymerized collagen I. For growth quantification, increase of the area of spheroids between day 0 and 4 was calculated using ImageJ.

28. Cell Cycle Analysis

Cells were fixed in ethanol 70 % in PBS, then pelleted and resuspended in PBS containing 100 µg/ml RNase A and 40 µg/ml propidium iodide (PI). Cells were analysed in a FACScanto cytometer from BD Biosciences (San Jose, CA, USA). The kinetics of cell cycle progression were analysed according to (174) by pulse-chase experiments using cells labeled with BrdU (20 µM, 1 h), then chased for different times in the presence or absence of colcemid (0.1 µg/ml). Cells were labeled with PI and analysed as above. For experiments of HU-mediated interference, cells were incubated in complete medium containing HU at a final concentration of 2 mM for the required times, washed with PBS and further incubated in HU-free medium for various times, as indicated in the corresponding Figures. For pulse-chase experiments, cells were treated with 2 mM HU for 3 h, washed with PBS and allowed to recover for 1 h in fresh medium. Then, BrdU and colcemid were added (final concentrations 20 µM and 0.1 µg/ml respectively). Cells were collected at the required times and resuspended in cold PBS. 1×10^6 cells were resuspended in 100 µl of ice-cold PBS/1 % FBS, then added dropwise to 5 ml of −20 ºC, 70 % ethanol and kept overnight at 4 ºC. The fixative was removed, 1 ml of 2 N HCl/Triton X-100 was added dropwise and cells were centrifugated, neutralized with 0.1 M sodium tetraborate, pH 8.5 and centrifugated again. The pellet was resuspended with 75 µl of BrdU staining mix (50 µl 0.5 % Tween 20 in PBS containing 1 % BSA, 20 µl FITC conjugated anti-BrdU, 50 µg RNAse) and incubated at RT for 45 min. Samples were

pelleted, resuspended in 0.5 ml of PBS containing 10 µg/ml propidium iodide and were analyzed using a FACScanto cytometer as described above.

29. DNA synthesis measurement: EdU Assay

We used the Click-iT® EdU Microplate Assay kit to measure DNA synthesis in cells, according to the manufacturer's protocol. Briefly, cells were incubated with EdU (5-ethynyl-2´-deoxyuridine, 10 µM) for 2 hours at 37 ºC and 5 % CO_2. After treatment with EdU, cells were fixed and incubated with Oregon Green 488 azide for 25 min at RT, protected from light. Then, cells were washed twice with blocking buffer, incubated for 30 min with the anti-Oregon Green antibody (conjugated to the HRP enzyme), washed twice with Amplex UltraRed buffer and incubated with Amplex UltraRed substrate. After 15 min, the reaction was stopped, and fluorescence of the obtained product was measured in a plate reader (excitation / emission 568/585 nm).

30. Comet Assays

The Alkaline and Neutral Comet Assay was performed according to the manufacturer's protocol (Trevigen, Gaithersburg, MD, USA). Briefly, cells were added in low melting point agarose (at 37 ºC) at a ratio of 1:10 (v/v) and then were pipetted onto microscope slides. After adhesion at 4 ºC for 30 minutes (in the dark), slides were immersed in lysis buffer (precooled at 4 ºC) overnight at 4 ºC. After lysis, slides were immersed in electrophoresis solution pH>13 (200 mM NaOH, 1 mM EDTA) at RT for 20 min (in the dark) for alkaline comet assay, or in neutral electrophoresis solution pH=9 (1.5 M $NaCH_3COO$, 500 mM Tris Base) for 30 min at 4 ºC for neutral comet assay. Slides were placed into an electrophoresis chamber and electrophoresis was conducted in the same buffer at 25 V (adjusting the current to 300 mA) for 30-45 minutes. For neutral comet assay, slides were immersed in DNA Precipitation Solution (7.5 M NH_4Ac) for 30 min at RT and in 70 % ethanol for 30 minutes. For alkaline comet assay, slides were immersed twice in distilled water for 5 minutes each and in 70 % ethanol for 5 minutes. Then slides were dried at 37 ºC for 30 minutes to bring all the cells in a single plane. Finally, DNA was stained with SYBR™ Green I Nucleic Acid Gel Stain 10,000X and images were taken using a Nikon Eclipse TS2 microscope with 10x objective lense. Quantitative analysis of the tail moment (product of the tail length and percent tail DNA) was performed using CASPLAB software. At least 100 randomly selected cells were analyzed per sample. Values were represented as the median of the tail moment of treated cells relative to the median of the tail moment of untreated cells.

31. Chromosomal Spreads

Cells were incubated with Colcemid Solution (200 ng/µl, Gibco, Madrid, Spain), treated with a hypotonic solution (2.5 ml, 0.055 M KCl) at 37 ºC for 30 min and fixed with fresh Carnoy's Fixative (3:1 ratio of methanol/glacial acetic acid). Cell suspensions were dropped on slides and dried at 60 ºC for 12 h. Slides were stained with freshly prepared Giemsa Solution (7 % Giemsa Stain, Sigma GS-500, in KH_2PO_4 Buffer, pH 6.8) after a 0.15 % trypsin treatment. An average of 10 images per condition were taken.

32. In Vivo Experiments

Experiments with mice met the Animal Welfare guidelines and followed protocols approved by the Ethics Committee of the University of Murcia (approval code: 482/2018). For tumor growth assays, 2.5×10^5 *Mgrn1*-KO B16F10-luc melanoma cells were intradermally injected into the flanks of C57BL/6J mice. Mice were sacrificed and scanned using a computed tomography (CT) equipment (Albira, Bruker, Billerica, MA, USA). Tumor volume was calculated from the images taken with the scan. Tumors and peripheral organs (lungs and liver) were excised, fixed and paraffin-treated for immunohistochemical analysis. This analysis included estimation of the number of mitotic cells/field using hematoxylin/eosin-stained preparations and evaluation of the percentage of cells positively stained for mKi67. For short-term lung colonization assays, *Mgrn1*-KO and control B16F10-luc cells were fluorescently labeled with either cell-permeable CellTracker Green CMFDA Dye (10 µM) or Orange CMTMR Dye (15 µM). Equal numbers of MGRN1-depleted and control cells (5×10^5 cells in 0.3 ml PBS, ratio 1:1) were co-injected in the tail vein of C57BL/6J mice. Mice were sacrificed after 30 min or 24 h. Lungs were examined for fluorescent cells under a confocal microscope (Leica TCS) equipped with a PL APO 10X/0.40 AN objective lense and Leica Software. An average of 15 images per mouse were taken. Data were presented as cell area/field/mouse. Cell area per field was calculated as the average of cell area covered by fluorescence per image using ImageJ.

33. Histological Analysis

Samples were fixed in 4 % neutral buffered formalin (Panreac Quimica), then paraffin embedded sections were stained with standard hematoxylin/eosin staining. To determine the proliferative index of tumors, an indirect ABC immunohistochemical procedure was employed, and samples were stained for Ki67 (mKi67 antibody, Ab16667 at 1:100). Mitotic index was estimated by the median (±standard deviation) of the number of mitoses in 10 high power fields (HPF, X400), according with recommendations of the American Joint Committee on Cancer staging system. The proliferative index was

estimated by the count of positive cells in 10 HPF (100 tumoral cells per field) and expressed by the percentage of the median (± SD). Examinations were performed using a direct light microscope (Zeiss Axio Scope A10, Karl Zeiss, Madrid, Spain) with a digital camera (Axio icC 3, Karl Zeiss) and using a digital image analysis software (Axio Vision SE64, Ver. 4.9.1).

34. Public database analysis

We used the GDC TCGA Melanoma (SKCM) cohort from the UCSC Xena database (https://xena.ucsc.edu/) for analysis of the correlation of high and low *MGRN1, RAB7 or TYRP1* mRNA expression levels with patient survival. This dataset comprises gene expression and clinical data for >450 melanoma patients. High and low expression tumors were defined as the upper and lower 33 % gene-expressing tumors. Kaplan-Meier survival curves were obtained with GraphPad Prism and were compared using a log-rank test. In addition, using this database we analyzed the outcome of the disease for patients with melanomas of low or high *MGRN1* expression carrying mutations in *BRAF*, *NRAS*, *NF1* and *TP53* genes.

We obtained the expression of the *MGRN1* gene in different types of tumors and normal tissues from human patients (TCGA and GTEx cohorts) using the data compiled in the GEPIA database (http://gepia.cancer-pku.cn/). Furthermore, transcript levels of *MGRN1* in melanoma, normal skin and *nevus* samples were collected from 6 independent datasets available at Gene Expression Omnibus (GEO) database (https://www.ncbi.nlm.nih.gov/geo/).

To compare the mutational status of the *MGRN1* gene among different human cancer types, to analyze mutations in *MGRN1*, *BRAF*, *NRAS*, *NF1* and *TP53* in melanoma patients, and to determine whether mutations in *MGRN1* and the selected genes show mutual exclusivity or co-occurrence in melanomas, we used the TCGA dataset from the cBioPortal database (https://www.cbioportal.org/). Mutation data for 363 patients were available in TCGA (PanCancer Atlas) SKCM cohort.

35. Patient samples

Forty-nine *nevi* and 33 melanoma patient samples and their histopathological information and clinical data were provided by Dr. Santos Alonso Alegre and Dr. María Dolores Boyano López from the University of the Basque Country (UPV).

For cohort UPV, the total number of melanoma patients included in the study is 33 (13 male, 18 female and 2 without clinical data available), with a mean age of 63 years (95 % CI: 58.0–69.0). Most melanomas were diagnosed in patients' lower extremities

(around 32 %) and trunks (around 29 %), followed by the upper extremities (around 14 %), head and neck (around 14 %), and acral areas (around 11 %). Staging was based on the AJCC (American Joint Committee on Cancer) system, and most patients were diagnosed as stage II (around 71 %), followed by stage I (around 13 %) and 0 (around 10 %), while only 6 % of the patients were considered to be at a stage related to metastasis, stage III or IV. However, 13 (39 %) of the 33 patients recruited developed metastasis. For those patients that developed metastasis, the mean interval from the removal of the primary tumor until the diagnosis of a metastasis was 0.9 years with a median interval of 0.6 years. By contrast, 16 patients remained disease-free (without recurrence or metastasis); mean follow-up of these patients was 4.3 years with a median of 3.7 years. The totality of patients that developed metastasis (100 %) showed a Breslow thickness > 1 mm, compared with the 56 % of patients that did not develop metastasis. Ulceration was more frequently detected on those patients that develop metastasis (82 % vs 19 %: $p < 0.0001$). According to the type of lesion, 46 % of melanoma samples were considered as nodular melanoma, followed by a 35 % of superficial spreading melanomas and a 12 % of acral-lentiginous melanomas. We also included in the study a group of 49 *nevi*, to compare MGRN1 expression in *nevi* vs melanoma samples. High and low *MGRN1* expression samples were defined as the upper and lower 50 % *MGRN1*-expressing samples, respectively.

For cohort LOCE, 52 melanoma metastases patient samples from lymph nodes and their histopathological information and clinical data (Breslow thickness, histological type, overall survival and progression free survival) were provided by Prof. Ghanem from the Laboratory of Oncology and Experimental Surgery (LOCE) of the Free University of Brussels. Melanoma samples were divided into two groups according to their *MGRN1* expression levels (low and high expression). Low expression melanomas were defined as the lower 50 % *MGRN1*-expressing samples and high *MGRN1* expression samples as the upper 50 %. According to the histological type of lesion, 49 % of melanoma samples were considered nodular melanoma, followed by 43 % of superficial spreading melanomas and 8 % of acral-lentiginous melanomas. Fifteen samples had no histological type data available. The mean interval of overall survival (OS, time in years of survival) was 9.1 years with a median interval of 4.2 years. Five samples had no OS data available. The mean interval of progression free survival (PFS, time in years of survival without progression of the disease) was 3 years with a median interval of 0.8 years. Seven samples had no PFS data available.

36. Statistical Analysis

All analyses were carried out using GraphPad Prism (GraphPad Software, San Diego, CA, USA, www.graphpad.com). For parametric data, comparison of two samples was performed with unpaired two-tailed Student's t-tests, and data are given as mean ± standard error of the mean (SEM) unless indicated otherwise. For comparison of three or more groups, one-way ANOVA with Tukey post-test (for multiple comparisons) was performed, and data are given as mean ± SEM, and to determine how a response is affected by two factors, two-way ANOVA was performed. Non-parametric data were analyzed with the Mann-Whitney test for comparison of 2 samples or the Kruskal-Wallis test with Dunn's post-test (for multiple comparisons) for comparison of three or more groups, and the median is indicated. Contingency graphs were analyzed with the Chi-square or Fisher's test and Kaplan-Meier curves were compared using a log-rank (Mantel-Cox) test. p values of less than 0.05 were considered statistically significant. * indicates $p < 0.05$, **, $p < 0.01$, ***, $p < 0.001$ and ****, $p < 0.0001$.

RESULTS

CHAPTER I

FUNCTIONAL CHARACTERIZATION OF MC1R-203

Given the role of the MC1R C-terminal extension in forward trafficking, coupling to intracellular effectors and desensitization, it can be speculated that the different structure of this domain in MC1R and MC1R-203 may lead to significant functional alteration(s). To test this possibility and to ascertain the potential relevance of the MC1R-203 transcript, we have assessed its relative expression in human melanoma cells and its functional coupling properties, as compared with the canonical form.

Expression of MC1R-203

We compared the expression of the canonical MC1R form and the MC1R-203 spliceoform in HBL human melanoma cells, a cell line of wildtype *MC1R*, *NRAS* and *BRAF* genotype (84), thus suitable to avoid potential interferences caused by the presence of MC1R variant residues or high basal ERK1/2 signaling. The relative expression of MC1R and MC1R-203 in HBL cells was assessed by PCR. A common forward primer encompassing the initiation codon located in exon 3 and a reverse primer matching the 3'UTRs were employed. Amplicons were identified by their different size (see Figure 1A for details). PCR amplification of cDNA from HBL cells followed by electrophoresis showed that the MC1R-203 spliceoform was expressed in basal conditions although at much lower levels than the canonical form, since MC1R transcripts appeared roughly ten-fold more abundant than MC1R-203 transcripts (Figure 1A). However, a more rigorous quantitative comparison of the levels of expression of both spliceoforms will require further analysis by quantitative PCR.

For functional expression, MC1R and MC1R-203 were cloned in pcDNA3 so as to encode for a protein with a Flag epitope at the N-terminus, immediately after the initial Met residue (175). The constructs only differ in the presence or absence of the sequence coding for the 66-amino acid extension in MC1R-203 and were verified by automated sequencing. We expressed both constructs in HEK293T cells and analyzed the electrophoretic pattern of the receptor isoforms by Western blot (Figure 1B). Consistent with its longer cytosolic extension, MC1R-203 showed a lower electrophoretic mobility, corresponding to an apparent molecular mass of *de novo* forms of ~33 kDa compared with ~25 kDa for the canonical protein. MC1R-203 protein was most likely glycosylated as MC1R, as shown by the presence of lower electrophoretic mobility bands. Moreover, MC1R and MC1R-203 were found at comparable levels upon forced expression in HEK293T cells. Considering that their rate of synthesis must be very similar by virtue of the identical structure of the constructs, the finding that MC1R-203 protein accumulated in transfected cells at equal or higher amounts than MC1R indicates a similar intracellular

stability of the protein. Interestingly, fusion of the MC1R C-terminus with tubulin β3-derived sequence in two intergenic splice variants reported by others (107, 109) decreased the intracellular levels and stability of the chimeric proteins compared with canonical MC1R (102). Accordingly, destabilization of MC1R by addition of a C-terminal cytosolic extension is not general but seemed specific to the sequence of the extension.

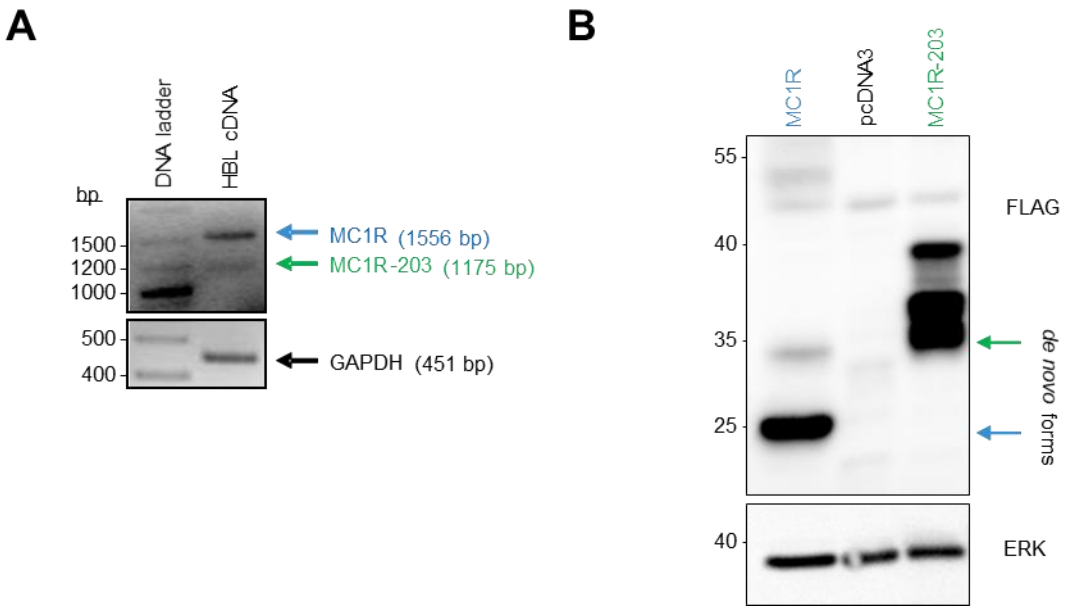

Figure 1. Expression of MC1R alternative splicing products. A) Relative expression of MC1R and MC1R-203 mRNA in HBL human melanoma cells. Total RNA from HBL cells was reverse-transcribed and amplified by PCR. Isoform-specific amplicons were identified by their size (1556 bp for MC1R and 1175 bp for MC1R-203, as analyzed by agarose gel electrophoresis). The GAPDH gene was employed as control. **B)** Electrophoretic pattern of MC1R splice isoforms. HEK293T cells were transfected to express Flag epitope-tagged MC1R isoforms and detergent-solubilized. Aliquots with comparable total protein contents were analyzed by Western blot probed with an anti-Flag antibody. ERK2 was used as loading control. The position of *de novo* bands is shown.

Functional coupling of MC1R-203

We next compared the functional coupling of the canonical and MC1R-203 spliceoforms to the cAMP cascade and the ERKs. HEK293T cells transfected to express MC1R or MC1R-203 were stimulated with the superpotent agonist NDP-MSH at a saturating concentration (10^{-7} M), for 30 or 180 min (Figure 2A). Maximal stimulation of cAMP synthesis at 30 min was approximately 4-fold more potent for canonical MC1R compared with MC1R-203. Three hours after stimulation, the cAMP levels declined comparably for both isoforms, indicative of receptor desensitization (175). Accordingly, the MC1R-203 splice variant was able to stimulate cAMP signaling, although with a residual potency around 25 %, and it appeared able to undergo homologous desensitization. Concerning

activation of the ERKs (Figure 2B), MC1R-203 was at least as efficient as canonical MC1R in triggering ERK signaling. Therefore, MC1R-203 did not behave as a simple hypomorphic isoform. Rather, it displayed biased signaling with impaired coupling to the cAMP cascade but full capacity to activate the ERKs. This behavior is reminiscent of common and penetrant RHC alleles such as R151C, R160W or D294H (117, 119).

Homologous desensitization of MC1R-dependent cAMP signaling involves phosphorylation of the C-terminal Thr308 and/or Ser316 residues and binding of ARRB2, which triggers internalization of the receptor-hormone complex (106, 123). We showed previously that the interaction of MC1R and ARRB2 also results in ARRB2 ubiquitylation, a process likely catalyzed by the E3 ubiquitin ligase MGRN1, since it is enhanced by MGRN1 overexpression and impaired by siRNA-mediated silencing (164). MGRN1 is a clinically relevant protein since the null *mahoganoid* mutation in mice results in a complex phenotype with coat color darkening, high embryonic mortality, congenital heart defects and spongiform neurodegeneration (129, 133, 141, 176, 177). Figure 2C shows that, as expected, co-expression of ARRB2 and MC1R resulted in appearance of high molecular weight ARRB2 bands corresponding to polyubiquitylated products whose levels augmented upon co-transfection of MGRN1. Surprisingly, ubiquitylation of ARRB2 was not detected at significant levels when the arrrestin was co-expressed with MC1R-203, either alone or in combination with MGRN1. Our previous work with canonical MC1R showed that this isoform interacts with MGRN1 and ARRB2 (164), and that MGRN1 can be co-immunoprecipitated with ARRB2 in the presence, but not in the absence, of MC1R. This indicated that MC1R acts to scaffold MGRN1 and ARRB2 to promote ARRB2 ubiquitylation (164). Thus, our results suggest that MC1R-203 is unable to scaffold a productive MGRN1-MC1R-ARRB2 ternary complex.

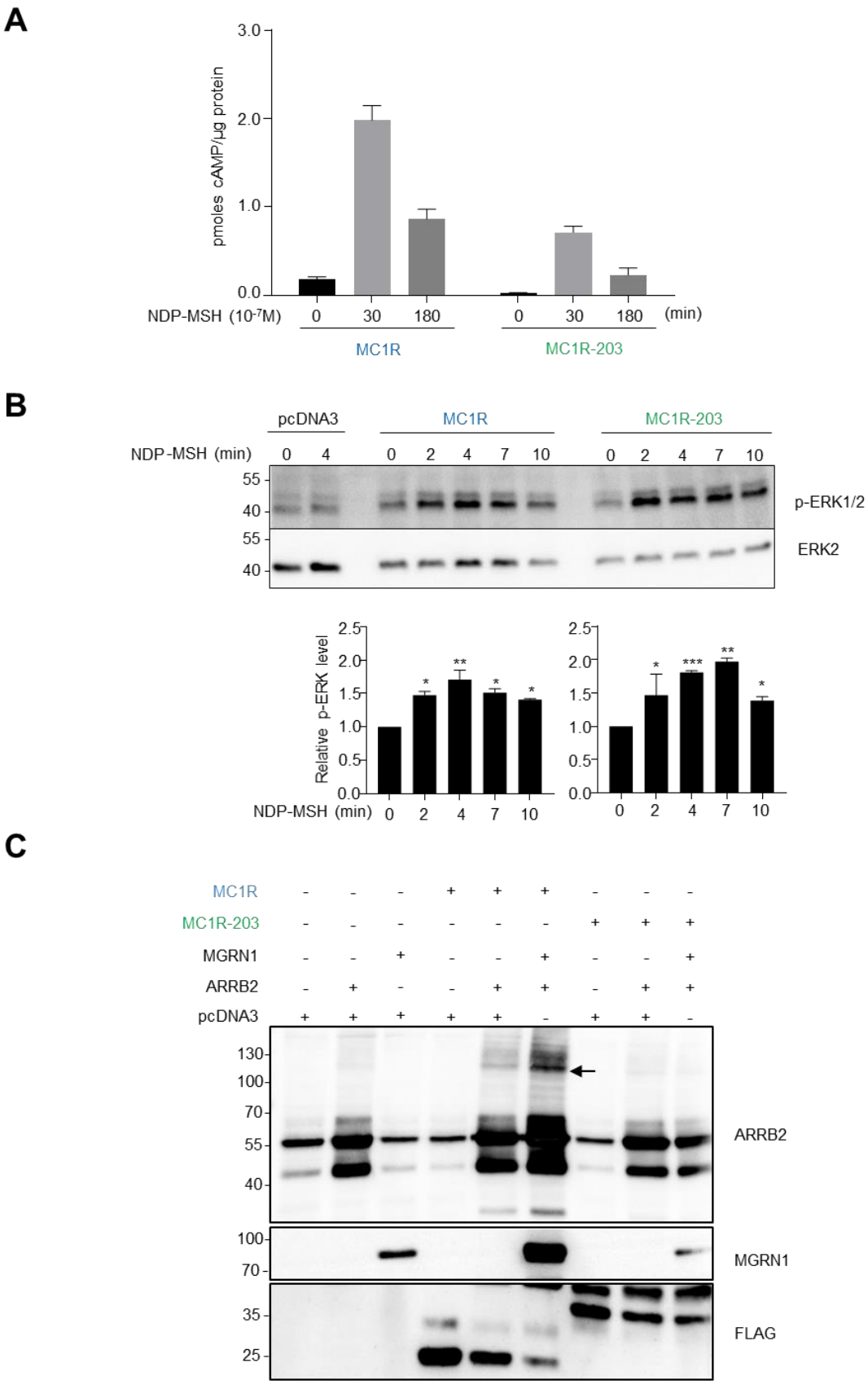

Figure 2. Functional analysis of MC1R alternative splicing variants. A) Activation of cAMP production downstream of MC1R splice variants. HEK293T cells were transfected to express MC1R or MC1R-203,

stimulated with NDP-MSH (10^{-7} mol/L, 30 or 180 min) and lysed in hot HCl. cAMP was determined with an enzyme immunoassay kit (R&D Systems) as per instructions. Results (mean ± sem, n = 2, quadruplicates in each independent experiment) are normalized for protein contents. **B)** Activation of ERK1/2. HEK293T cells were co-transfected with either MC1R or MC1R-203 in combination with cKIT as reported (9), stimulated with NDP-MSH (10^{-7} mol/L) and detergent-solubilized after times ranging from 2 to 10 min. Comparable amounts of total protein were analyzed by Western blot probed for active ERKs with a phosphospecific antibody recognizing the active phosphorylated forms of the kinases. A representative blot (top) and quantification (bottom) of 4 independent experiments with similar results is shown (graph shows mean ± SEM). **C)** MC1R-dependent ubiquitylation of ARRB2. HEK293T cells were transfected with the individual MC1R spliceoforms, ARRB2 and MGRN1, alone or in suitable combinations, as shown on top of each lane. Detergent-solubilized extracts were analyzed by Western blot probed for ARRB2 to detect ubiquitylated (high molecular weight) forms, and for MGRN1 or MC1R as controls. A representative blot out of two independent experiments is shown. The position of ubiquitylated forms is shown with an arrow. * indicates $p < 0.05$, **, $p < 0.01$, ***, $p < 0.001$ and ****, $p < 0.0001$.

In summary, we showed that unstimulated human melanoma cells express the MC1R-203 spliceoform, although at much lower levels than canonical MC1R. The presence of a 66-amino acid-long cytosolic extension immediately after Cys316 in MC1R-203 did not impair the intracellular stability of the protein, but it interfered with functional coupling to the cAMP cascade and with the ubiquitylation of ARRB2 associated with MC1R desensitization. One potential explanation for the inability of MC1R-203 to promote ARRB2 ubiquitylation would be a reduced or null interaction of this spliceoform with the E3-ubiquitin ligase MGRN1, thus suggesting that this protein may fulfill important functions in the biology of melanocytes. Conversely, MC1R-203 retained full capacity to activate ERK1/2 signaling. Accordingly, at least in a heterologous expression system, MC1R-203 behaved as a spliceoform with biased signaling, with full functional coupling to the ERKs but impaired activation of the cAMP cascade, as compared with canonical MC1R. Further work is required to clarify MC1R-203 expression levels and signaling in normal human melanocytes and other melanoma cell lines, as well as the roles of MGRN1 in these cells.

CHAPTER II

MAHOGUNIN RING FINGER 1 IS REQUIRED FOR GENOMIC STABILITY IN MOUSE MELANOCYTES AND MODULATES THE MALIGNANT PHENOTYPE OF MOUSE MELANOMA CELLS

To investigate the biological effects of Mgrn1 deficiency, we used immortalized *Mgrn1*-null melan-md1$^{md\text{-}nc/md\text{-}nc}$ (*mahoganoid* or *md*) mouse melanocytes (178) and CRISPR/Cas9 *Mgrn1*-KO clonal melan-a6 melanocytes, as well as genetically matched melan-a6 control cells. The strategy for the generation of *Mgrn1*-KO clones is described in Figure 1A. Clones were selected based on lack of *Mgrn1* expression (Figure 1B) and confirmed by *Mgrn1* gene amplification and sequencing (Figure 1C). Three independent clones were isolated for further analysis. These clones displayed early disruption of the *Mgrn1* open reading frame leading to an altered protein sequence following the first 22 amino acids and a premature truncation. Therefore, the resulting proteins lack all the relevant functional domains in wildtype *Mgrn1*, including the NLS and the RING motif.

A

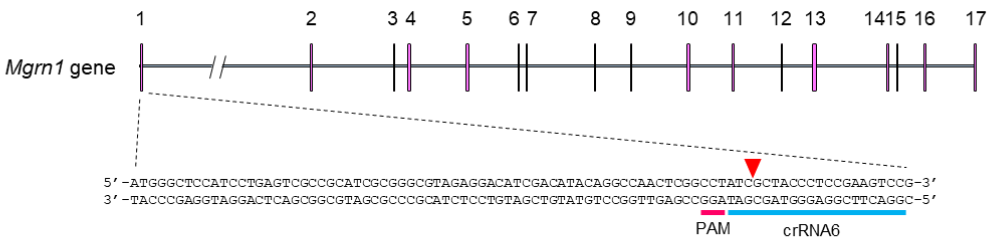

B

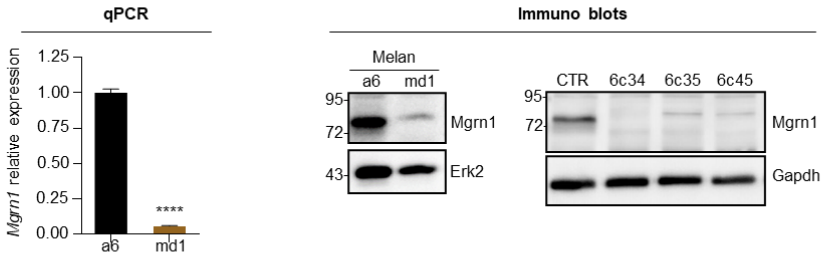

C

crRNA6 clones	Edited sequences on *Mgrn1* exon 1
CTR	Alleles 1 and 2: ^{58}AAC TCG GCC TAT **CG**C TAC CCT CCG AAG TCC GGA^{90}
6c34	Alleles 1 and 2: ^{58}AAC TCG GCC TAT **(CG)** C TAC CCT CCG AAG TCC GGA^{90}
6c35	Allele 1: ^{58}AAC TCG GCC TAT **C(GC)** TAC CCT CCG AAG TCC GGA^{90} Allele 2: ^{58}AAC TCG GCC TAT **CG**GC TAC CCT CCG AAG TCC GGA^{90}
6c45	Allele 1: ^{58}AAC TCG GCC TAT **C(G)** C TAC CCT CCG AAG TCC GGA^{90} Allele 2: ^{58}AAC (TCG GCC TAT **CGC** TAC CCT CCG A) AG TCC GGA^{90}

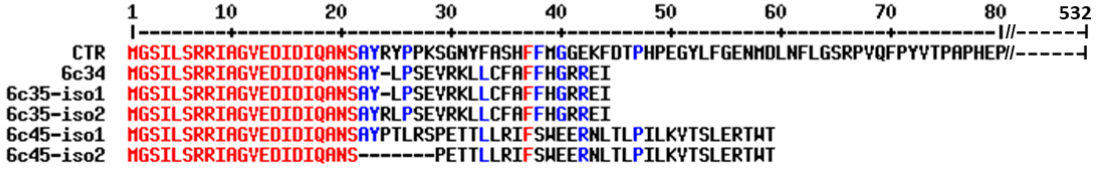

Figure 1. Generation of clones of *Mgrn1*-KO mouse melanocytes: strategy and validation. A) Schematic representation of *Mgrn1* highlighting the exon 1 sequence targeted by crRNA6. This 20 nt sequence pairs with the DNA target (blue bar on bottom strand), directly upstream of a 5'-NGG adjacent motif (PAM; in pink). **B)** Relative mRNA levels of *Mgrn1* in melan-a6 and melan-md1 cells estimated by qPCR (left) and representative immunoblots for Mgrn1 in melan-a6, melan-md1 and *Mgrn1*-KO melan-a6 cells (right). Erk2 or Gapdh were used as loading control. Graph shows mean ± SEM and t-test was used for statistical analysis (**** indicates $p < 0.0001$). **C)** Top: edited sequence (from nt 58 to 90) in exon 1 of *Mgrn1* in *Mgrn1*-KO clones 6c34, 6c35 and 6c45, compared with the consensus sequence in control (CTR) melan-a6 cells. Deleted nucleotides are shown between brackets in red and inserted nucleotides are indicated in green. Bottom: amino acid sequence of the resulting truncated Mgrn1 protein in *Mgrn1*-KO cells.

Effects of *Mgrn1* ablation on melanocyte morphology and motility

Mahoganoid-null and *Mgrn1*-KO melanocytes grown on 2D cultures in plastic plates showed a more differentiated phenotype, characterized by higher melanin content and a more dendritic appearance compared with the mouse littermate control cells melan-a6 (Figure 2A). A more dendritic and heavily pigmented phenotype of melan-md1 cells has been previously reported (179).

We confirmed the switch to a more differentiated morphology in melan-md1 melanocytes seeded in 2½D collagen systems, better mimicking the dermal extracellular matrix (Figure 2B). In these culture conditions, melan-md1 cells displayed twice as many dendrites as melan-a6 controls, and the dendrites were significantly longer. Clonal *Mgrn1*-KO cells also showed significantly higher dendricity than controls, but the differences were less marked (Figure 2C). On the other hand, melan-md1 cells were significantly bigger than melan-a6 controls (Figure 2D). There was also a trend towards increased cell size for *Mgrn1*-KO clones.

The microphthalmia-associated transcription factor (Mitf) is a central regulator of melanocyte biology (178). High levels of Mitf are associated with a highly differentiated and pigmented phenotype and a low proliferation rate. Since Mitf undergoes ubiquitylation leading to proteolysis, we tested the possibility that lack of Mgrn1 E3 ligase activity might stabilize Mitf, thus accounting for the differentiated phenotype of *Mgrn1*-KO cells. However, the levels of Mitf were similar in *Mgrn1*-null cells compared to their controls (Figure 2E), thus ruling out Mitf stabilization as responsible for the *mahoganoid* phenotype of melanocytes.

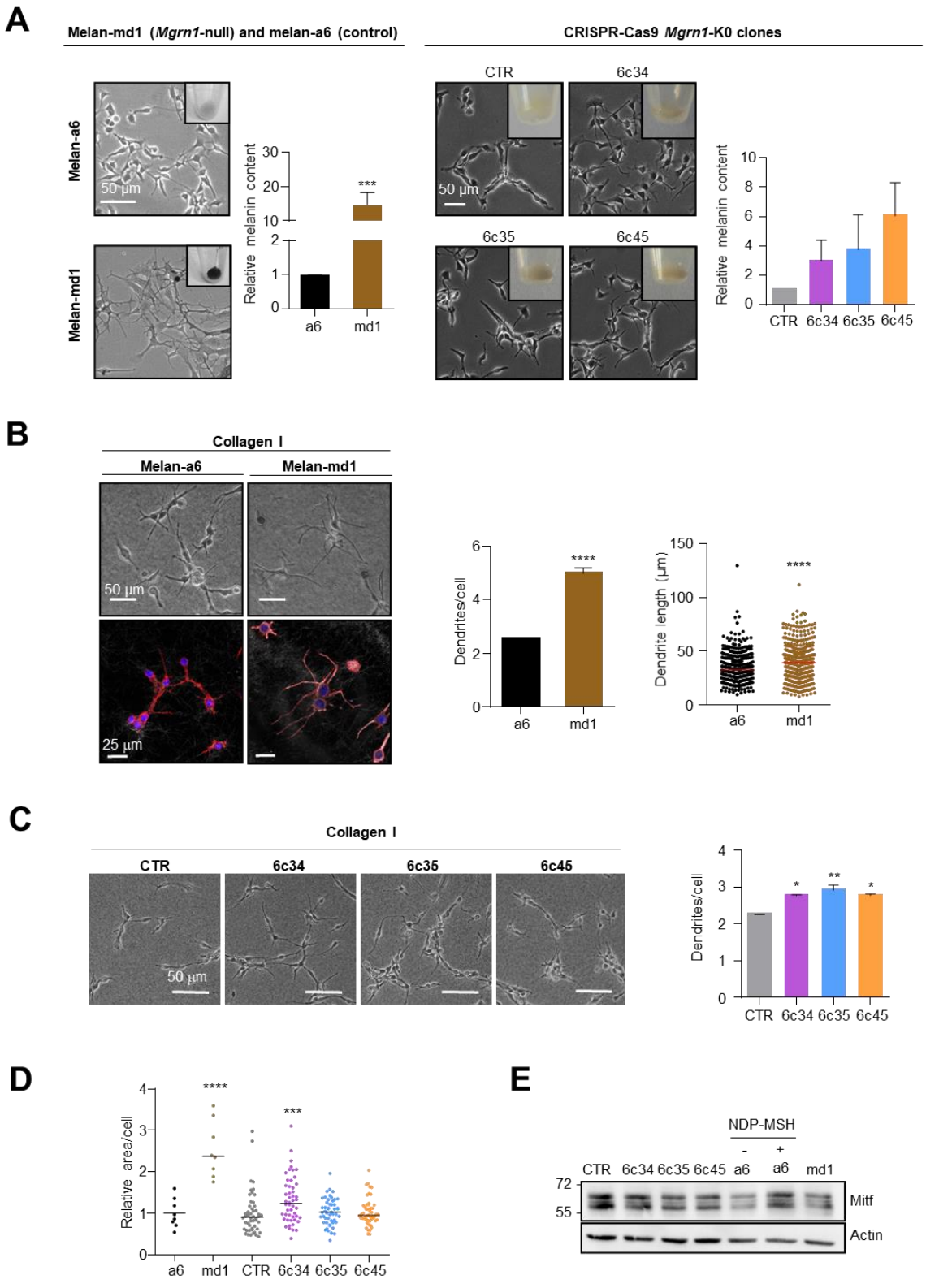

Figure 2. Induction of a more differentiated phenotype in mouse melanocytes lacking *Mgrn1* expression. A) Morphology of melan-a6 and melan-md1 cells (left) and CRISPR/Cas9 *Mgrn1*-KO clones 6c34, 6c35 and 6c45 (right) in 2D cultures. The inserts in the phase-contrast images show representative images of cell pellets. Histograms correspond to quantification of melanin content normalized for melan-a6 controls in the case of melan-md1 cells (*n* = 6), and for cells transfected with a non-targeting crRNA and

selected with puromycin (CTR) for CRISPR/Cas9 clones (*n* = 3). **B)** Increased dendricity of melan-md1 cells seeded on collagen I. Phase-contrast (upper) and confocal images (lower) stained for F-actin (red) and for nuclei (Hoechst staining, blue) are shown for melan-a6 and -md1 cells. Histograms show the quantification of the number of dendrites per cell (*n* = 100 randomly selected cells) and the length of dendrites (*n* = 300) in melan-a6 and melan-md1 cells on collagen I (right). **C)** Phase-contrast images of *Mgrn1*-KO clones on collagen I (left) and quantification of the number of dendrites per cell (right). **D)** Relative area per cell in melan-a6 (control), melan-md1 and *Mgrn1*-KO clonal cells. Data are normalized for the control melan-a6 cells. **E)** Lack of Mitf overexpression in *Mgrn1*-null melanocytes. A representative immunoblot for Mitf in melan-a6 and *Mgrn1*-null cells is shown. As a positive control, melan-a6 cells were treated with NDP-MSH (10^{-7} M for 24 h) to ascertain induction of Mitf. * indicates $p < 0.05$, **, $p < 0.01$, ***, $p < 0.001$ and ****, $p < 0.0001$.

In the light of the extensive crosstalk between cell shape and motility (180), we analyzed the adhesion and migration behavior of *Mgrn1*-null cells. *Mgrn1* ablation resulted in higher attachment to collagen I or collagen I + thin Matrigel (Figure 3A), where the adhesion of melan-md1 melanocytes was 2-fold higher relative to controls. Similar results were obtained for *Mgrn1*-KO clones (Figure 3B). Moreover, 2D cell motility measured by wound healing assays (Figure 3C) and random movements over 24 h (Figure 3D) was significantly reduced in cells lacking Mgrn1. Both melan-md1 and *Mgrn1*-KO cells also showed decreased 3D invasion into a collagen I matrix with serum-enriched medium as chemoattractant (Figure 3E).

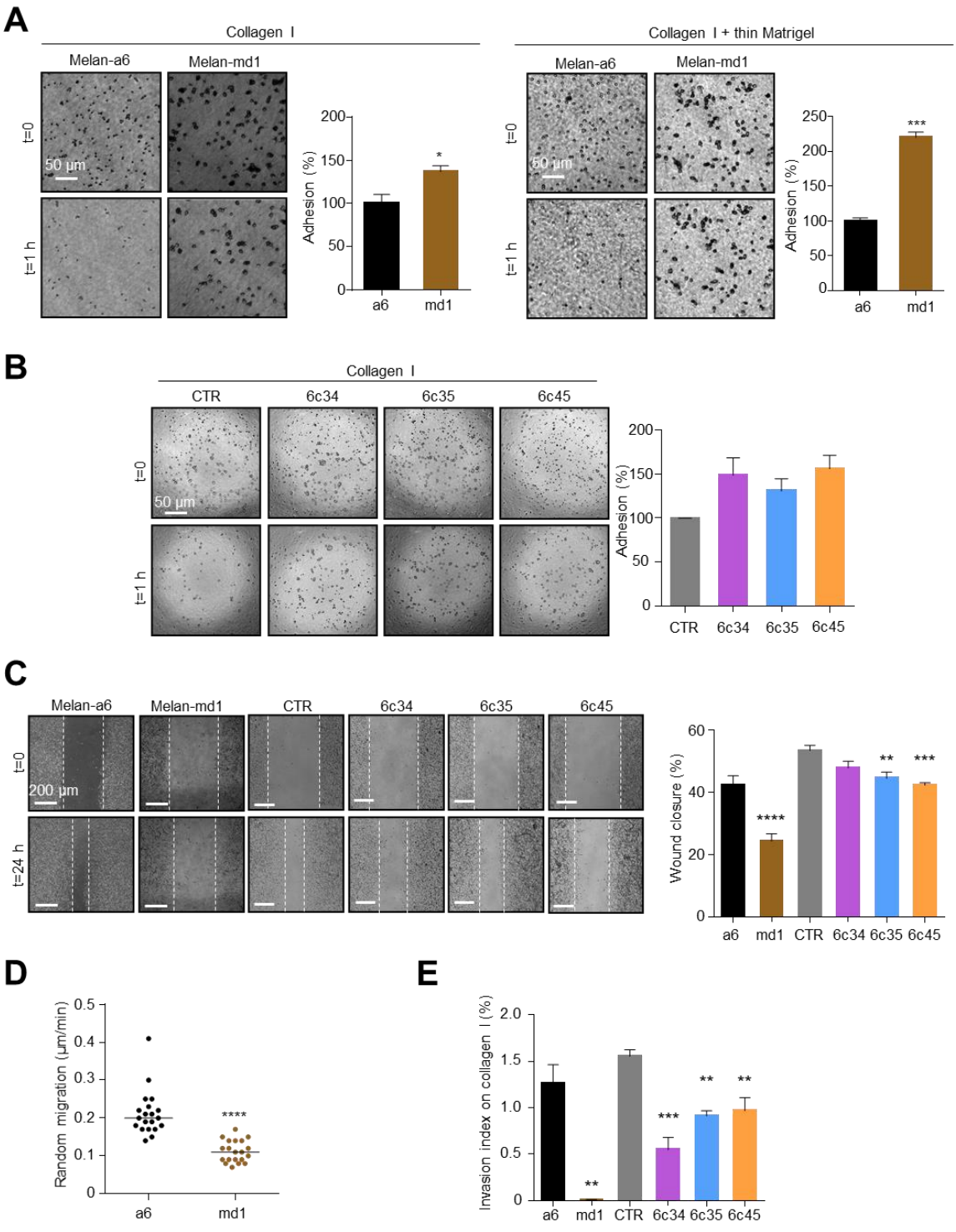

Figure 3. Changes in cell adhesion and motility in *Mgrn1*-null melanocytes. A) Phase-contrast images of melan-a6 and melan-md1 cells adhering to collagen I (left) and to a thin layer of matrigel on top of a thick layer of collagen I (right) after 1 h, and quantification of percentage of adhesion relative to control cells. **B)** Higher adhesion of *Mgrn1*-KO melan-a6-derived clones adhering to collagen I, quantified as in panel A. **C)** Wound healing assay of melan-a6 and melan-md1 cells (left) and *Mgrn1*-KO clones (right). The phase contrast images of monolayers of the indicated cells show the extent of closure 24 h after a scratch. The quantification of the percentage of wound closure is shown in the bar graph. **D)** Random migration of melan-

a6 and melan-md1 cells on collagen I. **E)** Altered invasion through collagen I after 24 h of *Mgrn1*-null melan-md1 and *Mgrn1*-KO clones relative to melan-a6 control cells. * indicates $p < 0.05$, **, $p < 0.01$, ***, $p < 0.001$ and ****, $p < 0.0001$.

Finally, we inhibited *Mgrn1* expression in melan-a6 cells using two specific siRNAs, separately or in combination (Figure 4A, B). Depletion of Mgrn1 increased dendricity (Figure 4C, D) and size (Figure 4E). Silencing *Mgrn1* gene expression in melan-a6 cells by specific siRNAs had similar effects on 2D and 3D motility (Figure 4F and 4G). Therefore, *Mgrn1* knockdown led to a differentiated phenotype with increased dendricity, pigmentation and size but lower motility. This phenotypic switch occurred without a significant change in Mitf expression.

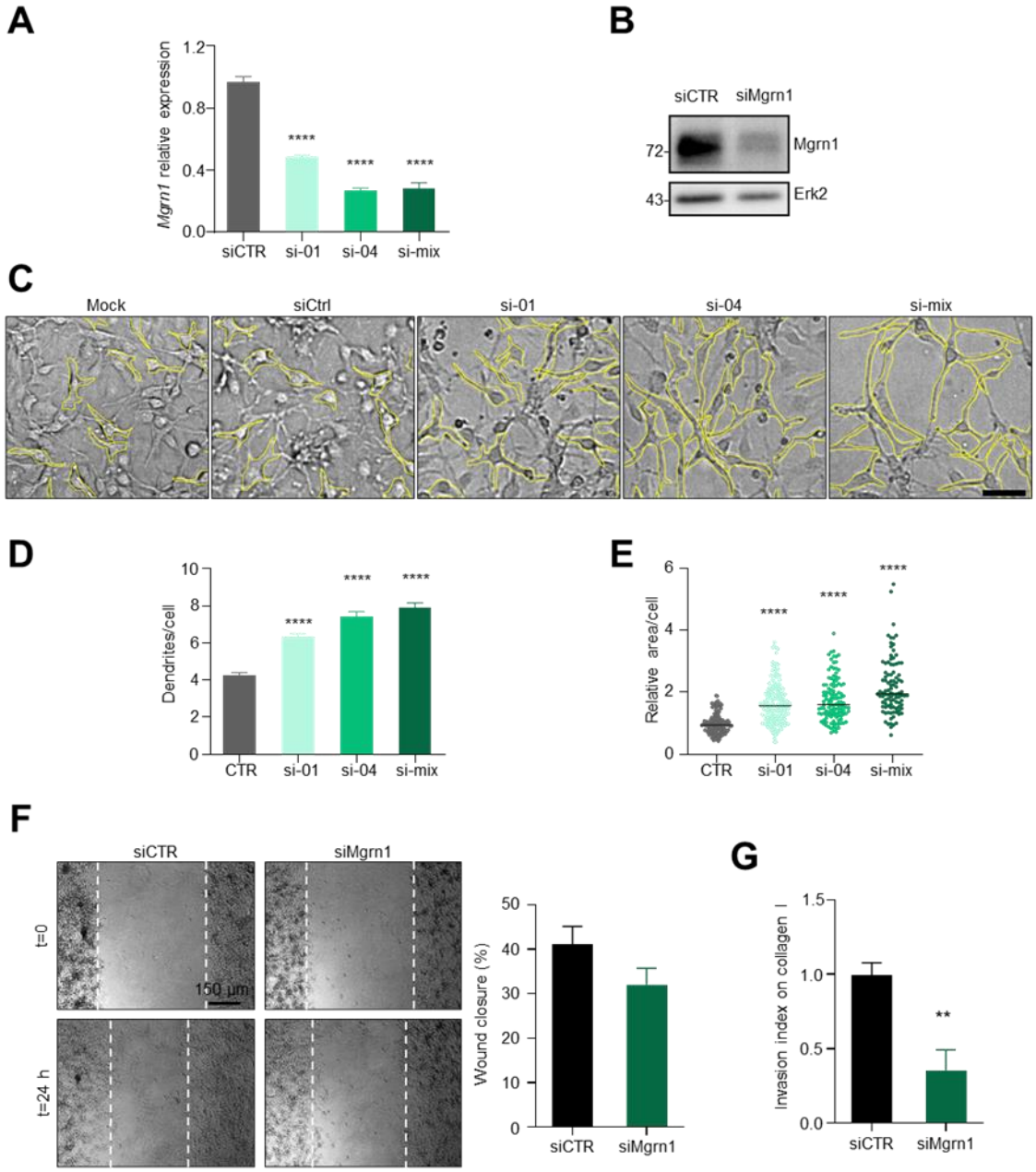

Figure 4. Changes in shape and motility of melan-a6 mouse melanocytes upon downregulation of *Mgrn1* expression with siRNA. A) *Mgrn1* mRNA levels in melan-a6 cells following depletion with siRNA with two different individual siRNAs (si-01 or si-04), or with a stoichiometric mixture of these oligonucleotides (si-mix). siCTR refers to cells treated with a control siRNA. The sequence of all oligonucleotides is specified in M&M Table 6. **B)** Representative immunoblots for Mgrn1 in melan-a6 cells after *Mgrn1* knockdown with si-mix. **C)** Phase contrast 2D images of Mgrn1-depleted melan-a6 cells. Cells were treated with the indicated siRNA. Their morphology was analyzed after manually drawing around the cell shape using imageJ (yellow). **D)** Quantification of the number of dendrites per cell in melan-a6 cells after *Mgrn1* knockdown. **E)** Quantification of the relative area per cell in Mgrn1-depleted melan-a6 cells. **F)** Phase-contrast images of confluent control (siCTR) and Mgrn1-depleted (si-mix *Mgrn1*) melan-a6 cells migrating to the center of a scratch after 24 h and quantification of the percentage of wound closure. **G)** Invasion index at 50 µm after 24 h for melan-a6 cells treated with control (siCTR) or Mgrn1-directed (siMgrn1) siRNA.

Effect of *Mgrn*1 knockdown on cell cycle progression

Data on the effect of Mgrn1 on cellular proliferation and cell cycle progression are still scarce and inconclusive. Previous work showed similar growth rates for melan-md1 and melan-a6 cells, suggesting that lack of Mgrn1 has little impact on cell proliferation, at least on the *Cdkn2a*-deficient background of these cell lines (179). On the other hand, a genome-wide functional screening for human cell cycle regulators performed by targeting with siRNA > 95 % of the protein-coding genes found increased number of cells in S phase in *MGRN1*-silenced U2OS cells (181), which was not investigated further. To extend these findings, we analyzed the growth and cell cycle progression of control and CRISPR-generated *Mgrn1*-KO melanocytes. Proliferation rates of control and *Mgrn1*-KO melanocytes in 2D cultures were compared by means of three different techniques, namely the trypan blue method (Figure 5A left), measurement of the fluorescence decay of an amine-reactive dye (Figure 5A, middle) and the MTT assay (Figure 5A, right). We did not find consistent and statistically significant differences between control and *Mgrn1*-KO cells. Moreover, the expression of the proliferation marker *Mki67* was similar in control compared with *Mgrn1*-KO clones (Figure 5B). Consistent with these results, siRNA-mediated depletion of Mgrn1 did not cause a significant change in the proliferation rate of melan-a6 cells grown on plastic dishes (Figure 5C). In 3D cultures, the growth of spheroids derived from *Mgrn1*-KO clones or control cells was also comparable (Figure 5D).

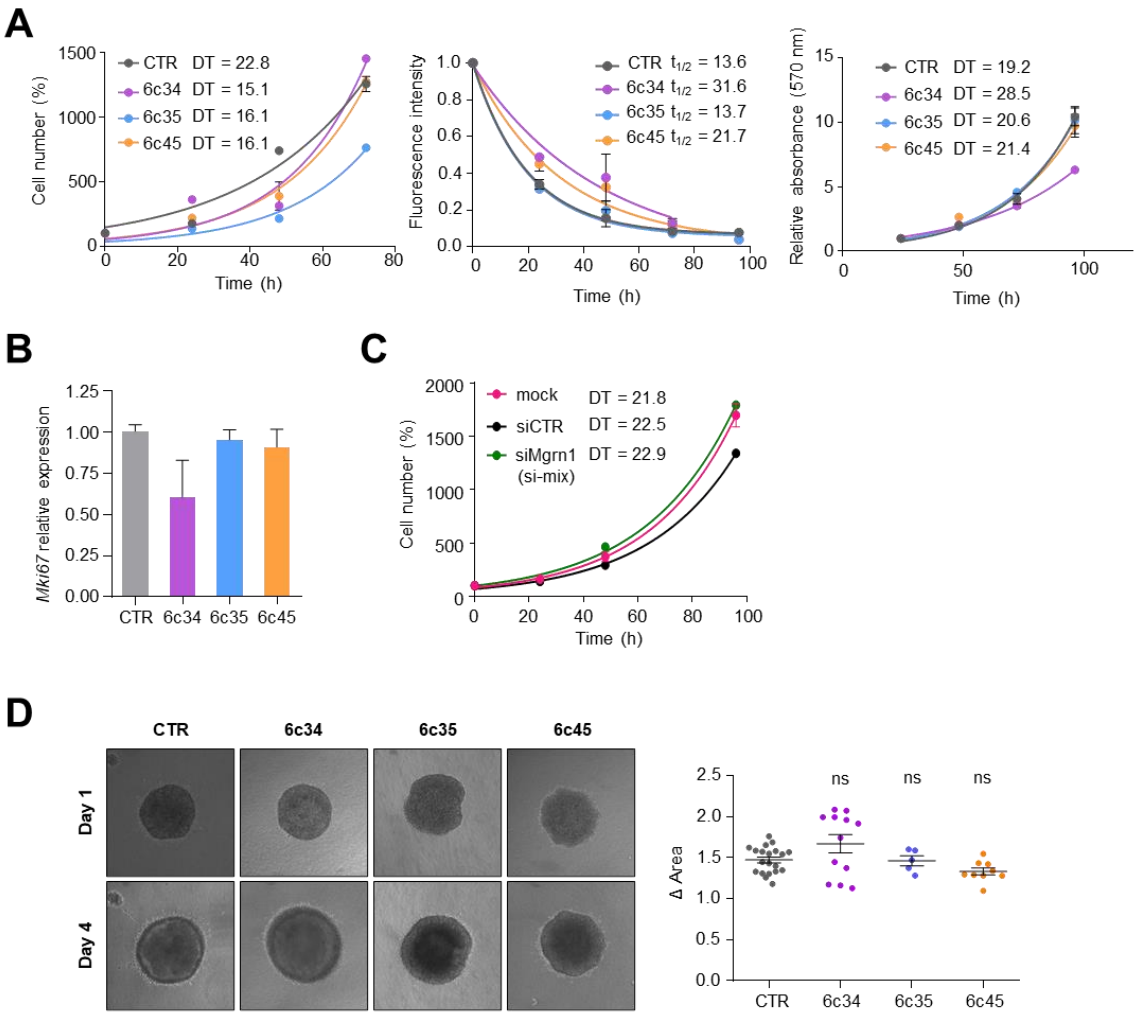

Figure 5. Proliferation rates and cell cycle progression of Mgrn1-depleted cells. **A)** Left: Growth curves for *Mgrn1*-KO clones in 2D cultures as determined by cell counting (represented as percentage of cell number relative to control at day 1 for a period of 4 days. Middle: Kinetics of decay of CFSE fluorescence intensity of melan-a6 and melan-md1 cells after signaling cells with an amine-reactive dye. Right: MTT assay represented as relative absorbance at 570 nm over 4 days. The corresponding doubling times (DT) or half-lives (t1/2) were calculated by non-linear regression and are shown in each graph as mean ± sem ($n \geq 3$). **B)** Relative expression of *Mki67* in control and *Mgrn1*-KO estimated by qPCR ($n = 4$). **C)** Growth curves for melan-a6 cells treated with a scrambled control siRNA (siCTR) or with *Mgrn1*-directed siRNA (siMgrn1, si-mix) obtained by cell counting over a period of 4 days. Untreated cells (mock) are also shown for comparison. Upon non-linear regression, doubling times of roughly 23 h were calculated, with no significant differences for cells treated with control or *Mgrn1*-directed siRNA. **D)** Representative images of the growth of spheroids from control (CTR) and *Mgrn1*-KO clones 6c34, 6c35 and 6c45 in a collagen I matrix between days 1 and 4 (left).The quantification of the increase in area of the spheroids did not yield statistically significant variations (right).

Next, we analyzed the mitotic cell cycle of *Mgrn1*-null cells. In asynchronous cultures, cell cycle profiles suggested a massive retention of melan-md1 cells in S phase (Figure 6A). *Mgrn1*-KO clonal cells also showed a significant, but much less dramatic, trend towards increased percentage of cells in S phase (Figure 6A). In summary, ablation of *Mgrn1* expression interfered with progression through the cell cycle, as it was associated with an increased fraction of cells in S phase, but its effect on the rate of proliferation was not significant. This phenotype was consistent with previous reports by others (179, 181) and was mild in *Mgrn1*-KO cells but much more severe in melan-md1 cells. This suggested that the aberrant cell cycle profile of melan-md1 cells could be due not only to loss of Mgrn1 but also to a genetic drift in culture. Accordingly, further studies on the alteration of cell cycle progression were performed exclusively using *Mgrn1*-KO clones.

To further explore the role of Mgrn1 on cell cycle progression, we assessed the expression levels of Mgrn1 along the different phases of the cycle. Cells were synchronized in G0-G1 by serum deprivation, in early S phase with hydroxyurea (HU) or thymidine and in G2/M with colcemid. For HU, two conditions were employed, a 12 h treatment, and the same treatment followed by wash-off and further incubation in HU-free medium for 1 h. Since long treatments with HU cause irreversible replication fork stalling and fork collapse (182) these two conditions should yield similar results. Compared with asynchronous cells, Mgrn1 levels were slightly lower in cultures enriched in G1 cells and augmented significantly upon transition from G1 to S phase (thymidine- or HU-treated cells). Cells arrested in G2/M with colcemid showed the same Mgrn1 levels as control cells (Figure 6B). HU inhibits ribonucleotide reductase, leading to exhaustion of the deoxyribonucleotide pool and stalling of replication forks. Although long HU treatments cause irreversible fork collapse, shorter treatments are normally reversible, as DNA synthesis can resume and stalled forks restart when the drug is removed from the culture medium (182), resulting in increased fractions of cells in S phase during recovery. We followed the kinetics of cell cycle changes and Mgrn1 accumulation in melan-a6 cells treated with HU for 4 h, followed by wash-off and recovery in HU-free medium. Upon HU release, the percentage of cells in S phase increased during the first 4 h after wash-off. Mgrn1 levels also rose over the first 3–4 h, then dropped towards control levels (Figure 6C). Interestingly, treatment with HU caused a clear change of the staining pattern of HA-labeled MGRN1 isoform S (+) expressed in melan-a6 cells. MGRN1 was predominantly cytosolic in control cells, but HU treatment caused a significant translocation to nuclei, thus increasing the contribution of nuclear MGRN1 to the total intensity of immunostaining (Figure 6D). Therefore, Mgrn1 expression and maybe also its nuclear compartmentalization, apparently fluctuated in a cell cycle-

dependent manner, being maximal during S phase. It should be noted that the presence of a N-terminal HA tag in the MGRN1 might interfere with myristoylation of glycine residue in position 2 of the protein. This post-translational modification, apparently targeting Mahogunin to mitochondria, has been recently described (183). Therefore, it is possible that our HA-labeled MGRN1 variant might have an altered subcellular compartmentalization. However, this variant bears the nuclear localization signals encoded by exon 12 and our previous data showed that it is able to shuttle between the cytosol and the nucleus (140). Accordingly, it appears suitable to follow the nucleocytoplasmic trafficking of Mahogunin, although our results should be interpreted with caution.

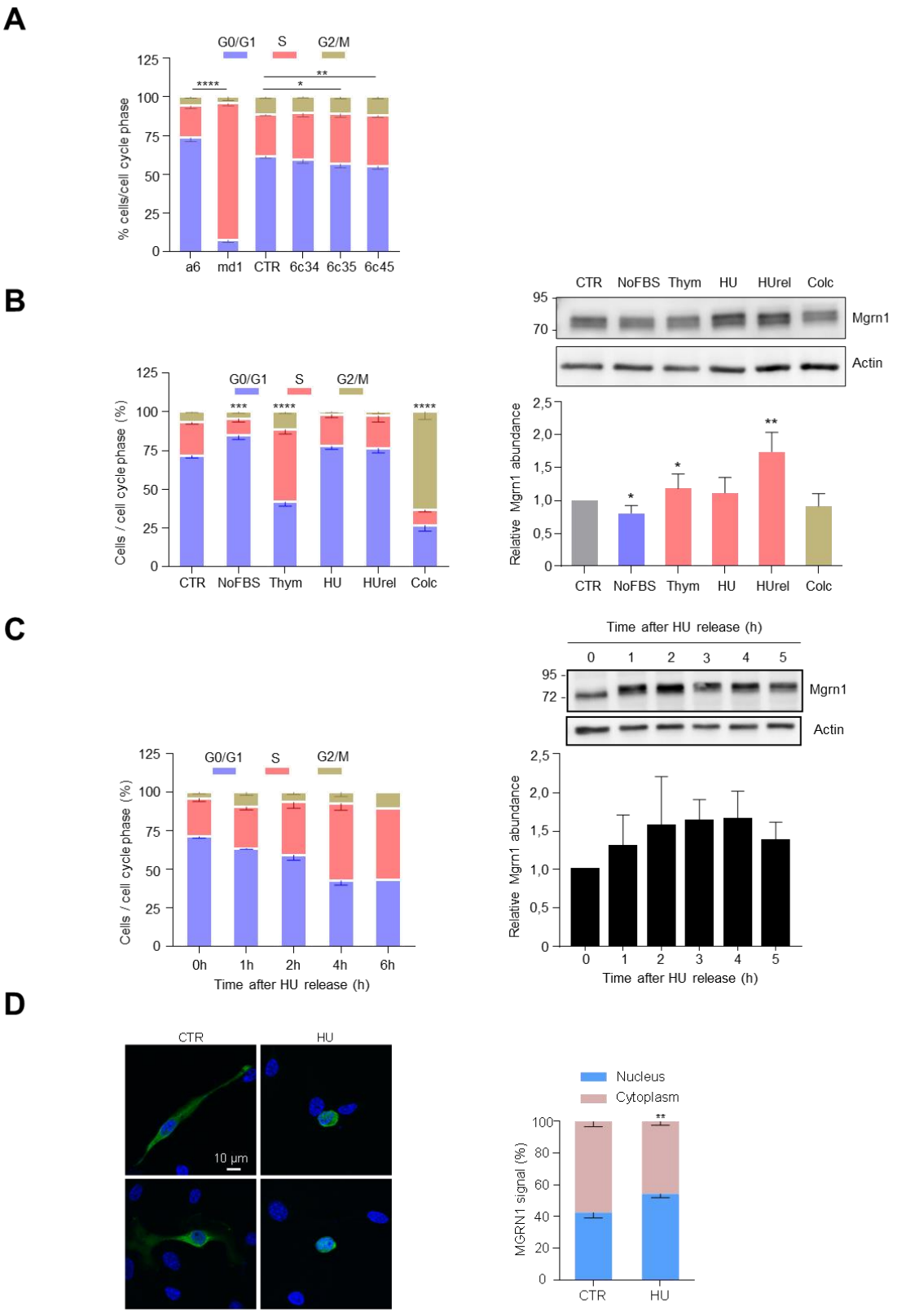

Figure 6. Cell cycle-dependent modulation of Mgrn1 expression in mouse melanocytes. A) Cell cycle analysis for propidium iodide-stained melan-a6 and *Mgrn1*-null cells (*n* = 6 for melan-a6 and –md1 cells, *n* = 12 for CRISPR/Cas9 *Mgrn1*-KO cells). The statistical analysis shown refers to the percentage of cells in

S phase. **B)** Left, cell cycle analysis of PI-stained melan-a6 cells synchronized by serum starvation (NoFBS), or treatments with thymidine (Thym), hydroxyurea (HU), HU followed by washoff and 1 h release in HU-free medium (HUrel) and colcemid (Colc). Statistical analysis as in panel A. Right, representative immunoblots for Mgrn1 in synchronized cells. The histogram below the blot corresponds to the quantification of the intensity of the Mgrn1 band, normalized to control asynchronous cell extracts (CTR). Results given as mean ± sem (*n* = 3 or higher). **C)** Left, time-dependent changes of cell cycle distribution for cells treated with HU for 4 h, followed by washoff and release in HU-free medium for the times shown. Right, representative immunoblot for Mgrn1 and quantification of the relative Mgrn1 expression at the different time points after release ($n \geq 2$). **D)** Melan-a6 cells transfected to express the HA-labeled S(+) isoform of MGRN1 were treated for 4 h with vehicle (CTR) or with HU, as indicated. Cells were stained for nuclei (with DAPI, blue signal) and for MGRN1 (with an αHA antibody, green signal), and observed in a confocal microscope. Representative images are shown on the left. The bar graph shows the percentage of the total MGRN1 signal associated to nuclei. * indicates $p < 0.05$, **, $p < 0.01$, ***, $p < 0.001$ and ****, $p < 0.0001$.

Since the results summarized in Figure 6 suggested a potential role of Mgrn1 during the S phase of the cycle, we next analyzed the kinetics of progression through S phase of synchronized cultures. We compared the percentage of control and *Mgrn1*-KO cells in S phase at different times following release from cell cycle block at the G1/S interphase with HU (Figure 7A).

As expected, the fraction of cells in S phase immediately after HU washoff was higher for the three *Mgrn*1-KO clones, at all the time points analyzed. Nevertheless, the kinetics of progression upon release of the block were similar for control and *Mgrn*1-KO cells. We probed S phase progression with higher sensitivity by pulse-chase experiments. Control and *Mgrn1*-KO cells were treated with HU as above, washed off, pulsed with 5-bromo-20-deoxyuridine (BrdU) to label newly synthesized DNA, and analyzed for total DNA (based on propidium iodide fluorescence) and newly synthesized DNA (based on BrdU staining) for up to 4 h in the presence of the microtubule depolymerizing agent colcemid to block mitosis. The fraction of BrdU-labeled cells in early or mid S phase was then estimated. The experimental protocol and the gating scheme for the FACS analysis of early and mid S phase are summarized in figure 7B. We did not include in this analysis cells in late S phase, as the experimental setup did not allow for an adequate discrimination of these cells and cells in G2 and M phases. As shown in Figure 7C, the kinetics of reentry into S phase and DNA synthesis were comparable for control cells and *Mgrn*1-KO cells.

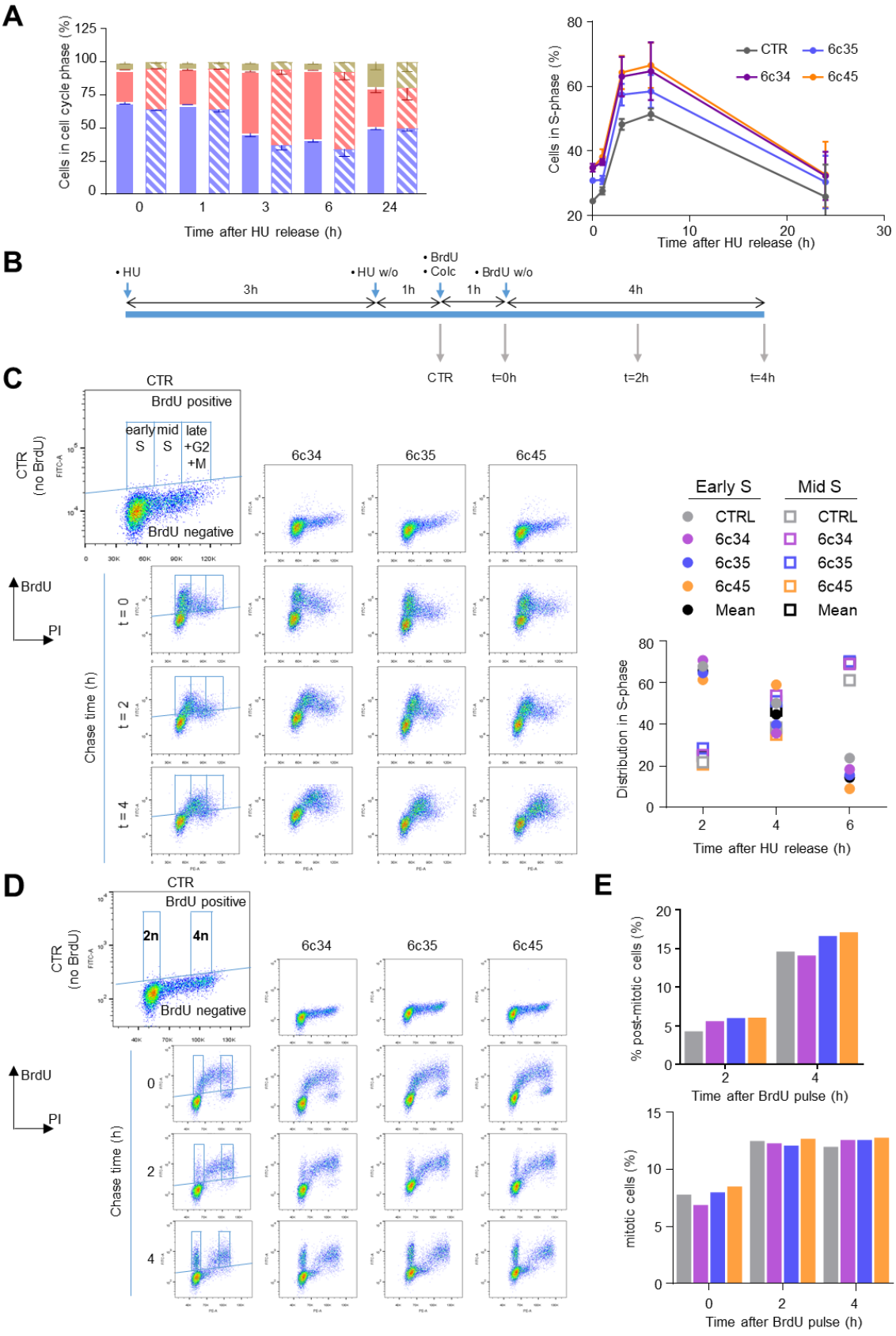

Figure 7. Kinetics of cell cycle progression in *Mgrn1*-KO cells. A) Left, cell cycle analysis of control (solid bars) and *Mgrn1*-KO 6c35 cells (dashed bars) at different times following release from block at the

G1/S interphase with HU (2 mM, 3 h). Right, kinetics of changes in the fraction of cells in S phase upon release from the HU block for control (CTR) and *Mgrn1*-KO clones. **B)** Pulse-chase analysis of cell cycle progression upon release from a HU-block. CTR cells and *Mgrn1*-KO clones treated with HU (2 mM, 3 h) were washed-off and pulsed with BrdU (1 h) in the presence of colcemid. Cells were further incubated in colcemid-containing BrdU-free medium and analyzed for BrdU intensity and DNA content (PI stain). The scheme shows the experimental design. **C)** Plots of BrdU intensity vs. DNA content. Boxes indicate the gates used for further analysis. Time-dependent changes of the distribution in early and mid S phase of CTR or *Mgrn1*-KO BrdU-labeled cells, according to gating scheme in panel B. **D)** Plots of BrdU intensity vs. DNA content (PI intensity) for CTR or *Mgrn1*-null clones pulsed with BrdU (1 h), then chased for 2 or 4 h. For each plot, BrdU-positive cells are subdivided according to their DNA content in 2n (post-mitotic cells) and 4n (mitotic cells), using the gating scheme indicated by boxes in the figure. **E)** Quantification of the percentage of post-mitotic and mitotic cells from the FACS analysis shown in D. Color code as in panels A and C.

Since Mgrn1 has been suggested to modulate microtubule stability and mitotic spindle orientation (158-160) we reasoned that its absence might lead to perturbation of the mitotic spindle checkpoint. To test this possibility, unperturbed cells were pulsed for 1 h with BrdU, then chased for up to 4 h in the absence of colcemid and analyzed by flow cytometry for newly synthesized DNA (BrdU staining) and total DNA (propidium iodide staining) (Figure 7D). Mitotic and post-mitotic cells were identified as BrdU-positive cells having 4n and 2n DNA content, respectively (see gating scheme in Figure 7D). As shown in Figure 7D and 7E, control and *Mgrn*1-KO cells completed mitosis at a comparable rate, arguing against significant activation of the mitotic checkpoint in the absence of Mgrn1. Similar results were obtained upon downregulation of Mgrn1 expression in melan-a6 cells by siRNA treatment (Figure 8).

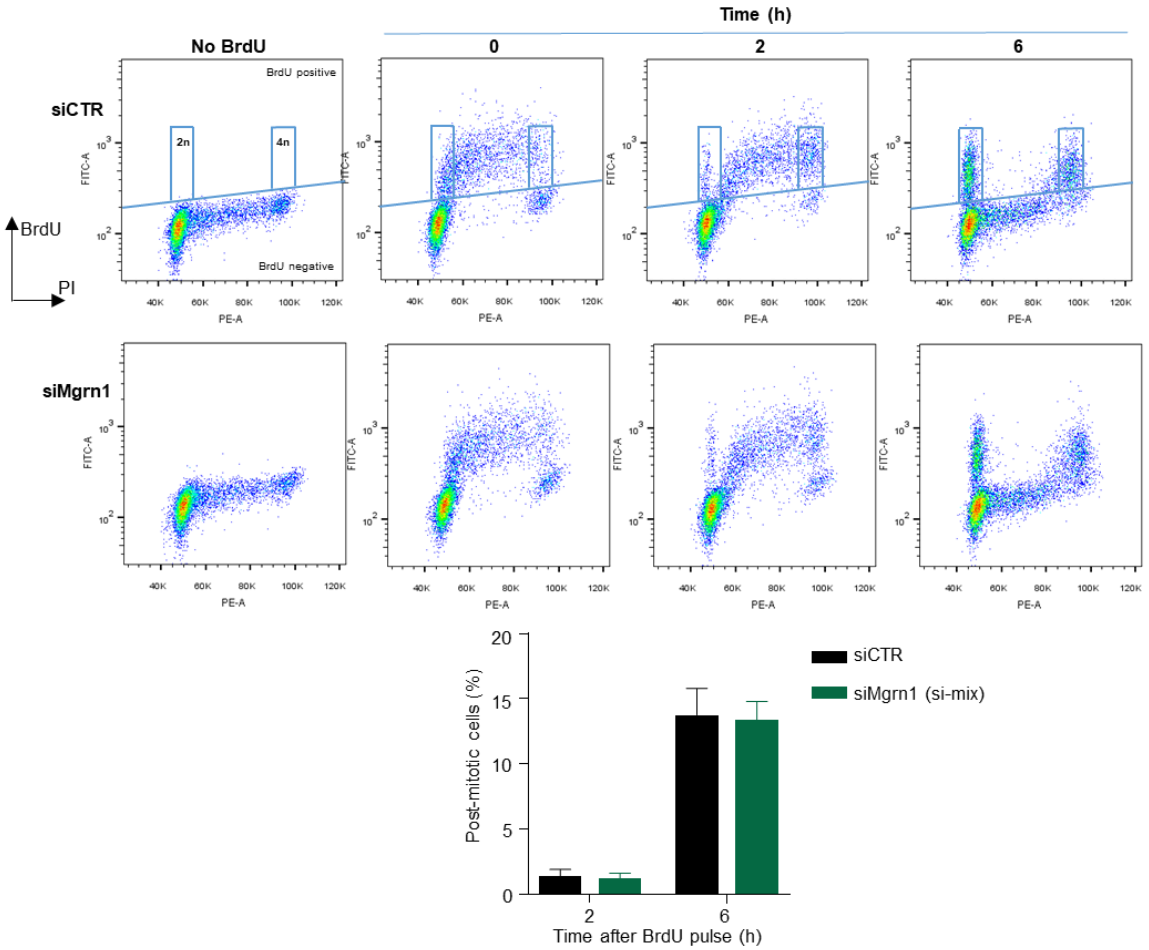

Figure 8. Cell cycle progression of Mgrn1-depleted cells. Cell cycle progression in melan-a6 cells treated with control and *Mgrn1*-specific siRNA. Cells pulsed with BrdU were chased for the times shown in BrdU-free medium, stained for newly synthesized DNA with an anti-BrdU antibody and for total DNA with propidium iodide (PI), and analyzed in a FACScanto flow cytometer. The histogram shows the percentage of post-mitotic cells, identified as BrdU-positive cells with a 2n chromosome number (PI staining), according to the gating scheme shown for siCTR cells (left column).

Overall, the data reported above showed that ablation of *Mgrn1* by CRISPR/Cas9 had a small but detectable effect on cell cycle progression, with accumulation of cells in S phase but little if any perturbation of the rate of DNA synthesis or the mitotic checkpoint.

Increased genomic instability in cells lacking Mgrn1

Progress from G1 to S and throughout the DNA synthesis phase is heavily dependent on the occurrence of DNA damage, which activates a complex signaling network, the DNA damage response (DDR), to delay or stop cell cycle progression. Double strand breaks (DSBs) are highly cytotoxic lesions that efficiently trigger the DDR. DSBs can be caused by chemical or physical insults, such as ionizing radiation or oxidizing agents,

and are also spontaneously formed in S phase by perturbations of the replication machinery (184).

Since the DDR and the regulation of cell cycle progression are intimately linked and share a substantial part of their molecular machineries, it was of interest to analyze *Mgrn1*-KO cells for the presence of DNA breaks. We compared DNA integrity in control and *Mgrn1*-null cells using comet assays. Quantitative tail moment measurements revealed a higher abundance of DNA breaks in *Mgrn1*-null cells, either melan-md1 cells or CRISPR-Cas9 generated clones (Figure 9A). Upon formation of DSBs, histone H2AX is rapidly phosphorylated to yield γ-H2AX, a key early step in DSB repair. Accordingly, γ-H2AX is an indicator of DNA DSBs. In agreement with the comet assays, melan-md1 and *Mgrn1*-KO cells displayed stronger γ-H2AX labeling than control cells (Figure 9B). Moreover, karyotype analysis indicated that whereas few mitotic spreads from wildtype melan-a6 cells showed numerical abnormalities, ~ 80 % of melan-md1 cells had chromosome numbers much higher than expected (Figure 9C). A statistically significant increase in the percentage of aneuploid cells was also found in *Mgrn1*-KO clones compared with control cells (Figure 9D). On the other hand, mitochondrial dysfunction (183) in *Mgrn1*-KO cells likely augment the production of reactive oxygen species (ROS), leading to higher oxidative stress (132, 185, 186). In DNA, ROS predominantly damage deoxyribose bases, with 8-oxo-7,8-dihydroguanine (8-oxodG) as the main oxidation product (187). We compared the levels of 8-oxodG in melan-a6 and *Mgrn1*-KO clones. These were quite variable, and even lower in one of the clones relative to controls (Figure 9E) since they varied in the order 6c35 < control melan-a6~6c34 < 6c45. Accordingly, base oxidation in nuclear DNA of *Mgrn1*-KO clones was not as marked as accumulation of DNA strand breaks, that was observed in all cases. Therefore, the high burden of strand breaks in *Mgrn1*-KO cells could not be accounted for merely on the basis of faster formation due to higher oxidative damage.

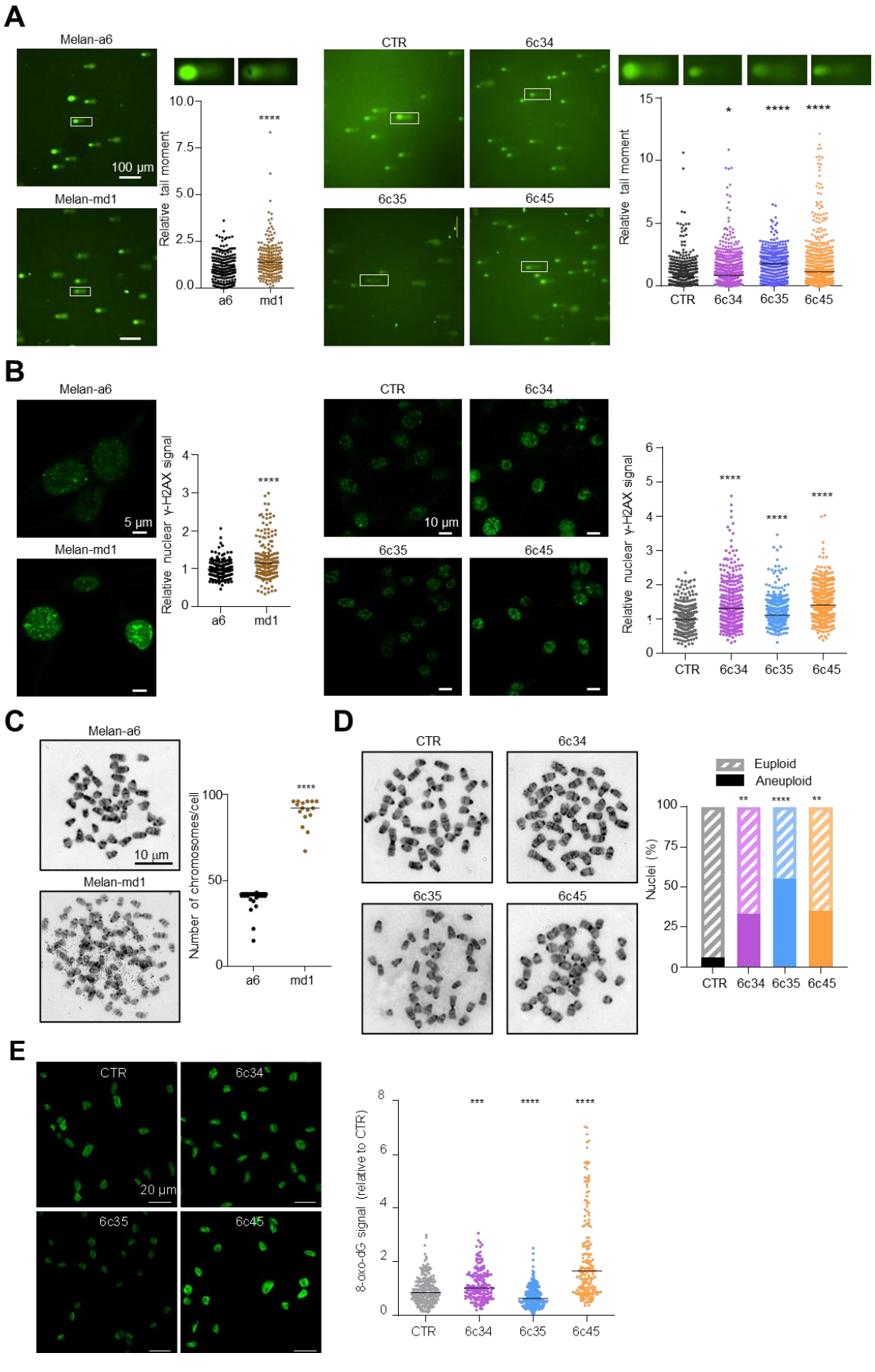
A
Melan-a6
100 µm
Melan-md1
Relative tail moment
a6
md1
CTR
6c34
6c35
6c45
B
Melan-a6
5 µm
Melan-md1
Relative nuclear γ-H2AX signal
10 µm
C
Melan-a6
10 µm
Melan-md1
Number of chromosomes/cell
D
Euploid
Aneuploid
Nuclei (%)
E
20 µm
8-oxo-dG signal (relative to CTR)

Figure 9. Genomic instability in *Mgrn1*-null cells. A) Representative comet assays performed with melan-a6 and melan-md1 cells (left) or *Mgrn1*-KO and control cells (CTR, right). Quantitative analysis of at least 100 randomly selected comets was performed using CASPLAB software. Histograms show the mean average of the tail moment of *Mgrn1*-null cells relative to controls (n = 5 independent experiments, each one with at least 100 comets analyzed). Representative images of comet tails at 40× magnification are shown above histograms. **B)** γ-H2AX immunostaining of melan-a6 control cells and melan-md1 cells (left), and *Mgrn1*-KO and control cells (right). Histograms show γ-H2AX nuclear intensity of *Mgrn1*-null cells relative to the corresponding control cells. **C)** Metaphase chromosome spreads of melan-a6 and melan-md1 cells. The dot plot illustrates numerical chromosome aberrations in *Mgrn1*-null cells in > 10 independent spreads. **D)** Same as in C for *Mgrn1*-KO clones. The graph represents the percentage of euploid (shaded) and aneupolid (solid) nuclei in *Mgrn1*-null cells compared to control cells. **E)** Detection of 8-oxodG in parental melan-a6 cells (CTR) and *Mgrn1*-KO clones. Cells were stained with an anti-8-oxodG monoclonal antibody, observed in a confocal microscope and the intensity of the 8-oxodG stain was quantified with ImageJ. The upper images correspond to representative fields, and the lower graph represents the relative intensity of the 8-oxodG. The experiment was repeated twice, and at least 100 cells were analyzed in each case. * indicates $p < 0.05$, **, $p < 0.01$, ***, $p < 0.001$ and ****, $p < 0.0001$.

Higher steady-state levels of DNA lesions can result from an increased rate of formation and/or a decreased rate of clearance by DNA repair processes. To estimate the relative contribution of these two non-mutually exclusive mechanisms to the high DSB burden in *Mgrn1*-KO cells, we analyzed the kinetics of repair of DNA strand breaks generated by exogenous agents. To this end, we challenged control or *Mgrn1*-KO cells with a short and intense oxidative pulse (Luperox 150 µM, 10 min, 4 ºC) previously shown to result in formation of strand breaks in melanocytes (84), then allowed them to recover for up to 6 h in peroxide-free medium at 37 ºC. Clearance of DNA breaks was followed by comet assays. As shown in Figure 10A, the rate of break clearance was lower for *Mgrn1*-KO cells.

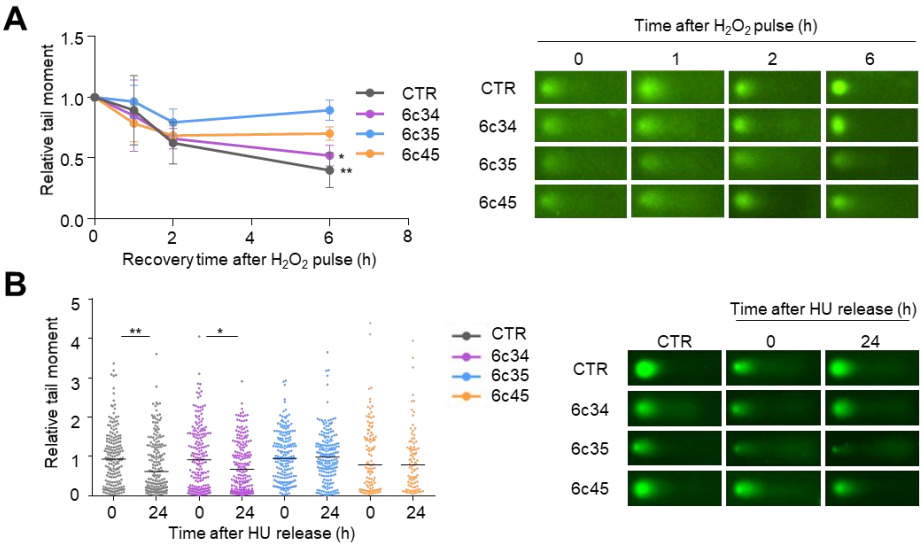

Figure 10. Impaired repair of DNA strand breaks in *Mgrn1*-KO melanocytes. A) Clearance of DNA breaks generated by an oxidative challenge. *Mgrn1*-KO cells or the corresponding control were challenged with Luperox (150 µM, 10 min, 4 °C), washed and allowed to recover for the times shown in peroxide-free medium. The presence of DNA breaks was estimated by means of comet assays. The graph indicates the evolution of tail moments, normalized to the value at time 0 (n = 3). A representative comet for each experimental condition is shown on the right. **B)** Clearance of HU-induced lesions in *Mgrn1*-KO cells. Cells were treated with HU (2 mM, 6 h), then allowed to recover in HU-free medium for 24 h. The presence of DNA breaks after the treatment with HU (time 0) or after a 24 h recovery was analyzed by comet assays, as in A. * indicates $p < 0.05$, **, $p < 0.01$, ***, $p < 0.001$ and ****, $p < 0.0001$.

To extend these data, we analyzed the repair of breaks generated upon prolonged replicative stress caused by long HU treatment (6 h). Within a 24 h recovery, control melan-a6 cells were able to repair most of the ensuing DNA breaks. Conversely, one clone of *Mgrn1*-KO cells exhibited a lower but still significant repair capacity, and the other two clones under study did not achieve a statistically significant clearance of the HU-induced lesions (Figure 10B). Of note, these clones (6c35 and 6c45) were also less efficient in repairing DNA strand breaks generated by an oxidative pulse and exhibited the highest levels of DNA damage under basal conditions. Therefore, lack of Mgrn1 expression decreased the ability of melanocytes to cope with strand breaks generated by oxidizing agents or by HU-induced replicative stress. This might explain, at least partially, the genomic instability in *Mgrn1*-KO cells.

Effects of Mgrn1 ablation on growth and invasive properties of melanoma cells

So far, we have shown that knockdown of *Mgrn1* in normal mouse melanocytes (i) induced a more differentiated cellular morphology, (ii) increased cell adhesion to collagen matrices and impaired 2D and 3D motility, (iii) altered cell cycle progression and (iv) led to genomic instability with accumulation of DNA damage. Similar changes might have important implications for the behavior and aggressiveness of melanoma cells. To test this possibility, we knocked down *Mgrn1* expression in B16-F10 melanoma cells by CRISPR/Cas9 and selected two independent *Mgrn1*-KO clones for further analysis (Figure 11A-C). As previously shown for *Mgrn1*-KO melan a6-cells, the proliferation rate of B16-derived *Mgrn1*-KO clones was not significantly different compared with control cells (Figure 11D).

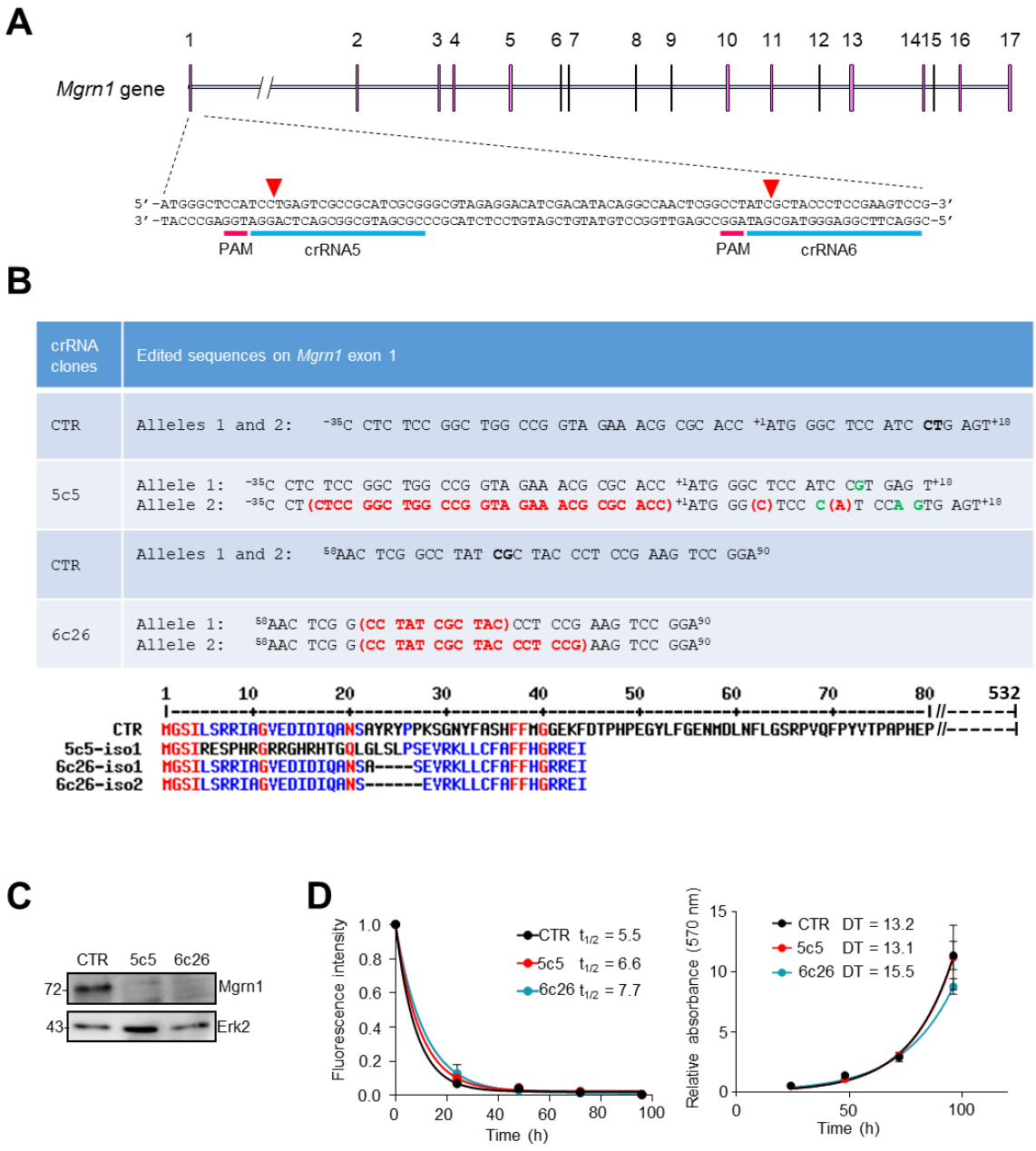

Figure 11. Generation of *Mgrn1*-KO B16 mouse melanoma cells: strategy, validation and effect on the rate of proliferation. A) Schematic representation of *Mgrn1* and sequence in exon 1 targeted by crRNA5 and crRNA6. Both 20 nt sequences pair with the DNA target highlighted with a blue bar on the bottom strand, directly upstream of a 5'-NGG adjacent motif (PAM; in pink). **B)** Edited sequences (from -35 to +18 nt and from +58 to +90 nt) in exon 1 of the *Mgrn1* gene in *Mgrn1*-KO clones 5c5 and 6c26, compared with the consensus sequence in control (CTR) B16F10 cells. Deleted nucleotides are represented between brackets in red and inserted nucleotides are indicated in green. The amino acid sequence of the resulting truncated Mgrn1 protein in *Mgrn1*-KO cells is shown below. **C)** Representative immunoblots for Mgrn1 in *Mgrn1*-KO B16F10 melanoma clones. **D)** Analysis of cell division of *Mgrn1*-KO B16F10 cells by measuring the decrease in CFSE fluorescence intensity and calculation of half-lifes (t1/2) (left) and by the MTT assay measuring the increase in relative absorbance at 570 nm and determining the doubling times (DT) (right) for a period of 4 days.

These clones phenocopied the effects of *Mgrn1* ablation in melan-a6 melanocytes. Indeed, *Mgrn1*-KO B16 melanoma cells were more differentiated, as shown by higher melanin contents (Figure 12A), and presented higher levels of DNA damage as shown by comet assays, γ-H2AX staining and altered ploidy (Figure 12B–D).

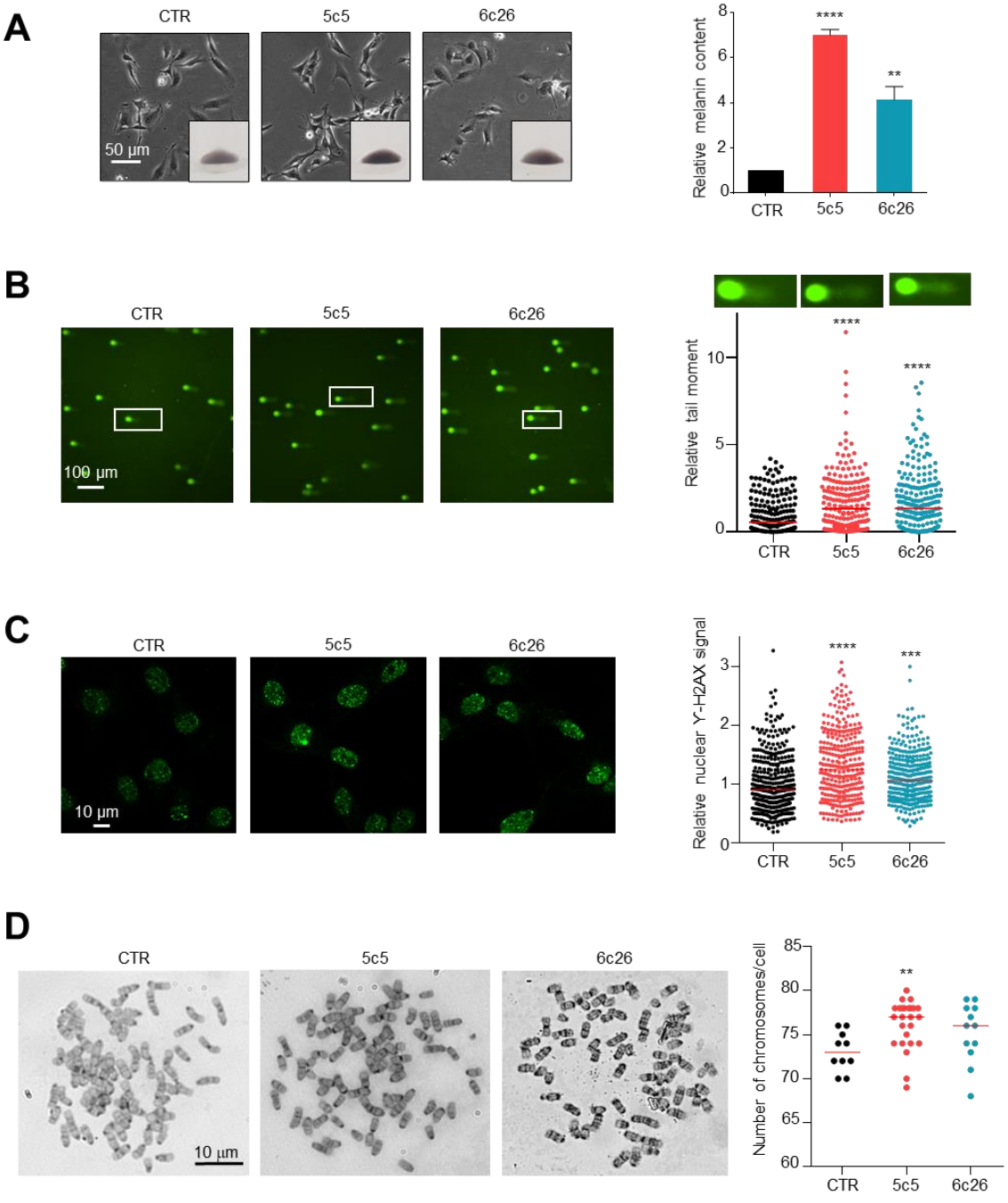

Figure 12. Increased genomic instability in *Mgrn1*-KO B16 mouse melanoma cells. A) Micrographs of *Mgrn1*-null B16F10 cells in 2D cultures. Inserts show representative images of cell pellets. Quantification of the relative melanin content is shown on the right. **B)** Alkaline comet analysis of DNA in control (CTR) and *Mgrn1*-null B16F10 cells. Histograms show the mean average of the tail moment of *Mgrn1*-null cells relative to control cells (*n* = 3 independent experiments, each one with at least 70 comets analyzed). Representative

images acquired at 40x magnification are shown above each histogram. ****p < 0.0001. **C)** Confocal images of γ-H2AX immunostaining in *Mgrn1*-KO and control B16F10 cells. Histograms show γ-H2AX nuclear intensity of *Mgrn1*-null cells relative to controls. **D)** Micrographs of metaphase chromosome spreads of control and *Mgrn1*-KO B16F10 cells after Giemsa staining. The dot plot represents the number of chromosomes per cell.

Moreover, B16 *Mgrn1*-KO clones displayed significantly increased cellular adhesion to collagen I (Figure 13A), and impaired migration in 2D scratch assays (Figure 13B) and 3D collagen I invasion assays (Figure 13C). We performed short-term lung colonization assays. *Mgrn1*-KO and control B16F10 cells were labeled with green or orange fluorescent dyes respectively, and co-injected in equal numbers in the tail vein of C57BL/6J mice. Mice were sacrificed after 30 min or 24 h and the lungs were examined for fluorescent cells. Thirty min after inoculation, comparable numbers of control and *Mgrn1*-KO cells were present in the lungs. However, significantly fewer *Mgrn1*-KO cells remained 24 h after the injection, indicative of impaired colonization potential upon repression of Mgrn1 (Figure 13D). On the other hand, tumors generated by intradermal injection of *Mgrn1*-KO cells showed a numerically lower mean size than those derived from control B16 cells, but the differences did not reach statistical significance due to the high dispersion of the data (Figure 13E). Nevertheless, a lower rate of tumor growth was also suggested by immunochemical staining of the proliferation marker Ki67, which was stronger in tumors arising from control cells (Figure 13F). Moreover, estimation of the mitotic index in haematoxylin/eosin-stained preparations revealed a significantly lower number of mitotic cells in *Mgrn1*-KO tumors (Figure 13G). These *in vivo* experiments showed that, at least in the B16 mouse melanoma model, Mgrn1 expression may regulate the malignant phenotype, with effects on proliferation, adhesion, motility, lung colonization potential and maybe also on the rate of tumor growth. Therefore, Mgrn1 expression might be an important determinant of the phenotype and aggressiveness of mouse melanoma cells.

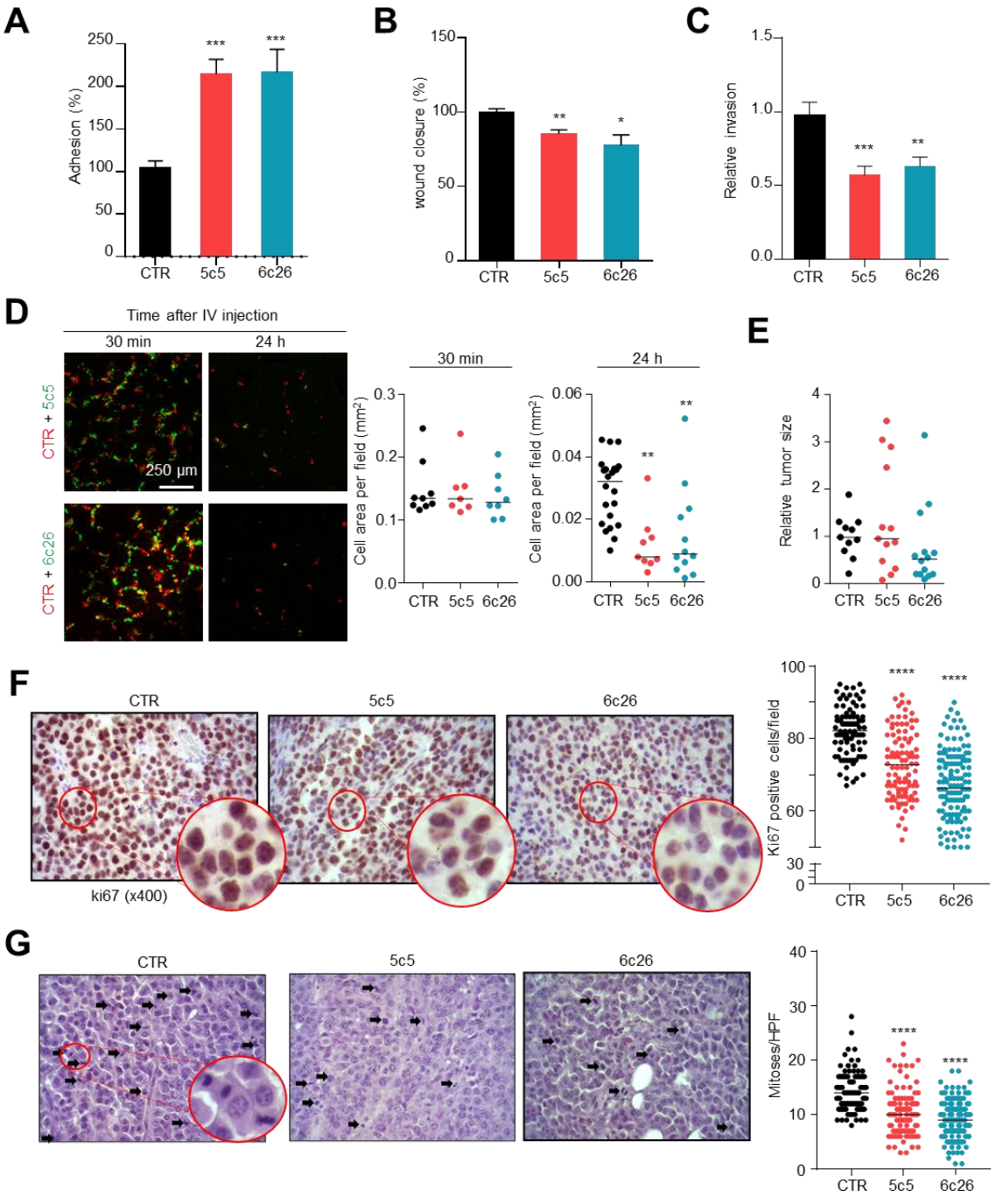

Figure 13. Modulation of melanoma cells adhesion, migration and invasive properties by Mgrn1. A) Percentage of adhesion to a collagen I matrix of *Mgrn1*-KO B16F10 clones (5c5, 6c26) relative to control cells. **B)** Wound closure of *Mgrn1*-KO B16F10 cells after a scratch assay (24 h). Results expressed as the percentage of wound closure relative to control cells. **C)** Decreased invasion through collagen I after 24 h of *Mgrn1*-KO B16F10 clones relative to melan-a6 control cells. **D)** Short term lung colonization assay. Micrographs on the left correspond to representative confocal microscopy images of the lungs of mice sacrificed 30 min or 24 h after injection in the tail vein of equal numbers of control (red) and *Mgrn1*-KO (green) B16F10 cells. Dot plots on the right show the cell area occupied by control (CTR) or the indicated *Mgrn1*-KO cells, as a measure of the relative abundance of each cell type. **E)** Relative size of tumors derived from control or *Mgrn1*-KO B16F10 cells intradermally injected into the flanks of C57BL/6J mice and analyzed

18 days after injection. At least 4 mice per group were analyzed, and the experiment was repeated 3 times. **F)** Immunohistochemical staining of ki67 in tumors grown as in E. Representative micrographs (left) show zoomed areas for better comparison of the relative intensities of the stain. The dot plot on the right shows the percentage of ki67-positive cells in control and *Mgrn1*-KO cells. **G)** Estimation of mitotic index in tumors grown as above. Representative micrographs of haematoxylin/eosin-stained preparations were counted for mitotic figures (highlighted with arrows). The mitotic index was estimated by the median of the number of mitoses in 10 high power fields (HPF, X400), and is shown in the dot plot on the right.

CHAPTER III

MGRN1 EXPRESSION AS A PROGNOSIS MARKER OF MELANOMA AGGRESSIVENESS

The data summarized in the previous chapter highlighted an important role of *Mgrn1* expression in modulating the behavior of mouse melanoma cells. Based on these results, we were interested in studying the possible role of MGRN1 in the biology of normal, premalignant and malignant human melanocytes, since *MGRN1* expression could be an important determinant of melanoma prognosis.

As a first step in this study, we analyzed a possible relationship of *MGRN1* expression and survival of melanoma patients. For this purpose, we interrogated the UCSC Xena database (https://xena.ucsc.edu/) for correlations of high and low *MGRN1* mRNA levels and clinical data, in a set of > 450 melanoma patients (TCGA dataset). High and low expression tumors were defined as the upper and lower 33 % *MGRN1*-expressing tumors, respectively. For comparison, we performed a similar analysis for two genes known to modulate melanoma progression by different and well-defined mechanisms. These genes were *RAB7*, that modulates the function of the endolysosomal pathway (188) and *TYRP1*, whose action relies on miR-16 sequestration (189). For these genes, low and high levels of expression in melanoma were defined as for *MGRN1*. The results are shown in Figure 1A. Kaplan-Meier curves showed that low expression of *MGRN1* in tumors was significantly associated with better survival. Moreover, we found that the differences between the survival of patients in the high and low expression groups were similar for *MGRN1*, *RAB7* and *TYRP1* (median survival of 1083, 942 and 1167 days for tumors of high expression of *MGRN1*, *RAB7* and *TYRP1*, versus 1932, 1932 and 2300 days for the melanomas with low expression of these genes). Of note, *TYRP1* expression is considered one of the best predictors of survival of melanoma patients described to date (190).

Using the data compiled in the GEPIA database (http://gepia.cancer-pku.cn/), we compared the relative expression of the *MGRN1* gene in different types of tumors from human patients (TCGA and GTEx cohorts) (Figure 1B). This analysis indicated that melanoma is one of the cancers with higher expression of *MGRN1*. In fact, only in acute myeloid leukemia (LAML) was its expression clearly higher than in melanoma (SKCM). Interestingly, these data also suggested that the expression of *MGRN1* might be higher in melanoma compared with healthy skin, further suggesting a role for MGRN1 in the malignant phenotype of melanoma cells (Figure 1C).

Furthermore, the analysis of pooled data from 6 independent datasets available at Gene Expression Omnibus (GEO) database (https://www.ncbi.nlm.nih.gov/geo/) confirmed a

significant enrichment of *MGRN1* in melanoma compared with either normal skin or *nevi* (Figure 1D). Interestingly, this analysis pointed to a lower expression in *nevi* compared with normal skin. However, this finding did not reach statistical significance, probably due to the limited number of samples.

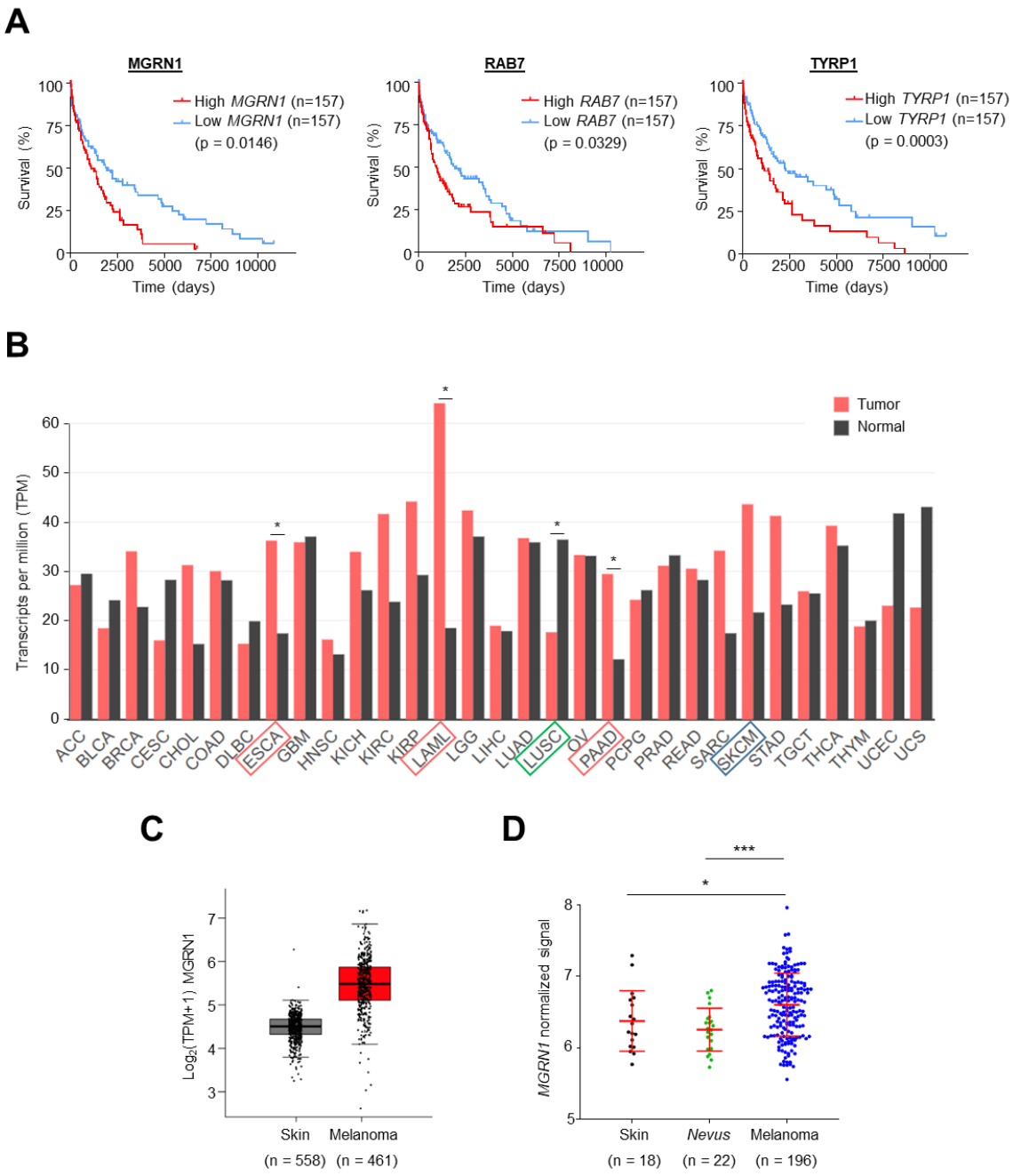

Figure 1. Analysis of survival of melanoma patients and *MGRN1* expression in patient samples using public databases. A) Kaplan-Meier curves for survival of melanoma patients (TCGA cohort from UCSC Xena database). Patients were stratified as a function of high and low *MGRN1* (left), *RAB7* (middle) or *TYRP1* (right) levels in primary tumor specimens (*n* = 157 in each case). Log-rank (Mantel-Cox) test was used for statistical analysis**. B)** Analysis of *MGRN1* expression across different tumor types (TCGA dataset) and normal tissues (GTEx dataset), available in GEPIA database. Median expression is represented by the

height of the bar. Tumor abbreviations in X axis with red boxes indicate higher expression of *MGRN1* in tumor than paired normal samples, in green represent lower expression of *MGRN1* in tumor, and in blue SKCM samples vs. paired normal samples. ANOVA was used for statistical analysis. **C)** Representation of the normalized *MGRN1* expression levels in normal skin and melanoma samples, available in GEPIA database. **D)** Comparison of the normalized *MGRN1* expression levels between normal skin, *nevus*, and melanoma samples, using GEO database. Graphs show mean ± SEM and one-way ANOVA was used for statistical analysis. * indicates $p < 0.05$, **, $p < 0.01$, ***, $p < 0.001$ and ****, $p < 0.0001$.

Next, we looked for mutations in the *MGRN1* gene in melanoma patients. For this analysis, we used the TCGA dataset from the cBioPortal database (https://www.cbioportal.org/). We found that 14 out of 363 melanomas presented somatic mutations in *MGRN1*, accounting for a mutation rate of 4 %. The types of mutations found were one fusion, one splice mutation, 2 nonsense and 10 missense mutations (Figure 2A). Among the missense mutations, only 2 were conservative (G166V and D466E), the other 8 being potentially pathological changes.

When we compared the mutational status of the *MGRN1* gene among different human cancer types, we found that melanoma was the sixth cancer with a higher rate of genomic alterations, after uterine corpus endometrial carcinoma (UCEC), breast invasive cancer (BRCA), diffuse large B-cell lymphoma (DLBC), colon adenocarcinoma (COAD) and uterine carcinosarcoma (UCS) (Figure 2B). However, most of the alterations found in BRCA, DLBC and USC were amplifications, and, in terms of protein sequence-altering mutations, melanoma ranked second only after UCEC. The 4 % rate of *MGRN1* mutations in melanoma is low compared with major melanoma driver genes such as *BRAF* or *NRAS* (mutated in roughly 50 % and 20 % of melanomas, respectively, see below), but nevertheless it is far from being negligible. For comparison, mutations are almost twice as frequent in *MGRN1* than in *MITF* (~ 2.3 %), a gene known to be mutated in a subset of melanomas (191). Moreover, well-known cancer susceptibility genes have comparable rates of mutation in human cancers. For instance, *BRCA1* is mutated in 1-7 % of breast cancer samples and *BRCA2* in another 1-3 % of the patients, independently of family history or age at diagnosis (192). In summary, analysis of data deposited in publicly available databases showed that: i) melanomas display a significant rate of mutations in *MGRN1*, ii) *MGRN1* might be overexpressed in melanoma compared with normal tissue, and iii) high *MGRN1* expression is significantly associated with a poorer prognostic.

A

14 Mutations

Sample ID	Protein Change	Mutation Type
TCGA-EE-A20F-06	*MGRN1-C16orf96*	Fusion
TCGA-D9-A1JX-06	*P71S*	Missense
TCGA-FS-A1ZK-06	*P71S*	Missense
TCGA-EE-A2GI-06	*E270K*	Missense
TCGA-EE-A2GO-06	*P266L*	Missense
TCGA-EE-A29D-06	*S492F*	Missense
TCGA-D3-A2JG-06	*P458Q*	Missense
TCGA-D3-A2JC-06	*G166V*	Missense
TCGA-3N-A9WC-06	*V339E*	Missense
TCGA-D3-A2JP-06	*G41**	Nonsense
TCGA-EE-A181-06	*S407**	Nonsense
TCGA-EE-A29X-06	*K152N*	Missense
TCGA-FS-A1ZP-06	*X510_splice*	Splice
TCGA-WE-A8ZO-06	*D466E*	Missense

B

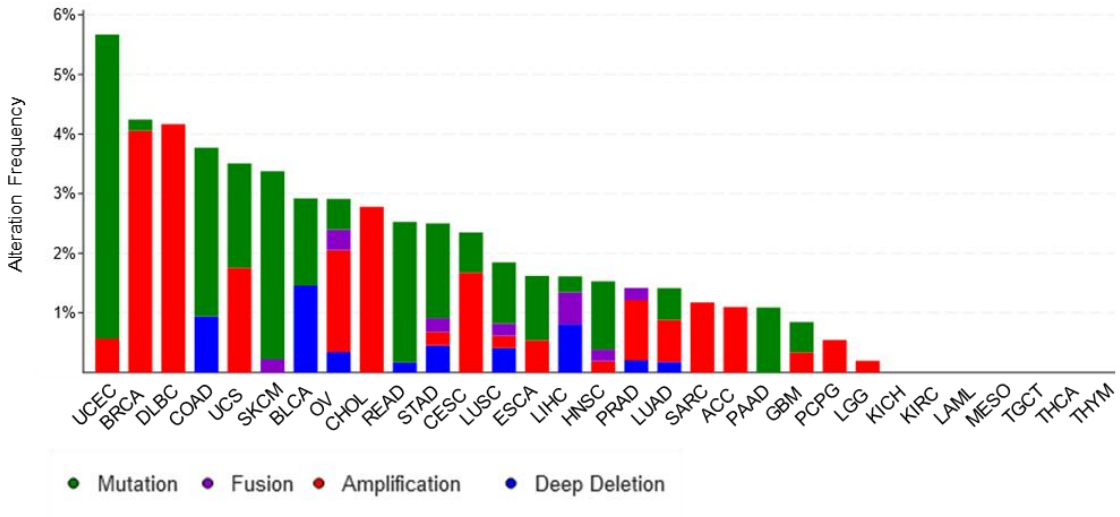

Figure 2. Determination of mutational status of the *MGRN1* gene in melanoma and among different human cancer types. A) Type of *MGRN1* mutations and resulting protein changes found in melanoma human samples of the TCGA dataset from the cBioPortal database. **B)** Genetic alterations frequency of the *MGRN1* gene in different human tumor types (TCGA dataset from the cBioPortal database). Genetic alteration types are indicated on the graph with a color code.

To validate these *in silico* analyses and further study the possible association of *MGRN1* expression with some aspects of melanoma biology in human clinical samples, we analyzed *MGRN1* expression in 49 *nevi* and 33 melanoma biopsies kindly supplied by Dr. María Dolores Boyano López and Dr. Santos Alonso Alegre, from the University of the Basque Country (UPV). Additionally, we studied *MGRN1* expression in a collection

of about 50 lymph node melanoma metastases provided by Prof. Ghanem, from the Laboratory of Oncology and Experimental Surgery (LOCE) of the Free University of Brussels. Both sample collections have been successfully used in previous studies (189, 193, 194), and clinical information on the patients is available. The measurements of *MGRN1* gene expression in these cohorts were performed by slightly different approaches during short stays at the corresponding laboratories. The Brussels (LOCE) samples were analyzed by conventional qPCR and the Bilbao (UPV) collection by digital PCR. This approach can detect gene expression differences smaller than two-fold. For both sample collections, and owing to the limited number of samples, high and low *MGRN1* expression groups were defined as the upper and lower 50 % *MGRN1*-expressing samples, respectively (as opposed to the upper and lower 33 % employed for the data in public databases). Moreover, since the set of clinical data on the patients was not the same for both cohorts, not all the parameters of interest could be studied for the two collections. Concerning the interpretation of the data, it must be born in mind that the samples are not directly comparable since the UPV set corresponds to the primary tumor whereas all the LOCE samples were lymph node metastases, even though clinical data on the primary tumor (mostly Breslow index and histological type) were also available. In addition, the techniques for mRNA quantification were not identical. It must also be taken into account that the samples might correspond to different clinical stages, since a fraction of the UPV tumors come from metastasis-free patients, whereas all the LOCE patients carried metastatic tumors. However, despite these limitations, we considered that it was interesting to perform the analyses described below to complement the *in silico* studies and to augment the robustness of potential associations.

Consistently with GEO datasets, we confirmed that melanoma samples from the UPV set showed a significantly higher *MGRN1* expression than *nevi* (Figure 3A). This suggests that the transition from a benign to a premalignant or malignant lesion could be accompanied by an increase in the expression of *MGRN1*. Next, we looked at a possible correlation between the levels of *MGRN1* expression in melanoma samples and the development of metastases, or with the tumor stage. For staging, we employed the tumor, node, metastasis staging system (TNM staging system), created by the AJCC, American Joint Committee on Cancer (195). Stage 0 refers to melanoma *in situ*. Localized tumors are classified as stage I-II, tumors with lymph node involvement as stage III, and tumors that cause distant metastases as stage IV (196). Moreover, some stages are subdivided with capital letters, whereby an earlier letter corresponds to a lower stage in terms of tumor thickness, ulceration, and spread (197). No significant differences in *MGRN1* expression levels were observed, neither between samples

belonging to early or late stages of tumor development (Figure 3B), nor between samples associated or not with metastasis (Figure 3C). Obviously, this analysis was not possible for the LOCE samples, since all of them corresponded to lymph node metastases.

Clinical and histopathological features have been used routinely for prognosis of melanoma. Currently, this prognosis is mostly based on a restricted set of histopathological factors such as Breslow index, presence or absence of ulceration, level of local invasion and mitotic rate. We observed a similar percentage of ulceration in lesions with high and low *MGRN1* expression (Figure 3D). Breslow thickness, which is a measurement of the depth of invasion, is the most important histopathological factor to predict prognosis of melanoma (196, 198, 199). The value of the Breslow thickness did not show significant differences between high and low *MGRN1*-expressing samples, neither for the UPV nor for the LOCE collections (Figure 3E). However, for both cohorts we observed a trend towards a higher Breslow index for the high *MGRN1* expression tumors. To further analyze this point, we performed a similar analysis for the TCGA dataset, to achieve a higher statistical power owing to the larger number of samples. Moreover, the TCGA dataset allows for comparing the 33 % upper and lower expression tumors. In this case, a strong statistical significance was found ($p= 0.0012$), thus confirming the trend of the UPV and LOCE collections and suggesting that high expression of *MGRN1* is actually associated with a higher tumor thickness at diagnosis (Figure 3E).

Lastly, we analyzed whether the expression of *MGRN1* in melanoma samples of the UPV cohort was related to the metastasis-free period (time, in months, from the diagnosis of melanoma to the appearance of metastasis in those patients who developed metastasis during the follow-up) and disease-free period (time, in months, from the diagnosis of melanoma to the end of the study in those patients who did not develop metastasis during the follow-up). For this purpose, Kaplan-Meier curves were obtained for the samples with high and low *MGRN1*, both for metastasis-free time (Figure 3F, left) and disease-free time (Figure 3F, middle). Interestingly, we observed that patients with high *MGRN1* expression tumors had a significantly shorter disease-free period than patients with samples with low expression ($p= 0.0022$). A similar trend was observed for the metastasis-free patients, although in this case the difference did not reach statistical significance, most likely due to the limited number of samples and to the fact that samples were divided in two groups (50 % higher or lower expression) rather than 3 (33 % higher or lower expression). Since the analysis of the metastasis-free survival was obviously impossible for the LOCE cohort, in this case we used the progression-free survival, defined as the length of time during and after the treatment that a patient lives with the

disease but it does not get worse. In this case, no statistical difference was observed for the low and high *MGRN1* expression groups, most likely because the primary tumor was already spread in all these patients (Figure 3F, right).

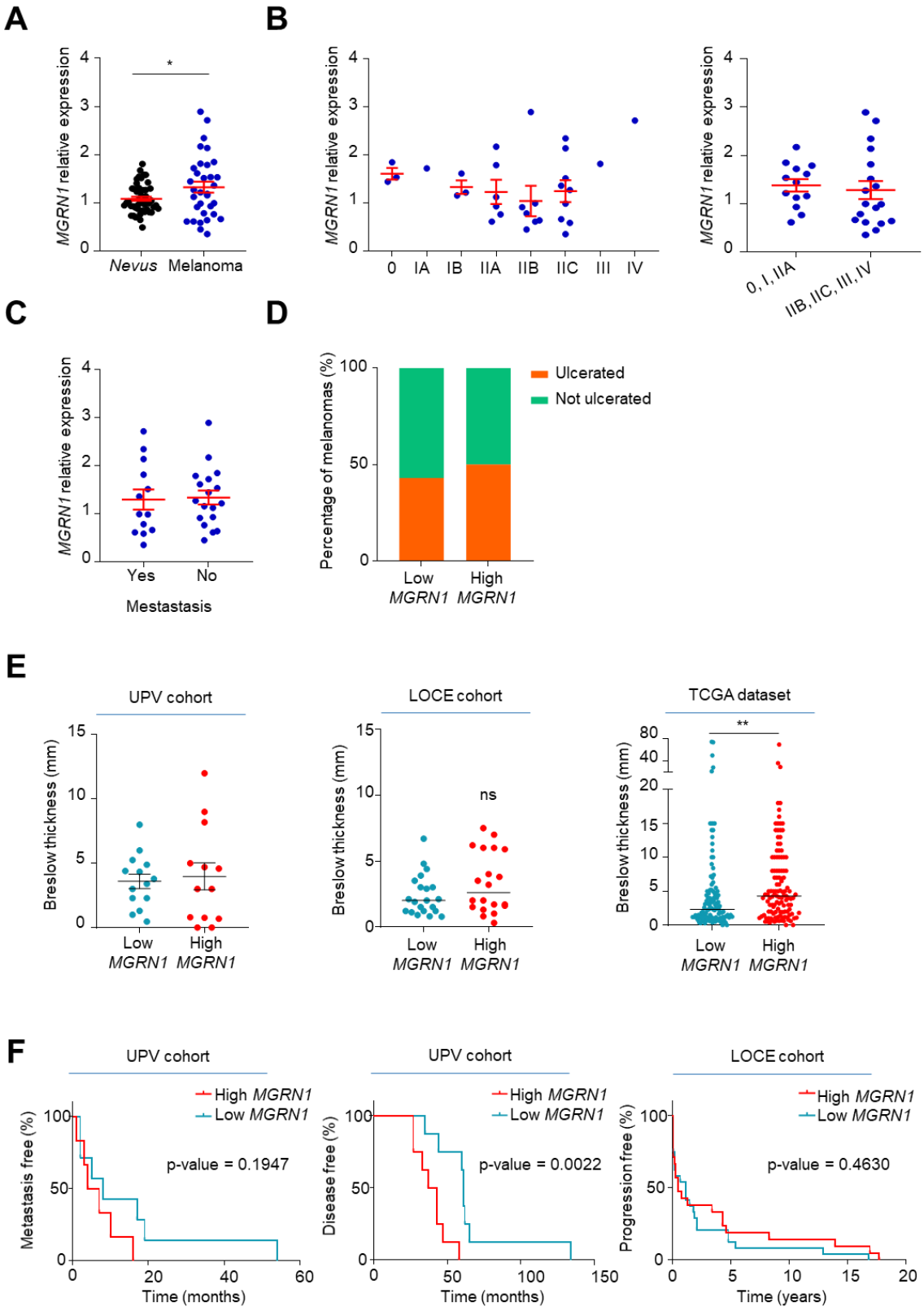

Figure 3. Analysis of *MGRN1* expression in samples from melanoma patients. A) Relative expression of *MGRN1* in *nevus* and melanoma samples. About 40 samples per group were analyzed. **B)** Analysis of *MGRN1* expression levels in melanoma samples at different stages (0, IA, IB, IIA, IIB, IIC, III and IV) separately (left) or grouped (right). **C)** Analysis of *MGRN1* expression levels in melanoma samples and the development of metastases. A logarithmic transformation was used to normalize the data distribution in A, B and C. Graphs show mean ± SEM of *MGRN1* relative expression to *GAPDH* in A, B and C. T-test was used for statistical analysis. **D)** Comparison of the presence or absence of ulceration in melanoma samples with high and low expression of *MGRN1*. Fisher's test was used for statistical analysis. **E)** Comparison of the Breslow thickness in melanoma samples (from UPV (left), LOCE (middle) or TCGA (right) cohorts) with high and low expression of *MGRN1*. Graphs show mean ± SEM (left) or median (middle and right) and t-test was used for statistical analysis. **F)** Curve of the metastasis-free period (left), disease-free period (middle) or progression-free survival (right) in melanoma patients from UPV (left and middle) or LOCE (right) cohorts, after Kaplan-Meier adjustment, classified into two groups according to the level of *MGRN1* expression (high and low). Log-rank (Mantel-Cox) test was used for statistical analysis**.** * indicates $p < 0.05$, **, $p < 0.01$, ***, $p < 0.001$ and ****, $p < 0.0001$.

For the UPV cohort, we also analyzed whether the levels of *MGRN1* expression in melanoma samples were associated with other characteristics such as age and gender of the patient, localization of the primary tumor and histological type of melanoma. The results showed that 73 % of the melanomas with high *MGRN1* expression were diagnosed in patients older than 60 years. Conversely, melanomas with lower *MGRN1* expression were equally distributed between patients younger or older than 60 years (Figure 4A). Additionally, most of the samples with high *MGRN1* expression belonged to males (67 %), while 81 % of low *MGRN1* expression tumors came from females (Figure 4B). Interestingly, numerous studies have shown a better prognosis for women and increased death rates in patients over 60 years old, specially men (https://seer.cancer.gov/). However, findings should be interpreted with caution, since the TCGA data did not confirm a statistically significant difference in the distribution by gender or age of high versus low *MGRN1* expression melanomas (not shown).

Regarding the location of the tumor (Figure 4C), low *MGRN1* expression melanomas were most often found in the legs, lower extremities, LE (43 %), while the percentage of high *MGRN1* expression melanomas in this location dropped to 21 %. Notably, melanomas arising in the head/neck (HN) and acral melanomas (AA) were more frequent (3-fold and 2-fold, respectively) among high *MGRN1* expression tumors, compared with low *MGRN1* expression melanomas. Head/neck and trunk anatomical localizations have also been described as having a worse prognosis (200).

The histological type of lesion in the high and low expression of *MGRN1* groups was analyzed for the two cohorts under study (Figure 4D). For the UPV collection, this analysis showed that 42 % of the samples ranked as high *MGRN1* expression were

superficial spreading melanomas (SSM) compared with 29 % of samples with lower *MGRN1* levels. On the other hand, most of the samples with low expression of *MGRN1* correspond to nodular melanomas (NM, 57 %) compared with 33 % of samples with high levels of *MGRN1*. Finally, the percentage of tumors with high expression of *MGRN1* classified as acral-lentiginous melanoma (ALM) was 17 %, compared with 7 % in the lower expression of *MGRN1* group. It is widely accepted that NM and ALM are associated with the poorest prognosis (201, 202). However, this distribution was different for the LOCE collection. In any case, the low *MGRN1* expression group was enriched in SSM compared with the UPV cohort, and, conversely, the high *MGRN1* expression group contained a higher percentage of NMs. Indeed, 71 % of melanomas with high *MGRN1* expression were NMs compared with 35 % of low expression tumors. Interestingly, the percentage of ALMs in the high expression group was also around 3 times higher (14 % vs. 4 % in the low expression group). Therefore, in both cohorts ALMs were more frequent in the high MGRN1 expression tumors.

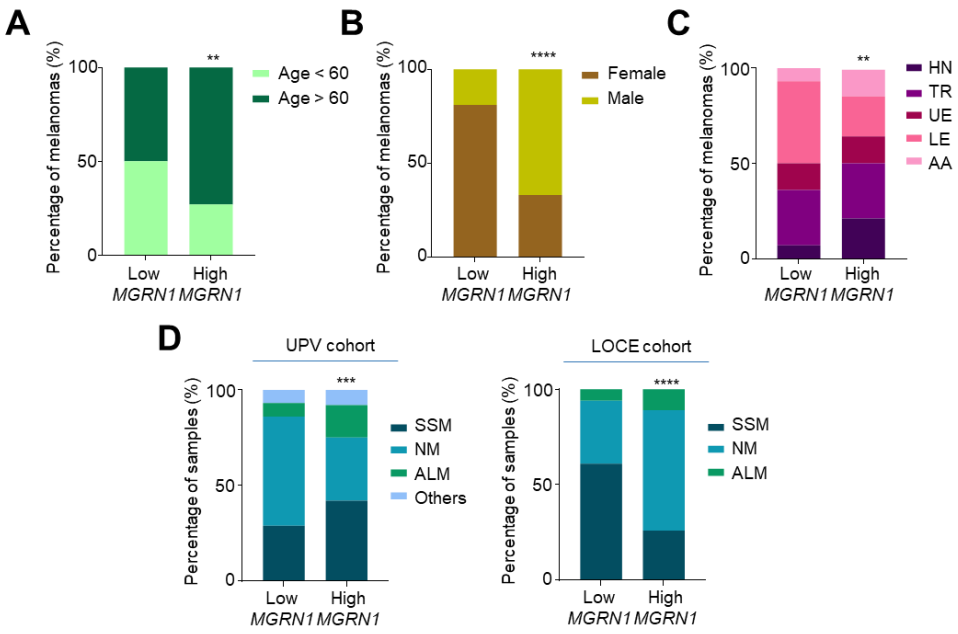

Figure 4. Data distribution of *MGRN1* expression and some clinical factors in melanoma samples. A) Percentage of melanomas with low or high *MGRN1* expression associated to a certain age range, **B)** sex, **C)** tumor location (HN: head and neck; TR: trunk; UE: upper extremities; LE: lower extremities and AA: acral areas) and **D)** histopathological type (SSM: superficial spreading melanoma; NM: nodular melanoma; ALM: acral-lentiginous melanoma and others) in UPV cohort (D left) and LOCE cohort (D right). Fisher's test (A, B and D (left)) and Chi-square (C and D (right)) test were used for statistical analysis. * indicates $p < 0.05$, **, $p < 0.01$, ***, $p < 0.001$ and ****, $p < 0.0001$.

To further explore the relationship between *MGRN1* expression and clinical outcome, and before addressing mechanistic aspects of the role of MGRN1 in human

melanocytes, we wanted to find out whether *in silico* analyses might suggest functional interactions with genes frequently mutated in melanoma. For this study, we selected the 3 genes that define the main molecular subtypes of melanomas, namely *BRAF*, *NRAS* and *NF1*. As already mentioned, *NRAS*, *BRAF* and *NF1* encode for proteins of the mitogenic signaling pathway leading to activation of the ERK1/2 kinases (57), and mutations in these genes define the 3 most prevalent molecular subtypes of melanoma. BRAF lies downstream of NRAS. NF1 is a member of the large family of mammalian Ras-GTPase-activating protein (GAP)-related proteins. Its best understood function is to downregulate the levels of activated RAS proteins by promoting the hydrolysis of RAS-bound GTP to yield an inactive RAS-GDP complex (203). We also included *TP53* in these analyses, since this gene is highly mutated in human cancers and has been found mutated in a significant percentage of melanomas (204-206). Since mutations in genes participating in the same functional pathway are normally mutually exclusive, we first analyzed whether mutations in *MGRN1* and the selected genes show mutual exclusivity or co-occurrence in melanomas. For this purpose, we used the TCGA dataset from the cBioPortal software. We found that *MGRN1* mutations tended to be mutually exclusive with *TP53* mutations, but not with mutations in *NRAS*, *NF1* or *BRAF* (Figure 5A). This suggests that MGRN1 does not play a significant role in the NRAS-BRAF-MEK-ERK pathway.

Then, we interrogated the UCSC Xena database (TCGA dataset) for the outcome of the disease for patients with melanomas of low or high *MGRN1* expression carrying mutations in these genes. For *BRAF*-wildtype (WT) or *BRAF*-mutated melanomas, the effects of *MGRN1* expression on patient survival was similar, with a trend for better survival of patients expressing lower levels of *MGRN1* (Figure 5B). Unexpectedly, the statistically significant pro-survival effect of low *MGRN1* expression observed in *NRAS*-WT and *NF1*-WT patients was completely lost in the *NRAS*- or *NF1*-mutated melanomas (Figure 5 C and D). Since both types of mutations lead to NRAS activation, this suggests that when NRAS is hyperactive, then the level of expression of *MGRN1* is no longer relevant as a determinant of the patient's outcome. This observation cannot be explained in the absence of molecular data, but it can be speculated that activation of the PI3K-AKT pathway downstream of NRAS might override the effect of low *MGRN1* expression. This would occur in *NRAS*- and *NF1*-mutated tumors but not in *BRAF*-mutated melanomas.

Concerning *TP53*, the survival of patients with tumors harboring the WT gene was significantly dependent on *MGRN1* expression, but this effect was lost in patients with *TP53*-mutated tumors (Figure 5E). One rationale for this effect might be that TP53 could

lie downstream of MGRN1 in a functional pathway relevant for the aggressiveness of melanoma. Although other alternative interpretations are also possible, this hypothesis is consistent with the mutual exclusivity of mutations in the *TP53* and *MGRN1* genes, suggested by the data presented in Figure 5A.

A

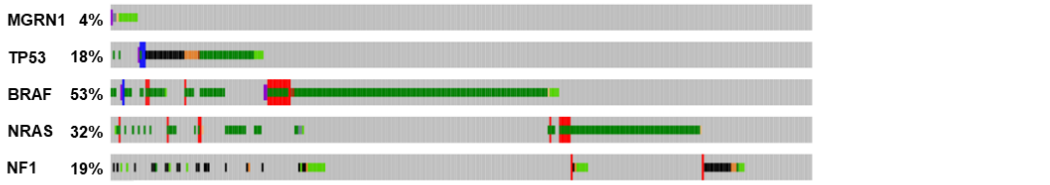

A	B	Neither	A Not B	B Not A	Both	Log2 Odds Ratio	p-Value	q-Value ▲	Tendency
BRAF	NRAS	69	179	101	14	<-3	<0.001	**<0.001**	**Mutual exclusivity**
BRAF	NF1	127	168	43	25	-1.186	0.002	**0.010**	**Mutual exclusivity**
TP53	NF1	247	48	49	19	0.997	0.023	0.075	Co-occurrence
TP53	NRAS	209	39	87	28	0.786	0.036	0.089	Co-occurrence
MGRN1	NF1	286	9	63	5	1.335	0.100	0.200	Co-occurrence
NRAS	NF1	197	98	51	17	-0.578	0.120	0.200	Mutual exclusivity
TP53	BRAF	135	35	161	32	-0.383	0.199	0.284	Mutual exclusivity
MGRN1	BRAF	165	5	184	9	0.691	0.284	0.355	Co-occurrence
MGRN1	NRAS	239	9	110	5	0.272	0.471	0.505	Co-occurrence
MGRN1	TP53	284	12	65	2	-0.458	0.505	0.505	Mutual exclusivity

B

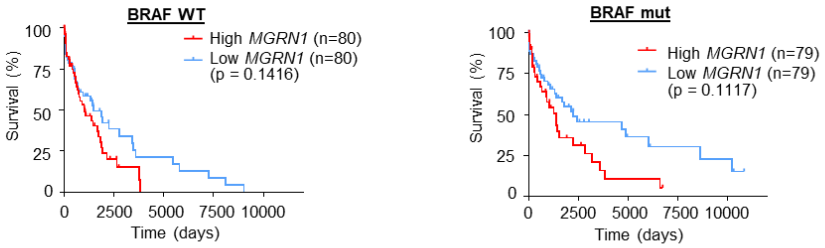

C

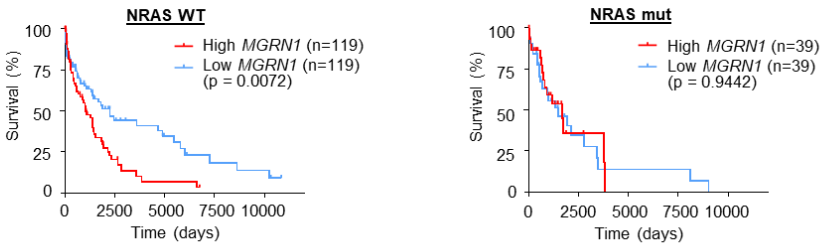

D

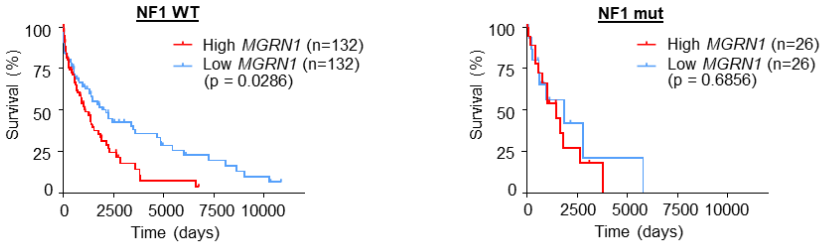

E

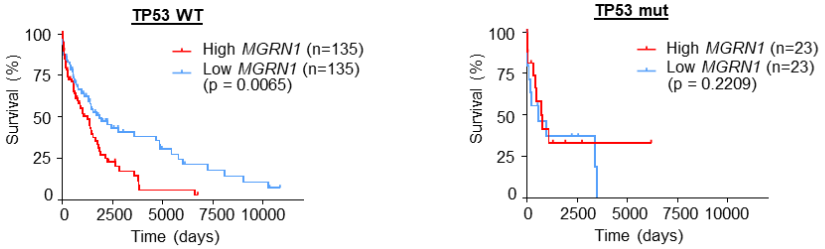

Figure 5. *In silico* analysis of *MGRN1* mutational status and functional interactions with *BRAF*, *NRAS*, *NF1* and *TP53* genes. A) Top: Percentage of somatic mutations in *MGRN1*, *TP53*, *BRAF*, *NRAS* and *NF1* in melanoma human samples of the TCGA dataset from the cBioPortal database (363 melanoma patients). Genetic alteration types are indicated on the graph with a color code. Bottom: Determination of the mutual exclusivity or co-occurrence tendency between mutations in *MGRN1* and selected genes in melanomas. **B)** Kaplan-Meier curves for survival of patients with melanomas (*n* = 158, TCGA cohort from UCSC Xena database) with low or high *MGRN1* expression carrying WT or mutated (mut) forms in *BRAF*, **C)** *NRAS*, **D)** *NF1* and **E)** *TP53* genes. Log-rank (Mantel-Cox) test was used for statistical analysis.

To summarize the findings described in this chapter, we have attempted a preclinical validation of MGRN1 as a modulator of pathological melanocyte biology. For this purpose, we used the data available in public databases (mostly TCGA), as well as two cohorts of clinical samples provided by researchers in the UPV (Bilbao) and LOCE (Brussels). Our study strongly suggests a role of MGRN1 as a determinant of human melanoma aggressiveness, consistent with the results previously presented in Chapter 2 for mouse melanoma. Indeed, our data indicated that:

i) *MGRN1* expression is higher in melanoma than in normal skin or *nevi*.

ii) *MGRN1* is mutated in a subset of melanomas. The rate of *MGRN1* mutations in melanoma is significant and comparable to other cancer-associated genes.

iii) low *MGRN1* expression in melanoma is associated with longer patient survival. In fact, the level of *MGRN1* expression is a good predictor of patient outcome, which compares well with other genes known to influence survival of melanoma patients, such as *TYRP1* (190).

Interestingly, the potentiation of survival afforded by low *TYRP1* expression on one hand, and low *MGRN1* expression on the other appeared to be additive, as shown in Figure 6. Therefore, a low *TYRP1*/low *MGRN1* gene expression profile affords a prediction of favorable clinical outcome of unprecedent statistical power. These data warrant further analysis of *MGRN1* as a clinically useful prognostic marker and underline the need for mechanistic studies to find out the potential molecular basis for the poorer outcome of the disease in patients with melanomas expressing high levels of *MGRN1*.

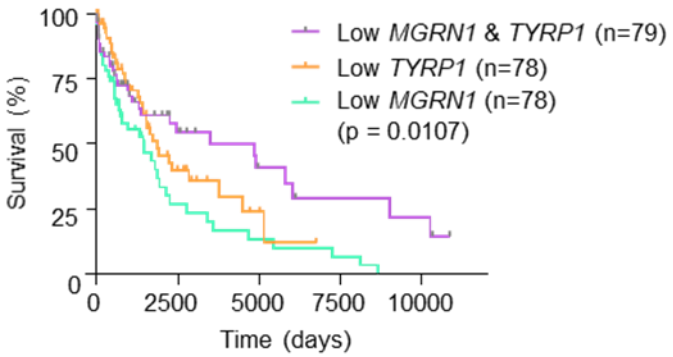

Figure 6. Analysis of survival of melanoma patients with low *MGRN1* and *TYRP1* expression. Kaplan-Meier curve for survival of melanoma patients (TCGA cohort from UCSC Xena database) with low *MGRN1*, *TYRP1* or *MGRN1* and *TYRP1* expression levels (*n* = 78-79 in each case). Log-rank (Mantel-Cox) test was used for statistical analysis**.**

CHAPTER IV

ROLE OF MGRN1 IN GENOMIC INTEGRITY IN HUMAN MELANOMA CELLS

The results presented in previous chapters showed a positive association of *MGRN1* expression in melanoma with a worse prognosis. Moreover, we found that lack of Mgrn1 in mouse melanocytic cells increased genomic instability and the analysis of clinical samples suggested a possible functional relationship between MGRN1 and TP53. Therefore, we decided to study whether MGRN1 deficiency has similar effects on human melanoma cells and its role in the DNA damage response. To this end, we knocked down *MGRN1* expression in HBL cells by CRISPR/Cas9 (Figure 1A). We selected three *MGRN1*-KO clones validated by estimation of MGRN1 protein levels (Figure 1B) and *MGRN1* gene sequencing (Figure 1C). Additionally, we transiently silenced *MGRN1* expression in HBL cells with specific interfering siRNAs (siMGRN1), which almost completely abrogated *MGRN1* gene and protein expression (Figure 1D).

A

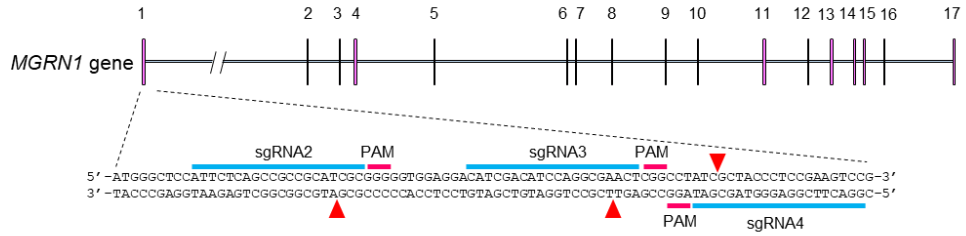

B

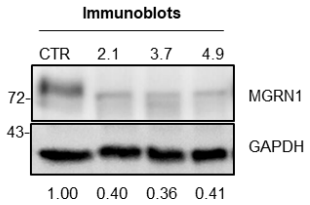

C

sgRNA clones	Edited sequences on MGRN1 exon 1
CTR	Alleles 1 and 2: ^{30}GGG GGT GGA GGA CAT CGA CAT CCA GGC GAA CTC GGC^{65}
3.7	Alleles 1 and 2: ^{30}GGG (GGT GGA GGA CAT CGA CAT CCA GGC GAA CTC G)GC^{65}
CTR	Alleles 1 and 2: ^{10}ATT CTC AGC^{18} ^{70}CGC TAC CCT CCG AAG TCC^{87}
4.9	Alleles 1 and 2: ^{10}ATT CTC ACC^{18} ^{70}CGGC TAC CCT CAG AAG TCC^{87}

D

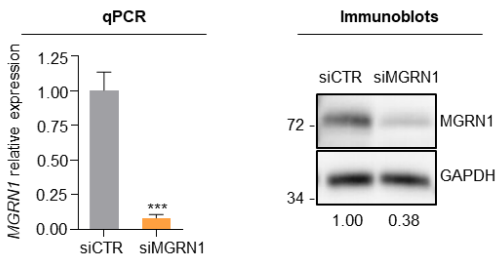

Figure 1. Generation of *MGRN1*-KO clones and validation of *MGRN1* silencing. A) Schematic representation of *MGRN1* gene. Exon 1 sequences targeted by sgRNA oligos for CRISPR/Cas9 (highlighted in blue) are indicated (PAM sequence is represented with a pink bar and cleavages sites with a red triangle). **B)** Representative immunoblots of MGRN1 and GAPDH (as loading control) in control HBL cells and *MGRN1*-KO clones. Quantification of relative protein levels are showed below. **C)** Top: Exon 1 sequence consensus in control (CTR) HBL cells and edited sequences on *MGRN1* exon 1 in *MGRN1*-KO clones 3.7 and 4.9. Deleted nucleotides are shown between brackets in red, replaced nucleotides in red and inserted nucleotides are indicated in green. Bottom: amino acid sequence of the resulting truncated MGRN1 protein in *MGRN1*-KO clones. **D)** Left: *MGRN1* expression levels analyzed by qPCR in control (siCTR) and transiently silenced HBL cells (siMGRN1). Graph shows mean ± SEM and t-test was used for statistical analysis (***, $p < 0.001$). Right: Representative immunoblots of MGRN1 and GAPDH (as loading control) in control and transiently silenced HBL cells. Quantification of relative protein levels are showed below.

Aberrant cell cycle progression and increased DNA damage in MGRN1-deficient human melanoma cells

To determine if the MGRN1-deficient phenotype in human melanoma cells was consistent with our previous results in mouse melanocytes, we analyzed cell cycle progression and DNA damage in control and MGRN1-depleted cells using asynchronous cultures. In agreement with our previous observations, we observed an increased S phase population following depletion of MGRN1 by transfection with siMGRN1, compared with cells transfected with a control scrambled siRNA (siCTR, Figure 2A). We also found a two-fold increase in the G2/M population for cells depleted of MGRN1. In accordance, MGRN1-deficient cells showed a significant decrease in EdU incorporation into DNA (Figure 2B), indicating that MGRN1 depletion might impair cellular proliferation.

However, no consistent alteration of cell cycle profiles was observed in *MGRN1*-KO stable clones generated by CRISPR/Cas9 (Figure 2C). This suggested the induction of functionally redundant protein(s) and/or compensatory mechanism(s) that may become operative upon prolonged depletion of MGRN1, but that would not function upon acute downregulation of MGRN1, i.e. in short-term experiments performed with siRNA.

To further explore the effect of MGRN1 depletion on cell cycle progression, we analyzed the kinetics of DNA synthesis by pulse-chase experiments. Cells were pulsed with BrdU for 1 hour, washed, and chased for up to 6 hours. Then they were analyzed by FACS for BrdU incorporation and for total DNA (with PI). Mitotic cells were considered those with a 4n total DNA content, and post-mitotic cells the BrdU-positive cells with 2n total DNA. As shown in Figure 2D, MGRN1-depleted cells showed a higher percentage of mitotic cells, whereas control cells showed a higher percentage of post-mitotic cells (BrdU-labeled and 2n total DNA). This was consistent with the previously observed aberrant

cell cycle profiles, with accumulation of cells in the G2/M phase. Therefore, acute depletion of MGRN1 in human melanoma cells induced an aberrant cell cycle progression, as previously shown for mouse melanocytes and melanoma cells.

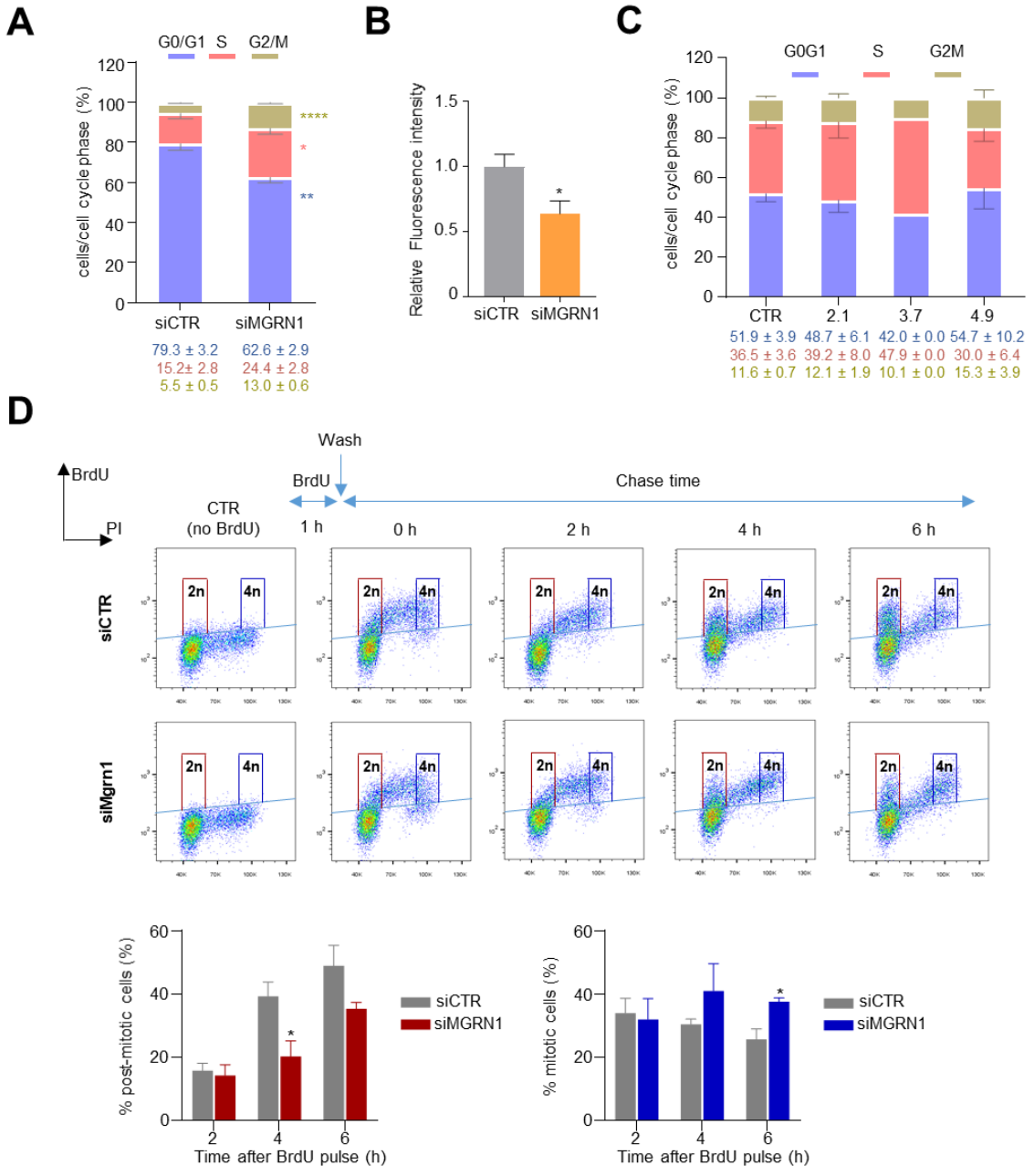

Figure 2. Cell cycle progression in cells lacking MGRN1. A) Cell cycle analysis of propidium iodide (PI)-stained control and *MGRN1*- silenced HBL cells indicating the percentage of cells in each cell cycle phase (G0/G1 in blue, S in red and G2/M in brown). Results are the mean ± SEM. T-test was used for statistical analysis. **B)** EdU incorporation in HBL control and transiently silenced cells using the Click-iT® EdU Microplate Assay kit. The graph shows mean ± SEM. T-test was used for statistical analysis. **C)** Cell cycle analysis of control and *MGRN1*-KO HBL cells treated as in A. Results are the mean ± SEM. One-way ANOVA was used for statistical analysis. **D)** Pulse-chase analysis of cell cycle progression in PI-stained control and *MGRN1* transiently silenced HBL cells. Cells were pulsed with BrdU (20 μM, 1 h), washed and

chased for 2, 4 or 6 h. Top: Plots of BrdU intensity vs. DNA content (PI stain). BrdU-positive cells are subdivided according to their DNA content in 2n (post-mitotic cells) and 4n (mitotic cells), using the gating scheme indicated by boxes. Bottom: Percentage of post-mitotic and mitotic cells analyzed by FACS. Graph shows mean ± SEM. Two-way ANOVA was used for statistical analysis. *, $p < 0.05$, **, $p < 0.01$, ***, $p < 0.001$ and ****, $p < 0.0001$.

To assess the occurrence of DNA damage in *MGRN1*-deficient cells, we analyzed the presence of the phosphorylated form of histone H2AX (γ-H2AX) using an immunocytochemical technique. H2AX is quickly phosphorylated in response to DNA damage, forming nuclear foci near DSBs required for recognition and repair of the breaks (207). The presence of these foci is commonly accepted as a marker of DNA DSBs. HBL MGRN1-depleted cells and *MGRN1*-KO clones presented significantly higher levels of γ-H2AX labeling compared with control cells, suggesting a higher presence of DSBs in the absence of MGRN1 (Figure 3A).

Additionally, H2AX phosphorylation has been described in response to single-strand DNA breaks, replication stress, apoptotic DNA fragmentation and during DNA replication or progression through mitosis (207). Therefore, as a complement to γ-H2AX analysis, we used the comet assay to assess DNA damage. The comet assay in alkali conditions is employed to evaluate DSBs and SSBs, while the neutral comet assay exclusively detects DSBs (208). Quantitative tail moment measurements in alkaline comet assays revealed a higher abundance of DNA breaks in *MGRN1*-depleted cells and *MGRN1*-KO clones (Figure 3B), consistent with γ-H2AX labeling. We compared these data with results obtained by neutral comet assays, for HBL cells transfected with siCTR or siMGRN1. This comparison suggested that many of the DNA breaks induced by MGRN1 deficiency were SSBs, since the differences in tail moment were smaller in the neutral assay (that does not detect SSBs) compared with the alkaline assay.

Furthermore, analysis of 8-oxodG levels indicated higher levels of oxidative DNA damage in MGRN1-depleted cells compared with control cells (Figure 3C), consistent with a higher oxidative stress in MGRN1-deficient cells, maybe as a result of mitochondrial dysfunction (132, 183). However, the small difference in the 8-oxodG signal suggested that oxidative damage by itself might not explain the higher difference of strand breaks abundance in *MGRN1*-silenced cells.

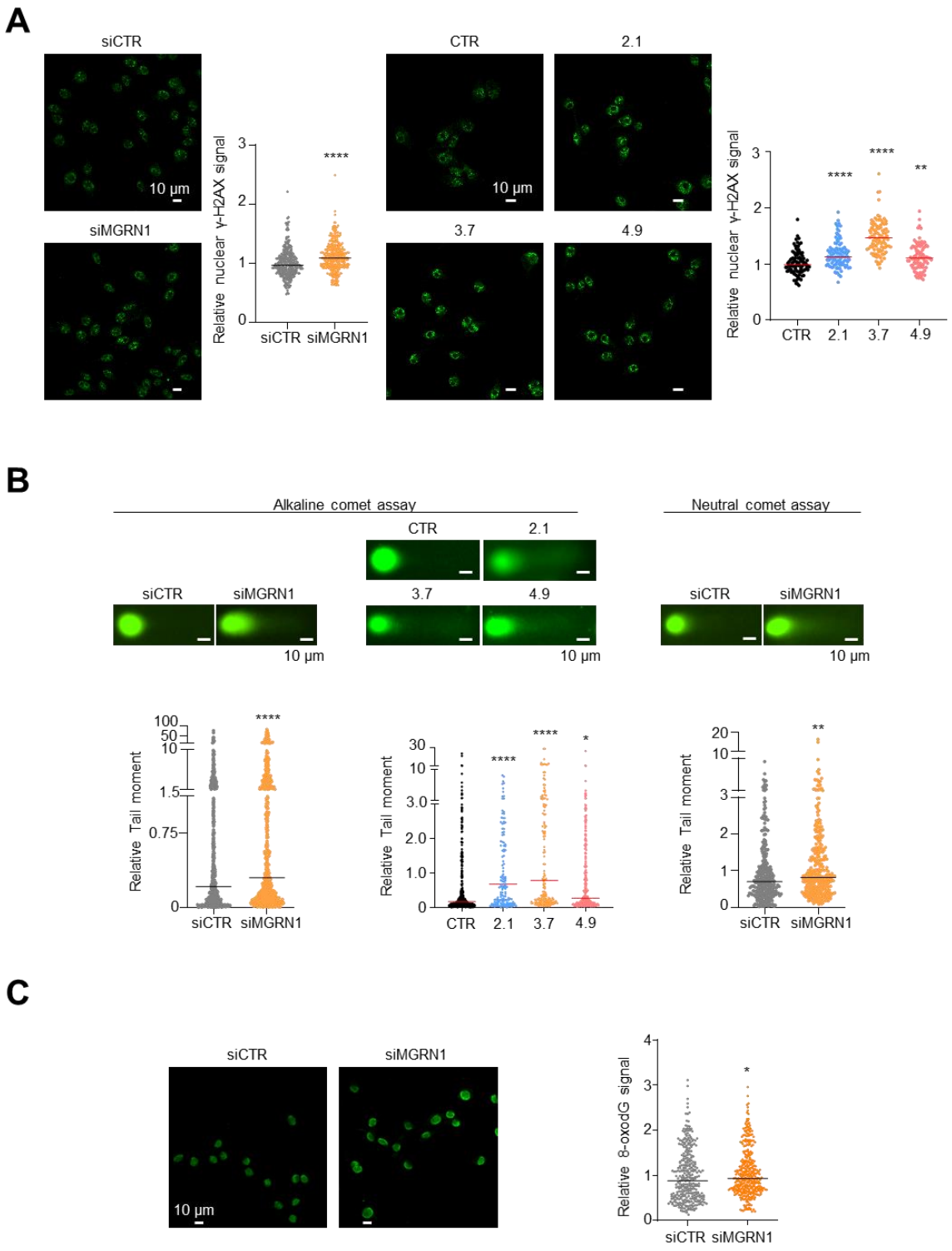

Figure 3. DNA damage in control and MGRN1-deficient cells. A) Representative images of cells immunostained for γ-H2AX and quantification of γ-H2AX staining intensity in control and *MGRN1*-silenced cells (left) and in *MGRN1*-KO clones and control cells (right). **B)** Alkaline (left) and neutral comet assays (right) performed to detect DNA breaks in control cells, *MGRN1*-silenced cells and *MGRN1*-KO clones. Representative images of comets are displayed over graphs showing the median of tail moments, analyzed using CASPLAB software. **C)** 8-oxodG staining in control and *MGRN1*-silenced cells. Micrographs show

nuclear staining of 8-oxodG and the graph shows the median of 8-oxodG intensity (right). *, $p < 0.05$, **, $p < 0.01$, ***, $p < 0.001$ and ****, $p < 0.0001$.

Replication stress likely contributed to the DNA breaks burden in MGRN1-deficient cells

In kinetic terms, the accumulation of DNA breaks observed in MGRN1-depleted cells could result from a lower rate of repair and/or a higher rate of formation. To explore these possibilities, we analyzed the kinetics of DSB repair and the susceptibility of cells to genotoxic agents. Control and MGRN1-depleted cells were treated with neocarzinostatin (NCS, 1 h at 0.5 µg/ml final concentration) and allowed to recover in NCS-free medium for up to 24 h. NCS is an antibiotic used in cancer chemotherapy to induce DNA DSBs (209, 210). Immediately after the NCS challenge, i.e. at recovery time 0 h, MGRN1-depleted cells and control cells exhibited a similar DNA fragmentation as shown by comet tail measurements, thus suggesting that downregulation of MGRN1 did not augment the susceptibility to NCS treatment. Moreover, after 24 h of recovery in NCS-free medium, comet tails were also similar in MGRN1-deficient cells and control cells, indicating a comparable extent of clearance of DNA breaks. However, we found a slight delay in repair kinetics at shorter recovery times (6 h) upon repression of MGRN1 (Figure 4A). Similar results were obtained for γ-H2AX labeling in *MGRN1*-KO clones. Treatment with NCS significantly increased γ-H2AX nuclear intensity (Figure 4B) but absence of MGRN1 did not cause a higher sensitivity to NCS-induced damage as measured by the fold increase in γ-H2AX staining in NCS-treated cells relative to their corresponding controls (Figure 4C). Curiously, while one of the *MGRN1*-KO clones (clone 2.1) showed a slightly higher susceptibility to damage, clone 3.7 exhibited even less damage compared to control and 2.1 cells (Figure 4C).

In summary, the data in Figure 4 suggested that downregulation or abrogation of MGRN1 expression did not increase the susceptibility of HBL human melanoma cells to an exogenous genotoxic agent, nor did it block DNA repair. However, these data did not exclude a slight impairment of the repair pathways involved in DNA break clearance.

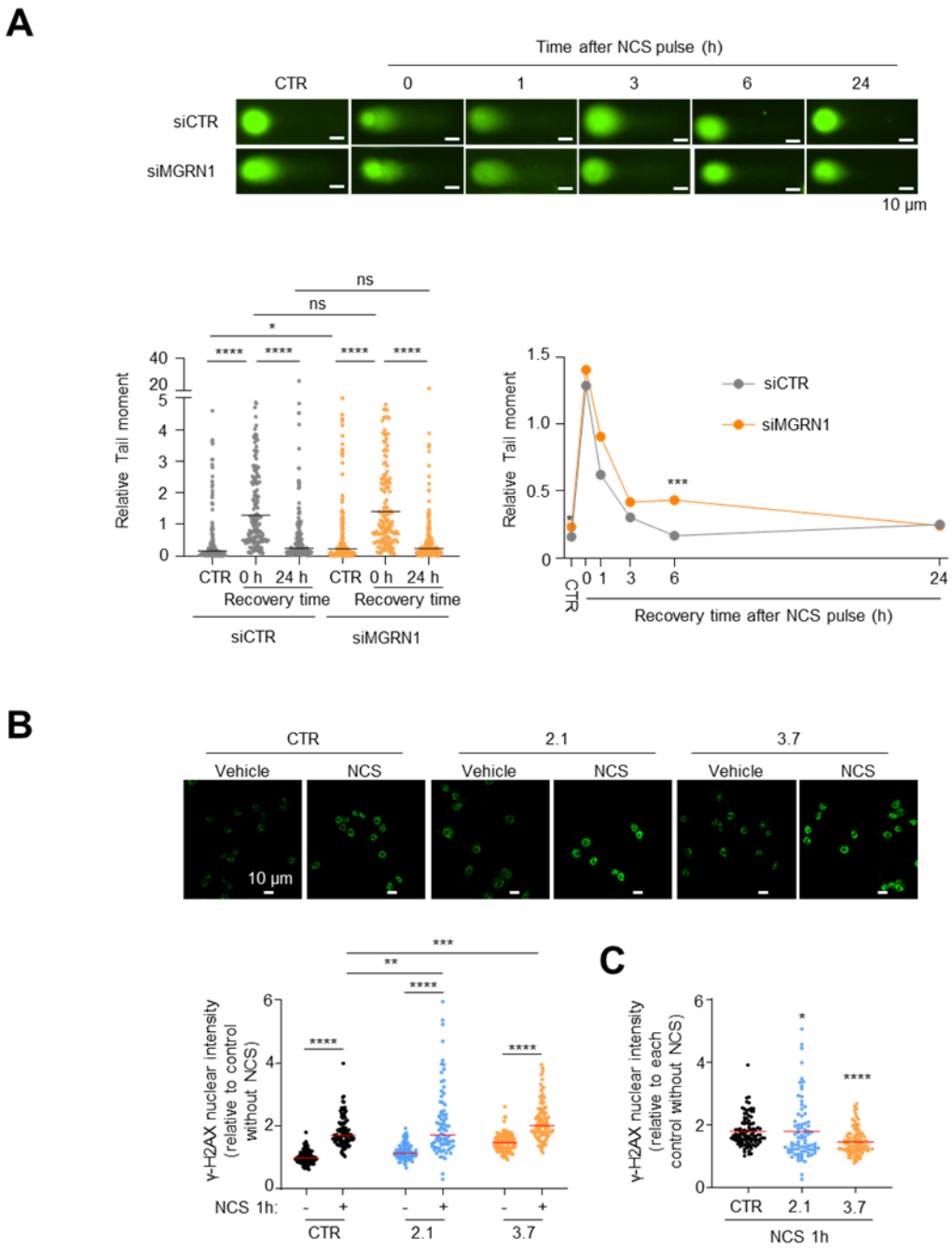

Figure 4. Kinetics of DSBs repair and susceptibility to genotoxic agents in control and MGRN1-depleted cells. A) Alkaline comet assay of control and *MGRN1*-silenced cells treated with neocarzinostatin (NCS) for 1 h at 0.5 µg/ml and allowed to recover in NCS-free medium for up to 24 h. Representative images of comet assays are displayed above graphs showing the median of tail moments analyzed using CASPLAB at the indicated times of recovery. **B)** γ-H2AX immunostaining in control and *MGRN1*-KO cells with and without NCS treatment (1 h, 0.5 µg/ml). Representative micrographs show γ-H2AX nuclear foci in green. Graphs plot the median of γ-H2AX nuclear intensity relative to control MGRN1- expressing cells without NCS or **C)** relative to the control intensity of each clone without NCS. *, $p < 0.05$, **, $p < 0.01$, ***, $p < 0.001$ and ****, $p < 0.0001$.

In addition to external insults such as genotoxic agents, DNA damage can be produced endogenously. A major source of endogenous DNA damage is replication. Due to various natural impediments, replication forks can slow down or even stop their progression, a phenomenon known as DNA replication stress (211). DNA damage is induced when cells are unable to adequately stabilize stalled replication forks, thus contributing to genomic instability (171). Replication stress can be induced by agents that promote replication fork stalling, such as hydroxyurea (HU), a ribonucleotide reductase inhibitor that depletes the cellular pool of dNTPs. Most replication forks restart their progression when released from a short HU-induced replication block (182). In contrast, if replication forks are unable to resume progression, they can collapse, thus producing DNA breaks (212). Considering these effects of HU, we analyzed DNA breaks formation in response to replication stress generated by HU (2 mM, 6 h), in the presence or absence of MGRN1, by using alkaline comet assays. As expected from previous experiments, in the absence of HU MGRN1-depleted cells displayed a higher burden of DNA breaks than controls (Figure 5A). Moreover, a 6 h treatment with HU did not result in further accumulation of DNA breaks, neither in cells treated with siCTR nor in cells deprived of MGRN1 by transfection with siMGRN1. However, 24 h after release, MGRN1-depleted cells showed a significant increase in DNA breaks compared with control cells. It is worth noting that we also observed a trend for increased DNA breaks in control cells 24 h after HU clearance. This trend was not statistically significant using the Kruskal-Wallis analysis (Figure 5A), but it reached significance when it was analyzed by Mann-withney ($p < 0.0147$).

To further characterize the presence of DNA break in control or MGRN1-depleted cells treated with HU, we performed the comet assay under neutral conditions to detect DSBs exclusively. The results showed that stalling replication forks by HU treatment did not augment the amount of DSBs in control or MGRN1-depleted cells immediately after the 6 h HU challenge (Figure 5B), just as it did not increase the number of total breaks detected by the alkaline assay. Therefore, it would appear that the 6 h HU treatment did not cause the collapse of stalled forks and their processing to DSBs. However, 24 h after release from the HU block, the abundance of DSBs was significantly higher in MGRN1-deprived cells than in control cells, although the difference was much smaller than the one observed for the alkaline assay. These results confirmed the presence of an excess DNA breaks in MGRN1-depleted cells treated with HU and allowed to recover for 24 h. They also suggested that this excess might mostly correspond to an accumulation of SSBs in response to HU-induced replicative stress. Likely, this accumulation of SSBs

may be partially due to an inability to restart stalled replication forks in the absence of MGRN1.

As previously mentioned, H2AX can be phosphorylated not only in response to DSBs induction, but also in response to SSBs and during replication stress (207), and it has been shown that during HU-induced blocks γ-H2AX rapidly accumulates and labels extensive SSBs regions at stalled replication forks, before DSB formation (182, 213). We compared γ-H2AX immunostaining in control and MGRN1-depleted cells treated for 6 h with HU, immediately after release or 24 h after removal of HU (Figure 5C). These measurements confirmed higher γ-H2AX labeling in siMGRN1-treated cells compared with controls in the absence of HU (control conditions). On the other hand, immediately after removal of the stalling agent (recovery time 0 h), γ-H2AX was also slightly but significantly higher in MGRN1-depleted cells. Surprisingly, 24 h after removal of HU, we found comparable γ-H2AX labeling in control and MGRN1-depleted cells. This was in contrast with the significantly higher incidence of DNA breaks in MGRN1-depleted cells detected by comet assays.

In summary, in the absence of an external perturbation, MGRN1-depleted cells showed significantly higher levels of both DNA breaks and γ-H2AX, confirming the data presented in Figure 3. Upon HU-induced replicative stress, MGRN1-deprived cells accumulated more DNA breaks than control cells, particularly 24 h after release from the HU block. Nevertheless, at this recovery time γ-H2AX staining was comparable for cells transfected with siMGRN1 and control cells transfected with siCTR. These results suggested that absence of MGRN1 may intensify fork stalling upon HU-induced replication stress and/or impair the stabilization and restart of stalled forks during release from the HU block. On the other hand, a possible explanation for the paradoxical findings of increased number of DNA breaks but similar γ-H2AX staining 24 h after recovery from the HU block might be inefficient H2AX phosphorylation in the absence of MGRN1.

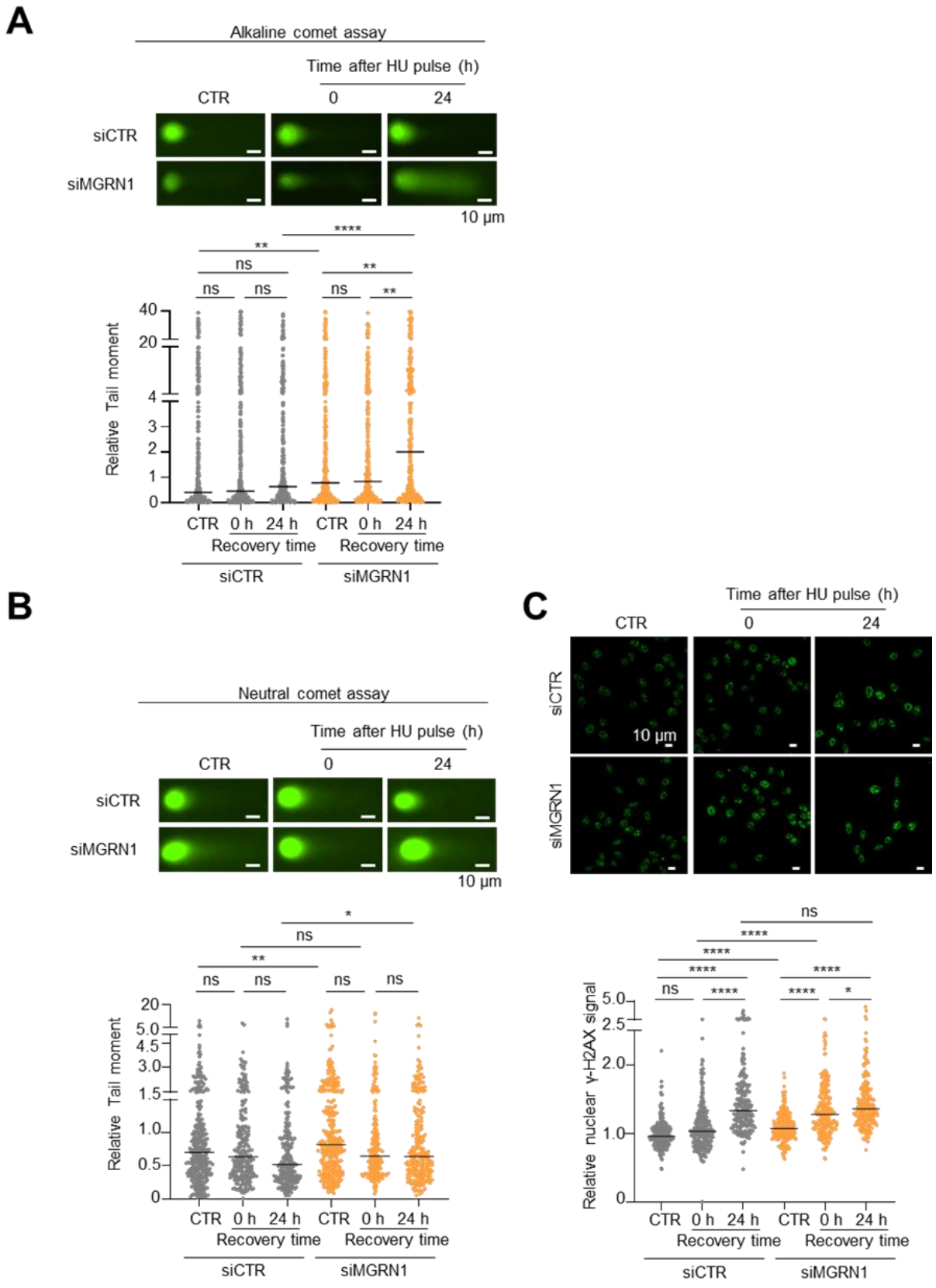

Figure 5. Kinetics of DNA breaks formation upon HU-induced replication stress in control and MGRN1-depleted cells. A) Alkaline comet assay of control and siMGRN1-treated cells challenged with HU (6 h at 2 mM) and allowed to recover in HU-free medium for 24 h. Representative images of comet assays

and plots of the median tail moment at recovery times 0 and 24 h. **B)** Neutral comet assay performed as above. **C)** γ-H2AX immunostaining of cells treated as above. Representative micrographs show γ-H2AX nuclear foci in green. Graph shows the median of γ-H2AX stain intensity relative to control cells. *, $p < 0.05$, **, $p < 0.01$, ***, $p < 0.001$ and ****, $p < 0.0001$.

To further study a possible role of MGRN1 in the progression of replication forks, we performed DNA fiber assays (Figure 6). This assay allows the analysis of individual DNA fibers labeled with two consecutive pulses of the nucleotides IdU (5-Iodo-20-deoxyuridine) and CldU (5-Chloro-20-deoxyuridine). The technique provides information on the rate of DNA synthesis at individual replication forks, on the presence of new origins of replication and on stalled/collapsed forks (171). The experimental setup is summarized in Figure 6A. After a first pulse of IdU (25 µM, 20 min), cells were washed, HU (2 mM, 2 h) was added when required, then washed and pulsed again with CldU (100 µM, 20 min). The halogenated nucleotides were then labeled in red (IdU) or green (CldU) with suitable antibodies and the fibers were visualized using a confocal microscope. Representative images are shown in Figure 6A.

First, to determine if absence of MGRN1 augmented the incidence of stopped or collapsed forks, we analyzed DNA fibers that had not incorporated the second label, i.e. CldU (Figure 6B). In agreement with the previous results, we detected increased replication fork stalling in MGRN1-deficient cells compared with control cells. This increase was similar to that observed in control cells after 2 h of treatment with 2 mM HU. The detection of significantly more stalled forks after treating cells expressing normal levels of MGRN1 with HU provided a convenient internal positive control for the experiment. Of note, the effect on fork stalling of MGRN1 downregulation or HU treatment were quantitatively similar.

We were also interested in studying the elongation rate in control and MGRN1-deficient cells by measuring the length of fibers (1 micrometer ~ 2.59 kilobases) (Figure 6C). No significant differences were found in elongation rates between control and *MGRN1*-silenced cells, neither in basal conditions nor in response to HU-induced replicative stress. As expected, we observed a lower rate of incorporation of the label in HU-treated cells regardless of the presence or absence of MGRN1, again providing a positive control for the technique. Moreover, no alteration was found in the number of new origins (DNA fiber composed only of CldU) among the experimental groups (Figure 6D).

Collectively, these results suggested that while the lack of MGRN1 most likely induced replication fork stalling, MGRN1 did not seem to play an important role in regulating the DNA elongation rate in progressing forks or in activating new replication origins.

Lastly, we studied the presence of stalled forks in *MGRN1*-KO clones (Figure 6E). *MGRN1*-KO cells also exhibited a trend to a greater number of stalled forks than control cells under basal conditions. Moreover, upon HU treatment the number of stalled forks increased in control cells but produced only minor, if any, changes in *MGRN1*-KO cells. These results basically recapitulated those obtained for *MGRN1*-silenced cells and further suggested that absence of MGRN1 expression promoted fork stalling. A causal relationship between this effect and the higher levels of DNA damage in MGRN1-deprived or null cells seems very likely, but this association remains to be formally established.

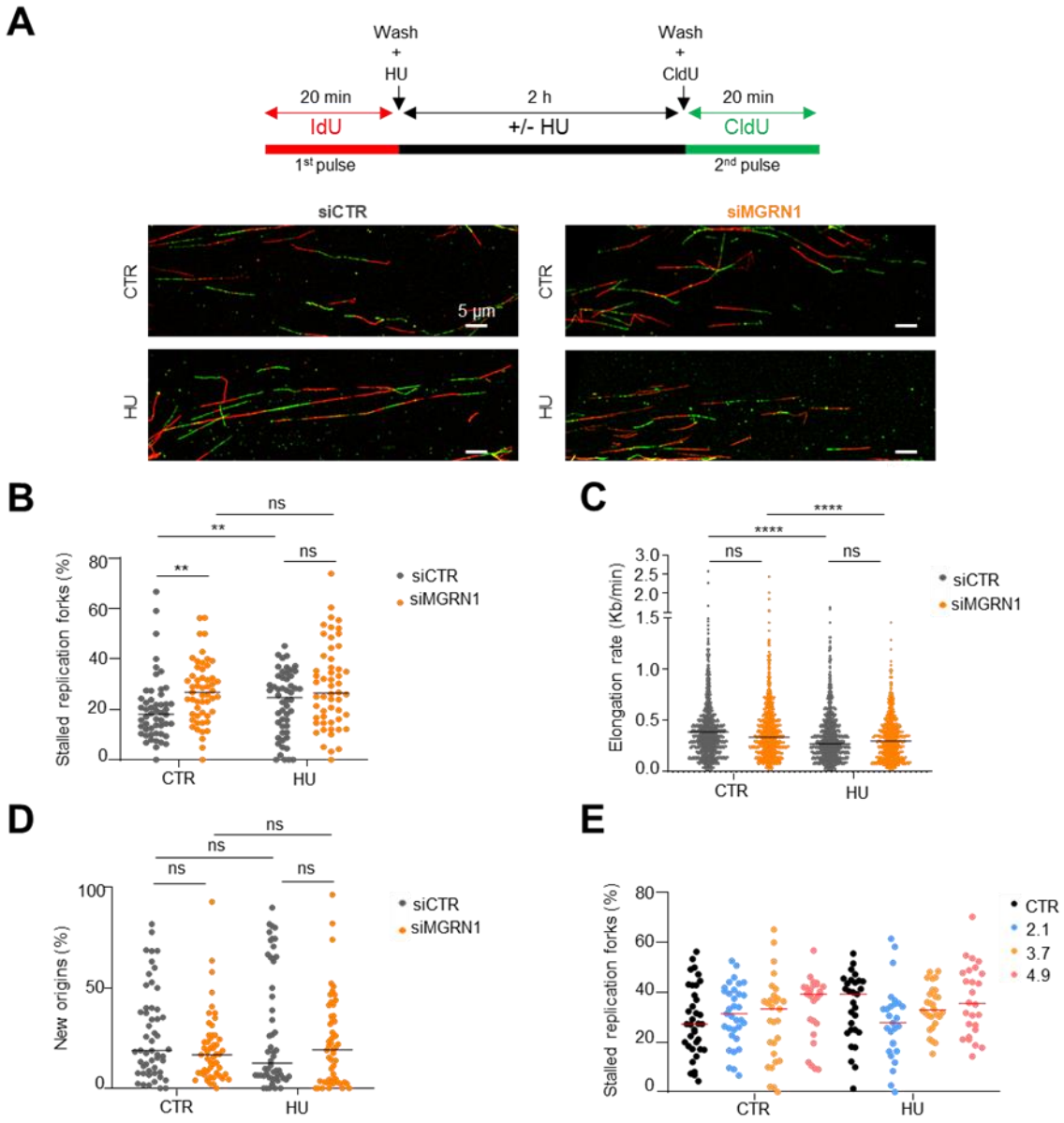

Figure 6. DNA fiber assay in control (CTR) and HU-treated cells. A) Top: Schematic representation of the pulse-chase protocol. Bottom: Representative confocal images of DNA fibers in control and *MGRN1*-

silenced cells with and without HU treatment (2 h at 2 mM). **B)** Quantification of stalled, **C)** elongation rates and **D)** incidence of new replication origins, in the experimental conditions described above. **E)** Quantification of stalled forks in control and *MGRN1*-KO clones with and without HU treatment. No significant changes were found. Graphs show the median percentage of stalled forks, new origins or median elongation rate analyzed using FiberQ software. * $p < 0.05$, **, $p < 0.01$, ***, $p < 0.001$ and ****, $p < 0.0001$.

Impaired activation of the ATR-CHK1 signaling axis in cells lacking MGRN1

To prevent or reduce the adverse effect of replication stress on the fidelity of DNA replication, cells activate replication stress response pathways. These pathways consist of highly regulated and coordinated mechanisms that allow cells to preserve the stability and functionality of disturbed replication forks (171). The replication stress response is primarily mediated by the ataxia-telangiectasia-mutated and Rad3-related (ATR) kinase. Activation of ATR followed by ATR-mediated phosphorylation and activation of its main effector, the checkpoint kinase 1 (CHK1), lead to several events, including stabilization and restart of replication forks, inhibition of origin firing, retardation of cell cycle progression and induction of DNA damage repair (214). Additionally, ATR phosphorylates TP53 at Ser15 (215), to mediate transient cell cycle arrest.

Since lack of MGRN1 apparently increased cellular replication stress, we analyzed the activation of the replication stress response in control and MGRN1-deprived cells. To this end, cells were treated with HU (2 mM, 4 h) and the levels and phosphorylation status of the main proteins that participate in this pathway were determined at 0, 1, 3 and 5 h after release from HU. Considering the fact that ATR phosphorylation in Thr1989 requires ATR activation but is not essential for downstream signaling (216, 217), we studied the activation of ATR-CHK1 pathway by using the activating CHK1 phosphorylation at Ser317 as a reporter. Our data indicated a trend towards impaired ATR phosphorylation at Thr1989, that did not reach statistical significance, and a statistically significant reduction of active p-CHK1 (Ser317) in HU-treated MGRN1-depleted cells compared with HU-treated control cells (Figure 7). Consistent with these data we also observed reduced levels of TP53 phosphorylation at Ser15 in the absence of MGRN1.

In parallel to ATR, ataxia-telangiectasia-mutated (ATM) controls the DNA damage response through its main effector CHK2 (218). Although ATM is primarily activated by DSBs in DNA, it is known that ATR can activate ATM by phosphorylation at Ser1981 upon replication fork stalling (218). Interestingly, we also found an obvious trend towards lower levels of ATM phosphorylation at Ser1981 in *MGRN1*-depleted cells after the HU pulse. Although the decrease in ATM phosphorylation in MGRN1-depleted cells did not reach statistical significance in our experimental setup, the trend was clear and

consistently found in all the timepoints analyzed. Thus, statistical significance would likely be reached with additional biological replicates. Nevertheless, the presumedly ATM-specific CHK2 phosphorylation at Thr68 was similar in cells with normal or reduced MGRN1 expression. This phosphorylation of CHK2 has an overlapping role with CHK1 in induction of G2/M arrest (218). In brief, these results indicated that MGRN1 was required for adequate activation of the ATR-CHK1-TP53 signaling axis in response to replication stress. This pathway is essential for stabilization and resumption of stalled replication forks among other important functions. Therefore, inefficient activation of this pathway is fully consistent with our previous observations suggesting numbers of stalled forks in MGRN1-deprived cells.

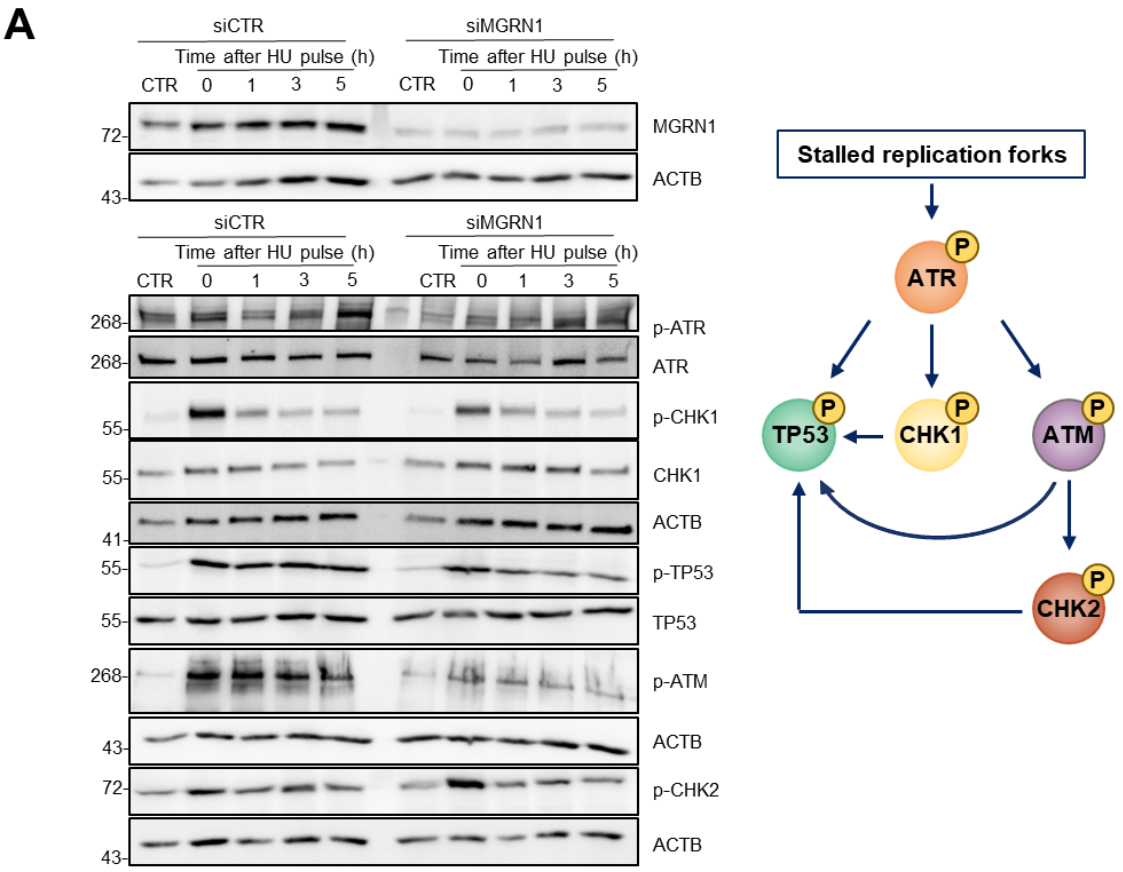
A
siCTR
siMGRN1
Time after HU pulse (h)
CTR 0 1 3 5
72-
43-
MGRN1
ACTB
268-
268-
55-
55-
41-
55-
55-
268-
43-
72-
43-
p-ATR
ATR
p-CHK1
CHK1
ACTB
p-TP53
TP53
p-ATM
ACTB
p-CHK2
ACTB
Stalled replication forks
ATR
TP53
CHK1
ATM
CHK2
P

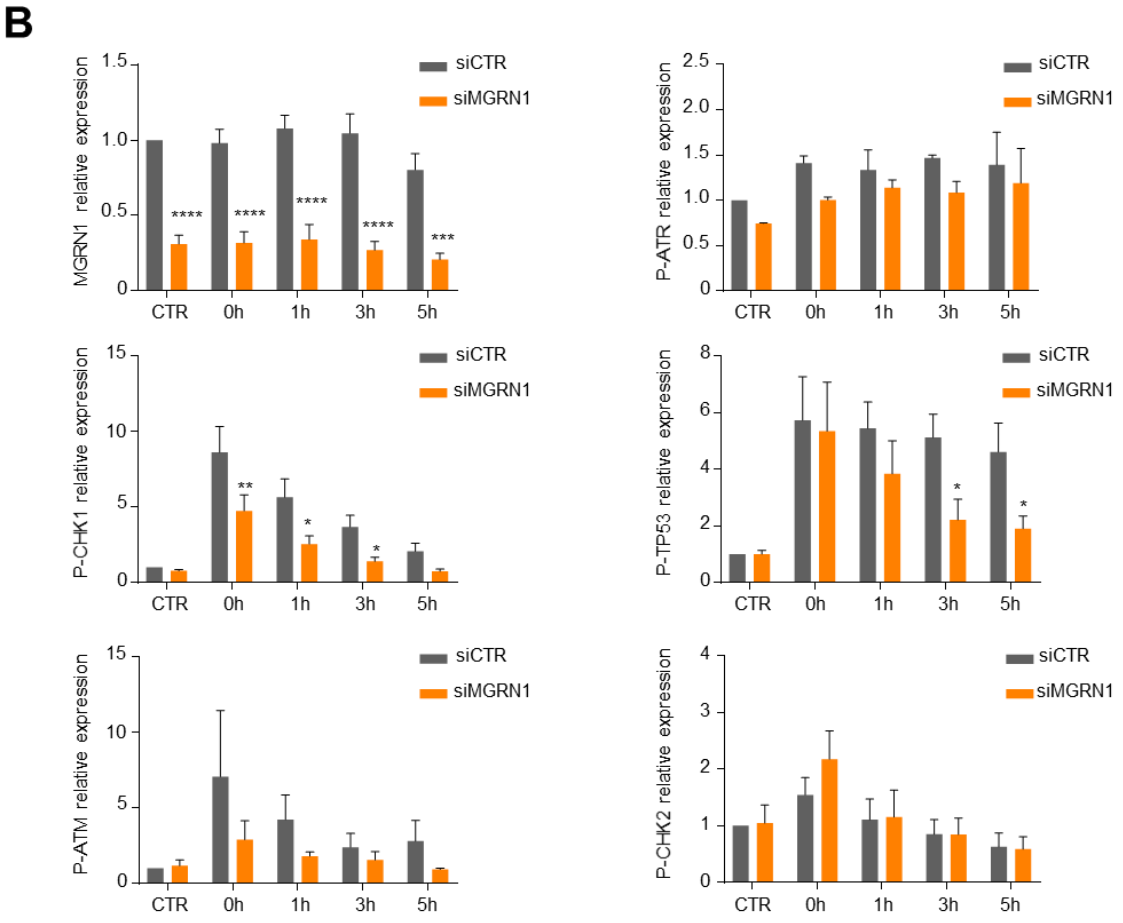
B
MGRN1 relative expression
P-ATR relative expression
P-CHK1 relative expression
P-TP53 relative expression
P-ATM relative expression
P-CHK2 relative expression
siCTR
siMGRN1
CTR
0h
1h
3h
5h

Figure 7. Analysis of the HU-induced replication stress response in *MGRN1*-silenced and control cells. A) Left: Representative immunoblots of p-ATR (Thr1989), ATR, p-CHK1 (Ser317), CHK1, p-TP53 (Ser15), TP53, p-ATM (Ser1981) and p-CHK2 (Thr68). Proteins were extracted from control (siCTR) and *MGRN1*-silenced (siMGRN1) cells without (CTR) or with an HU pulse (2 mM, 4 h) at different times after release. A MGRN1 blot is shown as a control for efficient silencing and ACTB as loading control. Right: Simplified scheme of the replication stress response pathway. **B)** Relative intensity of the protein specific bands normalized to control cells without HU. Results given as mean ± SEM. Two-way ANOVA was used for statistical analysis. *, $p < 0.05$, **, $p < 0.01$, ***, $p < 0.001$ and ****, $p < 0.0001$.

After having verified that MGRN1 modulates the replication stress response, we wondered whether MGRN1 might also play a role in the response to DNA damage induced by exogenous genotoxic agents. Neocarzinostatin (NCS) is a clastogenic drug that mediates the formation of DSBs in DNA. For control and *MGRN1*-silenced cells, we analyzed the response to DSBs induced by NCS (0.5 µg/ml, 1 h) at different times after removal of NCS. According to the literature, ATM is activated in response to DSBs in DNA by autophosphorylation at Ser1981, and active ATM catalyzes the activatory phosphorylation of CHK2 (214). Therefore, we measured the levels of phosphorylation of ATM at Ser1981 and the phosphorylation of CHK2 at Thr68 downstream of ATM. Moreover, since both ATM and CHK2 phosphorylate TP53 at Ser15 (215), we also analyzed this phosphorylation event. We did not find significant differences in ATM, CHK2 or TP53 phosphorylation levels between MGRN1-depleted and control cells treated with NCS (Figure 8).

Following DSB formation, activation of ATM signaling produces single-stranded DNA regions (ssDNA), which activate ATR signaling (218). In agreement with the similar activation of ATM and CHK2, the ATR-CHK1 axis was efficiently and comparably activated by NCS treatment in control and MGRN1-deprived cells. Therefore, absence of MGRN1 was compatible with normal activation of the ATR-CHK1 pathway in cells treated with an exogenous clastogenic agent. Moreover, the normal activation of both ATM and ATR signaling in MGRN1-deprived cells treated with NCS was fully consistent with the normal repair of NCS-induced DNA damage summarized in Figure 4 of this chapter.

In summary, inefficient CHK1 activation found in MGRN1-depleted cells in response to HU appeared specifically related with a deficient activation of the replicative stress response, rather than being a consequence of an intrinsic pathway malfunctioning, since the ATR-CHK1 pathway was normally activated in response to NCS-induced DSBs.

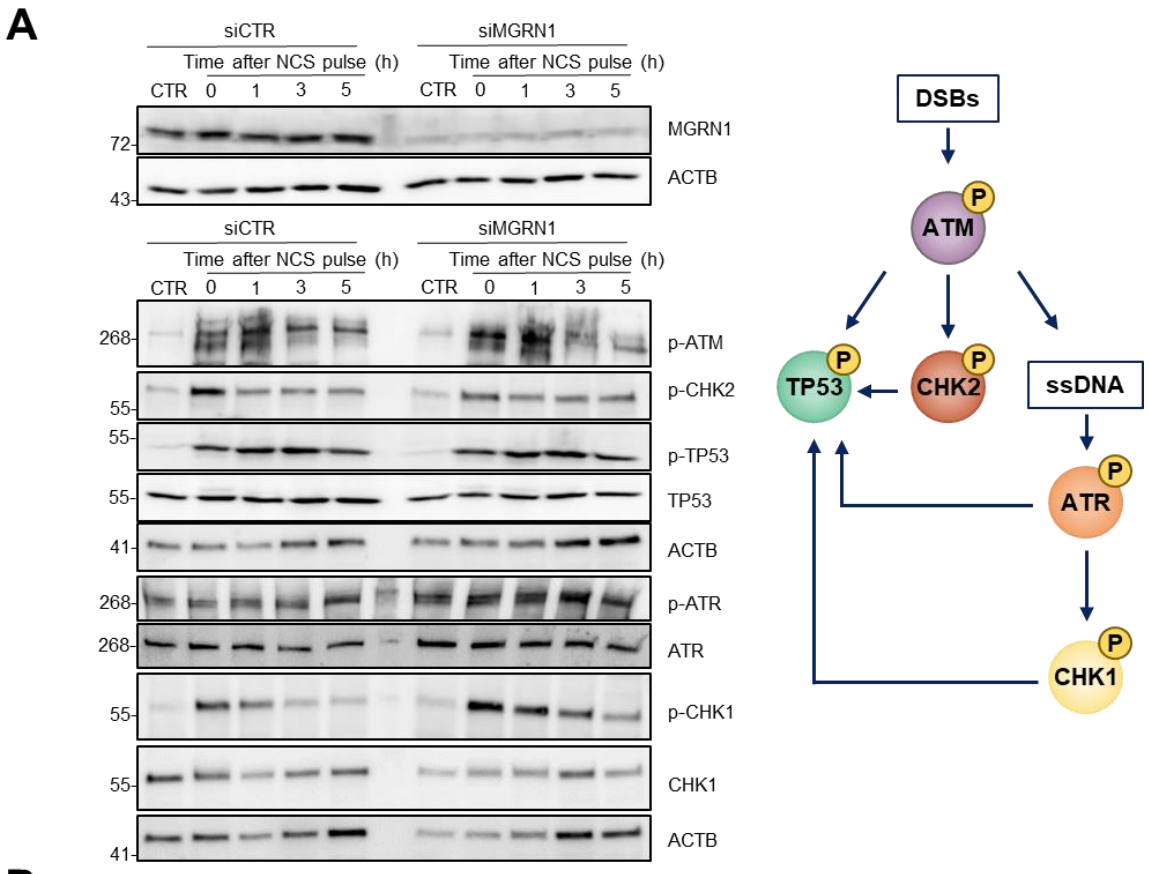
A
siCTR
siMGRN1
Time after NCS pulse (h)
CTR 0 1 3 5
72
43
MGRN1
ACTB
268
55
55
55
41
268
268
55
55
41
p-ATM
p-CHK2
p-TP53
TP53
ACTB
p-ATR
ATR
p-CHK1
CHK1
ACTB
DSBs
ATM
TP53
CHK2
ssDNA
ATR
CHK1
P

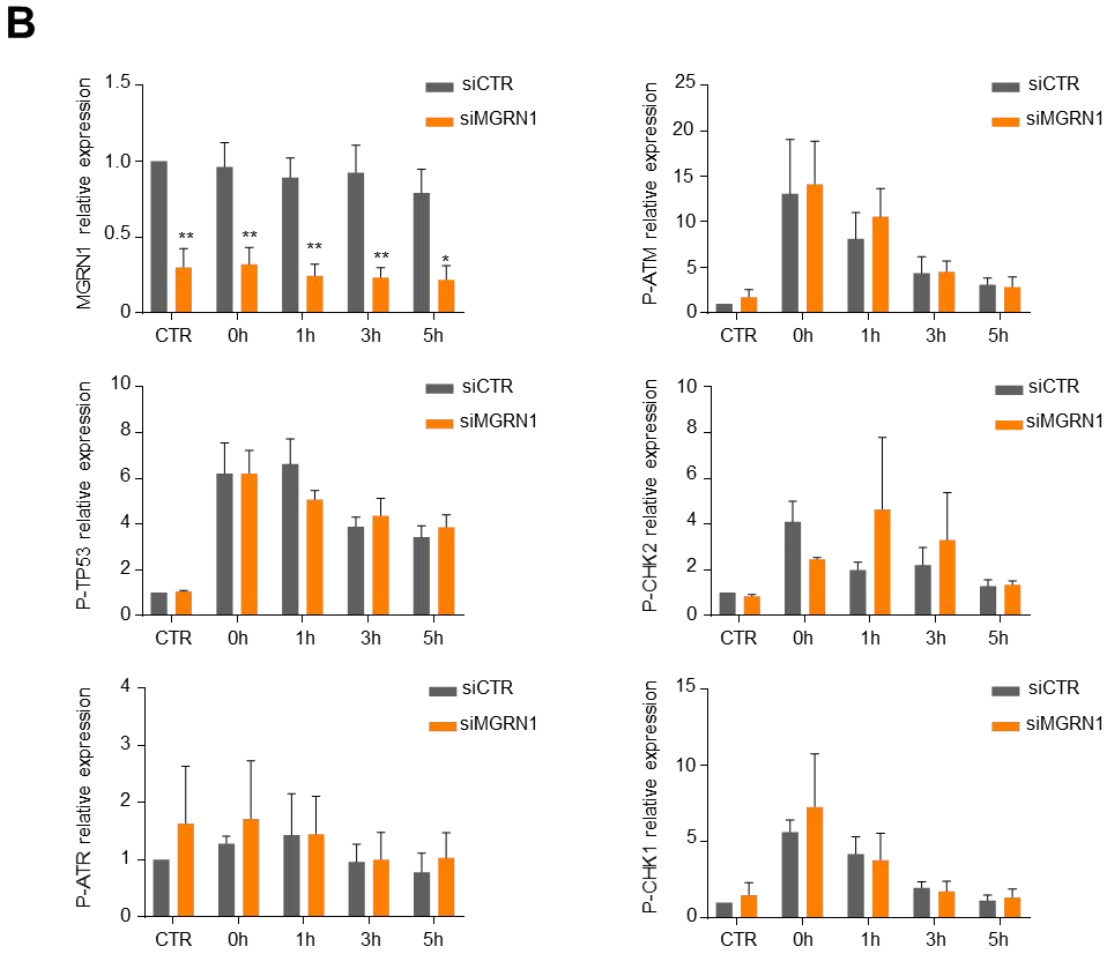
B
MGRN1 relative expression
P-ATM relative expression
P-TP53 relative expression
P-CHK2 relative expression
P-ATR relative expression
P-CHK1 relative expression
siCTR
siMGRN1
CTR
0h
1h
3h
5h

Figure 8. Activation of the ATM and ATR pathways in *MGRN1*-silenced and control cells. A) Left: Representative immunoblots of p-ATM (Ser1981), p-CHK2 (Thr68), p-TP53 (Ser15), TP53, p-ATR (Thr1989), ATR, p-CHK1 (Ser317) and CHK1. Proteins were extracted from control (siCTR) and *MGRN1*-silenced (siMGRN1) cells without (CTR) or with NCS pulse (0.5 µg/ml, 1 h) at different times after removal of NCS. MGRN1 was used as a control for silencing and ACTB as loading control. Right: Simplified scheme of the NCS-induced DSBs response pathway. **B)** Relative intensity of the specific bands normalized to control cells without NCS. Results given as mean ± SEM. Two-way ANOVA was used for statistical analysis. *, $p < 0.05$, **, $p < 0.01$, ***, $p < 0.001$ and ****, $p < 0.0001$.

Lack of effect of MGRN1 on ATR recruitment to stalled replication forks

The previous results showed that the activation of the ATR-CHK1 axis in response to replication stress was altered in *MGRN1*-silenced cells. Next, we wanted to find out the specific step(s) of the pathway accounting for this impaired activation of CHK1.

The first phase in the activation of ATR under replication stress conditions is the detection of stalled replication forks and the recruitment of ATR to these regions (217, 219). The current model posits that fork stalling generates ssDNA regions that are rapidly detected and coated by replication protein A (RPA), a heterotrimeric ssDNA-binding protein complex consisting of 3 different subunits, RPA1, RPA2 and RPA3 (214, 219). RPA-coated ssDNA (RPA-ssDNA), through its direct binding to the ATR-interacting protein (ATRIP), recruits the ATR-ATRIP complex to the stalled forks (214, 219). However, the recruitment of the ATR-ATRIP complex is not sufficient to activate ATR. Rather, activation of ATR depends on colocalization with other functional regulators of ATR, such as DNA topoisomerase 2-binding protein 1 (TOPBP1) (219).

To analyze whether MGRN1 participates in the detection of stalled replication forks and/or the formation of RPA-ssDNA complexes, we studied by immunofluorescence the number of RPA1 foci generated after treatment with HU (2 mM, 4 h) in cells lacking MGRN1 and control cells (Figure 9A). Furthermore, we measured the levels and localization of p-ATR as well as its colocalization with RPA1 foci (Figure 9B-C). The results showed that the formation of foci labeled by an anti-RPA1 antibody after the HU pulse was similar in the presence or absence of MGRN1. In contrast, MGRN1-depleted cells exhibited an aberrant structure of p-ATR foci. In control cells, the intensity of p-ATR staining in the nucleus, the formation of p-ATR foci and its location outside nucleoli increased after HU treatment. Conversely, MGRN1-depleted cells contained slightly higher levels of p-ATR under basal conditions compared with control cells, but the intensity of p-ATR staining did not augment after the HU pulse. Furthermore, no increase in p-ATR foci outside nucleoli was observed upon HU treatment and the colocalization of p-ATR with RPA1 (quantified by medians of Mander's coefficients) was impaired in

comparison with control cells. To summarize, our data showed that reduction of MGRN1 levels did not impair the formation of RPA foci in cells submitted to replicative stress. However, it impaired the increase in p-ATR in response to HU and, moreover, it apparently altered the distribution of p-ATR within nuclei as shown by a deficient recruitment to RPA foci upon HU-induced fork stalling.

To confirm the normal formation of RPA foci in MGRN1-deprived cells, we performed subcellular fractionation with CSK buffer. This technique allows for the discrimination between chromatin-bound proteins and soluble proteins (220) and we used it to compare in control and MGRN1-silenced cells treated with HU the binding to chromatin of RPA1, RPA2 and ATRIP, responsible for the localization of ATR to ssDNA, a step required for ATR activation (Figure 9D). In MGRN1-depleted and control cells, we observed comparable levels of chromatin-bound RPA1, RPA2, and ATRIP in response to HU treatment. Therefore, perturbation of the ATR-CHK1 axis in HU-treated cells should likely occur downstream of recognition by RPA of ssDNA associated with stalled forks. Moreover, since ATRIP binding to chromatin was not impaired in MGRN1-depleted cells, then it is likely that ATR was also recruited to the foci. However, the decreased colocalization of p-ATR and RPA suggested that, once located to these regions, ATR was not adequately phosphorylated and hence activated in MGRN1-deprived cells. Interestingly, the data suggested that in cells expressing normal levels of MGRN1, the fraction of chromatin-bound MGRN1 increased upon HU-induced replicative stress. Unfortunately, we could not compare the binding to chromatin of ATR in control and MGRN1-depleted cells, because no signal was detected with our ATR antibody under any of the experimental conditions tested, suggesting that ATR indirectly bound to chromatin via ATRIP was washed out during the procedure.

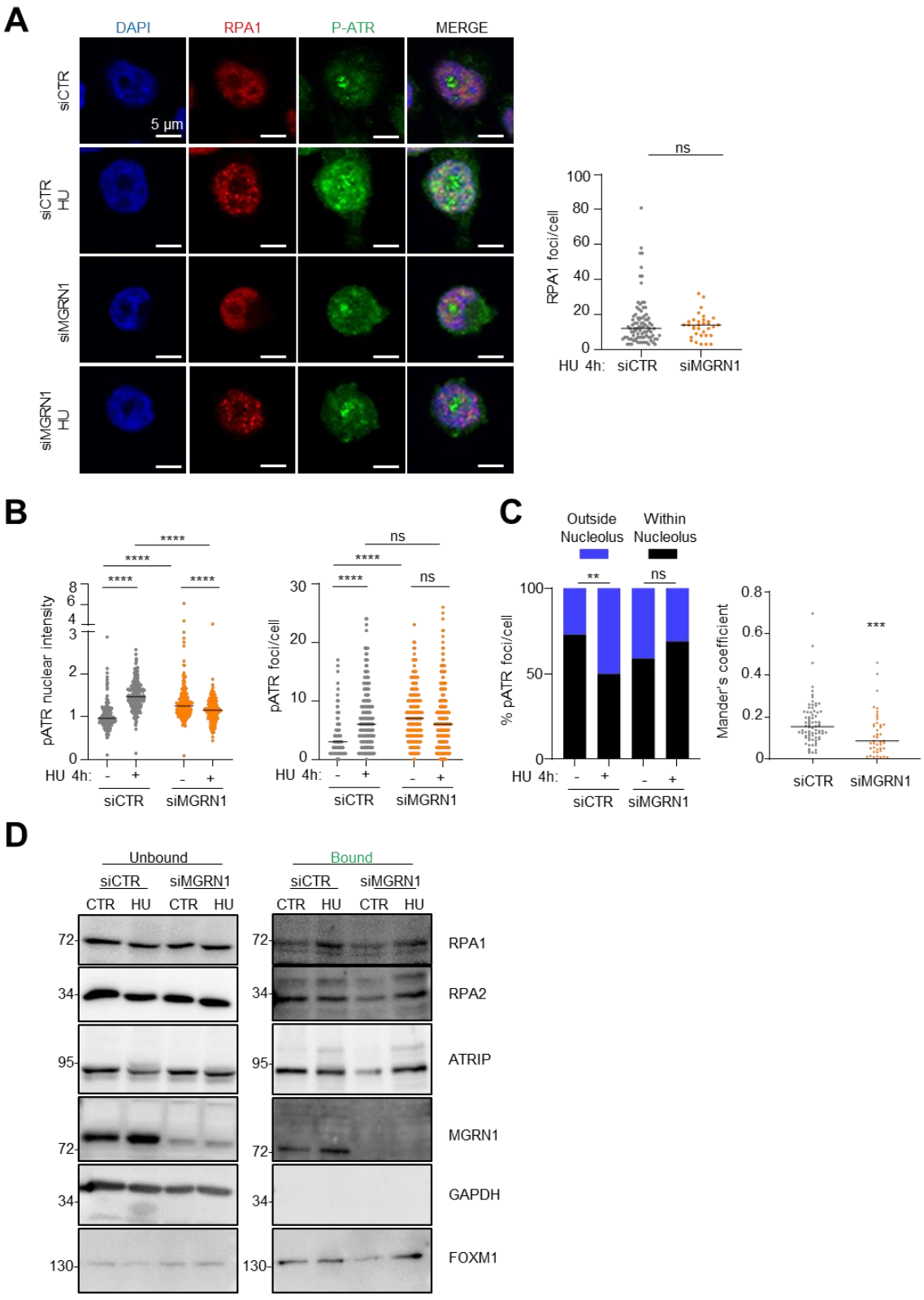

Figure 9. Recruitment of RPA, ATRIP and ATR to HU-induced lesions in *MGRN1*-silenced and control cells. A) RPA1 and p-ATR (Thr1989) immunostaining in control and *MGRN1*-silenced cells treated with 2 mM HU for 4 h. Left: Representative confocal micrographs showing DAPI stain in blue, RPA1 in red and p-ATR in green. Right: Quantification of RPA1 foci in cells that respond to HU by forming > 2 RPA1 foci. The

graph shows the median and Mann Whitney test used for statistical analysis. **B)** Quantification of the intensity of the nuclear p-ATR signal relative to control cells (siCTR) without HU (left) and number of p-ATR foci per cell (right). The graph shows the median value and two-way ANOVA was used for statistical analysis. **C)** Left: Quantification of the percentage of p-ATR foci per cell outside (blue) or inside (black) nucleoli. Data are represented as a stacked bar chart and chi-square was used for statistical analysis. Right: Quantification of Mander's coefficient as a measure of colocalization. The median and the results of Man-Whitney test for statistical analysis are shown. **D)** Representative immunoblots of chromatin-bound/unbound proteins (RPA1, RPA2, ATRIP and MGRN1) obtained by the CSK buffer assay in control and *MGRN1*-silenced cells treated with HU as above. GAPDH is used as a control of fractionation and FOXM1 as a chromatin-bound positive control. *, $p < 0.05$, **, $p < 0.01$, ***, $p < 0.001$ and ****, $p < 0.0001$.

Identification of CDK2 and RPA1 as MGRN1 interactors

In an attempt to identify the precise step(s) targeted by MGRN1 in the pathway leading from fork stalling to CHK1 activation, we wished to find out whether MGRN1 interacts with protein partners known to participate in this pathway. For this purpose, we expressed an HA epitope-labeled MGRN1 isoform S(+) (MGRN1-HA) in HBL melanoma cells and we carried out the immunoprecipitation (IP) of MGRN1-HA followed by mass spectrometry (MS) analysis. These experiments were performed in the laboratory of Prof. L. Fajas, at the Center for Integrative Genomics of the University of Lausanne (Switzerland), during a short stay. The IP was also performed in HBL cells transiently transfected with pcDNA3 as a negative control. The results were represented as the number of spectra detected by MS, corresponding to specific proteins in each sample. Figure 10A lists only the proteins for which the number of spectra in the HA-MGRN1 IP sample was at least 2-fold higher than the value in the pcDNA3 negative control, i.e. a 2-fold enrichment in the HA-MGRN1 sample was taken as the cutoff for possible interactors.

We observed a higher number of spectra corresponding to MGRN1 and ATRN, a well-known MGRN1 partner (161), in the IP sample compared with the control. This provided a convenient internal control for the correct IP of MGRN1-HA under conditions preserving protein-protein interactions. Furthermore, the results indicated a possible interaction between MGRN1 and some proteins involved in replication, DNA damage response and/or proliferation, including DCAF13, RPA1, CDK1, PCNA, CDK2, RCC1, SSBP1, RPA2, ARPC4 and SPOUT1. The possible interaction of MGRN1 with RPA1 and/or RPA2 was fully consistent with the suggested recruitment of MGRN1 to chromatin in HU-treated cells, observed previously. Concerning the other potential partners, we were particularly interested in Cyclin-dependent kinase 2 (CDK2) because this kinase plays a crucial role in the progression through S phase of the cell cycle, and also participates in DNA repair processes (221). Moreover, some studies have demonstrated that CDK2 is

essential for efficient activation of the ATR-CHK1 axis in response to replication stress (222). Given the importance of CDK2 and RPA1 for the stimulation of the ATR-CHK1 pathway, we focused on these proteins as possibly involved in the role of MGRN1 during replicative stress.

A

	Alternate ID	Fold change (IP/ctrl)	MGRN1-HA	PCDNA3
1	MGRN1	130	367	3
2	PRPH	8,3	8	0
3	GPI	7,2	7	0
4	CISD1	7,2	7	0
5	KCTD21	7,2	7	0
6	CTNNB1	6,2	6	0
7	PDIA6	6,2	6	0
8	HSPB1	5,7	16	3
9	SCGB1D2	5,2	5	0
10	ATRN	5,2	5	0
11	RAB38	5,2	5	0
12	LDHB	4,3	16	4
13	DCAF13	4,3	8	2
14	PPP2R1A	4,1	4	0
15	PGK1	4,1	4	0
16	MIC13	4,1	4	0
17	EXOSC5	4,1	4	0
18	PDCD2	4,1	4	0
19	YWHAG	4,1	4	0
20	CAD	3,7	7	2
21	SBSN	3,7	7	2
22	RAB32	3,2	9	3
23	ATP5F1A	3,2	6	2

	Alternate ID	Fold change (IP/ctrl)	MGRN1-HA	PCDNA3
24	CFL1	2,7	10	4
25	RPA1	2,7	5	2
26	HADHB	2,7	5	2
27	RAB27A	2,7	5	2
28	RAB1A	2,5	7	3
29	DUSP23	2,4	11	5
30	CDK1	2,3	13	6
31	PPIA	2,1	25	13
32	PCNA	2,1	12	6
33	PSMA7	2,1	12	6
34	CDK2	2,1	10	5
35	RCC1	2,1	8	4
36	SSBP1	2,1	6	3
37	EXOSC8	2,1	6	3
38	NLE1	2,1	6	3
39	RPL34	2,1	4	2
40	CNP	2,1	4	2
41	RPA2	2,1	4	2
42	ARPC4	2,1	4	2
43	CLIC1	2,1	4	2
44	SPOUT1	2,1	4	2
45	PGAM1	2,1	4	2

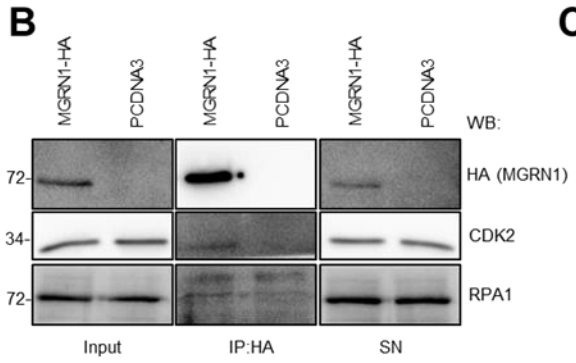

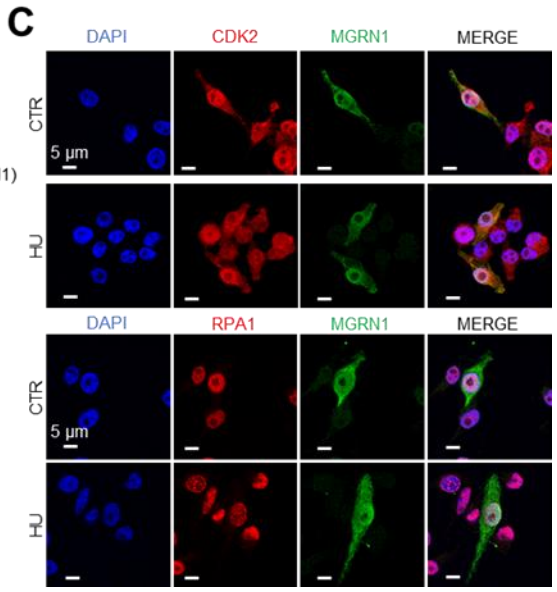

Figure 10. Identification of MGRN1 interacting partners in HBL cells. A) Co-immunoprecipitation of MGRN1-HA and subsequent mass spectrometry (MS) analysis. The table shows alternate ID (protein identification) of proteins that match with spectra, the fold change (>2) for the number of spectra determined in immunoprecipitates of MGRN1-HA transfected samples relative to the negative control transfected with empty pcDNA3 (ctrl), the total number of spectra in the immunoprecipitates of cells transfected with MGRN1-HA (≥ 4) and in pcDNA3 transfected negative controls. Bait protein is shown in green, known interactor (positive control) of MGRN1 in blue, and possible interactors involved in proliferation, DNA damage response and replication in yellow. **B)** Co-immunoprecipitation analysis of extracts from HBL cells transfected with MGRN1-HA or empty pcDNA3 and treated with HU (2 mM, 4 h). Representative immunoblots of HA-MGRN1, CDK2 and RPA1 proteins showing input (samples before immunoprecipitation), IP:HA (samples immunoprecipitated with anti-HA beads) and SN (supernatant of the immunoprecipitated samples). **C)** Representative micrographs of HBL cells transfected MGRN1-MYC and labeled with an anti-MYC antibody (in green) and with antibodies against CDK2 or RPA1 (red). DAPI (blue) was used to detect nuclei. Cells were treated with 2 mM HU for 4 h.

To validate the results obtained by IP/MS, we performed co-immunoprecipitation assays followed by Western Blot (Figure 10B). We confirmed the interaction between MGRN1 and CDK2 in HBL HU-treated cells since the kinase was immunoprecipitated by an anti-HA antibody only in the presence of MGRN1-HA. Concerning RPA1, the results were less clear-cut because a band of the expected size was detected in Western blots of cells expressing MGRN1-HA and in the negative controls transfected with empty pcDNA3. However, the intensity of the band immunoprecipitated from MGRN1-HA-containing extracts was noticeably higher, thus suggesting that a MGRN1-RPA1 interaction did actually occur. Moreover, we studied MGRN1 colocalization with RPA1 and CDK2 by confocal microscopy (Figure 10C). Due to the inability to detect specifically endogenous MGRN1 because of cross-reactivity of the anti-MGRN1 antibody with other endogenous protein(s), cells were transiently transfected with MGRN1-MYC and labeled for MGRN1 with an anti-MYC antibody. In addition, samples were labeled for CDK2 or RPA1 (before and after HU treatment) to assess the extent of their colocalization with MGRN1-MYC and their subcellular distribution. Concerning CDK2, its location was preferentially nuclear, as expected. Moreover, in control and HU-treated cells successfully expressing exogenous MGRN1, co-localization of MGRN1-MYC and CDK2 was observed in the merged images. These observations further supported a MGRN1-CDK2 interaction. On the other hand, RPA1 staining was exclusively nuclear and again, the staining of MGRN1-MYC suggested significant co-localization with RPA1, consistent with a RPA1-MGRN1 interaction.

According to the results shown in Figure 10, the proteomic approach as well as confocal microscopy and co-immunoprecipitation analysis by Western blot suggested the occurrence of MGRN1-CDK2 and MGRN1-RPA1 interactions. Our next goal was to

determine the effects of the MGRN1-CDK2 interaction on CDK2 intracellular levels, subcellular localization, and activity. First, we studied CDK2 relative levels in HBL cells under control conditions and following MGRN1 repression (Figure 11A) or overexpression (Figure 11B). Immunoblots showed that repression of MGRN1 significantly reduced the levels of CDK2. Consequently, cells transiently transfected with MGRN1-HA showed a small increase in CDK2 levels compared to control cells. Nevertheless, this increase did not reach statistical significance, probably due to the limited efficiency of transfection, the fact that endogenous MGRN1 is expressed in both conditions and the variability between the various experiments. However, the obvious trend towards higher CDK2 levels upon overexpression of MGRN1 was consistent with the lower CDK2 accumulation observed upon repression of MGRN1. These data suggested that CDK2 was stabilized by its interaction with MGRN1.

Next, we analyzed by immunostaining and confocal microscopy possible changes in CDK2 subcellular localization following repression of MGRN1 (Figure 11C). MGRN1-depleted cells showed a lower intensity of CDK2 staining, consistent with the lower expression of the kinase previously found by Western blot. Moreover, quantification of the CDK2 signal in whole cells and in nuclei indicated that the decrease in CDK2 staining was very similar in both cases. Accordingly, the fraction of nuclear CDK2 was not significantly different in control cells and MGRN1-deprived cells.

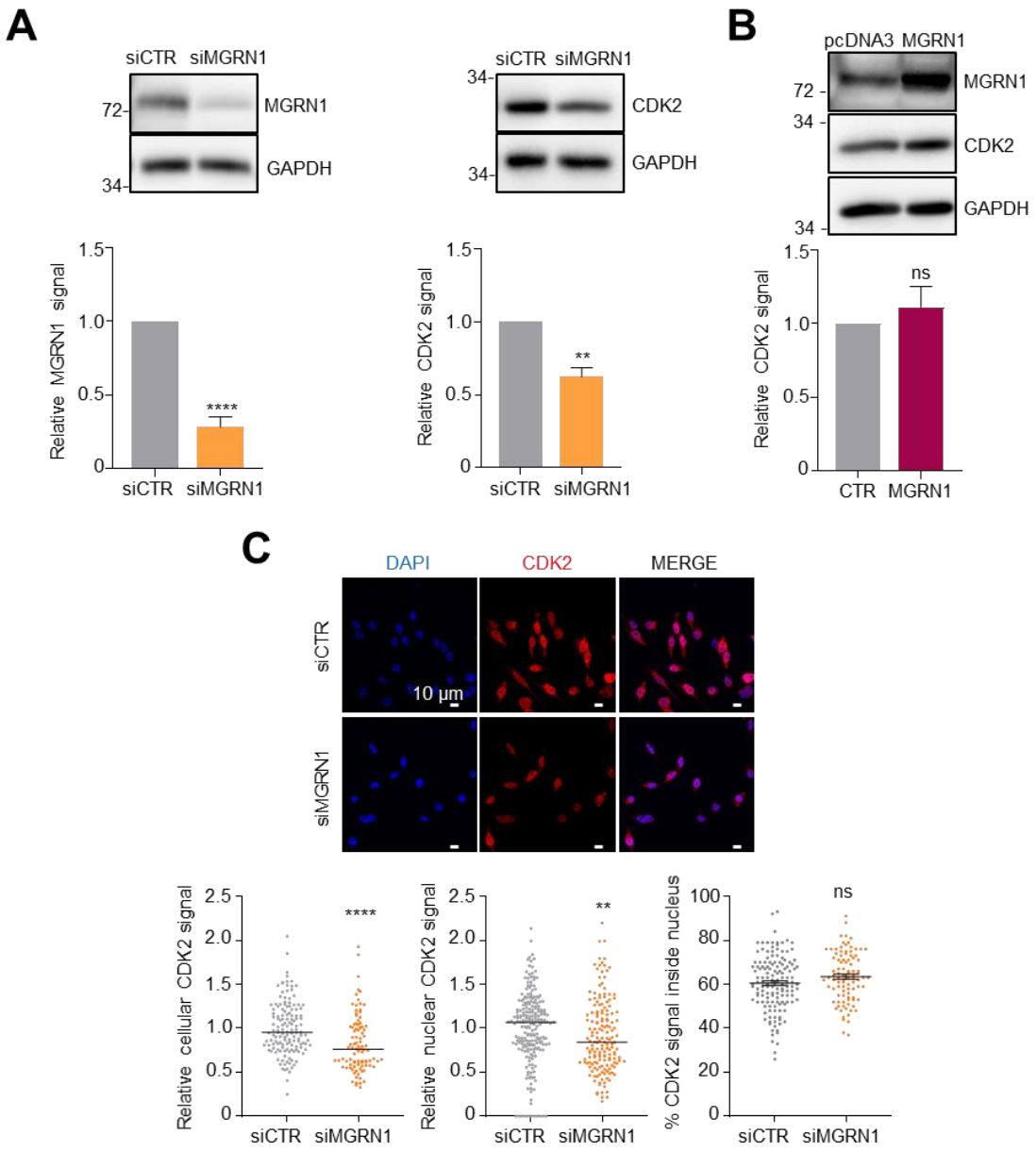

Figure 11. CDK2 abundance and localization in *MGRN1*-silenced cells, cells transiently transfected with MGRN1-HA and control cells. A) Representative immunoblots of MGRN1 and CDK2 in HBL control and *MGRN1*-silenced cells. **B)** Same for control and MGRN1-transfected cells. GAPDH was used as loading control. The graphs show the mean ± SEM of MGRN1 and CDK2 relative expression. T-tests were used for statistical analysis. **C)** Representative confocal micrographs of DAPI (blue) and CDK2 (red) labeling in control and *MGRN1*-silenced cells. Graphs show the median CDK2 relative cellular intensity (left), nuclear intensity (middle) and the mean ± SEM of the percentage of the CDK2 signal inside nuclei (right) in HBL control and *MGRN1*-silenced cells. Mann-Whitney (left) or T-test (right) were used for statistical analysis. *, $p < 0.05$, **, $p < 0.01$, ***, $p < 0.001$ and ****, $p < 0.0001$.

Finally, we were interested in analyzing the possible involvement of CDK2 on the alteration of the response to replicative stress in MGRN1-depleted cells. To this end, we employed the SU9516 cell-permeant inhibitor, which selectively inhibits CDK2 activity

(223). To define the appropriate experimental conditions, we treated HBL cells with 0, 2.5 or 5 µM SU9516 for 24 h and protein extracts were analyzed by Western Blot (Figure 12A). We used the phosphorylation of RB1 and the expression of FOXM1 as surrogates for CDK2 activity. Indeed, RB1 is a well-known substrate for CDK2 that is phosphorylated by the kinase to promote E2F1 release and hence progress through the S phase of the cell cycle (224). Once released from the RB1-E2F1 complex, E2F1 activates the expression of S phase genes such as FOXM1. The level of expression of this gene can therefore be used as a readout of E2F1 transcriptional activity that should decrease when CDK2-dependent phosphorylation of RB1 is inhibited. Treatment with 5 µM SU9516 decreased both the phosphorylation of RB1 and FOXM1 expression (Figure 12A). Moreover, HBL cells treated with SU9516 showed an altered cell cycle progression, with a G_2/M block, as previously reported (222, 223) (Figure 12B).

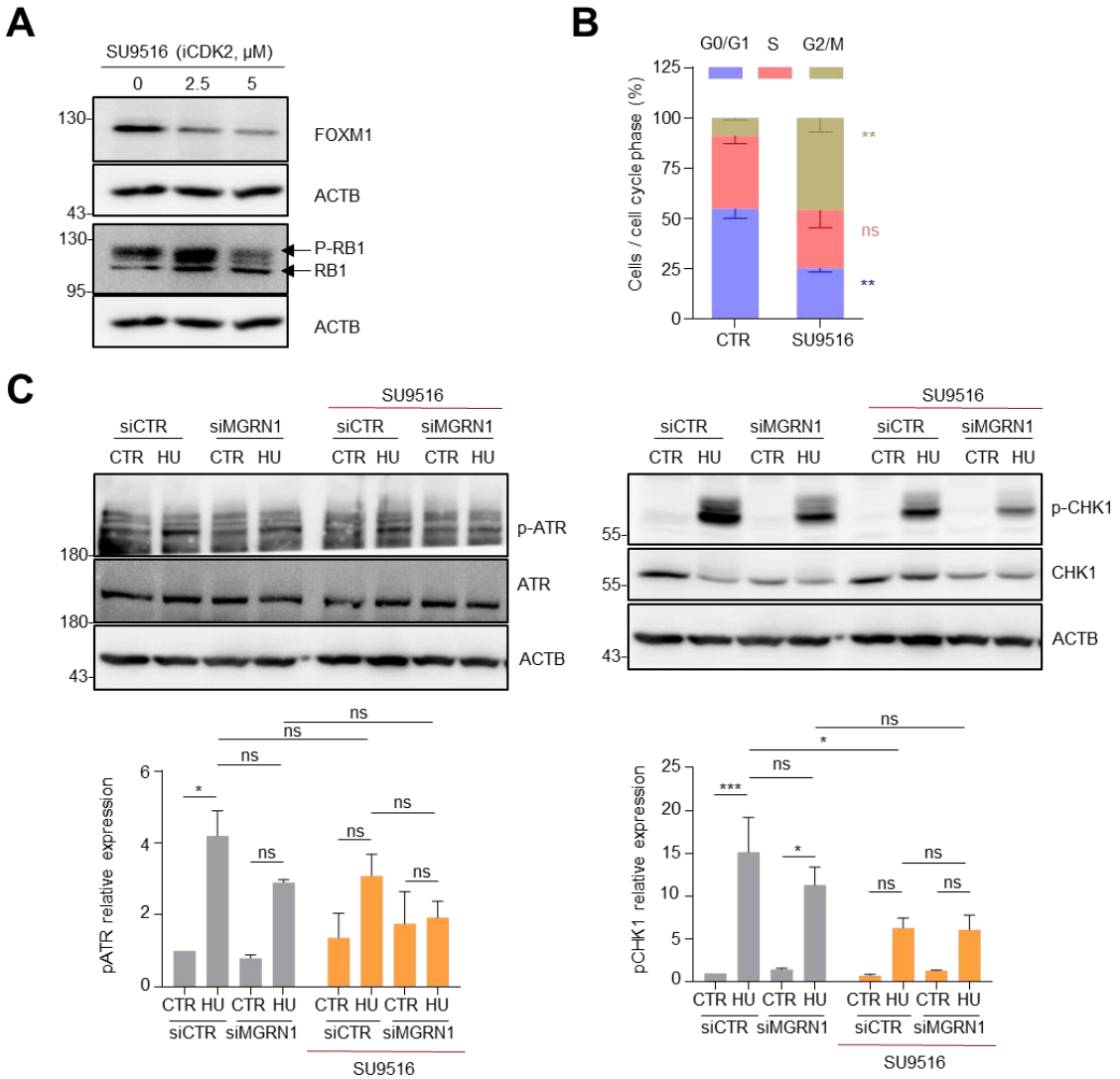

Figure 12. Effect of the CDK2 specific inhibitor SU9516 on activation of the ATR-CHK1 pathway in cells depleted of MGRN1. A) Representative immunoblots of FOXM1 and RB1 in HBL cells treated with the indicated concentration of SU9516 for 24 h. ACTB was used as loading control. **B)** Cell cycle analysis of PI-stained HBL cells treated with 5 µM SU9516 for 24 h. The graph indicates the mean ± SEM of the percentage of cells in each cell cycle phase. T-test was used for statistical analysis. **C)** Representative immunoblots of p-ATR (Thr1989), ATR, p-CHK1 (Ser317) and CHK1. Proteins were extracted from control (siCTR) and *MGRN1*-silenced (siMGRN1) cells without (CTR) or with HU treatment (2 mM, 4 h) in the presence or absence of SU9516 (5 µM for 24 h). ACTB was used as loading control. The graphs show the quantification of the band intensities normalized to control cells without HU and SU9516 (mean ± SEM). Two-way ANOVA was used for statistical analysis. *, $p < 0.05$, **, $p < 0.01$, ***, $p < 0.001$ and ****, $p < 0.0001$.

To determine if the inefficient activation of the ATR-CHK1 signaling axis observed in the absence of MGRN1 could be related with CDK2, we compared the phosphorylation of ATR and CHK1 proteins after treatment with HU (2 mM, 4 h) in the presence or absence of MGRN1 (i.e. in cells transfected with siCTR or siMGRN1, respectively), with or without CDK2 inhibition by SU9516 (5 µM for 24 h) (Figure 12C). HU-induced replication stress led to increased phosphorylation of ATR and CHK1 in cells expressing normal levels of MGRN1. As expected based on previous results, in cells lacking MGRN1, phosphorylation of ATR and CHK1 was impaired as compared with control cells. On the other hand, SU9516 decreased significantly CHK1 activation induced by HU in cells treated with siCTR and hence expressing normal levels of MGRN1. This finding supported the involvement of CDK2 in the activation of the ATR-CHK1 axis under conditions of replicative stress. Moreover, in cells treated with SU9516 to inhibit CDK2, repression of MGRN1 had little or no further effect on p-ATR and p-CHK1 levels, suggesting that CDK2 activity was required to mediate the inhibitory effect of MGRN1 deprivation on ATR-CHK1 signaling. Thus, the results summarized in Figure 12 pointed to a functional link between MGRN1 and CDK2 on the activation of ATR and its downstream effector CHK1. However, this evidence is still scarce and preliminary and further work is required to fully demonstrate this hypothesis.

DISCUSSION

DISCUSSION

In the present work, we have addressed several poorly known aspects of the biological functions of MC1R and its intracellular partner MGRN1 within melanocytes and/or melanoma cells. Hypomorphic variants of human MC1R are associated with lightly pigmented phenotypes and with an increased melanoma risk (80, 90, 91). In turn, the loss-of-function *mahoganoid* mutation leads to a complex phenotype with increased pigmentation, propensity to neurodegeneration and congenital heart defects, among other physiopathological alterations. However, a hypothetic role of MGRN1 on melanoma genesis or progression has never been analyzed.

Concerning unknown aspects of MC1R, we focused on the expression and signaling properties of an uncharacterized intragenic splice variant, MC1R-203, whose signaling properties, intracellular partners and levels of expression were unknown. The MC1R-203 and the canonical protein only differ in that MC1R-203 has an additional 66 amino acids C-terminal cytosolic extension. Consistent with the presence of all the functionally relevant functional domains of GPCRs, MC1R-203 was able to activate cAMP and ERK signaling upon binding of an agonist. However, whereas cAMP signaling is significantly impaired as compared with canonical MC1R, activation of the ERKs was comparable. Therefore, MC1R-203 behaved as an imbalanced signaling form with a bias favoring the mitogenic ERK cascade over the differentiation-promoting cAMP pathway. This behavior has already been described for many of the natural variant alleles of canonical MC1R associated with the red hair color phenotype (110).

On the other hand, MC1R has been reported to act as a scaffold for MGRN1 and ARRBs, a cytosolic arrestin responsible for the homologous desensitization of receptor signaling. As a result of the formation of an ARRB2-MC1R-MGRN1 complex, the arrestin becomes ubiquitylated (164). We found that MC1R-203 was unable to potentiate ARRB2 ubiquitylation, suggesting that this spliceoform might be unable to act as a scaffold. This would be consistent with the major role of the C-terminal domain of MC1R in the interaction with the ARRBs and may modulate receptor desensitization. In any case, since we found that MC1R-203 was a minority form expressed at much lower levels than the canonical protein, the functional relevance of these findings and the physiological role of the alternative transcript will probably be limited. With this in mind, we switched our efforts to the analysis of the roles of MGRN1.

The multiple pathological implications of the *mahoganoid* mouse mutation clearly demonstrate that MGRN1 plays important physiological functions (161, 177). These pathological effects of MGRN1 loss have been related with mitochondrial dysfunction

with increased oxidative stress (132), aberrant microtubule dynamics and stability with altered mitotic spindle orientation (158-160), defects of microtubule-dependent transport of intracellular organelles (225), deregulation of the transcriptional response to proteotoxic stress (143), and others. However, despite its relationship with components of the cytoskeleton, no study on the regulation by MGRN1 of cell shape and movement of normal or cancer cells has yet been reported. Moreover, the likely roles of MGRN1 in maintaining genomic stability and normal cell cycle progression have not been explored, despite the potential genotoxic effects of oxidative stress and/or mitotic spindle missorientation.

Our studies on mouse and human MGRN1 mostly aimed at assessing a possible role of this protein in melanoma. Using murine and/or human immortalized normal melanocytes and melanoma cells as models, we showed that MGRN1 knockdown induced a phenotype characterized by: i) cell morphology changes with increased size, higher number of dendrites, longer protrusions and higher melanin content, ii) impaired cell motility and higher adhesion to collagen matrices, iii) abnormal cell cycle progression with increased percentage of cells in S phase, and iv) decreased genome stability with accumulation of DNA damage.

Concerning genomic stability, ablation by CRISPR/Cas9 or transient downregulation of MGRN1 by siRNA led to higher abundance of DSBs as demonstrated by staining of γ-H2AX foci and comet assays. Thus, normal MGRN1 expression was required for genomic stability, and it was of interest to look for the cause of the high DNA damage found in MGRN1-deficient cells.

Melanocytic cells lacking MGRN1 are likely exposed to a higher oxidative stress due to mitochondrial dysfunction (132, 183) and to increased melanogenesis since ROS are generated at several steps of the melanogenic pathway (185, 186). Conceivably, an augmented formation of DNA breaks resulting from enhanced ROS production might thus contribute to the higher steady-state level of these lesions in melanocytes and melanoma cells lacking MGRN1. However, the burden of DNA breaks in *Mgrn1*-KO cells did not correlate with the abundance of 8-oxodG, the prevailing product of DNA base oxidation. Eight-oxodG is a good marker of DNA exposure to ROS and it was only slightly increased in MGRN1-deficient cells. Therefore, it appeared that increased oxidative damage in the absence of MGRN1 cannot be accounted for convincingly exclusively on the basis of augmented oxidative stress.

Replication is a well-known endogenous source of DNA damage (226), and FACS analysis of cell cycle progression showed increased populations of MGRN1-depleted

melanocytes and melanoma cells in the S and G2/M phases of the cell cycle. Our findings of disturbed cell cycle kinetics in mouse and human *MGRN1*-KO cells were consistent with a genome-wide functional screening for human cell cycle regulators that found increased numbers of cells in S phase in MGRN1-silenced U2OS cells (181). Moreover, a recent RNA-sequencing analysis of genes regulated by MGRN1 after proteasomal stress identified “cell cycle phase” as the biological process with the most significant gene ontology functional enrichment score (143). Therefore, our study and previous reports by others firmly established a role of MGRN1 on cell cycle progression. Moreover, impairment of this MGRN1 function when its levels of expression were downregulated apparently promoted a form of replicative stress, as indicated by DNA fiber assays showing accumulation of stalled forks.

Stalled forks are a major endogenous source of DNA breaks and genomic instability since stalled replication forks that are not properly stabilized and restarted can collapse giving raise to DNA breaks (212). Thus, a causal link between fork stalling mediated by MGRN1 deprivation and increased DNA damage appeared likely. Stalled forks trigger a potent DNA damage response (DDR) by activating ATR and its effector kinase CHK1, leading to downstream activation of TP53 to slow down proliferation and activate DNA repair pathways (215). Therefore, we analyzed the functional status of the ATR-CHK1-TP53 axis in control and MGRN1-deprived cells. We found that the activation of this pathway following HU-induced replicative stress was deficient when expression of MGRN1 was low. However, this pathway, as well as the ATM-CHK2-TP53 axis involved in the response to DSBs, were normally induced by the clastogenic agent NCS. This suggested that the role of MGRN1 in ATR activation within the context of a DDR was specifically associated with the detection of stalled forks, rather than with the clearance of DNA breaks irrespective of their origin. This raised the question of the specific step involving MGRN1 within the pathway that leads from fork stalling to ATR-CHK1-TP53 activation. Our data indicated that this step was located upstream of CHK1 activation, and probably also upstream of ATR activation, but that, even in the absence of MGRN1, replicative stress led to the formation of RPA-coated foci and to the recruitment to chromatin of ATRIP, the obligatory partner of ATR in lesion recognition and activation of the kinase. Therefore, our data were consistent with MGRN1 acting between ATR recruitment to the stalled fork and ATR activation.

Interestingly, a proteomic approach suggested that MGRN1 bound several proteins involved in cell cycle progression and/or DNA repair pathways, including RPA1 and CDK2. It is known that CDK2 phosphorylates ATRIP at Ser224 (227) and a phosphorylation-incompetent S224A ATRIP mutant does not sustain as efficiently as WT

ATRIP the G2/M checkpoint activation, suggesting that CDK2-mediated phosphorylation of this site in ATRIP is required for optimal activation of the ATR-mediated DDR (228). Significantly, a specific inhibitor of CDK2 employed at a concentration that decreased RB1 phosphorylation and FOXM1 expression, abrogated the effect of MGRN1 deprivation on CHK1 activation by HU-mediated replicative stress. This result suggested a possible functional relationship between CDK2 activity and MGRN1 during activation of the ATR-CHK1 axis during replicative stress. This would be consistent with observations by others showing that pharmacological inhibition of Cdk2 impaired activation of Chk1 due to reduced phosphorylation (229, 230).

A hypothetic model consistent with the data discussed above is shown in the following scheme.

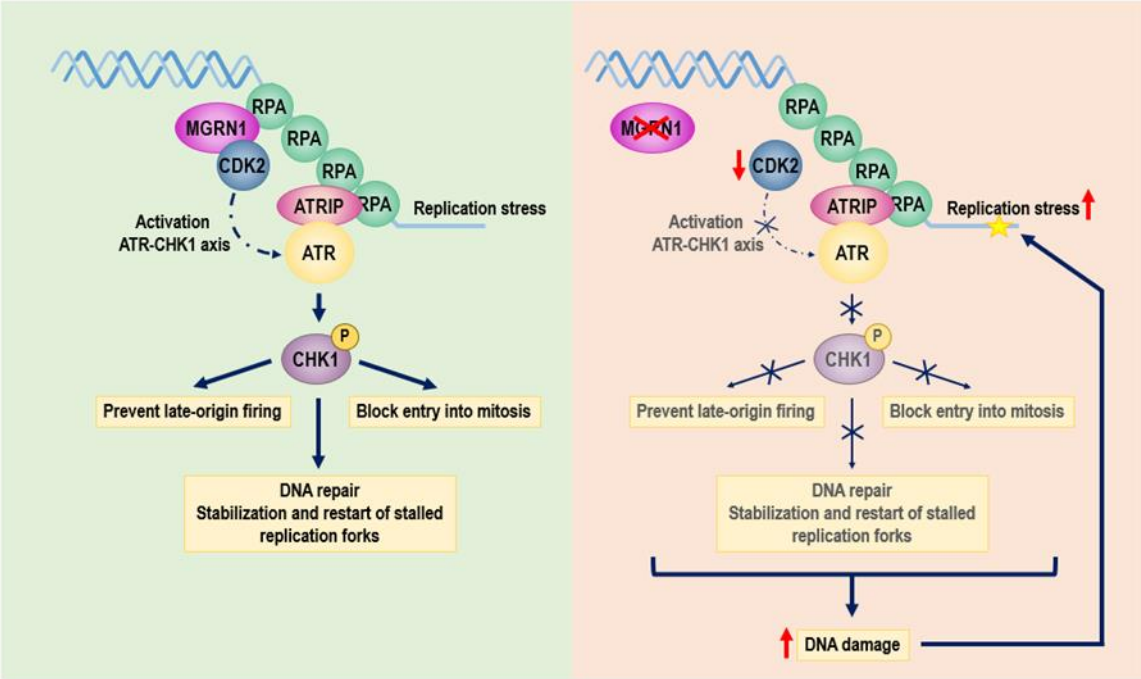

According to this hypothesis, MGRN1 might act to recruit CDK2 to RPA-coated regions in stalled replication forks, by virtue of its ability to bind RPA1 and CDK2. This would facilitate phosphorylation of CDK2 substrate(s), probably ATRIP, to foster ATR activation and trigger the downstream phosphorylation of the effector kinase CHK1. In the absence of MGRN1, CDK2 engagement would be compromised, thus resulting in a less efficient activation of ATR, impaired fork stabilization and hence, increased genomic instability. This hypothesis is attractive, but the available evidence is, overall, still scarce and a link between CDK2 and ATR activation dependent on MGRN1 remains to be formally proven.

Another aspect of this hypothesis that deserves some attention is its potential relationship with the small but significant impairment of DNA break clearance in the absence of MGRN1. Our results showed that strand breaks caused by exogenous challenges (either an oxidative pulse or treatment with NCS) or following replication fork stalling by HU were less efficiently cleared in the absence of MGRN1, thus suggesting that defective break repair also contributed to the high burden of DNA breaks in human or mouse MGRN1-deficient cells. A role of MGRN1 on DNA repair might again be consistent with its participation in the activation of the ATR-mediated DDR, since repair pathways are activated downstream of ATR. Moreover, several proteins involved in DNA repair are CDK2 substrates (reviewed in (221, 230)), and therefore CDK2 might also play direct roles by phosphorylating repair proteins. Interestingly, human MC1R, a GPCR that activates DNA damage repair in melanocytes (231-233) (reviewed in (7, 234)) interacts with MGRN1 and promotes its nuclear localization (140). Given that activation of MC1R in human melanoma cells stimulates the clearance of DNA strand breaks generated by oxidative stress (84), a possible involvement of MGRN1 in this MC1R-dependent genoprotective action cannot be ruled out and deserves further analysis.

The effect of MGRN1 ablation on cellular proliferation was subtle, according to our results. Pulse-chase experiments where newly synthesized DNA was labeled with BrdU did not reveal substantial alterations of the rate of DNA synthesis in mouse melanocytes. However, while *Mgrn1*-KO mouse cells complete mitosis at a comparable rate than control cells, MGRN1 absence in human melanoma cells induce a higher percentage of mitotic cells and a slower mitotic exit. Again, this is consistent with the impaired activation of the ATR-CHK1 axis in MGRN1-deprived cells. Of note, the impact of DDR on cell cycle progression is heavily dependent on activation of TP53 (235). Mouse melanocytes studies reported here were performed in cells with alterations in this pathway since B16 melanoma cells lack expression of functional TP53 (236) and melan-a6 and melan-md1 cells were derived from mice heterozygous for a Cdkn2a deletion (179). Therefore, it can be speculated that the DDR induced by accumulation of DNA damage in MGRN1-deficient cells might have a higher impact on cell proliferation in cells bearing an intact ARF/TP53 module. Consistent with this possibility, we found that in human melanoma mutations in TP53 and in MGRN1 seem mutually exclusive, suggesting that these genes belong to the same functional pathway. However, this hypothesis remains to be proven.

Whatever the molecular mechanism underlying the genoprotective effect of MGRN1, it is conceivable that genomic instability, which is a major driver of tumorigenesis, might promote the malignant transformation of MGRN1-null cells. However, a higher rate of melanoma or other malignancies has not yet been reported for *mahoganoid* mice. On

the other hand, with a rate of ~ 4 % protein sequencing-altering alterations, *MGRN1* mutations are not infrequent in human melanoma according to the TCGA database. For comparison, around 2 % of melanomas are mutated in *MITF* (~ 2.3 %), a gene considered responsible for a subset of melanomas (191). Moreover, a higher prevalence of *MGRN1* mutations is found in other tumor types such as endometroid cancers, with ~ 6 % of these tumors in the TCGA cohort harboring non-synonymous *MGRN1* mutations. Therefore, the possibility that *MGRN1* might behave as a cancer susceptibility gene deserves further analysis. In this context, it will be interesting to analyze the rate of *MGRN1* mutations in melanoma families without mutations in known susceptibility genes such as *CDKN2A*, *CDK4*, *BAP1*, *TERT*, *POT1*, *ACD*, *TERF2IP*, and *MITF*. Interestingly, mutations in these genes are only found in 30-50 % of melanoma families thus indicating that other melanoma susceptibility genes remain to be discovered (237).

In addition to a contribution of MGRN1 to melanomagenesis, a role of its expression level in melanoma progression is likely, according to our data. In keeping with this possibility, a study on osteosarcoma patients showed recurrent amplifications of the 16p13 region where MGRN1 is located (138), and another investigation reported hypomethylation of CpG sites in MGRN1 in blood cells from breast cancer patients (139). Here we showed that loss of *MGRN1* expression in mouse melanocytes promoted a differentiated phenotype with increased pigmentation, dendricity and adhesion to collagen I on one hand, and decreased motility on the other. This phenotypic switch was independent on changes in MITF expression. Cellular adhesion is intimately connected with migration and invasion, and it is known that microtubules are key regulators of these processes (238). Given that MGRN1 regulates microtubule dynamics through ubiquitylation of α-TUB (225) our findings of altered adhesion, migration and invasion in Mgrn1-null cells are not surprising.

In agreement with these data on cell adhesion and motility, we found low rates of lung colonization following injection of *Mgrn1*-KO B16 melanoma cells in the tail vein of mice, compared with *Mgrn1*-expressing cells. Importantly, complete knockdown of *Mgrn1* was not required to reduce the invasion potential of melanocytic cells, as a siRNA-mediated decrease in Mgrn1 abundance to ~25 % residual levels lowered invasion indexes on collagen I to > 50 % of control values. Concerning human melanoma, analysis of data in the TCGA database, as well as quantitative determination of *MGRN1* expression in clinical samples, were consistent with our *in vivo* data in the B16 mouse model, as highlighted by the inverse relationship between *MGRN1* expression and patient survival. Moreover, a statistically significant correlation of low *MGRN1* expression and higher survival probability was also observed for two prevalent types of cancer, namely lung

squamous cell carcinoma ($p = 0.0049$) and ovarian cancer ($p = 0.0029$) according to the TCGA database. Nevertheless, no correlation was observed for the majority of datasets suggesting that the effect of MGRN1 levels on patient survival might be specific to a restricted set of tumor types. This indicates that the physiological relevance of MGRN1 might be critically dependent on the cellular context despite a relatively widespread expression, as previously suggested by others (145).

It can therefore be speculated that *MGRN1* expression and/or functional status might play a dual role in a subset of malignancies including melanoma. On one hand, by promoting genomic instability, low *MGRN1* expression or *MGRN1*-loss-of-function mutations might contribute to melanomagenesis. On the other hand, high *MGRN1* expression within malignant melanocytes might foster a less differentiated and more aggressive phenotype with increased motility and higher metastatic potential. This hypothesis is consistent with the higher expression of *MGRN1* in melanoma compared with normal skin or *nevi*, and with the association of high MGRN1 levels with relevant clinical parameters such as Breslow index and, even more importantly lower patient survival. Of note, the combination of low *MGRN1* and low *TYRP1* expression afforded an excellent correlation with better prognostic according to the TCGA dataset, and, if validated in other cohorts, might be of clinical use. Therefore, the data presented here warrant further studies to clarify MGRN1 role in human melanoma, in search of clinical applications.

CONCLUSIONS

CONCLUSIONS

1. The MC1R-203 spliceoform is a minority transcript of the *MC1R* gene with hypomorphic signaling to the pro-differentiation cAMP cascade but normal activation of the mitogenic ERK pathway. As such, it displayed biased signaling comparable to many red hair color-associated natural *MC1R* variants.
2. MC1R-203 was unable to mediate the MGRN1-dependent ubiquitylation of ARRB2, the cytosolic arrestin responsible for desensitization of MC1R.
3. Loss of *Mgrn1* expression in mouse melanocytic cells promoted a differentiated phenotype with increased pigmentation, dendricity, size and adhesion, and decreased motility. The rates of lung colonization after injection of melanoma cells in the tail vein of mice were lower for *Mgrn1*-KO B16 cells compared with *Mgrn1*-expressing control cells.
4. *MGRN1* knockdown or MGRN1-depletion with siRNA in mouse and human melanocytic cells increased the fraction of cells in the S and G2/M phases of the cell cycle and promoted genomic instability with accumulation of DNA damage.
5. Strand breaks caused by an exogenous challenge or following replication fork stalling by HU were less efficiently cleared in the absence of MGRN1 in mouse and human melanocytic cells. However, no substantial alterations of the rate of DNA synthesis were found.
6. *In silico* analysis of public databases and quantification of *MGRN1* mRNA in clinical specimens showed that expression of *MGRN1* was significantly higher in human melanoma samples compared with *nevi* and that higher *MGRN1* expression in melanoma was significantly associated with shorter survival of melanoma patients and probably also higher Breslow index at diagnosis.
7. According to the TCGA dataset, melanomas have a significant rate of *MGRN1* mutations, comparable with several cancer-associated genes.
8. Depletion of MGRN1 increased cellular replicative stress as evidenced by accumulation of stalled replication forks, likely contributing to the genomic instability in MGRN1-deficient cells.
9. In human melanoma cells, MGRN1 was required for proper activation of the ATR-CHK1-TP53 signaling axis in response to replication stress, but was dispensable for RPA, ATRIP and likely also ATR recruitment at DNA damage sites.
10. MGRN1 interacted with CDK2 and RPA1. These interactions could contribute to the positive effect of MGRN1 on activation of the ATR-CHK1-TP53 pathway.

REFERENCES

REFERENCES

1. Ward WH, Farma JM. Cutaneous Melanoma: Etiology and Therapy. 2017.
2. Chang AE, Karnell LH, Menck HR. The National Cancer Data Base report on cutaneous and noncutaneous melanoma: a summary of 84,836 cases from the past decade. The American College of Surgeons Commission on Cancer and the American Cancer Society. Cancer. 1998;83(8):1664-78.
3. Miller AJ, Mihm MC. Melanoma. N Engl J Med. 2006;355(1):51-65.
4. Plonka PM, Passeron T, Brenner M, Tobin DJ, Shibahara S, Thomas A, et al. What are melanocytes really doing all day long...? Exp Dermatol. 2009;18(9):799-819.
5. Yamaguchi Y, Hearing VJ. Melanocytes and their diseases. Cold Spring Harb Perspect Med. 2014;4(5).
6. Buscà R, Ballotti R. Cyclic AMP a key messenger in the regulation of skin pigmentation. Pigment Cell Res. 2000;13(2):60-9.
7. García-Borrón JC, Abdel-Malek Z, Jiménez-Cervantes C. MC1R, the cAMP pathway, and the response to solar UV: extending the horizon beyond pigmentation. Pigment Cell Melanoma Res. 2014;27(5):699-720.
8. Goding CR. Melanocytes: the new Black. Int J Biochem Cell Biol. 2007;39(2):275-9.
9. Hirobe T. How are proliferation and differentiation of melanocytes regulated? Pigment Cell Melanoma Res. 2011;24(3):462-78.
10. Cichorek M, Wachulska M, Stasiewicz A, Tymińska A. Skin melanocytes: biology and development. Postepy Dermatol Alergol. 2013;30(1):30-41.
11. Kushimoto T, Basrur V, Valencia J, Matsunaga J, Vieira WD, Ferrans VJ, et al. A model for melanosome biogenesis based on the purification and analysis of early melanosomes. Proc Natl Acad Sci U S A. 2001;98(19):10698-703.
12. Maul GG, Brumbaugh JA. On the possible function of coated vesicles in melanogenesis of the regenerating fowl feather. J Cell Biol. 1971;48(1):41-8.
13. Hearing VJ. Determination of melanin synthetic pathways. J Invest Dermatol. 2011;131(E1):E8-E11.
14. García-Borrón JC, Solano F. Molecular anatomy of tyrosinase and its related proteins: beyond the histidine-bound metal catalytic center. Pigment Cell Res. 2002;15(3):162-73.
15. Raper HS. The Tyrosinase-Tyrosine Reaction: Production of l-3.4-Dihydroxyphenylalanine from Tyrosine. Biochem J. 1926;20(4):735-42.
16. Olivares C, Solano F. New insights into the active site structure and catalytic mechanism of tyrosinase and its related proteins. Pigment Cell Melanoma Res. 2009;22(6):750-60.
17. d'Ischia M, Wakamatsu K, Cicoira F, Di Mauro E, Garcia-Borron JC, Commo S, et al. Melanins and melanogenesis: from pigment cells to human health and technological applications. Pigment Cell Melanoma Res. 2015;28(5):520-44.
18. Aroca P, Solano F, Salinas C, García-Borrón JC, Lozano JA. Regulation of the final phase of mammalian melanogenesis. The role of dopachrome tautomerase and the ratio between 5,6-dihydroxyindole-2-carboxylic acid and 5,6-dihydroxyindole. Eur J Biochem. 1992;208(1):155-63.
19. Jimenez-Cervantes C, Garcia-Borron JC, Valverde P, Solano F, Lozano JA. Tyrosinase isoenzymes in mammalian melanocytes. 1. Biochemical characterization of two melanosomal tyrosinases from B16 mouse melanoma. Eur J Biochem. 1993;217(2):549-56.
20. Olivares C, Jiménez-Cervantes C, Lozano JA, Solano F, García-Borrón JC. The 5,6-dihydroxyindole-2-carboxylic acid (DHICA) oxidase activity of human tyrosinase. Biochem J. 2001;354(Pt 1):131-9.
21. Di Donato P, Napolitano A. 1,4-benzothiazines as key intermediates in the biosynthesis of red hair pigment pheomelanins. Pigment Cell Res. 2003;16(5):532-9.

22. Greco G, Wakamatsu K, Panzella L, Ito S, Napolitano A, d'Ischia M. Isomeric cysteinyldopas provide a (photo)degradable bulk component and a robust structural element in red human hair pheomelanin. Pigment Cell Melanoma Res. 2009;22(3):319-27.
23. Martínez-Vicente I, Jiménez-Cervantes C, García-Borrón J. Epidermis y fotoprotección. El lado oscuro del sol. Boletín SEBBM nº 206. Diciembre 2020.
24. Napolitano A, Panzella L, Monfrecola G, d'Ischia M. Pheomelanin-induced oxidative stress: bright and dark chemistry bridging red hair phenotype and melanoma. Pigment Cell Melanoma Res. 2014;27(5):721-33.
25. Panzella L, Leone L, Greco G, Vitiello G, D'Errico G, Napolitano A, et al. Red human hair pheomelanin is a potent pro-oxidant mediating UV-independent contributory mechanisms of melanomagenesis. Pigment Cell Melanoma Res. 2014;27(2):244-52.
26. Clark WH, Elder DE, Guerry D, Epstein MN, Greene MH, Van Horn M. A study of tumor progression: the precursor lesions of superficial spreading and nodular melanoma. Hum Pathol. 1984;15(12):1147-65.
27. Gogas H, Eggermont AM, Hauschild A, Hersey P, Mohr P, Schadendorf D, et al. Biomarkers in melanoma. Ann Oncol. 2009;20 Suppl 6:vi8-13.
28. Zaidi MR, Day CP, Merlino G. From UVs to metastases: modeling melanoma initiation and progression in the mouse. J Invest Dermatol. 2008;128(10):2381-91.
29. Nikolaou V, Stratigos AJ. Emerging trends in the epidemiology of melanoma. Br J Dermatol. 2014;170(1):11-9.
30. Rastrelli M, Tropea S, Rossi CR, Alaibac M. Melanoma: epidemiology, risk factors, pathogenesis, diagnosis and classification. In Vivo. 2014;28(6):1005-11.
31. Schadendorf D, Fisher DE, Garbe C, Gershenwald JE, Grob JJ, Halpern A, et al. Melanoma. Nat Rev Dis Primers. 2015;1:15003.
32. Ali Z, Yousaf N, Larkin J. Melanoma epidemiology, biology and prognosis. EJC Suppl. 2013;11(2):81-91.
33. IARC. International Agency for Research on Cancer. 2020 [Available from: https://www.gco.iarc.fr/today.

34. SEER. Cancer Stat Facts: Melanoma of the Skin. Natl. Cancer Institute. Bethesda MD. 2014-2018 [Available from: https://seer.cancer.gov/statfacts/html/amyl.html.

35. Mayer JE, Swetter SM, Fu T, Geller AC. Screening, early detection, education, and trends for melanoma: current status (2007-2013) and future directions: Part I. Epidemiology, high-risk groups, clinical strategies, and diagnostic technology. J Am Acad Dermatol. 2014;71(4):599.e1-.e12; quiz 610, 599.e12.
36. Bishop JN, Bataille V, Gavin A, Lens M, Marsden J, Mathews T, et al. The prevention, diagnosis, referral and management of melanoma of the skin: concise guidelines. Clin Med (Lond). 2007;7(3):283-90.
37. Markovic SN, Erickson LA, Rao RD, Weenig RH, Pockaj BA, Bardia A, et al. Malignant melanoma in the 21st century, part 1: epidemiology, risk factors, screening, prevention, and diagnosis. Mayo Clin Proc. 2007;82(3):364-80.
38. Porras BH, Cockerell CJ. Cutaneous malignant melanoma: classification and clinical diagnosis. Semin Cutan Med Surg. 1997;16(2):88-96.
39. Piliang MP. Acral lentiginous melanoma. Clin Lab Med. 2011;31(2):281-8.
40. Jones OT, Ranmuthu CKI, Hall PN, Funston G, Walter FM. Recognising Skin Cancer in Primary Care. Adv Ther. 2020;37(1):603-16.
41. Kibbi N, Kluger H, Choi JN. Melanoma: Clinical Presentations. Cancer Treat Res. 2016;167:107-29.
42. Elwood JM, Jopson J. Melanoma and sun exposure: an overview of published studies. Int J Cancer. 1997;73(2):198-203.
43. Gallagher RP, Lee TK. Adverse effects of ultraviolet radiation: a brief review. Prog Biophys Mol Biol. 2006;92(1):119-31.

44. Westerdahl J, Ingvar C, Måsbäck A, Jonsson N, Olsson H. Risk of cutaneous malignant melanoma in relation to use of sunbeds: further evidence for UV-A carcinogenicity. Br J Cancer. 2000;82(9):1593-9.
45. Titus-Ernstoff L, Perry AE, Spencer SK, Gibson JJ, Cole BF, Ernstoff MS. Pigmentary characteristics and moles in relation to melanoma risk. Int J Cancer. 2005;116(1):144-9.
46. Benvenuto-Andrade C, Oseitutu A, Agero AL, Marghoob AA. Cutaneous melanoma: surveillance of patients for recurrence and new primary melanomas. Dermatol Ther. 2005;18(6):423-35.
47. Kubica AW, Brewer JD. Melanoma in immunosuppressed patients. Mayo Clin Proc. 2012;87(10):991-1003.
48. Casula M, Paliogiannis P, Ayala F, De Giorgi V, Stanganelli I, Mandalà M, et al. Germline and somatic mutations in patients with multiple primary melanomas: a next generation sequencing study. BMC Cancer. 2019;19(1):772.
49. Hocker TL, Singh MK, Tsao H. Melanoma genetics and therapeutic approaches in the 21st century: moving from the benchside to the bedside. J Invest Dermatol. 2008;128(11):2575-95.
50. Shain AH, Bastian BC. From melanocytes to melanomas. Nat Rev Cancer. 2016;16(6):345-58.
51. Russo AE, Torrisi E, Bevelacqua Y, Perrotta R, Libra M, McCubrey JA, et al. Melanoma: molecular pathogenesis and emerging target therapies (Review). Int J Oncol. 2009;34(6):1481-9.
52. Network CGA. Genomic Classification of Cutaneous Melanoma. Cell. 2015;161(7):1681-96.
53. Davies H, Bignell GR, Cox C, Stephens P, Edkins S, Clegg S, et al. Mutations of the BRAF gene in human cancer. Nature. 2002;417(6892):949-54.
54. Libra M, Malaponte G, Navolanic PM, Gangemi P, Bevelacqua V, Proietti L, et al. Analysis of BRAF mutation in primary and metastatic melanoma. Cell Cycle. 2005;4(10):1382-4.
55. Demunter A, Stas M, Degreef H, De Wolf-Peeters C, van den Oord JJ. Analysis of N- and K-ras mutations in the distinctive tumor progression phases of melanoma. J Invest Dermatol. 2001;117(6):1483-9.
56. Kiuru M, Busam KJ. The NF1 gene in tumor syndromes and melanoma. Lab Invest. 2017;97(2):146-57.
57. Chang F, Steelman LS, Shelton JG, Lee JT, Navolanic PM, Blalock WL, et al. Regulation of cell cycle progression and apoptosis by the Ras/Raf/MEK/ERK pathway (Review). Int J Oncol. 2003;22(3):469-80.
58. Curtin JA, Busam K, Pinkel D, Bastian BC. Somatic activation of KIT in distinct subtypes of melanoma. J Clin Oncol. 2006;24(26):4340-6.
59. Easty DJ, Gray SG, O'Byrne KJ, O'Donnell D, Bennett DC. Receptor tyrosine kinases and their activation in melanoma. Pigment Cell Melanoma Res. 2011;24(3):446-61.
60. Dai DL, Martinka M, Li G. Prognostic significance of activated Akt expression in melanoma: a clinicopathologic study of 292 cases. J Clin Oncol. 2005;23(7):1473-82.
61. Tsao H, Zhang X, Benoit E, Haluska FG. Identification of PTEN/MMAC1 alterations in uncultured melanomas and melanoma cell lines. Oncogene. 1998;16(26):3397-402.
62. Huang FW, Hodis E, Xu MJ, Kryukov GV, Chin L, Garraway LA. Highly recurrent TERT promoter mutations in human melanoma. Science. 2013;339(6122):957-9.
63. Zhang T, Dutton-Regester K, Brown KM, Hayward NK. The genomic landscape of cutaneous melanoma. Pigment Cell Melanoma Res. 2016;29(3):266-83.
64. Gandini S, Sera F, Cattaruzza MS, Pasquini P, Zanetti R, Masini C, et al. Meta-analysis of risk factors for cutaneous melanoma: III. Family history, actinic damage and phenotypic factors. Eur J Cancer. 2005;41(14):2040-59.

65. Badenas C, Aguilera P, Puig-Butillé JA, Carrera C, Malvehy J, Puig S. Genetic counseling in melanoma. Dermatol Ther. 2012;25(5):397-402.
66. Kamb A, Shattuck-Eidens D, Eeles R, Liu Q, Gruis NA, Ding W, et al. Analysis of the p16 gene (CDKN2) as a candidate for the chromosome 9p melanoma susceptibility locus. Nat Genet. 1994;8(1):23-6.
67. Quelle DE, Zindy F, Ashmun RA, Sherr CJ. Alternative reading frames of the INK4a tumor suppressor gene encode two unrelated proteins capable of inducing cell cycle arrest. Cell. 1995;83(6):993-1000.
68. Rizos H, Darmanian AP, Holland EA, Mann GJ, Kefford RF. Mutations in the INK4a/ARF melanoma susceptibility locus functionally impair p14ARF. J Biol Chem. 2001;276(44):41424-34.
69. Chudnovsky Y, Khavari PA, Adams AE. Melanoma genetics and the development of rational therapeutics. J Clin Invest. 2005;115(4):813-24.
70. Serrano M, Hannon GJ, Beach D. A new regulatory motif in cell-cycle control causing specific inhibition of cyclin D/CDK4. Nature. 1993;366(6456):704-7.
71. Midgley CA, Desterro JM, Saville MK, Howard S, Sparks A, Hay RT, et al. An N-terminal p14ARF peptide blocks Mdm2-dependent ubiquitination in vitro and can activate p53 in vivo. Oncogene. 2000;19(19):2312-23.
72. Tao W, Levine AJ. Nucleocytoplasmic shuttling of oncoprotein Hdm2 is required for Hdm2-mediated degradation of p53. Proc Natl Acad Sci U S A. 1999;96(6):3077-80.
73. Kefford RF, Newton Bishop JA, Bergman W, Tucker MA. Counseling and DNA testing for individuals perceived to be genetically predisposed to melanoma: A consensus statement of the Melanoma Genetics Consortium. J Clin Oncol. 1999;17(10):3245-51.
74. Goldstein AM, Chidambaram A, Halpern A, Holly EA, Guerry IV D, Sagebiel R, et al. Rarity of CDK4 germline mutations in familial melanoma. Melanoma Res. 2002;12(1):51-5.
75. Zuo L, Weger J, Yang Q, Goldstein AM, Tucker MA, Walker GJ, et al. Germline mutations in the p16INK4a binding domain of CDK4 in familial melanoma. Nat Genet. 1996;12(1):97-9.
76. Tsao H, Chin L, Garraway LA, Fisher DE. Melanoma: from mutations to medicine. Genes Dev. 2012;26(11):1131-55.
77. Duffy DL, Zhao ZZ, Sturm RA, Hayward NK, Martin NG, Montgomery GW. Multiple pigmentation gene polymorphisms account for a substantial proportion of risk of cutaneous malignant melanoma. J Invest Dermatol. 2010;130(2):520-8.
78. Nathan V, Johansson PA, Palmer JM, Howlie M, Hamilton HR, Wadt K, et al. Germline variants in oculocutaneous albinism genes and predisposition to familial cutaneous melanoma. Pigment Cell Melanoma Res. 2019;32(6):854-63.
79. Sturm RA, Fox C, McClenahan P, Jagirdar K, Ibarrola-Villava M, Banan P, et al. Phenotypic characterization of nevus and tumor patterns in MITF E318K mutation carrier melanoma patients. J Invest Dermatol. 2014;134(1):141-9.
80. Valverde P, Healy E, Jackson I, Rees JL, Thody AJ. Variants of the melanocyte-stimulating hormone receptor gene are associated with red hair and fair skin in humans. Nat Genet. 1995;11(3):328-30.
81. García-Borrón JC, Sánchez-Laorden BL, Jiménez-Cervantes C. Melanocortin-1 receptor structure and functional regulation. Pigment Cell Res. 2005;18(6):393-410.
82. Hennessy A, Oh C, Diffey B, Wakamatsu K, Ito S, Rees J. Eumelanin and pheomelanin concentrations in human epidermis before and after UVB irradiation. Pigment Cell Res. 2005;18(3):220-3.
83. Hunt G, Kyne S, Ito S, Wakamatsu K, Todd C, Thody A. Eumelanin and phaeomelanin contents of human epidermis and cultured melanocytes. Pigment Cell Res. 1995;8(4):202-8.
84. Castejón-Griñán M, Herraiz C, Olivares C, Jiménez-Cervantes C, García-Borrón JC. cAMP-independent non-pigmentary actions of variant melanocortin 1 receptor: AKT-

mediated activation of protective responses to oxidative DNA damage. Oncogene. 2018;37(27):3631-46.
85. Kadekaro AL, Leachman S, Kavanagh RJ, Swope V, Cassidy P, Supp D, et al. Melanocortin 1 receptor genotype: an important determinant of the damage response of melanocytes to ultraviolet radiation. FASEB J. 2010;24(10):3850-60.
86. Song X, Mosby N, Yang J, Xu A, Abdel-Malek Z, Kadekaro AL. alpha-MSH activates immediate defense responses to UV-induced oxidative stress in human melanocytes. Pigment Cell Melanoma Res. 2009;22(6):809-18.
87. Box NF, Wyeth JR, O'Gorman LE, Martin NG, Sturm RA. Characterization of melanocyte stimulating hormone receptor variant alleles in twins with red hair. Hum Mol Genet. 1997;6(11):1891-7.
88. Bastiaens M, ter Huurne J, Gruis N, Bergman W, Westendorp R, Vermeer BJ, et al. The melanocortin-1-receptor gene is the major freckle gene. Hum Mol Genet. 2001;10(16):1701-8.
89. Healy E, Flannagan N, Ray A, Todd C, Jackson IJ, Matthews JN, et al. Melanocortin-1-receptor gene and sun sensitivity in individuals without red hair. Lancet. 2000;355(9209):1072-3.
90. Bliss JM, Ford D, Swerdlow AJ, Armstrong BK, Cristofolini M, Elwood JM, et al. Risk of cutaneous melanoma associated with pigmentation characteristics and freckling: systematic overview of 10 case-control studies. The International Melanoma Analysis Group (IMAGE). Int J Cancer. 1995;62(4):367-76.
91. Palmer JS, Duffy DL, Box NF, Aitken JF, O'Gorman LE, Green AC, et al. Melanocortin-1 receptor polymorphisms and risk of melanoma: is the association explained solely by pigmentation phenotype? Am J Hum Genet. 2000;66(1):176-86.
92. Bastiaens MT, ter Huurne JA, Kielich C, Gruis NA, Westendorp RG, Vermeer BJ, et al. Melanocortin-1 receptor gene variants determine the risk of nonmelanoma skin cancer independently of fair skin and red hair. Am J Hum Genet. 2001;68(4):884-94.
93. Duffy DL, Box NF, Chen W, Palmer JS, Montgomery GW, James MR, et al. Interactive effects of MC1R and OCA2 on melanoma risk phenotypes. Hum Mol Genet. 2004;13(4):447-61.
94. Beaumont KA, Shekar SN, Shekar SL, Newton RA, James MR, Stow JL, et al. Receptor function, dominant negative activity and phenotype correlations for MC1R variant alleles. Hum Mol Genet. 2007;16(18):2249-60.
95. Sturm RA. Skin colour and skin cancer - MC1R, the genetic link. Melanoma Res. 2002;12(5):405-16.
96. Pasquali E, García-Borrón JC, Fargnoli MC, Gandini S, Maisonneuve P, Bagnardi V, et al. MC1R variants increased the risk of sporadic cutaneous melanoma in darker-pigmented Caucasians: a pooled-analysis from the M-SKIP project. Int J Cancer. 2015;136(3):618-31.
97. Raimondi S, Sera F, Gandini S, Iodice S, Caini S, Maisonneuve P, et al. MC1R variants, melanoma and red hair color phenotype: a meta-analysis. Int J Cancer. 2008;122(12):2753-60.
98. Tagliabue E, Gandini S, Bellocco R, Maisonneuve P, Newton-Bishop J, Polsky D, et al. Variants as melanoma risk factors independent of at-risk phenotypic characteristics: a pooled analysis from the M-SKIP project. Cancer Manag Res. 2018;10:1143-54.
99. Box NF, Duffy DL, Chen W, Stark M, Martin NG, Sturm RA, et al. MC1R genotype modifies risk of melanoma in families segregating CDKN2A mutations. Am J Hum Genet. 2001;69(4):765-73.
100. Landi MT, Bauer J, Pfeiffer RM, Elder DE, Hulley B, Minghetti P, et al. MC1R germline variants confer risk for BRAF-mutant melanoma. Science. 2006;313(5786):521-2.
101. Herraiz C, Garcia-Borron JC, Jiménez-Cervantes C, Olivares C. MC1R signaling. Intracellular partners and pathophysiological implications. Biochim Biophys Acta Mol Basis Dis. 2017;1863(10 Pt A):2448-61.

102. Herraiz C, Olivares C, Castejón-Griñán M, Abrisqueta M, Jiménez-Cervantes C, García-Borrón JC. Functional Characterization of MC1R-TUBB3 Intergenic Splice Variants of the Human Melanocortin 1 Receptor. PLoS One. 2015;10(12):e0144757.
103. Katritch V, Cherezov V, Stevens RC. Structure-function of the G protein-coupled receptor superfamily. Annu Rev Pharmacol Toxicol. 2013;53:531-56.
104. Tan CP, McKee KK, Weinberg DH, MacNeil T, Palyha OC, Feighner SD, et al. Molecular analysis of a new splice variant of the human melanocortin-1 receptor. FEBS Lett. 1999;451(2):137-41.
105. Sánchez-Más J, Sánchez-Laorden BL, Guillo LA, Jiménez-Cervantes C, García-Borrón JC. The melanocortin-1 receptor carboxyl terminal pentapeptide is essential for MC1R function and expression on the cell surface. Peptides. 2005;26(10):1848-57.
106. Sánchez-Laorden BL, Jiménez-Cervantes C, García-Borrón JC. Regulation of human melanocortin 1 receptor signaling and trafficking by Thr-308 and Ser-316 and its alteration in variant alleles associated with red hair and skin cancer. J Biol Chem. 2007;282(5):3241-51.
107. Dalziel M, Kolesnichenko M, das Neves RP, Iborra F, Goding C, Furger A. Alpha-MSH regulates intergenic splicing of MC1R and TUBB3 in human melanocytes. Nucleic Acids Res. 2011;39(6):2378-92.
108. Smith AG, Box NF, Marks LH, Chen W, Smit DJ, Wyeth JR, et al. The human melanocortin-1 receptor locus: analysis of transcription unit, locus polymorphism and haplotype evolution. Gene. 2001;281(1-2):81-94.
109. Dalziel M, Nunes NM, Furger A. Two G-rich regulatory elements located adjacent to and 440 nucleotides downstream of the core poly(A) site of the intronless melanocortin receptor 1 gene are critical for efficient 3' end processing. Mol Cell Biol. 2007;27(5):1568-80.
110. Herraiz C, Journé F, Ghanem G, Jiménez-Cervantes C, García-Borrón JC. Functional status and relationships of melanocortin 1 receptor signaling to the cAMP and extracellular signal-regulated protein kinases 1 and 2 pathways in human melanoma cells. Int J Biochem Cell Biol. 2012;44(12):2244-52.
111. Mountjoy KG, Robbins LS, Mortrud MT, Cone RD. The cloning of a family of genes that encode the melanocortin receptors. Science. 1992;257(5074):1248-51.
112. Suzuki I, Cone RD, Im S, Nordlund J, Abdel-Malek ZA. Binding of melanotropic hormones to the melanocortin receptor MC1R on human melanocytes stimulates proliferation and melanogenesis. Endocrinology. 1996;137(5):1627-33.
113. D'Orazio J, Fisher DE. Central role for cAMP signaling in pigmentation and UV resistance. Cell Cycle. 2011;10(1):8-9.
114. Kanetsky PA, Swoyer J, Panossian S, Holmes R, Guerry D, Rebbeck TR. A polymorphism in the agouti signaling protein gene is associated with human pigmentation. Am J Hum Genet. 2002;70(3):770-5.
115. Lu D, Willard D, Patel IR, Kadwell S, Overton L, Kost T, et al. Agouti protein is an antagonist of the melanocyte-stimulating-hormone receptor. Nature. 1994;371(6500):799-802.
116. Yang YK, Ollmann MM, Wilson BD, Dickinson C, Yamada T, Barsh GS, et al. Effects of recombinant agouti-signaling protein on melanocortin action. Mol Endocrinol. 1997;11(3):274-80.
117. Herraiz C, Journé F, Abdel-Malek Z, Ghanem G, Jiménez-Cervantes C, García-Borrón JC. Signaling from the human melanocortin 1 receptor to ERK1 and ERK2 mitogen-activated protein kinases involves transactivation of cKIT. Mol Endocrinol. 2011;25(1):138-56.
118. Katz M, Amit I, Yarden Y. Regulation of MAPKs by growth factors and receptor tyrosine kinases. Biochim Biophys Acta. 2007;1773(8):1161-76.
119. Herraiz C, Jiménez-Cervantes C, Zanna P, García-Borrón JC. Melanocortin 1 receptor mutations impact differentially on signalling to the cAMP and the ERK mitogen-activated protein kinase pathways. FEBS Lett. 2009;583(19):3269-74.

120. Cao J, Wan L, Hacker E, Dai X, Lenna S, Jimenez-Cervantes C, et al. MC1R is a potent regulator of PTEN after UV exposure in melanocytes. Mol Cell. 2013;51(4):409-22.
121. Cui R, Widlund HR, Feige E, Lin JY, Wilensky DL, Igras VE, et al. Central role of p53 in the suntan response and pathologic hyperpigmentation. Cell. 2007;128(5):853-64.
122. Levy C, Khaled M, Fisher DE. MITF: master regulator of melanocyte development and melanoma oncogene. Trends Mol Med. 2006;12(9):406-14.
123. Abrisqueta M, Herraiz C, Pérez Oliva AB, Sanchez-Laorden BL, Olivares C, Jiménez-Cervantes C, et al. Differential and competitive regulation of human melanocortin 1 receptor signaling by β-arrestin isoforms. J Cell Sci. 2013;126(Pt 16):3724-37.
124. Kennedy C, ter Huurne J, Berkhout M, Gruis N, Bastiaens M, Bergman W, et al. Melanocortin 1 receptor (MC1R) gene variants are associated with an increased risk for cutaneous melanoma which is largely independent of skin type and hair color. J Invest Dermatol. 2001;117(2):294-300.
125. Maresca V, Flori E, Bellei B, Aspite N, Kovacs D, Picardo M. MC1R stimulation by alpha-MSH induces catalase and promotes its re-distribution to the cell periphery and dendrites. Pigment Cell Melanoma Res. 2010;23(2):263-75.
126. Swope VB, Abdel-Malek ZA. MC1R: Front and Center in the Bright Side of Dark Eumelanin and DNA Repair. Int J Mol Sci. 2018;19(9).
127. Böhm M, Wolff I, Scholzen TE, Robinson SJ, Healy E, Luger TA, et al. alpha-Melanocyte-stimulating hormone protects from ultraviolet radiation-induced apoptosis and DNA damage. J Biol Chem. 2005;280(7):5795-802.
128. He L, Lu XY, Jolly AF, Eldridge AG, Watson SJ, Jackson PK, et al. Spongiform degeneration in mahoganoid mutant mice. Science. 2003;299(5607):710-2.
129. Phan LK, Lin F, LeDuc CA, Chung WK, Leibel RL. The mouse mahoganoid coat color mutation disrupts a novel C3HC4 RING domain protein. J Clin Invest. 2002;110(10):1449-59.
130. Bagher P, Jiao J, Owen Smith C, Cota CD, Gunn TM. Characterization of Mahogunin Ring Finger-1 expression in mice. Pigment Cell Res. 2006;19(6):635-43.
131. Walker WP, Oehler A, Edinger AL, Wagner KU, Gunn TM. Oligodendroglial deletion of ESCRT-I component TSG101 causes spongiform encephalopathy. Biol Cell. 2016;108(11):324-37.
132. Sun K, Johnson BS, Gunn TM. Mitochondrial dysfunction precedes neurodegeneration in mahogunin (Mgrn1) mutant mice. Neurobiol Aging. 2007;28(12):1840-52.
133. Cota CD, Bagher P, Pelc P, Smith CO, Bodner CR, Gunn TM. Mice with mutations in Mahogunin ring finger-1 (Mgrn1) exhibit abnormal patterning of the left-right axis. Dev Dyn. 2006;235(12):3438-47.
134. Cheng D, Xiong C, Li J, Sui C, Wang S, Li H, et al. The effect of mahogunin gene mutant on reproduction in male mice: a new sight for infertility? Andrologia. 2014;46(2):98-105.
135. Fernandez LP, Milne RL, Pita G, Floristan U, Sendagorta E, Feito M, et al. Pigmentation-related genes and their implication in malignant melanoma susceptibility. Exp Dermatol. 2009;18(7):634-42.
136. Guo JF, Zhang L, Li K, Mei JP, Xue J, Chen J, et al. Coding mutations in NUS1 contribute to Parkinson's disease. Proc Natl Acad Sci U S A. 2018;115(45):11567-72.
137. COSMIC. Catalogue Of Somatic Mutations In Cancer 2020 [Available from: https://cancer.sanger.ac.uk/cosmic.
138. Man TK, Lu XY, Jaeweon K, Perlaky L, Harris CP, Shah S, et al. Genome-wide array comparative genomic hybridization analysis reveals distinct amplifications in osteosarcoma. BMC Cancer. 2004;4:45.

139. Tang Q, Holland-Letz T, Slynko A, Cuk K, Marme F, Schott S, et al. DNA methylation array analysis identifies breast cancer associated RPTOR, MGRN1 and RAPSN hypomethylation in peripheral blood DNA. Oncotarget. 2016;7(39):64191-202.
140. Pérez-Oliva AB, Olivares C, Jiménez-Cervantes C, García-Borrón JC. Mahogunin ring finger-1 (MGRN1) E3 ubiquitin ligase inhibits signaling from melanocortin receptor by competition with Galphas. J Biol Chem. 2009;284(46):31714-25.
141. Jiao J, Kim HY, Liu RR, Hogan CA, Sun K, Tam LM, et al. Transgenic analysis of the physiological functions of Mahogunin Ring Finger-1 isoforms. Genesis. 2009;47(8):524-34.
142. Lange A, Mills RE, Lange CJ, Stewart M, Devine SE, Corbett AH. Classical nuclear localization signals: definition, function, and interaction with importin alpha. J Biol Chem. 2007;282(8):5101-5.
143. Benvegnù S, Mateo MI, Palomer E, Jurado-Arjona J, Dotti CG. Aging Triggers Cytoplasmic Depletion and Nuclear Translocation of the E3 Ligase Mahogunin: A Function for Ubiquitin in Neuronal Survival. Mol Cell. 2017;66(3):358-72.e7.
144. Benvegnù S, Wahle T, Dotti CG. E3 ligase mahogunin (MGRN1) influences amyloid precursor protein maturation and secretion. Oncotarget. 2017;8(52):89439-50.
145. Chakrabarti O, Hegde RS. Functional depletion of mahogunin by cytosolically exposed prion protein contributes to neurodegeneration. Cell. 2009;137(6):1136-47.
146. Joazeiro CA, Weissman AM. RING finger proteins: mediators of ubiquitin ligase activity. Cell. 2000;102(5):549-52.
147. Kim BY, Olzmann JA, Barsh GS, Chin LS, Li L. Spongiform neurodegeneration-associated E3 ligase Mahogunin ubiquitylates TSG101 and regulates endosomal trafficking. Mol Biol Cell. 2007;18(4):1129-42.
148. Freemont PS. RING for destruction? Curr Biol. 2000;10(2):R84-7.
149. Weissman AM. Themes and variations on ubiquitylation. Nat Rev Mol Cell Biol. 2001;2(3):169-78.
150. Majumder P, Chakrabarti O. Mahogunin regulates fusion between amphisomes/MVBs and lysosomes via ubiquitination of TSG101. Cell Death Dis. 2015;6:e1970.
151. Kaul Z, Chakrabarti O. Tumor susceptibility gene 101 regulates predisposition to apoptosis via ESCRT machinery accessory proteins. Mol Biol Cell. 2017;28(15):2106-22.
152. Gunn TM, Silvius D, Bagher P, Sun K, Walker KK. MGRN1-dependent pigment-type switching requires its ubiquitination activity but not its interaction with TSG101 or NEDD4. Pigment Cell Melanoma Res. 2013;26(2):263-8.
153. Mukherjee R, Chakrabarti O. Regulation of Mitofusin1 by Mahogunin Ring Finger-1 and the proteasome modulates mitochondrial fusion. Biochim Biophys Acta. 2016;1863(12):3065-83.
154. Mukherjee R, Bhattacharya A, Sau A, Basu S, Chakrabarti S, Chakrabarti O. Calmodulin regulates MGRN1-GP78 interaction mediated ubiquitin proteasomal degradation system. FASEB J. 2019;33(2):1927-45.
155. Chhangani D, Mishra A. Mahogunin ring finger-1 (MGRN1) suppresses chaperone-associated misfolded protein aggregation and toxicity. Sci Rep. 2013;3:1972.
156. Chhangani D, Nukina N, Kurosawa M, Amanullah A, Joshi V, Upadhyay A, et al. Mahogunin ring finger 1 suppresses misfolded polyglutamine aggregation and cytotoxicity. Biochim Biophys Acta. 2014;1842(9):1472-84.
157. Chhangani D, Endo F, Amanullah A, Upadhyay A, Watanabe S, Mishra R, et al. Mahogunin ring finger 1 confers cytoprotection against mutant SOD1 aggresomes and is defective in an ALS mouse model. Neurobiol Dis. 2016;86:16-28.
158. Srivastava D, Chakrabarti O. Mahogunin-mediated α-tubulin ubiquitination via noncanonical K6 linkage regulates microtubule stability and mitotic spindle orientation. Cell Death Dis. 2014;5:e1064.

159. Srivastava D, Chakrabarti O. Ubiquitin in regulation of spindle apparatus and its positioning: implications in development and disease. Biochem Cell Biol. 2015;93(4):273-81.
160. Srivastava D, Mukherjee R, Mookherjee D, Chakrabarti O. Mahogunin-mediated regulation of Gαi localisation during mitosis and its effect on spindle positioning. Biochem Cell Biol. 2016;94(4):359-69.
161. Walker WP, Gunn TM. Shades of meaning: the pigment-type switching system as a tool for discovery. Pigment Cell Melanoma Res. 2010;23(4):485-95.
162. Overton JD, Leibel RL. Mahoganoid and mahogany mutations rectify the obesity of the yellow mouse by effects on endosomal traffic of MC4R protein. J Biol Chem. 2011;286(21):18914-29.
163. Cooray SN, Guasti L, Clark AJ. The E3 ubiquitin ligase Mahogunin ubiquitinates the melanocortin 2 receptor. Endocrinology. 2011;152(11):4224-31.
164. Abrisqueta M, Olivares C, Herraiz C, Castejón-Griñán M, Sirés-Campos J, García-Borrón JC, et al. Human melanocortin 1 receptor-mediated ubiquitination of nonvisual arrestins. Role of Mahogunin Ring Finger 1 E3 ligase. Biochim Biophys Acta Mol Cell Res. 2018;1865(1):76-94.
165. Pérez Oliva AB, Fernéndez LP, Detorre C, Herráiz C, Martínez-Escribano JA, Benítez J, et al. Identification and functional analysis of novel variants of the human melanocortin 1 receptor found in melanoma patients. Hum Mutat. 2009;30(5):811-22.
166. Oliveros JC, Franch M, Tabas-Madrid D, San-León D, Montoliu L, Cubas P, et al. Breaking-Cas-interactive design of guide RNAs for CRISPR-Cas experiments for ENSEMBL genomes. Nucleic Acids Res. 2016;44(W1):W267-71.
167. Ran FA, Hsu PD, Wright J, Agarwala V, Scott DA, Zhang F. Genome engineering using the CRISPR-Cas9 system. Nat Protoc. 2013;8(11):2281-308.
168. Whittaker JR. Quantitative measurement by microdensitometry of tyrosinase (dopa oxidase) development in whole small ascidian embryos. Histochemistry. 1981;71(3):349-59.
169. Herraiz C, Calvo F, Pandya P, Cantelli G, Rodriguez-Hernandez I, Orgaz JL, et al. Reactivation of p53 by a Cytoskeletal Sensor to Control the Balance Between DNA Damage and Tumor Dissemination. J Natl Cancer Inst. 2016;108(1).
170. Wilkinson S, Paterson HF, Marshall CJ. Cdc42-MRCK and Rho-ROCK signalling cooperate in myosin phosphorylation and cell invasion. Nat Cell Biol. 2005;7(3):255-61.
171. Nieminuszczy J, Schwab RA, Niedzwiedz W. The DNA fibre technique - tracking helicases at work. Methods. 2016;108:92-8.
172. Ghesquière P, Elsherbiny A, Fortier E, McQuaid M, Mazzaferri J, Bélanger F, et al. An open-source algorithm for rapid unbiased determination of DNA fiber length. DNA Repair (Amst). 2019;74:26-37.
173. Del Duca D, Werbowetski T, Del Maestro RF. Spheroid preparation from hanging drops: characterization of a model of brain tumor invasion. J Neurooncol. 2004;67(3):295-303.
174. Fleisig H, Wong J. Measuring cell cycle progression kinetics with metabolic labeling and flow cytometry. J Vis Exp. 2012(63):e4045.
175. Sánchez-Más J, Guillo LA, Zanna P, Jiménez-Cervantes C, García-Borrón JC. Role of G protein-coupled receptor kinases in the homologous desensitization of the human and mouse melanocortin 1 receptors. Mol Endocrinol. 2005;19(4):1035-48.
176. Jiao J, Sun K, Walker WP, Bagher P, Cota CD, Gunn TM. Abnormal regulation of TSG101 in mice with spongiform neurodegeneration. Biochim Biophys Acta. 2009;1792(10):1027-35.
177. Upadhyay A, Amanullah A, Chhangani D, Mishra R, Prasad A, Mishra A. Mahogunin Ring Finger-1 (MGRN1), a Multifaceted Ubiquitin Ligase: Recent Unraveling of Neurobiological Mechanisms. Mol Neurobiol. 2016;53(7):4484-96.
178. Goding CR, Arnheiter H. MITF-the first 25 years. Genes Dev. 2019;33(15-16):983-1007.

179. Hida T, Wakamatsu K, Sviderskaya EV, Donkin AJ, Montoliu L, Lynn Lamoreux M, et al. Agouti protein, mahogunin, and attractin in pheomelanogenesis and melanoblast-like alteration of melanocytes: a cAMP-independent pathway. Pigment Cell Melanoma Res. 2009;22(5):623-34.
180. Kaverina I, Straube A. Regulation of cell migration by dynamic microtubules. Semin Cell Dev Biol. 2011;22(9):968-74.
181. Mukherji M, Bell R, Supekova L, Wang Y, Orth AP, Batalov S, et al. Genome-wide functional analysis of human cell-cycle regulators. Proc Natl Acad Sci U S A. 2006;103(40):14819-24.
182. Petermann E, Orta ML, Issaeva N, Schultz N, Helleday T. Hydroxyurea-stalled replication forks become progressively inactivated and require two different RAD51-mediated pathways for restart and repair. Mol Cell. 2010;37(4):492-502.
183. Gunn TM, Silvius D, Lester A, Gibbs B. Chronic and age-dependent effects of the spongiform neurodegeneration-associated MGRN1 E3 ubiquitin ligase on mitochondrial homeostasis. Mamm Genome. 2019;30(5-6):151-65.
184. Bouwman BAM, Crosetto N. Endogenous DNA Double-Strand Breaks during DNA Transactions: Emerging Insights and Methods for Genome-Wide Profiling. Genes (Basel). 2018;9(12).
185. Denat L, Kadekaro AL, Marrot L, Leachman SA, Abdel-Malek ZA. Melanocytes as instigators and victims of oxidative stress. J Invest Dermatol. 2014;134(6):1512-8.
186. Smit NP, van Nieuwpoort FA, Marrot L, Out C, Poorthuis B, van Pelt H, et al. Increased melanogenesis is a risk factor for oxidative DNA damage--study on cultured melanocytes and atypical nevus cells. Photochem Photobiol. 2008;84(3):550-5.
187. Lee TH, Kang TH. DNA Oxidation and Excision Repair Pathways. Int J Mol Sci. 2019;20(23).
188. Alonso-Curbelo D, Riveiro-Falkenbach E, Pérez-Guijarro E, Cifdaloz M, Karras P, Osterloh L, et al. RAB7 controls melanoma progression by exploiting a lineage-specific wiring of the endolysosomal pathway. Cancer Cell. 2014;26(1):61-76.
189. Gilot D, Migault M, Bachelot L, Journé F, Rogiers A, Donnou-Fournet E, et al. A non-coding function of TYRP1 mRNA promotes melanoma growth. Nat Cell Biol. 2017;19(11):1348-57.
190. Journe F, Id Boufker H, Van Kempen L, Galibert MD, Wiedig M, Salès F, et al. TYRP1 mRNA expression in melanoma metastases correlates with clinical outcome. Br J Cancer. 2011;105(11):1726-32.
191. Bertolotto C, Lesueur F, Giuliano S, Strub T, de Lichy M, Bille K, et al. A SUMOylation-defective MITF germline mutation predisposes to melanoma and renal carcinoma. Nature. 2011;480(7375):94-8.
192. Huszno J, Kołosza Z, Grzybowska E. mutation in breast cancer patients: Analysis of prognostic factors and survival. Oncol Lett. 2019;17(2):1986-95.
193. Penas C, Apraiz A, Muñoa I, Arroyo-Berdugo Y, Rasero J, Ezkurra PA, et al. RKIP Regulates Differentiation-Related Features in Melanocytic Cells. Cancers (Basel). 2020;12(6).
194. Sevilla A, Morales MC, Ezkurra PA, Rasero J, Velasco V, Cancho-Galan G, et al. BRAF V600E mutational load as a prognosis biomarker in malignant melanoma. PLoS One. 2020;15(3):e0230136.
195. Gershenwald JE, Scolyer RA, Hess KR, Sondak VK, Long GV, Ross MI, et al. Melanoma staging: Evidence-based changes in the American Joint Committee on Cancer eighth edition cancer staging manual. CA Cancer J Clin. 2017;67(6):472-92.
196. Foth M, Wouters J, de Chaumont C, Dynoodt P, Gallagher WM. Prognostic and predictive biomarkers in melanoma: an update. Expert Rev Mol Diagn. 2016;16(2):223-37.
197. Keung EZ, Gershenwald JE. The eighth edition American Joint Committee on Cancer (AJCC) melanoma staging system: implications for melanoma treatment and care. Expert Rev Anticancer Ther. 2018;18(8):775-84.

198. Stiegel E, Xiong D, Ya J, Funchain P, Isakov R, Gastman B, et al. Prognostic value of sentinel lymph node biopsy according to Breslow thickness for cutaneous melanoma. J Am Acad Dermatol. 2018;78(5):942-8.
199. Mancuso F, Lage S, Rasero J, Díaz-Ramón JL, Apraiz A, Pérez-Yarza G, et al. Serum markers improve current prediction of metastasis development in early-stage melanoma patients: a machine learning-based study. Mol Oncol. 2020;14(8):1705-18.
200. Callender GG, Egger ME, Burton AL, Scoggins CR, Ross MI, Stromberg AJ, et al. Prognostic implications of anatomic location of primary cutaneous melanoma of 1 mm or thicker. Am J Surg. 2011;202(6):659-64; discussion 64-5.
201. Lideikaitė A, Mozūraitienė J, Letautienė S. Analysis of prognostic factors for melanoma patients. Acta Med Litu. 2017;24(1):25-34.
202. Borkowska AM, Szumera-Ciećkiewicz A, Spałek MJ, Teterycz P, Czarnecka AM, Rutkowski P. Clinicopathological Features and Prognostic Factors of Primary Acral Melanomas in Caucasians. J Clin Med. 2020;9(9).
203. Philpott C, Tovell H, Frayling IM, Cooper DN, Upadhyaya M. The NF1 somatic mutational landscape in sporadic human cancers. Hum Genomics. 2017;11(1):13.
204. Hilke FJ, Sinnberg T, Gschwind A, Niessner H, Demidov G, Amaral T, et al. Distinct Mutation Patterns Reveal Melanoma Subtypes and Influence Immunotherapy Response in Advanced Melanoma Patients. Cancers (Basel). 2020;12(9).
205. Ticha I, Hojny J, Michalkova R, Kodet O, Krkavcova E, Hajkova N, et al. A comprehensive evaluation of pathogenic mutations in primary cutaneous melanomas, including the identification of novel loss-of-function variants. Sci Rep. 2019;9(1):17050.
206. Xia J, Jia P, Hutchinson KE, Dahlman KB, Johnson D, Sosman J, et al. A meta-analysis of somatic mutations from next generation sequencing of 241 melanomas: a road map for the study of genes with potential clinical relevance. Mol Cancer Ther. 2014;13(7):1918-28.
207. Podhorecka M, Skladanowski A, Bozko P. H2AX Phosphorylation: Its Role in DNA Damage Response and Cancer Therapy. J Nucleic Acids. 2010;2010.
208. Fairbairn DW, Olive PL, O'Neill KL. The comet assay: a comprehensive review. Mutat Res. 1995;339(1):37-59.
209. Povirk LF. DNA damage and mutagenesis by radiomimetic DNA-cleaving agents: bleomycin, neocarzinostatin and other enediynes. Mutat Res. 1996;355(1-2):71-89.
210. Yuan SS, Chang HL, Hou MF, Chan TF, Kao YH, Wu YC, et al. Neocarzinostatin induces Mre11 phosphorylation and focus formation through an ATM- and NBS1-dependent mechanism. Toxicology. 2002;177(2-3):123-30.
211. Bétous R, Goullet de Rugy T, Pelegrini AL, Queille S, de Villartay JP, Hoffmann JS. DNA replication stress triggers rapid DNA replication fork breakage by Artemis and XPF. PLoS Genet. 2018;14(7):e1007541.
212. Pond KW, de Renty C, Yagle MK, Ellis NA. Rescue of collapsed replication forks is dependent on NSMCE2 to prevent mitotic DNA damage. PLoS Genet. 2019;15(2):e1007942.
213. Saintigny Y, Delacôte F, Varès G, Petitot F, Lambert S, Averbeck D, et al. Characterization of homologous recombination induced by replication inhibition in mammalian cells. EMBO J. 2001;20(14):3861-70.
214. Wilhelm T, Said M, Naim V. DNA Replication Stress and Chromosomal Instability: Dangerous Liaisons. Genes (Basel). 2020;11(6).
215. Abraham RT. Cell cycle checkpoint signaling through the ATM and ATR kinases. Genes Dev. 2001;15(17):2177-96.
216. Nam EA, Zhao R, Glick GG, Bansbach CE, Friedman DB, Cortez D. Thr-1989 phosphorylation is a marker of active ataxia telangiectasia-mutated and Rad3-related (ATR) kinase. J Biol Chem. 2011;286(33):28707-14.
217. Cimprich KA, Cortez D. ATR: an essential regulator of genome integrity. Nat Rev Mol Cell Biol. 2008;9(8):616-27.

218. Stiff T, Walker SA, Cerosaletti K, Goodarzi AA, Petermann E, Concannon P, et al. ATR-dependent phosphorylation and activation of ATM in response to UV treatment or replication fork stalling. EMBO J. 2006;25(24):5775-82.
219. Shiotani B, Zou L. ATR signaling at a glance. J Cell Sci. 2009;122(Pt 3):301-4.
220. Okuno Y, McNairn AJ, den Elzen N, Pines J, Gilbert DM. Stability, chromatin association and functional activity of mammalian pre-replication complex proteins during the cell cycle. EMBO J. 2001;20(15):4263-77.
221. Satyanarayana A, Kaldis P. A dual role of Cdk2 in DNA damage response. Cell Div. 2009;4:9.
222. Bačević K, Lossaint G, Achour TN, Georget V, Fisher D, Dulić V. Cdk2 strengthens the intra-S checkpoint and counteracts cell cycle exit induced by DNA damage. Sci Rep. 2017;7(1):13429.
223. Lane ME, Yu B, Rice A, Lipson KE, Liang C, Sun L, et al. A novel cdk2-selective inhibitor, SU9516, induces apoptosis in colon carcinoma cells. Cancer Res. 2001;61(16):6170-7.
224. Munro S, Carr SM, La Thangue NB. Diversity within the pRb pathway: is there a code of conduct? Oncogene. 2012;31(40):4343-52.
225. Mukherjee R, Majumder P, Chakrabarti O. MGRN1-mediated ubiquitination of α-tubulin regulates microtubule dynamics and intracellular transport. Traffic. 2017;18(12):791-807.
226. Saini N, Giacobone CK, Klimczak LJ, Papas BN, Burkholder AB, Li JL, et al. UV-exposure, endogenous DNA damage, and DNA replication errors shape the spectra of genome changes in human skin. PLoS Genet. 2021;17(1):e1009302.
227. Myers JS, Zhao R, Xu X, Ham AJ, Cortez D. Cyclin-dependent kinase 2 dependent phosphorylation of ATRIP regulates the G2-M checkpoint response to DNA damage. Cancer Res. 2007;67(14):6685-90.
228. Cortez D, Guntuku S, Qin J, Elledge SJ. ATR and ATRIP: partners in checkpoint signaling. Science. 2001;294(5547):1713-6.
229. Müller-Tidow C, Ji P, Diederichs S, Potratz J, Bäumer N, Köhler G, et al. The cyclin A1-CDK2 complex regulates DNA double-strand break repair. Mol Cell Biol. 2004;24(20):8917-28.
230. Deans AJ, Khanna KK, McNees CJ, Mercurio C, Heierhorst J, McArthur GA. Cyclin-dependent kinase 2 functions in normal DNA repair and is a therapeutic target in BRCA1-deficient cancers. Cancer Res. 2006;66(16):8219-26.
231. Jarrett SG, Wolf Horrell EM, D'Orazio JA. AKAP12 mediates PKA-induced phosphorylation of ATR to enhance nucleotide excision repair. Nucleic Acids Res. 2016;44(22):10711-26.
232. Jarrett SG, Wolf Horrell EM, Christian PA, Vanover JC, Boulanger MC, Zou Y, et al. PKA-mediated phosphorylation of ATR promotes recruitment of XPA to UV-induced DNA damage. Mol Cell. 2014;54(6):999-1011.
233. Jarrett SG, Wolf Horrell EM, Boulanger MC, D'Orazio JA. Defining the Contribution of MC1R Physiological Ligands to ATR Phosphorylation at Ser435, a Predictor of DNA Repair in Melanocytes. J Invest Dermatol. 2015;135(12):3086-95.
234. Wolf Horrell EM, Boulanger MC, D'Orazio JA. Melanocortin 1 Receptor: Structure, Function, and Regulation. Front Genet. 2016;7:95.
235. Blackford AN, Jackson SP. ATM, ATR, and DNA-PK: The Trinity at the Heart of the DNA Damage Response. Mol Cell. 2017;66(6):801-17.
236. Melnikova VO, Bolshakov SV, Walker C, Ananthaswamy HN. Genomic alterations in spontaneous and carcinogen-induced murine melanoma cell lines. Oncogene. 2004;23(13):2347-56.
237. Rossi M, Pellegrini C, Cardelli L, Ciciarelli V, Di Nardo L, Fargnoli MC. Familial Melanoma: Diagnostic and Management Implications. Dermatol Pract Concept. 2019;9(1):10-6.
238. Seetharaman S, Etienne-Manneville S. Microtubules at focal adhesions - a double-edged sword. J Cell Sci. 2019;132(19).

APPENDIX

BUFFERS AND REAGENTS COMPOSITION

- **Phosphate buffered saline (PBS)**: 137 mM NaCl, 2.7 mM KCl, 10 mM Na_2HPO_4, 1 mM KH_2PO_4, pH 7.2.

- **Tris Buffer Saline (TBS)**: 20 mM Tris, 137 mM NaCl, pH 7.4.

- **Trypsin-EDTA solution**: 0.5 % trypsin, 0.2 % EDTA in PBS.

- **Tris-acetate-EDTA buffer (TAE)**: 40 mM Tris, 1 mM EDTA and 30 mM acetic acid (0.175 % v/v).

- **Lysis buffer I**: 50 mM Tris-HCl pH 7.5, 1 mM EDTA, 1 % Igepal.

- **Lysis buffer II**: 150 mM sodium chloride, 1.0 Triton X-100, 0.5 % sodium deoxycholate, 0.1 % SDS, 50 mM Tris, pH 8.0.

Lysis buffer I/II were supplemented with 0.1 mM PMSF, 10 mM IAA, 10 mM NEM and phosphatase inhibitors (200 mM imidazol, 100 mM NaF, 100 mM sodium o-vanadate and 1 M β-Glycerol phosphate).

- **Polyacrylamide Gels**:

  - **Resolving gel (10% acrylamide)**: 1.6 ml H_2O, 1.33 ml Acrylamide/bisacrylamide (AA/bAA), 1.25 ml 1.5 M Tris-HCl 0.4 % SDS pH 8.8, 40 µl 10 % APS and 5 µl TEMED.

  - **Stacking gel (4% acrylamide)**: 1.2 ml H_2O, 270 µl AA/bAA, 0.5 ml 1.5 M Tris-HCl 0.4 % SDS pH 8.8, 20 µl 10 % APS and 2.5 µl TEMED.

- **4X Loading sample buffer**: 250 mM Tris pH 6.8, 8 % SDS, 20 % glycerol, 0.08 % bromophenol blue and 3.2 M β-mercaptoethanol.

- **Running buffer**: 25 mM Tris, 190 mM glycine, 0.1 % SDS, pH 8.3.

- **Transfer buffer**: 48 mM Tris, 39 mM Glycine, 0.04 % SDS, 20 % methanol, pH 9.2.

- **Washing buffer**: 1X TBS /0.1 %Tween-20.

- **Blocking buffer**: 2-5 % BSA or milk in TBST.

- **CSK Buffer:** 10 mM PIPES pH 6.8, 100 mM NaCl, 300 mM sucrose, 3 mM $MgCl_2$, 1 mM EGTA, 50 mM NaF, 0.1 mM Na_3VO_4 and 0.1 % Triton X-100.

- **IP100 buffer**: 25 mM Tris pH 7.5, 5 mM $MgCl_2$, 1.0 % Triton X-100, 10 % glycerol, 100 mM KCl and 0.3 mM DTT.

- **Comet electrophoresis solution, pH>13**: 200 mM NaOH and 1 mM EDTA.

- **Comet neutral electrophoresis solution, pH=9**: 1.5 M NaOAc and 500 mM Tris Base.

- **Comet DNA Precipitation Solution**: 7.5 M NH_4Ac.

- **Giemsa Solution**: 7 % Giemsa Stain in KH_2PO_4 Buffer, pH 6.8.